Large Eddy Simulation of Separated Boundary Layer Transition under Free-Stream Turbulence

Mostafa Langari

Submitted in partial fulfilment of the requirements for the award of Doctor of Philosophy

University of Sussex, Department of Engineering and Informatics

October, 2013

I hereby declare that I am responsible for the work submitted in this thesis, the original work is my own except as specified in acknowledgments or in footnotes, and the thesis has not been and will not be, submitted in whole or in part to another University for the award of any other degree.

Acknowledgements

I wish to thank Dr. Zhiyin Yang for his guidance and encouragement during the course of this project. His support and advice was essential for completion of the present work. I would also like to thank Dr. Gary Page for letting me work on his code.

I would like to thank Victor Wang, JingHua Li, and Gemma Febrer-Alles for their help and advice on code settings and Barani Gunasekaran for his tips on using *ICEM*. I would also like to acknowledge the financial support of Loughborough University and University of Sussex and thank the HPC staff at both universities for their technical support.

The last but foremost is that special thanks to my family for their endless support and encouragement throughout this crucial stage in my life.

Abstract

Physics of laminar-to-turbulent transition in a separated-reattached flow subjected to two free-stream turbulence levels have been explored using Large-Eddy Simulation (LES). Separation of the laminar boundary layer occurs at a curvature change over a flat plate with a semi-circular leading edge. A numerical trip has been used to generate the targeted free-stream turbulence levels. A dynamic Sub-grid-scale (SGS) model has been employed and excellent agreement has been achieved between the LES results and the experimental data.

Detailed investigation of the LES data has been carried out to explore the primary instability mechanism at low (< 0.2%) and high free-stream turbulence (5.6%). The flow visualisations and spectral analysis of the separated shear layer reveal that the two-dimensional Kelvin-Helmholtz instability mode, well known to occur at low free-stream turbulence levels, is bypassed at a higher level leading to earlier breakdown to turbulence.

The whole transition process leading to breakdown to turbulence has been revealed clearly by the flow visualisations and the differences between the low and high free-stream turbulence cases are clearly evident. Coherent structures are also visualised using iso-surfaces of the Q-criterion and for the high free-stream turbulence case the spanwise oriented two-dimensional rolls, which are clearly apparent in the low free-stream turbulence case, are not visible anymore. Detailed quantitative comparisons between the present LES results against experimental data and the previous LES results at low free-stream turbulence using a staggered grid have been done and a good agreement has been obtained, indicating that the current LES using a co-located grid with pressure smoothing can predict transitional flows accurately.

Comprehensive spectral analysis of the separated shear layer at two free-stream turbulence levels has been performed. Under very low free-stream turbulence condition, a distinct regular vortex shedding and trace of the low-frequency flapping phenomena were detected. Under the higher free-stream turbulence however, a mild high-frequency activity was observed. No low frequency oscillations could be detected.

Preface

This thesis considers transition within laminar separation bubble flow under low and relatively high levels of free-stream turbulence intensity. The work from this thesis has been published in the following papers:

i. Langari, Mostafa, Yang, Zhiyin, 2013. Numerical study of the primary instability in a separated boundary layer transition under elevated free-stream turbulence. *Physics of Fluids*, 25 (7). 076106-12.

ii. Langari, Mostafa, Yang, Zhiyin and Page, Gary J., 2013. Large-eddy simulation of transitional flows using a co-located grid. *International Journal of Computational Fluid Dynamics*. 27 (4-5). pp. 189-200.

iii. Langari, Mostafa, Yang, Zhiyin, 2010. On Transition Process in Separated-Reattached Flows. *Advances and Applications in Fluid Mechanics*, 8 (2). pp. 157-181.

Contents

List of Figures

Notations

A	Tripping disturbance level
C_s	Smagorinsky model constant
C	Dynamic SGS model constant
D	Plate thickness
DNS	Direct Numerical Simulation
ERCOFTAC	European Research Community On Flow, Turbulence and Combustion
E_u	Streamwise velocity spectra
E_v	Wall-normal velocity spectra
E_w	Spanwise velocity spectra
f	frequency
FST	Free-stream turbulence
h	Shear layer thickness
i	Streamwise axis index
j	Wall-normal axis index
k	Spanwise axis index
K	Wave number
KH	Kelvin-Helmholtz
l	mean bubble length
LES	Large eddy simulation
n_x	Number of cells in streamwise direction
n_y	Number of cells in wall-normal direction
n_z	Number of cells in spanwise direction
NS	Navier-Stokes
NFST	No free-stream turbulence
P	Pressure
r_1, r_2, r_3	components of 3D random vector
RANS	Reynolds-Averaged Numerical Simulation
SGS	subgrid scale
$\bar{S}_{ij}$	large-scale strain-rate
$\lvert\bar{S}\rvert$	is the magnitude of filtered strain rate tensor
Tij	subtest-scale (STS) stress

U, V, W	Velocity components
U_0	inlet velocity
u'	Root mean square value of the streamwise volocity
$\bar{U}_{target}(y)$	Targer mean velocity profile
$u'_{target}(y)$	Target rms profile
v'	Root mean square value of the wall-normal volocity
w'	Root mean square value of the spanwise volocity
x	Streamwise axis
y	Wall-normal axis
$y+$	Dimensionless distance from the wall
z	Spanwise axis
τ_{ij}^{s}	subgrid-scale stress
$\Delta x+$	Streamwise mesh size in wall-units
$\Delta y+$	Wall-normal mesh size in wall-units
$\Delta z+$	Spanwise mesh size in wall-units

Chapter 1

Introduction

Separated flows are important in many engineering applications from cooling of small electronic devices to airfoil and turbo-machinery design. Understanding the physics of such flows is important; as separation can lead to dramatic changes in drag, lift and heat transfer rates. The stall phenomenon which is characterised by a loss in lift and increase of drag is related to separation of boundary layer. In the stall condition reattachment of the separated boundary layer is hindered or may never happen which will cause large recirculation regions. If a separated flow reattaches downstream, it causes the formation of a separation bubble; its characteristics are a crucial aspect of the engineering design process.

Separation can be induced either in a flow containing sharp geometry gradients or by an adverse pressure gradient where the momentum in the boundary layer is not high enough to overcome the pressure gradient. Geometry induced separation happens in situations such as flow over a blunt plate and forward/ backward facing step geometries where the separation is fixed in space and happens at all values of Reynolds (Re) numbers (other than very low Re number in Stokes creeping flow). In a separation induced by adverse pressure gradient however, both separation and reattachment locations can change as flow parameters vary (Alving & Fernholz, 1996).

Considering the state of the boundary layer at separation and reattachment, three main types of separation bubbles are recognisable in the literature; laminar, transitional, and turbulent. In the laminar separation bubble the flow at both separation and reattachment is laminar. The transitional separation bubble has a laminar separation while reattachment is turbulent, and a turbulent separation bubble is one where flow is already turbulent at separation. The attention in the current study is on the transitional separation bubble. Laminar boundary layer separation occurs in many practical problems such as low Re number flow of airfoils and flows over steps, obstacles,

humps and other forms of localised variations of a surface geometry. A feature of laminar separated flow is that it becomes unstable even at relatively low Re numbers and therefore it usually involves unsteadiness and is likely to undergo a transition to turbulence. Unsteady behaviour and the mean flow pattern in a separated flow are therefore expected to be affected by instability and transition phenomena.

1.1 Motivation

Separation bubbles especially those which fail to reattach may result in a significant loss of lift if they form over aircraft wings, and a subsequent loss of engine efficiency if they form in compressor/turbines. The problem is particularly important in aircraft engines. Airfoils optimised to deliver maximum power at takeoff conditions may experience boundary layer separation at cruise situations due to the low density of air and so the lower Reynolds numbers at altitude. Separation becomes complicated by boundary layer transition. A considerable fraction of the boundary layer on both sides of a turbine airfoil may be transitional (Mayle, 1991), so accurate prediction of transition location is essential for accurate prediction of separation. Predicting the transition is complicated and may depend on a number of factors, particularly the free-stream turbulence intensity. Separation bubbles on flat plates subject to adverse pressure gradients have been considered in quite a few studies. Much has been learned from the work to date, but the nature of separated flow transition is still not completely clear, and existing models are still not as robust as needed for accurate prediction.

The location where transition starts and the spatial extent within which transition takes place, are of crucial interest in engineering design and performance prediction applications. The transition process is also known to influence the behaviour of separation bubbles. Transition in the shear layer of a separated flow is important because if it is not triggered early enough, the shear layer is possible to develop further away from the wall and entrainment may not be enough to cause the reattachment. The role of laminar-turbulent transition in aerodynamics and heat transfer applications has motivated considerable efforts in theoretical, experimental, and computational studies of the phenomenon.

To date, experimental data with high frequency instrumentation and modern computer calculation methods together with increased computational resources have

provided valuable understanding of the phenomenon. Experimental studies have provided fundamental knowledge of parameters influencing transition in bubbles, along with indications for related physical mechanisms. However, such data are limited in providing only limited temporal and spatial resolution of flow parameters and hence a thorough description of the transition process is very difficult if not impossible. Theoretical studies on the other hand, suffer from the limitation imposed by nonlinearity of the transition process at the later stages of transition. Building on the available experimental results some empirical correlation models have been proposed to predict the time-averaged structure and behaviour of separation bubbles however despite improvements such as introducing transition prediction methods, they are still unable to describe sufficiently the unsteady behaviour of transitional bubbles. Reliable transition models are essential for high performance airfoil design purposes and transition modelling techniques are in use to predict transition in such applications. Different approaches such as low-Re turbulence models and experimental correlations are employed (Langtry & Menter, 2005). Such models however, are reported to be of limited accuracy and non universal. Although most models in current use are semi-empirical in nature, a comprehensive understanding of underlying physics of transition process is required for their development (Roberts & Yaras, 2005).

Regarding the recent advancements in computing resources, the transitional bubble has increasingly been the subject of fundamental numerical studies. It is aimed in this research to simulate numerically a typical transitional bubble and supplement the current knowledge regarding the mechanisms and parameters involved in transition of a laminar separated flow.

1.2 Instability and Transition

For any system to be stable infinitesimal disturbances, which are always naturally present in any actual system, must not be amplified. Smooth laminar flows remain stable to small disturbances only when certain conditions are satisfied. When these conditions are not satisfied, the infinitesimal disturbances grow and the flow will shift to the chaotic turbulent condition through a sequence of events known as the transition process (instability of a laminar flow does not immediately lead to turbulence). It is known that the transition process is greatly affected by conditions such as the intensity

of fluctuations in the free stream and wall roughness. The sequence of events that lead to turbulence is also greatly dependant on flow situations; for example transition scenario in free shear flows such as mixing layers, jets, and wakes is different from that in wall-bounded shear flows (Kundu & Cohen, 2004).

1.2.1 Instability Modes and Mechanisms

Two fundamentally different instability mechanisms have been identified in hydrodynamic stability studies of laminar flows. Regarding the shape of the laminar velocity profile, if an inflection point exists in the profile the flow is unstable to small disturbances. This instability has been analysed theoretically by making an inviscid assumption in the equations describing the growth of disturbances, thus this type of instability was known as an *inviscid instability* (Schmid & Henningson, 2001). Velocity profiles of this type are common in the flows such as jets, mixing layers, wakes, and also in separated boundary layers. On the other hand, flows with laminar velocity profiles without inflection point are subject to *viscous instability* where inviscid theory predicts unconditional stability for this kind of profiles. Velocity profiles of this type are characteristic of boundary layer flows near solid walls in the absence of adverse pressure gradient.

The primary instability mechanism at the interface between two parallel streams with different velocities (where velocity shear and a vortex sheet exist) is an inviscid instability called the *Kelvin-Helmholtz* (KH) mechanism. When there is a velocity difference between two streams of fluid, the resulting shear layer is generally unstable; any small perturbation continues to grow and the KH instability causes the sheet to roll up into discrete vortices. The inviscid instability results in formation of KH rolls in the following manner. An external perturbation leads to oscillation of the vortex sheet. This oscillation then causes a pressure difference along the sheet so that the amplitude of the oscillation grows. The upper and lower parts of the sheet are then convected by the upper and lower flows respectively leading to rolling up of the layer.

A typical example of a flow with an inflection point is a jet flow. The transition process in a jet flow is schematically shown in Figure 1.1, where the KH instability is followed by further amplification and formation of stronger vortices through a pairing

process. Further downstream the vortices become distorted by the action of 3D disturbances and the flow breaks down to a large number of eddies leading to fully turbulent regime. A similar process is observed in other flows with an inflection point such as mixing layers and wakes.

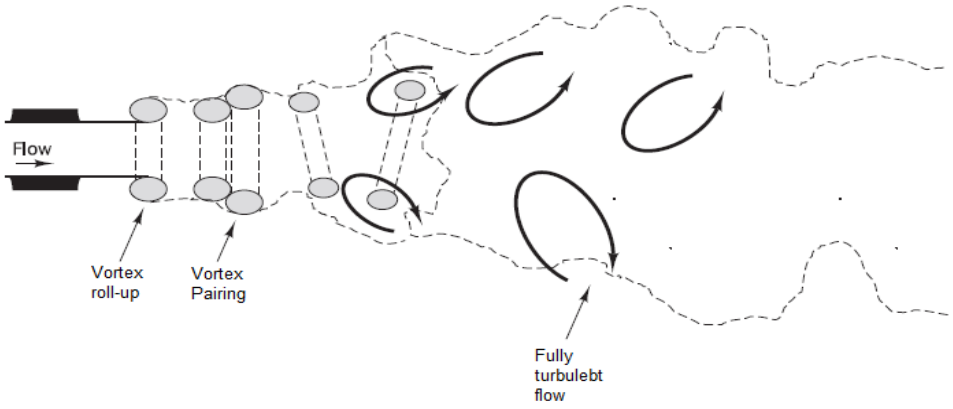

Fig. 1.1 Schematic of transition process in a jet flow (Versteeg & Malalasekera, 1995)

Another possible mechanism for instability, the so-called *Tollmien-Schlichting* (TS) instability, is typically associated with attached boundary layer transition. This is a viscous instability whereby two-dimensional TS waves are superimposed on the laminar boundary layer. These unstable two-dimensional disturbances are called TS waves, which are amplified in the flow direction. In such flows without a point of inflection, viscous instability theory predicts that there is a finite region of Re number wherein infinitesimal disturbances are amplified. If the Re number is high enough initial linear instability takes place. Depending on the amplitude of the waves at maximum linear amplification, it is possible that the amplified waves are weakened further downstream and the flow remains laminar. However if the amplitude is large enough, TS waves undergo a secondary nonlinear instability mechanism. Secondary instabilities cause the TS waves to become 3D and develop into hairpin Λ-vortices (vortex formation), which eventually burst into turbulent spots. The turbulent spots initiate transition to fully turbulent boundary layer flow through lateral and longitudinal growth and merging, yielding a fully turbulent flow state at the end of the transition (Mayle, 1991; Schlichting & Gersten, 2000). A schematic of the transition process in a

flat plate boundary layer at low level of disturbances is shown in Figure 1.2. The process above is known as *natural* transition and can be summarised as follows;

- The laminar boundary layer becomes susceptible to small disturbances at a critical Re number,
- An instability in the form of 2D TS waves is developed,
- Amplification of this instability takes place to a point where 3D instabilities grow and develop into vortices with large fluctuations,
- Turbulent spots emerge in highly fluctuating regions of the flow,
- Turbulent spots grow and convect downstream within the laminar layer, merging eventually into a fully developed turbulent boundary layer.

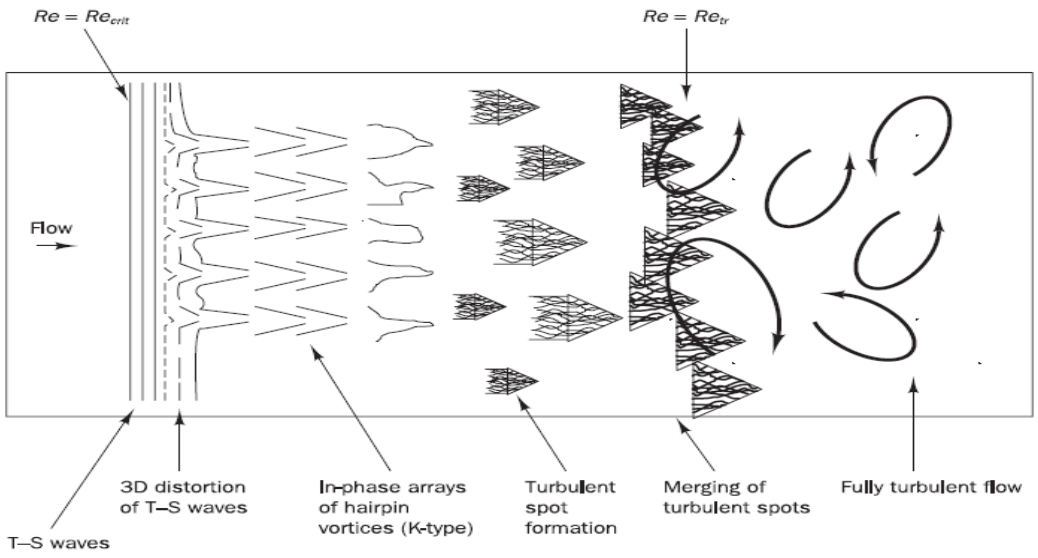

Fig. 1.2 Schematic of natural transition in a flat plate boundary layer (Versteeg & Malalasekera, 1995)

The transition process is well known to be sensitive to the disturbance level. Mayle (1991) distinguished between three main modes of transition; *natural*, *bypass*, and *separated-flow* transition. The "natural" transition as described above is the most basic mode and begins with a weak instability in the laminar boundary layer as first described by Tollmien and Schlichting (Schlichting & Gersten, 2000). It undergoes various stages of amplified instability before reaching to a fully turbulent state.

The second mode, the "bypass" transition, is brought about by large levels of disturbances in the external flow (such as free stream turbulence) and this mode completely bypasses the TS mode of instability. At high external turbulence levels, the first stages of the natural transition process are bypassed and turbulent spots are formed directly within the boundary layer by the influence of free stream turbulence.

Finally, "separated-flow" transition is the case where transition occurs in the free shear layer which is formed on the outer edge of a separated laminar boundary layer and may or may not involve TS instability. In the case the flow reattaches and a bubble forms, the bubble length depends on transition process in the free shear layer and, in general, may involve all of the stages listed above for natural transition (Mayle, 1991). The transition mechanisms and role of free stream turbulence for this mode (i.e. separated flow transition) is not yet fully understood and the current study intends to shed more light on the mechanisms and working parameters involved in this mode of transition.

1.2.2 Absolute vs. Convective Instability

Efforts for better qualitative and quantitative descriptions of shear flows behaviour, have led to introduction of concepts such as absolute and convective instabilities. Establishment of whether any flow is absolutely or convectively unstable is argued as essential for flow control applications to determine how a control input can influence the global development of the flow. Two levels of instability description are possible: *local* (instability of the local velocity profile), and *global* (instability of the entire flow field) (Huerre & Monkewitz, 1990). Considering each streamwise location (local level), if localised disturbances can spread both upstream and downstream the velocity profile is said to be locally absolutely unstable. An absolutely unstable region is defined as a flow region where perturbations added locally are amplified temporally and spatially and as time passes, influence the entire absolutely unstable flow region (Gaster 1962, 1965). In this case any transients produced by switching on the excitation or any residual background fluctuations will amplify and contaminate the entire region. Thus, for temporal and spatial amplification of disturbances in a transitional flow field *absolutely unstable* or *absolutely sensitive* regions need to be determined. In an absolutely unstable flow local absolute instability is dominant in a finite region. Shear

flows with a pocket of absolute instability may exhibit intrinsic dynamics where development of vortices do not depend on spatial amplification of external disturbances but rather on growth of initial local disturbances in time and temporally growing self-excited global modes may be present. Based on this concept, introducing a probe in experimental studies of any absolutely unstable system demands excessive care as any small disturbance may significantly alter the nature of the flow (Huerre & Monkewitz; 1985, 1990).

On the other hand, if locally introduced disturbances are carried away from the source only downstream, the velocity profile is said to be locally convectively unstable. In a convectively unstable region the locally introduced perturbations will not influence the original location of perturbation at later times and the instability wave decays to zero at all points in the flow at large time. Disturbances are convected away as they amplify, eventually leaving the basic flow undisturbed. Any transients produced by switching on the excitation or background fluctuations are convected downstream, and spatially growing waves can be recognised at the excitation frequency. A convectively unstable flow is very sensitive to low-level forcing and the dominant frequency is sensitive to and dependent on the background turbulence intensity and spectral content (Huerre & Monkewitz, 1985). In other words, locally convectively unstable shear flows exhibit extrinsic dynamics where spatial development of unsteady flow is mainly determined by external excitation characteristics (frequency, amplitude, etc). In this case, the flow behaves as an amplifier of external disturbances.

From the above descriptions one can conclude that fluid mechanical instabilities which start suddenly, e.g. as in the wake flow behind a body, are absolutely unstable whereas instability of a boundary layer in which transition occurs via several discrete instabilities are convectively unstable (Schlichting & Gersten, 2000). Schlichting & Gersten utilised these concepts and introduced two possible modes for transition: 1) a laminar-turbulent "*sudden change*" in the flow field when the instability becomes abruptly absolutely unstable, as for example in the wake behind a body in a flow, and 2) a laminar-turbulent "*transition"* for convectively unstable flows where instability carries through several processes leading to turbulence. The subject of convective and absolute instabilities is very rich in theoretical content and comprehensive theoretical

background as applied to fluid flows has been addressed by Huerre & Monkewitz (1985, 1990) and Brevdo (1988).

1.3 Computational Approach

Computational Fluid Dynamics (CFD) is based on the basic idea of employing appropriate numerical algorithms to find solutions to the equations governing the fluid flow. Numerical simulations of flows are mainly used for two purposes; study of fundamental flow physics or, engineering analysis.

In the first case, numerical simulation is used to describe the basic physical mechanisms governing the flow behaviour and help to understand, model, and control these mechanisms. In this kind of study, numerical simulation is required to produce highly accurate data. This implies that the physical model chosen to represent the fluid behaviour must be pertinent and the level of errors introduced by the numerical algorithm and the way they are used by the computers should be as low as possible. For the best possible accuracy, the simulation should provide data of high resolution and take into account all the space-time scales affecting the flow dynamics. This makes the problem difficult when the range of scales is very large, as it is in turbulent flows at high Re for example.

For engineering analysis purposes on the other hand, numerical simulation is used to predict flow characteristics in the design phase and the aim is no longer to generate data for analysing the flow dynamics itself, but rather to predict the values of physical parameters that depend on the flow, e.g. stresses imposed on the bodies within the flow. Here the goal is to reduce the cost and time to develop a prototype. In this case, the restrictions on the quality of representation of the physical phenomena ease off compared to what is required in the fundamental studies and the description does not have to be as detailed as for fundamental studies.

The significant feature of turbulent flows is the chaotic movement of fluid particles. These chaotic fluctuations of the flow variables can be instantaneously resolved by direct numerical simulation (DNS) of the exact governing equations. DNS solves the Navier-Stokes (NS) equations directly down to the smallest scales of the motion and

thus it is the ideal choice for studying fundamental features of transitional and turbulent flows. The challenge however is in the analysis of massive and apparently random data produced by DNS, as there are no criteria for selecting from it in a single lifetime of what is important. On the other hand, such simulations for real engineering problems are still impossible and can be applied only to simple flow problems at low Re numbers. This is due to the fact that the number of grid points required for sufficient spatial resolution is of the order of $Re^{9/4}$ and Re^3 for the CPU time (Pope, 2000). The common approach therefore is to account for the approximate effects of turbulence by employing appropriate turbulence models.

A large range of turbulence models have been developed and turbulence modelling is a subject of ongoing research. Two main classes involving modelling of turbulence at different levels are Reynolds-Averaged Numerical Simulation (RANS) and Large-Eddy Simulation (LES). Some hybrid models have also been developed to utilise benefits of both RANS and LES approaches e.g. Detached-Eddy Simulation (DES) model where near-wall regions are solved using RANS mode and the rest of the flow is treated using the LES approach.

In the RANS approach, statistical averages of the solution are calculated directly, and this approach is predominantly used in engineering applications. An instantaneous variable is decomposed into the sum of a statistical average and a fluctuating part. The fluctuating part cannot be represented directly by the numerical simulation (closure problem) and must be included via a turbulence model. The statistical averaging operation is often associated with time-averaging and thus the mathematical model is that of the steady Reynolds- averaged NS equations. Through this averaging operation the number of scales in the solution can be considerably reduced. The statistical character of the solution however prevents a fine description of the physical mechanisms. This approach therefore is not usable for fundamental studies.

LES on the other hand relies on a subgrid scale (SGS) model to account for smaller-scale motions and resolves only larger scales. In LES the contribution of the large energy-carrying structures to momentum and energy transfer is computed directly and the effects of the small structures which are not resolved by the numerical scheme are modelled. LES represents a three-dimensional time-dependent solution of the governing equations. Compared with turbulence modelling based on the RANS

equations -where grid resolution must be on the order of mean flow- a higher grid resolution on the order of some turbulent scale is required. It is however still considerably cheaper than DNS regarding the required grid resolution at higher Re numbers.

The unsteady and irregular behaviour of flows in transition and turbulent regimes make them very difficult to predict and understand. DNS or LES of flow equations are of primary interest for accurate and detailed study of the problem. An LES approach is employed in the current study, details of which are presented in the next chapter.

1.4 Previous Work

In this chapter, the current state of research on instability and transition within separated-reattached flows is reviewed. Earlier simulations were confined to 2D analysis (Pauley et al., 1990; Tafti & Vanka, 1991a; Ripley & Pauley 1993); for 3D cases, only primary (linear) instability was considered and full transition was not resolved (Tafti & Vanka, 1991b; Pauley, 1994; Rist, 1994). Numerical simulations with full resolution of transition to turbulence and downstream reattachment have been the subject of increasing research in the past decade.

In the case of separation over a plate with a sharp leading edge, it is well known that in flow regimes of sufficiently low Re number (laminar bubble) the flow does not display any unsteadiness and the reattachment length is steady and increases with Re number (Lane & Loehrke, 1980). At higher Re numbers beyond this regime, transitional/turbulent bubble is formed and the separated shear layer becomes unstable after separation. This flow regime is characterised by formation of unsteady 3D coherent structures in the separated and reattachment regions where the reattachment point is not fixed and fluctuates about a mean value (the mean reattachment position is defined as the location where the time-averaged streamwise surface velocity becomes zero). Increased mixing and unsteadiness tends to reduce the mean reattachment length in the higher Re regime; this approaches a value of about 4-5 plate thicknesses after a Re number of about 700 -based on the free stream velocity and plate thickness- (Lane & Loehrke, 1980). Ota & Narita (1978) from their experimental studies of the turbulent separation bubble suggested that a reattachment length of 4-5 plate thicknesses would

be independent of Re number. In an experimental study at Re number of 26000, Kiya & Sasaki (1983), measured a reattachment length of 5 plate thickness. Numerical studies of Tafti & Vanka (1991a, b) showed higher reattachment lengths in contrast to the experiments mentioned above. It was argued that the shorter reattachment distance observed in the experiments was due to the effect of free stream turbulence which was not included in the simulations.

1.4.1 Transition Mechanisms

Many studies have revealed that in the absence of any finite magnitude environmental disturbances, transition in the separated shear layer of a separation bubble is dominantly initiated through the inviscid Kelvin-Helmholtz instability mechanism. This mode of instability closely resembles that of the planar free-shear layer in mixing layers and jets (Ho & Huerre, 1984). Transition in attached boundary layers under such conditions however is developed through the viscous TS instability with generally lower amplifications than the inviscid case (Schlichting & Gersten, 2000; Ho & Huerre, 1984).

The DNS of Spalart & Strelets (2000) for a bubble induced by an adverse pressure gradient over a flat plate under very low incoming disturbances ruled out the transition in the bubble to be caused by convective amplification of entry-region disturbances (TS instability, as in attached boundary layer transition). They reported a wavering behaviour of the separated shear layer while gradually moving away from the wall and then the formation of Kelvin-Helmholtz vortices. The Kelvin-Helmholtz vortices rapidly developed into 3D structures and a sudden transition without the occurrence of vortex pairing was reported. The numerical study of Yang & Voke (2001) revealed a primary 2D instability of a separated shear layer (induced by a smooth leading edge) via Kelvin-Helmholtz mechanism. A similar mechanism was also observed by Abdalla & Yang (2004, 2005) in the free shear layer of a separation bubble over a sharp leading edge.

Rist & Maucher (2002) employed linear stability theory to analyse the effect of the shape of a velocity profile with reverse flow on the instability characteristics. Two regions with two different instability characteristics were observed; the outer separated shear layer region being unstable via an inviscid instability, and the inner near-wall

region of reverse flow with a viscous Re-dependent instability. The study revealed that depending on the distance of the separated layer from the wall and on the reverse flow intensity, one instability mode may dominate. A longer distance of the separated layer from the wall promotes the outer-layer inviscid mode whilst a higher intensity of reverse flow promotes the inner viscous instability. Later on Roberts & Yaras (2006) demonstrated that transition of a separated shear layer through the Kelvin-Helmholtz instability does not eliminate the existence of TS activity in the inner part of the flow. They emphasised the possibility of an interaction between the TS and Kelvin-Helmholtz instability modes, where the roll up of shear layer vorticity into vortical structures occurred at the dominant TS frequency. This was also observed from the coarse DNS study of McAuliffe & Yaras (2008), where the TS activity in the separated shear layer was followed by roll up of spanwise vorticity into discrete vortical structures which are typical for the Kelvin-Helmholtz instability. In the study of McAuliffe & Yaras (2008) on transition of a bubble formed due to adverse pressure gradient, it was reported that the transition process in the separation bubbles shares features from both attached boundary layer and free shear layer. Several studies have shown that under certain conditions Kelvin-Helmholtz instability plays a dominant role in the transition process of separation bubbles. In a number of experimental studies it has also been suggested that the TS instability mechanism may play a significant role in the breakdown to turbulence of separation bubble (Volino & Bohl, 2004; Roberts & Yaras, 2003). For accurate prediction of the extent of the bubble and the characteristics of the turbulent boundary layer downstream of the reattachment, it may be important to identify whether the transition process in a separation bubble is dominated by the TS or Kelvin-Helmholtz mechanism.

Recently McAuliffe & Yaras (2010) performed DNS of a separation bubble on a flat plate in an adverse pressure gradient with low incoming disturbances. Transition was initiated through receptivity of the separated laminar shear layer to small disturbances through the Kelvin-Helmholtz mechanism. Kelvin-Helmholtz instability developed in the separated layer, causing the vorticity in the shear layer to roll-up into distinct spanwise vortical structures; similar to the well-established instability characteristics of free shear layers. Examining the fluctuation levels in their study, two regions of instabilities with two fluctuation peaks was identified; one in the outer separated shear layer and the other in the reverse flow region near the wall. Based on

the linear stability analysis of Rist & Maucher (2002), they inferred that the instability would be characterised with the outer inviscid mode, as the dominant fluctuation peak was observed to occur in the separated shear layer. The coexistence of a less dominant near-wall fluctuation peak was associated with the presence of viscous TS instability. Along with the dominant inviscid Kelvin-Helmholtz instability leading to transition, the presence of this viscous instability near the wall was believed to play a role particularly in cases with high levels of reverse flow or thin separated shear layers. In the experimental study of Lang et al. (2004) similar fluctuation peaks in the inner and outer regions of separated flow had been observed. It seems that along with Kelvin-Helmholtz instability being the dominant primary mechanism in most cases, TS instability is also possible to exist and might be significant in certain situations.

The next stages of the transition process in separated shear layers after the dominant primary Kelvin-Helmholtz instability are less well understood and agreed. In planar free shear layers, the primary spanwise vortices generated by the Kelvin-Helmholtz instability are known to undergo an instability leading to the vortex pairing phenomenon (Ho & Huerre, 1984; Huang & Ho, 1990). Two sequential vortices rotate about each other and then merge while becoming stretched in the flow direction (Winant & Browand, 1974). This pairing of vortices is regarded as the governing secondary mechanism associated with growth of planar free shear layers (Ho & Huerre, 1984). A similar vortex pairing phenomenon has also been reported in some separated shear layer studies (Abdalla & Yang, 2004; Malkiel & Mayle, 1996). It is however emphasised that the existence of pairing is only limited to low Re numbers (McAuliffe & Yaras, 2010). Abdalla & Yang (2004) in a study of separated flow over a sharp leading edge, demonstrated transformation of Kelvin-Helmholtz rolls into 3D structures occurring via an alternative secondary instability known as helical instability associated with helical pairing of vortices. This helical-pairing instability was introduced as the cause of transition from 2D Kelvin-Helmholtz rolls into 3D Lambda (Λ)-shaped and rib structures. The same authors (2005) reported a similar scenario wherein Kelvin-Helmholtz rolls were transformed into Lambda-shaped vortices via a secondary instability mechanism (Fig 1.3).

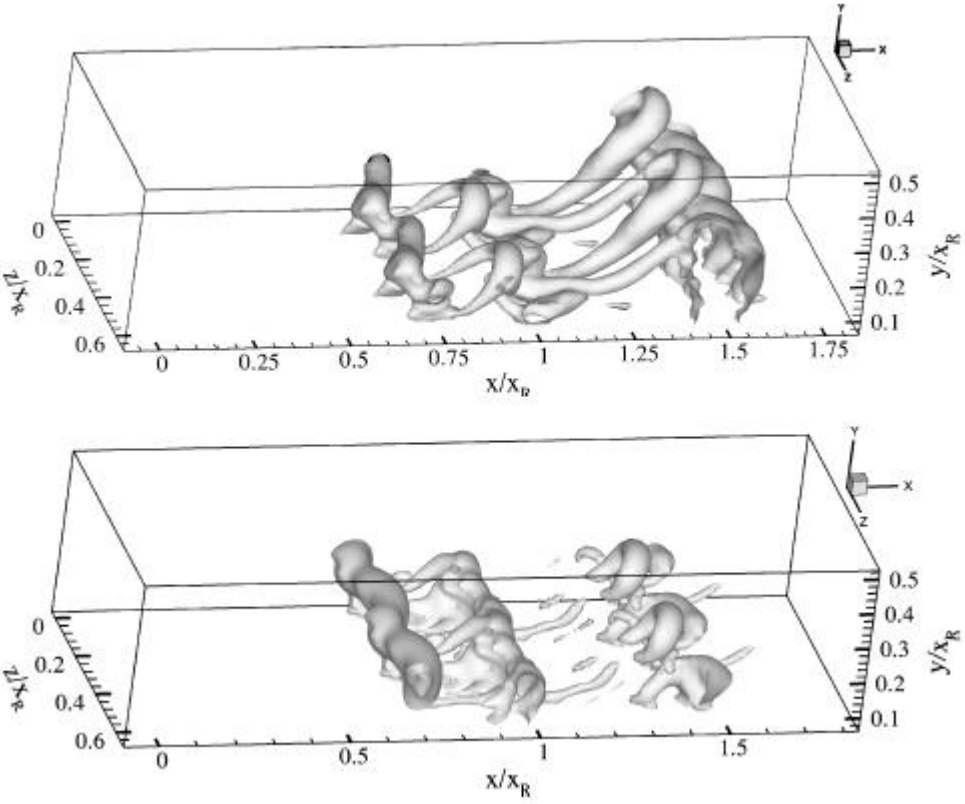

Fig. 1.3 Low-pressure isosurfaces displaying the evolution of the Kelvin–Helmholtz Rolls into the so-called Lambda-shaped vortices (Yang & Abdalla, 2005)

Another noticeable aspect of planar free shear layers is their non-uniformity in the spanwise direction which is related to development of streamwise counter-rotating vortex pairs (Ho & Huerre, 1984). This 3D behaviour is assumed to be associated with a further secondary instability mechanism superimposed on the 2D primary instability, analogous to the scenario in attached boundary layer transition where streamwise stretching of TS waves sets in (Schlichting & Gersten, 2000). Huang & Ho (1990) associated the small-scale turbulence generation in planar free shear layers with the interaction between these streamwise vortices and the spanwise vortices emerging from the primary instability. Malkiel & Mayle (1996) assumed a similar interaction of streamwise and spanwise vorticity for transition in separation bubbles, but this interaction has not yet been confirmed in any studies of transitional separation bubbles. Yang & Voke (2001) observed non-uniform spanwise structures with slow development of 3D motions associated with peak-valley wave structures. Development of 3D motions via a secondary instability mechanism was related to distortion of 2D spanwise vortices and formation of a spanwise peak-valley wave structure.

In some studies of separation bubbles (Spalart & Strelets, 2000; Roberts & Yaras, 2006; McAuliffe & Yaras, 2010), a rapid breakdown to turbulence occurring over a short streamwise distance has been reported. In DNS of Spalart & Strelets (2000) for a bubble over a flat plate with Re number of 36,500 (based on the length of the laminar separated layer and the edge velocity) and under very low incoming disturbances, the Kelvin-Helmholtz vortices developed into 3D structures very quickly and a sudden transition occurred without the occurrence of vortex pairing. In the study of McAuliffe & Yaras (2010) for a bubble over a flat plate with separation Re number of about 300 (based on the momentum thickness and edge velocity) amplification of the Kelvin-Helmholtz instability led to small-scale fluctuations developing within the braid (high-shear) region between spanwise vortices. These fluctuations then led to stretching and reorientation of the spanwise structures into hairpin vortices, which were shed downstream. Small vorticity distortions in the roll-up region were associated with small-scale turbulence activity between the spanwise vortices, where breakdown was observed to happen in a time-periodic manner. These vorticity distortions then were convected with large scale spanwise vortices, leading to complete breakdown to small-scale turbulence. Despite this breakdown to small-scale turbulence, spanwise vortical structures were observed to remain coherent downstream of transition. These structures however, were observed to become distorted and stretched resulting in some hairpin like structures. Similar hairpin structures were reported by Abdalla & Yang (2004a, b). It is believed that this reorientation of vorticity in the streamwise direction is a key mechanism for the reattachment process as it provides enhanced momentum exchange in the wall-normal direction. Similar structures in the reattachment region of turbulent separation bubbles were reported by Kiya & Sasaki (1983).

It appears that, although not entirely understood at the later stages, transition in laminar separated flows generally develops through the following stages;

- A primary 2D instability,
- A secondary instability leading to significant 3D motions and,
- A breakdown stage where fully turbulent flow emerges.

Downstream of the bubble a boundary layer re-forms but initially not in a standard form. The turbulent boundary layer very slowly recovers to an equilibrium log-law turbulent boundary layer state. Castro & Epik (1998) studied experimentally the

boundary layer development following a separation bubble and observed the energetic outer layer decayed very slowly in the downstream direction, hindering the inner layer reaching a standard form. It is believed that large scale energetic structures around the reattachment point modify their mixing-layer-like nature very slowly to that of canonical boundary layers. Yang & Voke (2001) observed a turbulent boundary layer shortly after reattachment but establishment of a standard log-law boundary layer was reported to take longer distances beyond their computational box. Alam & Sandham (2000) reported this recovery to take seven bubble lengths downstream of the mean reattachment. McAuliffe & Yaras (2010) also observed a delayed recovery of the reattached turbulent boundary layer, which was attributed to slow decay of turbulence kinetic energy in the outer region, resulting from the large scale structures formed during the transition in separated shear layer.

1.4.2 Shedding Phenomenon

One of the fundamental features of turbulent separated-reattached flows are the different frequencies of vortex shedding, associated with different unsteady phenomena within the bubble and shear layer. In a steady laminar separation bubble one can define a reattachment point or line where the skin friction is zero. In transitional and turbulent separation bubbles however, the instantaneous flow field is highly unsteady around the 'mean' reattachment point and the notion of a reattachment 'point' is misleading as it continuously varies with the time. In this case, it is possible that several small bubbles or vortices are periodically formed leading to a vortex shedding phenomenon. Tafti & Vanka (1991a) in their two-dimensional LES of a separation bubble on a blunt flat plate studied the effect of Re number. They considered four Re numbers (150, 250, 300, 1000, based on the free stream velocity and plate thickness). It was reported that the bubble at the first three Re numbers showed steady separation and reattachment. However, with increased Re number to 1000, the flow field was reported to show unsteadiness with formation of spanwise vortices which were shed periodically from the reattachment region.

Kiya & Sasaki (1983) in their experimental study of a turbulent bubble over a flat plate at high Re number (26000, based on free stream velocity and plate thickness), observed a peak frequency range of 0.6–0.8 U_0/l from velocity and pressure spectra

(U_0: free stream velocity, *l:* mean bubble length). This frequency band was stated to be the characteristic frequency of the large vortices shedding from the free shear layer of the bubble. Also a low frequency (0.12 U_0/l) flapping motion of the shear layer was reported near the separation line and it was suggested that this low frequency flapping motion might be caused by the large scale shrinkage and enlargement of the bubble. This low frequency flapping reported by Kiya & Sasaki was also confirmed by Cherry *et al*., (1984) in a study of a similar configuration but at a higher Re number with transition very close to separation, and it was proposed that the phenomenon would be an inherent feature of turbulent bubbles.

Tafti & Vanka (1991a, b) reported the roll up of a separated shear layer into spanwise vortices which then merged and shed downstream with a shedding frequency of 0.68 U_0/l. A sequence of events of vortex formation, merging, and shedding was observed. In their 2D simulation (1991a), despite the experimentally observed 3D nature of the flow field in the non-laminar bubbles, the vortex shedding dynamics were accurately captured. However, time signals of surface pressure and velocity near the separation showed no sign of the low frequency flapping phenomenon near the separation as reported earlier by Kiya & Sasaki and Cherry *et al*. The 3D calculations of Tafti & Vanka could however capture the low-frequency flapping of the bubble. It was argued that their 2D calculations were unable to capture this phenomenon as it was essentially characteristic of 3D turbulent separation (Cherry *et al*., 1984).

Yang & Voke (2001) observed vortex shedding from the separated shear layer on a flat plate with a semi-circular leading edge, although not periodic with a single frequency. The instantaneous reattachment position was reported to move over a distance up to 53% of the mean reattachment length. A characteristic shedding frequency variation in a range of 0.35-1.14 U_0/l was reported- giving an average value of 0.77 U_0/l which was comparable with the measured dominant shedding value of 0.65 U_0/l (Kiya & Sasaki 1983, 1985; Cherry *et al*. 1984). Yang & Voke also identified a low frequency peak within the velocity spectra and suggested that the low-frequency flapping (0.125-0.2 U_0/l) observed in experimental studies was associated with large shrinkage of the bubble caused by a big vortex shedding at a lower frequency. Abdalla & Yang (2004a) in their LES of a transitional bubble over a plate with a sharp leading edge extracted a characteristic frequency in the range 0.7-0.875 U_0/l along with some

less dominant modes between 0.3-0.6 U_0/l. They inferred that this frequency content must be related to pairing of vortices as the same order of frequency had been reported for the pairing phenomenon behind a backward facing step (Delcayre, 1997). No low-frequency flapping was observed. Abdalla (2004) proposed the low-frequency flapping was more apparent in the case of turbulent separation where rolled up vortices emerge even at the separation line. Yang & Abdalla (2009) studied the same problem but with higher free stream turbulence (2%) and reported a peak frequency band at about 0.8–0.9 U_0/l, in close agreement with the characteristic frequencies already measured in previous studies. Based on thorough spectral analysis, no low-frequency flapping was observed and since it was laminar flow at the leading edge (laminar separation), hence it was speculated that the low-frequency mode in separated–reattached flows may only appear in the case of turbulent separation as suggested earlier by Cherry *et al*. (1984).

1.4.3 Absolute vs. Convective Instability

Because of their importance in flow control (Huerre & Monkewitz, 1985; Yin et.al, 2000) and transition to turbulence (Yeo et.al, 2001), convective and absolute instabilities in fluid flows have been considered in a number of studies. Huerre & Monkewitz (1985) theoretically studied absolute and convective instabilities of free shear layers. It was demonstrated that spatially growing waves can only be observed if the mixing layer is convectively unstable. A criterion was developed for the flow to be absolutely unstable -instability developing in time- and to be described in terms of temporally growing disturbances.

Similarly, the possible presence of absolute instability regions in separation bubbles has been considered in some studies. Analysing local profiles of separated boundary layers, Hammond & Redekopp (1998) demonstrated that for certain profiles local absolute instability could be observed, depending on both reverse flow intensity and wall distance of the separated shear layer. These criteria were also confirmed by Rist & Maucher (2002) applying linear stability theory to local profiles of laminar separation bubble. A time-growing instability was identified in their 2D DNS of a laminar separation bubble. With the aid of special signal analysis techniques and a very low disturbance environment upstream of the bubble, it was observed that for a certain time, disturbances generated in the reattachment region amplified locally while shedding

upstream travelling waves. From their parametric study of velocity profiles along with 2D DNS of transitional bubble, it was suggested that for occurrence of time-growing (absolute) instability, in addition to the maximum reverse flow an extra parameter of wall distance and intensity of separated shear layer must be considered.

Alam & Sandham (2000) performed linear stability analysis of the mean flow velocity profiles obtained from their DNS data in the separated region. It was shown that for absolute instability to be sustained, reverse flow of the order of 15-20% was required (also Wissink & Rodi, 2003). A bubble with turbulent reattachment and maximum reverse flow of less than 8% was observed and thus the study concluded that the fundamental instability was convective in nature and the transition process was driven by convective instability. Spalart & Strelets (2000) however, in their DNS of a transitional bubble with very low inflow disturbances (less than 0.1% of free-stream velocity), dismissed the dependence of transitional flow on convective instability. Yang & Voke (2001) in their LES of a transitional bubble over a smooth leading edge observed a maximum reverse flow of less than 3% and hence discarded the existence of any absolute instability region in the bubble. Marxen et al. (2003) from their combined DNS and experimental studies on a laminar bubble under forced periodic disturbances concluded that transition was driven by convective amplification of a 2D TS wave while the dominant mechanism behind transition was an absolute secondary instability. Similar behaviour was proposed earlier by Maucher et al. (1997, 1998, 2000) where in the presence of large amplitude 2D wave, 3D modes were temporally amplified via an absolute secondary instability mechanism.

Jones et al. (2008) performed a DNS of a separation bubble formed over an airfoil and applied linear stability analysis upon the mean flow, which showed the bubble to be convectively unstable and no absolute instability was observed. It was however speculated that the persistence of turbulence after elimination of forcing (upstream introduction of disturbances) could imply the presence of some mechanism other than convective growth of disturbances. They proposed that in the absence of convectively driven transition within the shear layer, a three-dimensional absolute instability of 2D vortex shedding behaviour would cause transition in a manner not being predicted by linear stability analysis of the time-averaged flow field. The instability was associated

with production of streamwise vortices in braid region between successive spanwise vortices.

1.4.4 Role of Free Stream Turbulence

It is known that free-stream turbulence (FST) is a key parameter influencing the characteristics of a separated shear layer and its following reattachment. FST increases the shear-layer entrainment rates, decreases the mean reattachment length, and results in an earlier transition to turbulence in the separated boundary layer. In attached boundary layer studies with low (less than 1%) FST levels, natural transition is known to take place, whereas at sufficiently high FST, bypass transition is the main mechanism. Although there is no definitive threshold, beginning of this bypass mechanism is known to be strongly affected by disturbance level and also receptivity of shear layer to this disturbance. Eddies and organized disturbances may interact with an adjacent initially laminar boundary through different mechanisms which their joint effects in any given flow is difficult to predict and to be understood. One may look at the entrainment or external mechanisms, whether perturbations in the boundary layer originate from an upstream edge or inlet and grow within the boundary layer or internal disturbances induce directly by external disturbances that move above the layer. This is the general question of receptivity paths for bypass transition (Jacobs & Durbin; 1998, Leib et.al; 1999). Another issue is how the fluctuations are transformed within the boundary layer and how the layer itself is changed. Only very low level forcing leads to natural transition via TS waves. Moderate or high level forcing leads to bypass transition via formation of localised turbulent spots without TS precursors. Once induced, these disturbances grow within the boundary layer, although their development may be influenced by inflection of the boundary layer and by the free-stream distortion. When there is free-stream turbulence over the boundary layer, the question is whether free stream eddies are the primary source of transitional spots. In the research on bypass transition the issue of whether growth and final breakdown of the streaky structures arises from boundary layer internal dynamics, or from forcing by free-stream eddies is not fully understood. Such uncertainty is primarily due to experimental difficulties in following the details of the generation and growth of disturbances because of their randomness in space and time.

As mentioned earlier laminar flow is much more susceptible to separation than turbulent one and sometimes laminar separation is followed by transition that leads to reattachment of the turbulent flow. This is because the laminar shear layer is highly unstable and rolls-up into large Kelvin-Helmholtz vortices. In separated flows, transition is also possible to be accelerated by the separation along with influence of FST which is not yet fully understood especially at high levels of FST. Detailed response of a shear layer bounding a separated region to free-stream turbulence, is an open question. While we know that transition and reattachment locations move upstream significantly as FST increase and there are quantitative description of what happens under different FST conditions, the transition mechanism in not clear. To better describe the transition process and accurately predict or control it, an understanding of physical processes involved is essential.

Hillier & Cherry (1981) studied the effects of FST on the mean and fluctuating pressure distributions on a blunt flat plate. It was shown that increased FST level caused a reduction in the bubble length which was reported to be not affected by turbulent length scale. Kalter & Fernholz (2001) studied the effect of FST on a boundary layer with an adverse pressure gradient and a closed reverse-flow region. It was shown that the added FST shortened the mean reverse-flow region or completely eliminated it.

Castro & Haque (1988) provided detailed measurements of a separated region behind a flat plate with a splitter and studied how the different nature of the upstream flow can change the shear-layer structure. It was reconfirmed that FST leads to improvement in shear-layer entrainment rates and decreases the distance to reattachment. It also modified the low-frequency flapping motion of the shear layer. It was shown that FST caused an increased flapping motion of the shear layer just after separation, giving higher streamwise Reynolds stresses across the shear layer. A different turbulence structure around the reattachment was also reported as a result of FST. It was also speculated that different large eddy structures might also be present with FST.

Transition in separated flow can potentially contain characteristics of either natural or bypass transition. To investigate separated flow transition, Hughes & Walker (2001) considered a flow with wakes, in which the FST between wakes ranged from about 1%

to about 3%, and the FST in the wakes was about 8%. They observed evidence of TS waves. Hatman & Wang (1999) and Volino & Hultgren (2001) studied transition in the shear layer over separation bubbles with low FST. Their spectral data showed clear evidence of an instability along with harmonics very similar to the Kelvin-Helmholtz instabilities observed in free shear layers. The difference in the unstable frequencies compared to free shear layers was associated with the presence of a wall on one side of the bubble. The same authors also considered higher FST cases and observed broadband unsteadiness in the spectra of the streamwise fluctuating velocity and spikes at discrete frequencies were not present (unlike with the low FST case). It was stated that transition for the high FST situations appeared to be through a bypass mechanism. Volino (2002a, b) experimentally studied boundary layer separation, transition and reattachment under low-pressure turbine airfoil conditions, at different Re with low and high FST levels. It was found that higher Re or FST level caused the transition to move upstream. The spectral analysis in the cases with low FST revealed sharp peaks, while for the high FST case more broadband peaks were observed. From the frequencies of the peaks it was suggested that a TS instability mechanism was behind the transition at both high and low FST cases.

Yang & Abdalla (2005) considered the effects of 2% FST on the large-scale structures present in a separated boundary layer transition. They reported a 14% reduction of the mean bubble length and an earlier breakdown of the separated boundary layer. It was demonstrated that with increased FST the position of first unsteadiness moved closer to the separation line. Increased rates of randomness of the flow and degraded coherency of the early stage structures along both the span and streamwise directions were also reported as consequences of the added FST. At 2% FST, 2D Kelvin-Helmholtz rolls were not as apparent as in the case with no FST, but still observable in the early part of the bubble. Lambda-shaped (hairpin) vortices could hardly be identified and streamwise structures were enlarged in the spanwise direction and shortened in the streamwise direction compared with the case of no FST. It was concluded that in the presence of 2% FST the primary instability of the free shear layer was still the same as in the no FST case (Kelvin-Helmholtz instability mechanism) but secondary instability was different and needed to be further investigated.

Recently Yang & Abdalla (2009) investigated whether FST can affect the low-frequency shedding modes; their earlier studies with no FST did not show low frequency flapping. From a thorough spectra analysis they reported that the low-frequency flapping was also not observed with 2% FST. With a laminar flow at the leading edge (laminar separation) and 2% FST, they suggested that the low-frequency mode in separated–reattached flows may only appear in the case of turbulent separation, as suggested earlier (Cherry *et al*., 1984). A peak frequency band at about 0.8–0.9 U_0/l was also reported to occur at elevated FST, which was close to the characteristic frequencies already measured in previous studies (Kiya & Sasaki 1983, 1985; Cherry *et al*., 1984). They described how at 2% FST shedding still occurs with a characteristic shedding frequency corresponding to the same value as for no FST condition, and inferred that the primary instability mechanism in the no FST case (Kelvin-Helmholtz instab**i**lity) is still functioning in the presence of 2% FST. It was suggested that if the level of FST is increased further, a much more rapid transition may occur with a different transition mechanism, similar to the so called bypass transition in attached boundary layer flows.

McAuliffe & Yaras (2010) studied the effect of elevated FST (1.45% at separation) on a laminar boundary layer separation over a flat plate induced by adverse pressure gradient. Compared to the low-disturbance case (0.1% FST at separation) where the Kelvin-Helmholtz instability developed in the separated shear layer, at the higher FST this mechanism was reported to be bypassed. Streamwise streaks resulting from filtering of FST into the laminar boundary layer appeared upstream of separation, providing the conditions necessary for turbulent spot productions in the separated shear layer. Turbulent spots then grew and merged leading to full turbulence.

Palikaras et al. (2002) presented the effect of the free-stream velocity profile on the transition of separated flow on a flat plate. The flows examined were based on the T3L test case (ERCOFTAC Special Investigation Group for transition) where the separated boundary layer transition on a flat plate with a semi-circular leading edge was examined under various free-stream conditions regarding turbulence intensity and velocity magnitude. Two free-stream velocity distributions were studied; a uniform velocity and a mean shear velocity profile with positive gradient ($\partial \overline{U}/\partial y = 27.7\ s^{-1}$).

It was reported that the existence of mean shear inlet velocity distribution reduced the length and thickness of the separation bubble.

It is understood that there is some discrepancy about the transition mechanism in separated boundary layers, particularly under high FST conditions. Some of these differences may be due to physical differences in the boundary conditions of different studies. Although the general effect of FST on the increased entrainment rate and shorter bubble length is well known, the unsteady behaviour of the bubble and transition mechanisms involved in separated boundary layers particularly at higher FST conditions are less understood. The present study is particularly aimed at addressing this issue through spectral and coherent structures analysis of flow over a flat plate with semi-circular leading edge, at both high and low FST.

1.5 Summary

From the literature survey above it is understood that despite substantial work on transitional studies of the separation bubbles there are still open issues in the field. In most cases inviscid instability via the Kelvin-Helmholtz mechanism is believed to be the first dominant instability mechanism acting within the separated shear layers. There are, however, some reports indicating that transition of a separated shear layer through the Kelvin-Helmholtz instability does not eliminate the existence of TS activity in the bubble. The viscous instability near the wall may play a role particularly in cases with high levels of reverse flow or thin separated shear layers. More studies are needed to understand the criteria for the presence or dominance of these two primary modes. More research is needed on the later- stage instabilities of separated-reattached flows which are not yet fully understood. Role of free-stream turbulence intensity in transition and unsteady characteristics of the separated-reattached flows is not well understood and hence is the subject of ongoing research.

1.6 Objectives

This project is aimed for LES of a transitional separation bubble over a flat plate with a semicircular leading edge (T3L case of ERCOFTAC, 1999). LES data will be used to investigate the separated-reattached flow with particular emphasis on the

primary transition mechanism involved. The focus will be on the role of high free-stream turbulence on transitional characteristics of the bubble. This has a practical importance since typically high turbulence levels are present at some practical situations e.g. 5-10% in compressors and turbines. The main objectives of this research are outlined as follows;

- To study the primary instability mechanism in a geometry-induced separated flow,
- To study effects of high free-stream turbulence level on the KH instability of the shear layer observed at low turbulence levels, bubble dimension, and shedding frequencies associated with transitional separated-reattached flows,
- To study large-scale coherent structures at various stages of transition and their evolution.

Chapter 2

Governing Equations and Numerical Methods

All motions of any Newtonian fluid are governed by Navier-Stokes (NS) equations. For the majority of flows of interest, analytical solution of equations is impossible and numerical methods have to be employed. As stated in the previous chapter, direct numerical simulation of the exact NS equations, i.e. without modelling of any terms, is very demanding in terms of high grid resolution and very small time steps required for capturing all the length and time scales present in the problem. The broad range of space and time scales involved in a problem; therefore, can significantly increase the computational cost.

In LES, the flow field is spatially filtered; where the scales larger than the filter size are calculated directly using the filtered NS equations, and only scales smaller than the filter size have to be modelled. These small-scale turbulent motions are more universal and isotropic and recover faster to the equilibrium state compared to the larger eddies (Piomelli, 2001). This makes LES with sub-grid scale modelling more accurate than RANS and associated turbulence modelling techniques. Compared to DNS, LES is less expensive; as the small scale eddies are not resolved.

In LES any flow variable $q(\vec{x},\ t)$ is decomposed into a filtered (large-scale, resolved) part $\bar{q}(\vec{x},\ t)$, and a sub-filter (small, unresolved) part $q'(\vec{x},\ t)$;

$$q(\vec{x},t) = \bar{q}\,(\vec{x},t) + q'(\vec{x},t) \tag{2.1}$$

The filtering applied to the NS equations removes the small turbulence scales. Filtering can be classified into two categories, explicit and implicit. Implicit filtering is a common approach where the finite volume grid is employed to decompose the flow field into resolved, and sub-grid (smaller than grid size) scales.

For incompressible flow the filtered governing equations which describe the temporal and spatial development of large scale motions are;

$$\frac{\partial \bar{u}_i}{\partial x_i} = 0$$
$$\frac{\partial \bar{u}_i}{\partial t} + \frac{\partial}{\partial x_j}\left(\bar{u}_i \bar{u}_j\right) = -\frac{1}{\rho}\frac{\partial \bar{P}}{\partial x_i} + \nu \frac{\partial^2 \bar{u}_i}{\partial x_j x_j} - \frac{\partial \tau_{ij}^s}{\partial x_j} \tag{2.2}$$

Here, τ_{ij}^s is the subgrid-scale (SGS) stress tensor caused by nonlinearity of the convective term;

$$\tau_{ij}^s = \overline{u_i u_j} - \bar{u}_i \bar{u}_j \tag{2.3}$$

Equations (2.2) describe unsteady *large scale* random and three-dimensional fluid motions. Using a set of boundary conditions for the primitive variables and a model for the subgrid-scale stress tensor, these equations are solved numerically, to give $\bar{u}$ and $\bar{P}$. Both SGS model and boundary conditions may significantly influence the simulation in terms of numerical stability and accuracy of the computed flow field. The following sections will discuss subgrid-scale modelling and inlet conditions for LES.

2.1 Sub-Grid Scale Modelling

The sub-grid scale tensor appeared in the filtered NS equations is unknown and has to be modelled. The SGS stress describes the effects of the unresolved scales on the resolved scales. The main function of a SGS model is in fact to model correctly the energy transfer between the different turbulence scales. The role of SGS modelling in LES depends on the computational grid resolution. The coarser the mesh, LES will resolve less, and more scales have to be considered by the SGS model. On the other hand, at the DNS limit where the mesh resolution is such that all scales are properly resolved, the SGS model does not play a significant role.

A common approach for SGS modelling is the Boussinesq eddy-viscosity assumption (Sagaut, 2001) where the SGS stresses are related to the large-scale strain-rate $\bar{S}_{ij}$ as follows:

$$\tau_{ij}^{s} - \frac{\delta_{ij}}{3}\tau_{kk}^{s} = -2\nu_T \bar{S}_{ij}$$
$$\bar{S}_{ij} = \frac{1}{2}\left(\frac{\partial \bar{u}_i}{\partial x_j} + \frac{\partial \bar{u}_j}{\partial x_i}\right) \quad (2.4)$$

which assumes the energy transfer mechanism to be from the resolved to the subgrid scales, similar to the molecular diffusion mechanism represented by the diffusion term in the NS equations. Therefore the same mathematical structure can be used with the kinematic viscosity replaced by eddy viscosity ν_T, and the closure will consist of determining an expression for ν_T. Eddy viscosity is generally evaluated from algebraic relations to reduce numerical costs. The Smagorinsky model is a very simple eddy-viscosity model which is based on the equilibrium hypothesis which implies that the small scales dissipate entirely and instantaneously all the energy they receive from the large scales. The Smagorinsky model is defined as;

$$\nu_T = (C_s\Delta)^2|\bar{S}| \quad (2.5)$$

where C_s in the smagorinsky constant and depends on the flow type (for shear flows a value of 0.1 is suggested, but it was found that the separated flow can be highly affected by this constant). In the above equation, Δ is the filter width and is usually taken as twice the average grid size; $\Delta = 2(\Delta x\, \Delta y\, \Delta z)^{1/3}$. $|\bar{S}|$ is the magnitude of filtered strain rate tensor;

$$|\bar{S}| = (2\,\bar{S}_{ij}\,\bar{S}_{ij})^{1/2} \quad (2.6)$$

2.1.1 Dynamic procedure

Smagorinsky model is still often employed for performing LES. However it has a number of drawbacks. The model constant (C_s) has been accurately validated only for the simple flow of decaying turbulence. The same value of the model constant is often used for more complex flows in which it is not clear what the value should be. The presence of shear or the transition from laminar to turbulent flow are two of the factors

that can affect its value (Piomelli, 1999). A priori knowledge of C_s is vital for correct behaviour of the model and it is this feature that can potentially limit its application to flows that have not been studied before. Besides, the Smagorinsky model does not allow the eddy viscosity to fade away in near-wall regions. Therefore, a damping function is required in order to satisfy this condition. Near the walls, the eddy viscosity ν_T value may be reduced by introducing a damping function (Pope, 2000).

A more sophisticated approach to overcome the near-wall behavior and other deficiencies of the original Smagorinsky model is the dynamic model approach. Dynamic subgrid modelling techniques have been developed and applied successfully to a range of flows recently. Dynamic models produce the variation of *C* near the solid walls naturally and hence use of the ad hoc damping functions such as the well known Van Driest type are unnecessary. The variation of *C* with Re number and with the flow type allows for reliable LES of transitional flows. For the dynamic model (Germano et.al, 1991; Lilly, 1992), the anisotropic part of the SGS stresses are parameterised by an eddy viscosity assumption (equation 2.4) and the eddy viscosity given by,

$$\nu_T = C\bar{\Delta}^2|\bar{S}| \tag{2.7}$$

where the coefficient *C* is determined using the least squire approach of Lilly (1992). A second coarser spatial filter, called the "*test*" filter is applied leading to the test-filtered equations of motion, with the caret signs representing the test-filtered variables. A subtest-scale (STS) stress T_{ij} is similarly approximated by;

$$T_{ij} = 2C\hat{\Delta}^2 \left|\hat{\bar{S}}\right| \hat{\bar{S}}_{ij} \tag{2.8}$$

With the test-scale shears defined similarly to those for the grid scale. Subtracting the test-filtered average of τ_{ij} from T_{ij} :

$$L_{ij} = T_{ij} - \hat{\tau}_{ij} = \widehat{\overline{u_i}\,\overline{u_j}} - \hat{\bar{u}}_i\hat{\bar{u}}_j \tag{2.9}$$

The elements of *L* are the resolved components of the stress tensor associated with scales of motion between the test scale and the grid scale. These scales are normally called "test window". The test-window stresses, can be explicitly evaluated by subtracting the test-scale average of equation 2.4 from 2.8 to obtain;

$$L_{ij} = 2CM_{ij} \tag{2.10}$$

where

$$M_{ij} = \hat{\Delta}^2 \left|\hat{\bar{S}}\right| \hat{\bar{S}}_{ij} - \Delta^2 \, |\widehat{\bar{S}}|\bar{S}_{ij} \tag{2.11}$$

The value of *C* can be obtained from eq. 2.10 as follows. *Q* is defined as the square of the error in eq. 2.10, i.e;

$$Q = (L_{ij} - 2CM_{ij})^2 \tag{2.12}$$

Upon setting $\partial Q/\partial C = 0$, *C* is evaluated as;

$$C = \frac{1}{2} \frac{L_{ij}M_{ij}}{M_{ij}^2} \tag{2.13}$$

which represent the minimum of error *Q*. In the current simulation C is defined as;

$$C = \frac{1}{2} \frac{< L_{ij}M_{ij} >}{< M_{ij}M_{ij} >} \tag{2.14}$$

Where the angle brackets represent an average over the homogeneous spanwise direction *z*. The resulting *C* is a function of time and the inhomogeneous co-ordinates *x* and *y*. In finite volume calculations the test-filtered flow quantities can be computed by spatial averaging the calculated large scale variables over a few grid cells. In the current study, the averaging is performed over 9 cells.

2.2 Inlet Conditions for LES

In contrast to RANS approach, where all quantities specified at inlet boundary are usually constants (i.e., have only spatial variation but not changing in time), in LES the variables at inlet boundary change not only in space but also in time as it is usually turbulent flow at inlet. A method should be used to generate realistic turbulent fluctuations at the inlet. Turbulence at the inlet may have a significant contribution to the turbulence within the domain and have a great impact on the flow dynamics, and so the correct implementation of the inlet conditions is of considerable importance also a

great challenge. There are several methods to generate turbulent inflow conditions. Two basic approaches are synthesis methods and precursor methods.

In synthesis methods, artificial perturbations are added to the mean flow. Fluctuations are generated at the inlet with some specific characters. Successful simulations have been performed with this method (synthetic turbulence), using perturbations based upon Fourier series or other analytically generated disturbances (Keating et.al, 2004). The disturbances should lie in a reasonable range of acceptable values. If they are too small, turbulence will not be generated or supported and if too large, unphysical behaviour may happen. Estimate of reasonable magnitudes for disturbances may be obtained from previous simulations, if available for any specific application. In general, these magnitudes are ambiguous, and the quality of the solution can be judged only after the simulation. Because of the problems with generating correlations between velocity components, these methods can only offer an approximation of turbulence at the inlet which serves to trigger the development of realistic turbulence, and a section of domain must be provided for this to happen.

In precursor methods a separate calculation of turbulent flow is usually performed and information are extracted for use as the inlet condition for the main simulation. This kind of methods can provide realistic turbulence but of course very expensive too. The precursor simulation can be run concurrently with the main simulation, avoiding the problem of storing a large amount of data. A recycling-rescaling technique, first introduced by Spalart (1988) and simplified for incompressible flows by Lund et al. (1998) can be regarded one of precursor methods. This method is based on extracting profiles of dependent variables at some location downstream of the inflow boundary, rescaling, and then reintroducing them at the inflow plane in a dynamic manner. Normally, the flow between the recycled boundaries must be initialised by artificial disturbances in order to develop the flow into a realistic turbulent flow state. The advantage of this method is that the inflow is treated implicitly as part of the overall simulation.

There are many cases where instead of a fully developed flow, a flow that matches some predefined parameters such as a known turbulence profile is advantageous. In this case the flow is modified either by introducing artificial body force terms, or by explicit correction of the velocities within this section, or by suitable modification of the

mapped data. By linking these techniques to a feedback control algorithm based on the discrepancy between computed values and desired values at a given location in the flow, it is possible to drive the flow towards the required flow conditions. Xiao et al (2010) developed a rescaling/recycling method based on the work of Pierce (2001) and Lund et al. (1998) where a rescaling and recycling technique is performed in the extra section upstream of the inlet-plane simultaneously with the main simulation and a separate precursor simulation is unnecessary.

In the current LES two methods were used to mimic the free-stream turbulence and match the required free-stream turbulence condition as that of the experimental test case;

- A rescaling/recycling procedure at an inlet block (Xiao et al, 2010),
- A so-called numerical *trip* (Pokora et al., 2011) applied at an upstream plane normal to the free-stream.

2.2.1 Rescaling/recycling method

In this method, an extra inlet block is generated upstream of the actual inlet plane. The inflow condition for the inlet block is generated by recycling the velocity field of one plane downstream and mapping on the inlet plane. By rescaling the flow field over the entire inlet block, the flow will be statistically homogeneous in the streamwise direction. The target values for the mean velocity;

$$\overline{U}_{target}(y), \overline{V}_{target}(y), \overline{W}_{target}(y)$$

and rms profiles i.e.;

$$u'_{target}(y), v'_{target}(y), w'_{target}(y)$$

at the inlet plane, need to be prescribed (inflow conditions are assumed spanwise homogeneous). The procedure below is then followed.

The inlet block as well as the computational domain of interest is initialised. When initialising the velocity field at *x*-*z* planes with constant *y* in the inlet block, the

instantaneous turbulent velocity field is generated by superimposing white noise perturbations with the intensity of $u'_{target}(y), v'_{target}(y), w'_{target}(y)$ to the mean velocity $\overline{U}_{target}(y), \overline{V}_{target}(y), \overline{W}_{target}(y)$.

Simulation is run on both the inlet block and the domain of interest simultaneously. The flow field of the inlet block is then rescaled at every time steps as follows;

1. The mean velocity is calculated by space average in the *x*-*z* plane and time average with a weight that decreases exponentially backward in time;

$$\overline{U}^{n+1}(y) = \alpha\langle U(x,y,z)\rangle_{xz} + (1-\alpha)\overline{U}^{n}(y) = \alpha\frac{1}{mn}\sum_{i=1}^{m}\sum_{j=1}^{n} U(x_i, y, z_j) + (1-\alpha)\,\overline{U}^{n}(y)$$

   where $< >_{xz}$ represents the spatial averaging in the *x*-*z* plane, and $U(x,y,z)$ is the current instantaneous solution.

2. The rms of the velocity field is calculated similarly:

$$u'(y)^{n+1} = \sqrt{\alpha\,\langle[U(x,y,z) - \overline{U}^{\,n+1}(y)]^2\rangle_{xz} + (1-\alpha)[u'(y)^n]^2}$$

3. Velocity is then rescaled to create new instantaneous velocity field in the *x*-*z* plane at each *y*:

$$U^{new}(x_i, y, z_j) = \frac{u'_{target}(y)}{u'^{n+1}(y)}[U(x_i, y, z_j) - \overline{U}^{n+1}(y)] + \overline{U}_{target}(y)$$

4. The velocity field at a plane downstream in the inlet block is recycled back as the inflow conditions for the inlet block.

The above process is applied to the other two velocity components *V* and *W*.

2.2.2 Numerical trip

In a separate simulation, a numerical tripping method (Pokora et al., 2011) was employed to generate the targeted high free-stream turbulence level. The trip is applied

to the free-stream at each computational time step in a manner that the solution is perturbed with small random white-noise disturbances (u', v', w') = $U_0.A$ (r_1, r_2, r_3) in a plane parallel to the inflow (A is the disturbance level which can be adjusted according to the required turbulence level and r_1, r_2, r_3 are components of a 3D random vector). These perturbation velocities imposed on the mean velocity components generate the instantaneous flow field.

The perturbation is then applied to a stencil around the given cell with index *(I, J, K)* in the structured grid. As an example for the axial velocity, Figure 2.1 shows the perturbation distribution in *K* direction for a trip plane at a given *I* location.

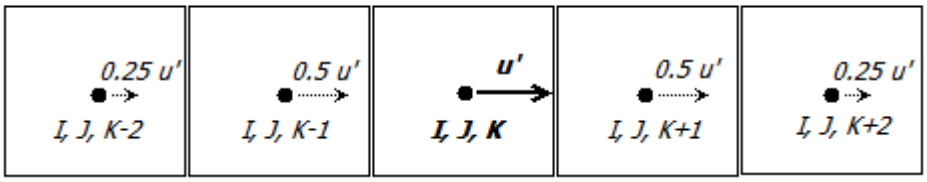

Fig. 2.1. Stencil showing the perturbation distribution in *K* direction for a trip applied at *I*

The perturbations at neighboring cells are updated such that 1/2 of the perturbation magnitude is imposed upstream I-1 and downstream *I*+1 of tripping plane and also to the adjacent cells $J \pm 1$ and $K \pm 1$. Also 1/4 of the disturbance magnitude is imposed at next level cells i.e. $J \pm 2$ and $K \pm 2$. Hence for a trip applied at *I* location, axial velocity is updated such that;

$$u_{I,J,K} \therefore u_{I,J,K} + u'_{I,J,K}$$
$$u_{I,J+1,K} \therefore u_{I,J+1,K} + 0.5\, u'_{I,J,K}$$
$$u_{I,J-1,K} \therefore u_{I,J-1,K} + 0.5\, u'_{I,J,K}$$
$$u_{I,J,K+1} \therefore u_{I,J,K+1} + 0.5\, u'_{I,J,K}$$
$$u_{I,J,K-1} \therefore u_{I,J,K-1} + 0.5\, u'_{I,J,K}$$
$$u_{I,J+2,K} \therefore u_{I,J+2,K} + 0.25\, u'_{I,J,K}$$
$$u_{I,J-2,K} \therefore u_{I,J-2,K} + 0.25\, u'_{I,J,K}$$
$$u_{I,J,K+2} \therefore u_{I,J,K+2} + 0.25\, u'_{I,J,K}$$
$$u_{I,J,K-2} \therefore u_{I,J,K-2} + 0.25\, u'_{I,J,K}$$

This procedure leads to an increased coherence of the disturbance; hence more realistic free stream turbulence could be generated.

2.3 Other Boundary Conditions

A convective boundary condition is used ensuring the convection of the flow through the outlet plane. No-slip condition is used for all the solid walls. A periodic boundary condition is used in the spanwise direction. Periodic condition implies that the computational domain repeats itself an infinite number of times.

Chapter3

Code Overview and Validation

In order to achieve the objectives outlined in chapter 1, a CFD code is employed. Although some commercial codes allow the introduction of new models, they do not offer enough flexibility therefore in-house codes are preferred. Here the in-house code DELTA is used to obtain the solution over the multi-block structured grid around the T3L geometry. DELTA has been developed in the Aeronautical and Automotive Engineering Department of Loughborough University since 1994. Originally, it was an Euler code but later it was developed to compute RANS equations and further developed for LES. The code has already been used for the calculation of a wide range of cases; external/internal, compressible/incompressible, and free/wall-bounded flows (Page, 2005; Page et.al, 2002; Pokora et al., 2011). This is the first application of DELTA with a dynamic SGS model introduced to resolve a transitional flow.

3.1 Characteristics of DELTA

DELTA is based on the finite volume approach for the solution of NS equations. It uses collocated flow variables arrangement, on a curvilinear coordinate system, in combination with Rhie-Chow pressure smoothing, to avoid pressure-velocity decoupling. DELTA adopts the SIMPLE pressure correction method, designed to handle both incompressible and compressible flow cases. The code initialises a flow field and then solves the momentum equations to obtain some intermediate flow variable values. Because these values will not necessarily satisfy the continuity equation, they are corrected by using a pressure correction, *dP*. This pressure correction is calculated by a pressure correction equation, which is derived from the combination of the momentum and continuity equations. When the correct values for flow variables have been obtained, the procedure is repeated for the next time step. Central difference scheme was used to discretise diffusive terms and a 2^{nd} order upwind scheme for calculation of the convective fluxes. For the time integration either an Euler implicit or an explicit scheme can be used. A Gauss-Seidel line solver (Ferziger & Peric, 2001) is

used to solve the pressure correction equation. The LES filtering procedure is implicit where the grid is used as a spatial filter, avoiding the need for explicit filtering procedure. Parallel version of DELTA using Message Passing Interface (MPI) libraries is employed to enable parallel processing based on flow domain decomposition in order to speed up the simulation.

A variety of grid file formats including mesh files created by ICEM can be imported. Input grids have to be structured, single or multi-block. For the boundary conditions and the exchange of information between the blocks, DELTA uses two extra rows of hallo-cells generated automatically along each face of every block. Boundary conditions are applied on the first row and the second is mainly used for the exchange of information in multi-block grids. DELTA has 150 subroutines where the main process of the program is governed by deltaFlow.f subroutine which is the base of the code controlling the order and application of different operations defined within the rest of the subroutines. Three user-defined files for controlling the simulation are; 1) a resource file (to set the parameters that govern the numerical and modelling issues of the simulation), 2) a boundary condition file, and 3) a topology file (to define the grid topology and the connections between faces of the blocks).

3.2 Code Validation

It is crucial that the flow at both laminar and fully turbulent states to be accurately computed, with ability to capture the full course of transition. The onset of instabilities and subsequent growth of disturbances within the shear layer should be accurately represented in order to correctly capture the transition location and its spatial extent towards a fully turbulent state. To assess the performance of the LES code in use with a dynamic subgrid scale model, it is validated against the well-established transitional separated-reattached over a flat plate with semi-circular leading-edge (T3L case of ERCOFTAC, 1999) at very low free-stream turbulence (Yang & Voke, 2001).

The ERCOFTAC Special Investigation Group for transition, initiated the study of transition in 1991 to improve understanding of transition mechanisms. Detailed experimental measurements were provided for the flow over flat plates with sharp or semi-circular leading edges. Details of experimental setup and inlet conditions of T3L

cases can be found on the ERCOFTAC database (1999). Although limited in providing near wall resolution, these experimental data have been the benchmark for assessing various numerical models of transitional flow. Due to the simple geometric configuration and hence possibility of accurate measurements, this flow provides a good basis to examine the physics of laminar to turbulent transition through boundary layer separation. According to this test case, separated boundary layer transition on a flat plate with a semi-circular leading edge with radius R = 5 mm is examined under different free-stream velocity and turbulence intensities. Figure 3.1 shows the sketch of the experiment with the location marked where free-stream turbulence level is measured. Four different turbulence grid configurations at three inlet velocities 2.5, 5.0, and 10.0m/s were used resulting in FST levels from 0.2% (no turbulence grid), 0.65%, 2.3%, and 5.6%.

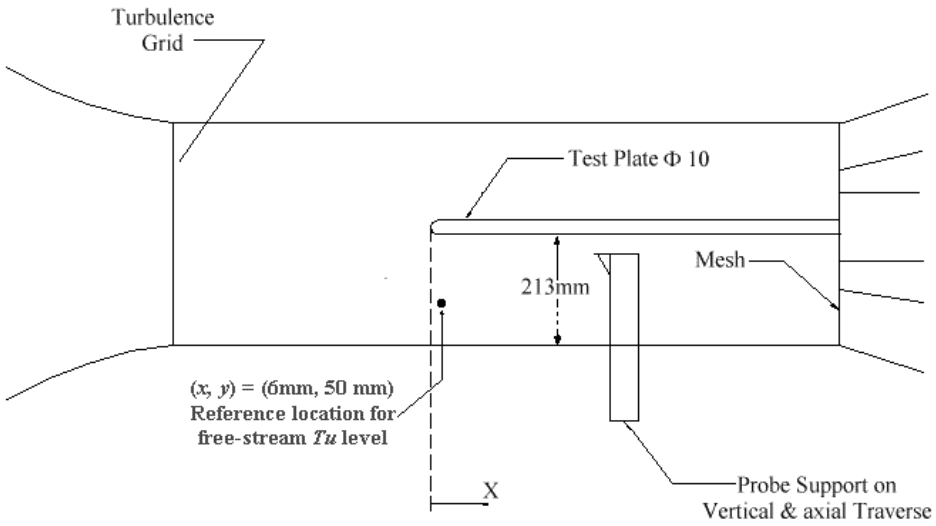

Fig.3.1. Sketch of the experimental setup

Matching the experimental Re and free stream conditions two cases with different FST levels at the leading edge were simulated in the current study at Re = 3450 based on the plate thickness and the uniform inlet velocity, one with FST levels nearly zero (0.2%) denoted as No-Free-Stream-Turbulence case (NFST) and one with FST = 5.6% denoted as FST case. In this section, the code is validated for the NFST case using the

experimental and LES data of Yang & Voke (2001). The FST case is studied in the next chapter.

3.2.1 Flow configuration

The flow geometry and computational grid are shown in Figure 3.2. LES domain extends 12*D* upstream and 16*D* downstream from the plate leading edge, 8.5*D* away from the plate in the free stream, and 8*D* in the spanwise direction (*D* = 10mm is the plate thickness, and co-ordinate origin located at the stagnation point). Using the multi-block functionality, the domain is divided into 14 blocks with a grid resolution of (n_x, n_y, n_z) = (310, 140, 64) for the outer region and a refined C-grid (420, 60, 64) around the plate covering the close wall region and the free shear layer region of the separation bubble, a total of 4.39 million mesh points. Based on the friction velocity at x/D = 10, which is far downstream from the separation bubble and well within the reattached turbulent boundary layer, y^+ of the nearest cell to the wall is about 0.4, the streamwise mesh sizes vary from Δx^+ = 3 to 55 and Δz^+ is 24.

The inflow velocity U_0 is constant aligned with the plate and applied at x = -12*D* upstream. To mimic the low turbulence level (< 0.2%) of the experiment, small random disturbances (white noise) are imposed on the mean velocity components at the inflow as (u', v', w') = $U_0.A$ (r_1, r_2, r_3), where A is the disturbance level (0.02 in current study) and r_1, r_2, r_3 are components of a 3D random vector. A convective boundary condition is used ensuring the convection of the flow through the outlet plane. Periodic boundary condition is used in the spanwise direction. At lateral boundaries free-slip condition is applied and no-slip wall condition is applied at the plate surface. Time step used in the present LES is Δt = 5.0×10^{-06} *sec* (0.0025 D/U_0) corresponding to a CFL_{max} value of 0.5.

The 2nd order central differencing scheme was used for spatial discretisation of diffusive terms. For time discretisation, a single stage backwards Euler scheme has been found to be computationally more efficient to use. This is justified by small time step used in the present LES and hence no noticeable impact on the accuracy. The simulation ran for 10 flow-through times (112,000 time steps) to allow the flow to become well established and reach a statistically stationary state. The averaged results

were gathered over further 50 flow-through times (560,000 steps) with samples taken every 20 time steps (28,000 samples, with sampling frequency of 10,000 Hz) and averaged over spanwise direction too. Comparisons of stresses and mean velocity profiles using sampling frequency of 20,000 Hz (samples taken every 10 time steps) showed almost no difference in the mean flow statistics. Instantaneous flow fields and time trace of velocity components at certain points were also stored during the simulations for spectral analysis.

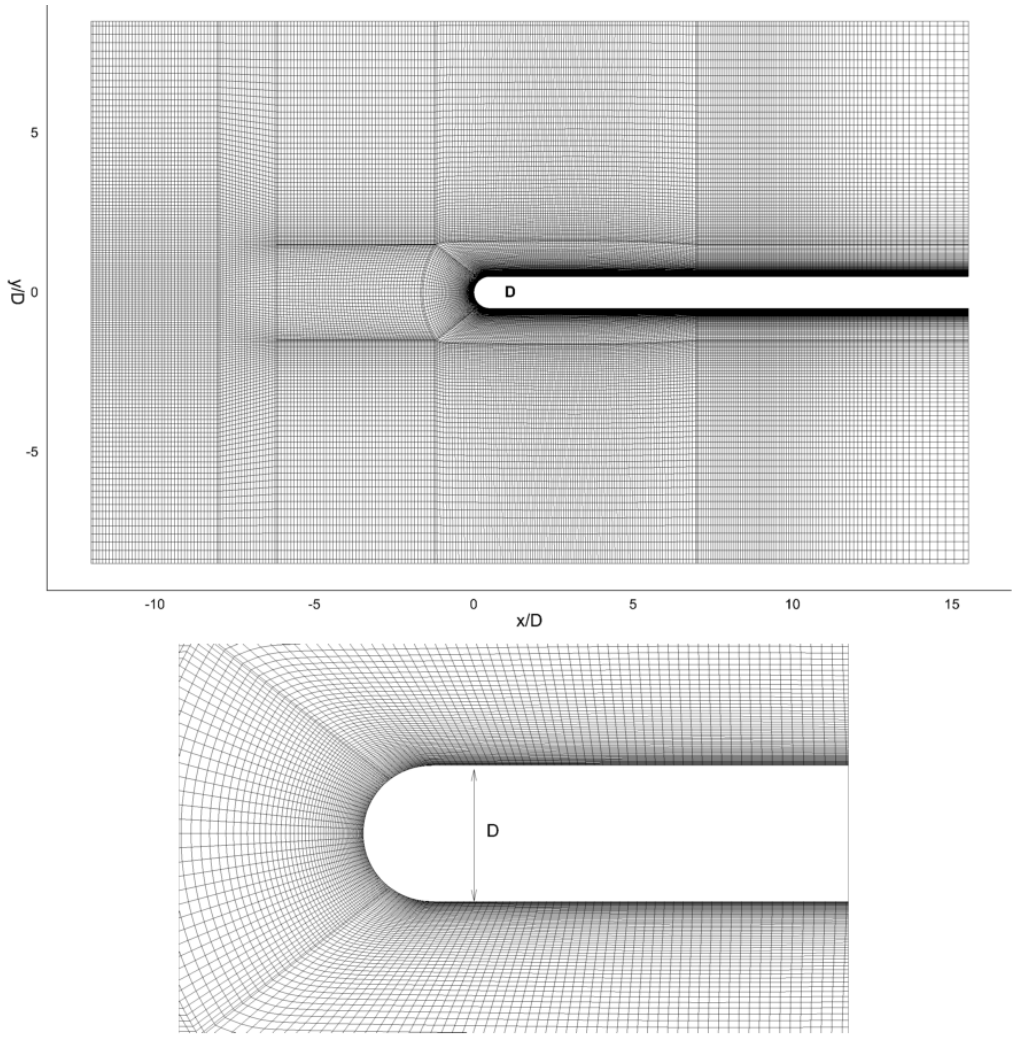

Fig. 3.2. Computational domain and mesh

3.2.2 Results

Time mean position of reattachment is an important aspect of separated-reattached flows. According to Le et al (1997) the mean reattachment location may be found via four methods; (1) location where the mean velocity $\overline{U} = 0$ at the first grid point away from the wall, (2) location where the wall-shear stress $\tau_w = 0$, or $dU/dy = 0$, (3) location of the mean dividing streamline, or (4) by a *p.d.f* method in which the mean reattachment location is determined by the location of 50% forward flow fraction. It was reported that the first three methods were within 0.1% of each other and about 2% different from the *p.d.f* method. The first method was used in the current study to determine the mean reattachment length.

Figure 3.3 shows the time-averaged velocity vectors. For the current transitional separated-boundary layer flow, the time averaged results are similar to a steady laminar separated flow but with different bubble shape and separation length. Figure 3.3 plainly shows a separation bubble starting from the separation point (the blend point where curvature changes) reattaching at a downstream location x = 34.97mm giving a mean reattachment length l of 2.997D. The measured mean reattachment length is about 2.75D, hence the predicted length in the current study is over-predicted by about 9% while it is 2.59D in the LES of Yang and Voke (2001), under-predicted by about 6%. This is a reasonably good agreement considering the effect of difference in blockage ratio.

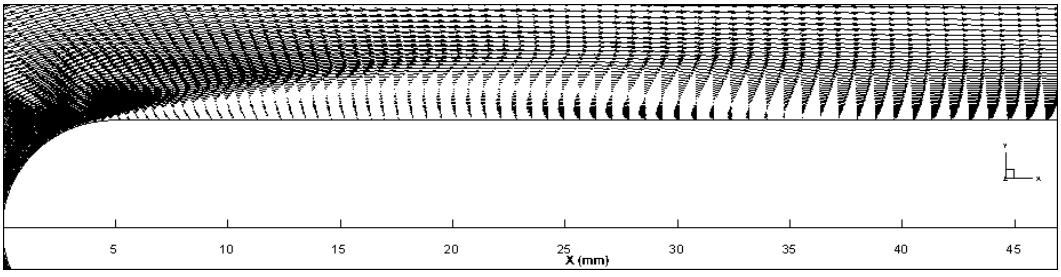

Fig. 3.3. Time-averaged velocity vectors (NFST case)

Streamwise variation of ratio of the maximum eddy viscosity to the kinematic (molecular) viscosity is presented in Figure 3.4. It is seen that the eddy viscosity ratio is

zero at separation, gradually increasing downstream of separation reaching a maximum value of approximately 3.0 downstream of the mean reattachment region and relaxing to a value around unity farther downstream.

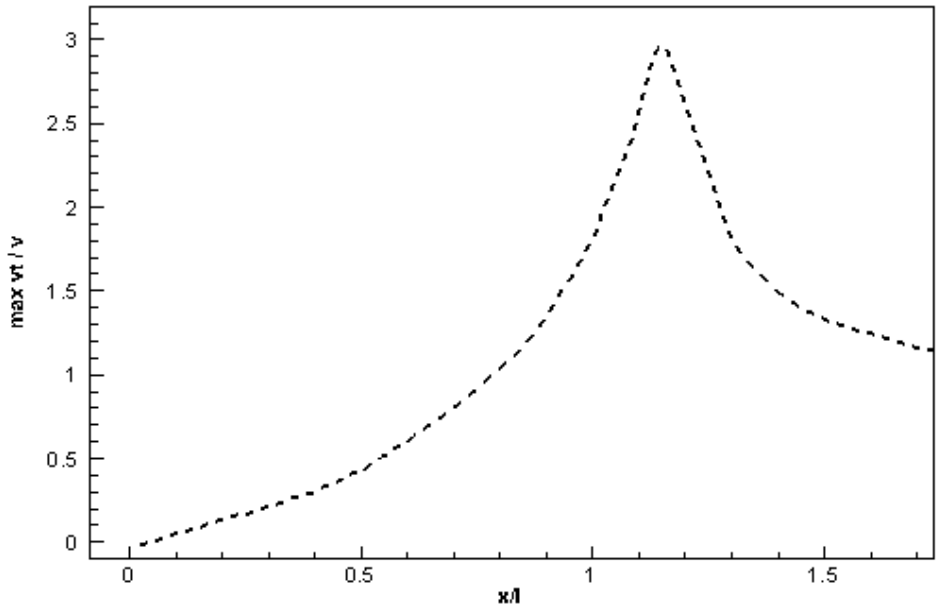

Fig. 3.4. Wall-normal maximum of the SGS viscosity ν_t/ν (NFST case)

Figures 3.5 and 3.6 show the simulated mean streamwise velocity and rms of fluctuations. Mean and rms values are normalised by the inlet velocity (U_0). Wall-normal direction is normalised by the measured mean reattachment length l. For the mean velocity a very good agreement has been obtained between the current predicted profiles with the experimental data and LES results of Yang & Voke (2001) at all seven streamwise stations. There is hardly any difference between the current LES results and the LES results of Yang & Voke (2001) in terms of the mean velocity predictions while for the rms the present LES results have a slightly better overall agreement with the experimental data, especially at the 5th location where the current predictions follow the experimental data much more closely although at the 6th location the peak value is better predicted by Yang and Voke (2001). However, at the last location further away from the wall the current predictions are much better than the results by Yang and Voke (2001). It is also interesting to note that the present rms results show double peaks inside the separation bubble at the 2nd and 3rd locations, especially apparent at the 3rd

location whereas the LES results of Yang and Voke (2001) only show one peak. Unfortunately the measurements could not be done very close to the wall inside the bubble so that the first peak near the wall cannot be confirmed by the experimental data.

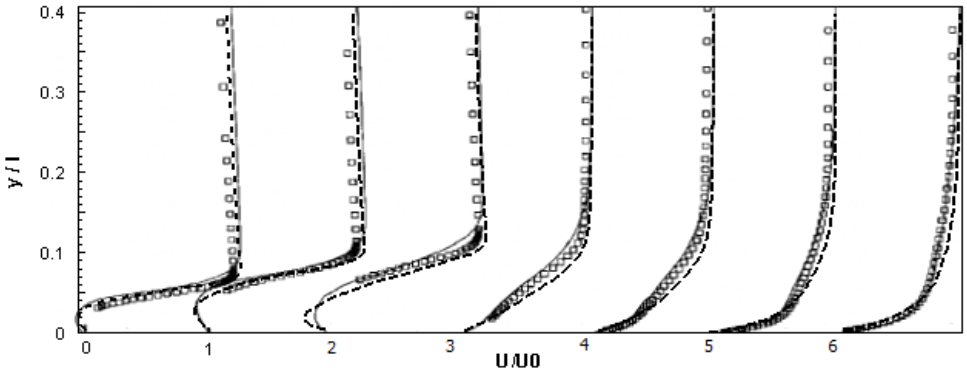

Fig. 3.5. Mean streamwise velocity at seven streamwise stations (NFST-case), Left to right: *x/l* = 0.22, 0.44, 0.66, 1.09, 1.27, 1.64, 2.55. Present LES (dashed), LES of Yang & Voke (solid line), Exp. Data (symbols)

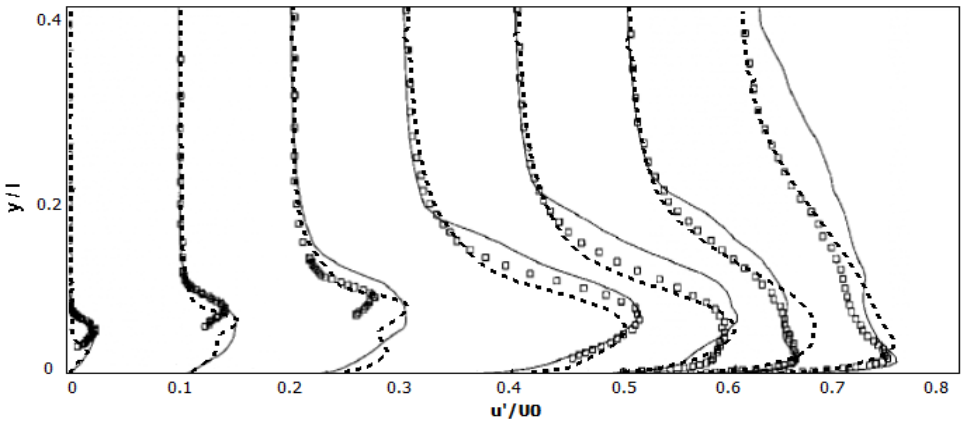

Fig. 3.6. rms streamwise velocity fluctuation *u′* at seven streamwise stations (FST-case), Left to right: *x/l* = 0.22, 0.44, 0.66, 1.09, 1.27, 1.64, 2.55. Present LES (dashed), LES of Yang & Voke (solid line), Exp. Data (symbols)

Profiles of vertical velocity rms *v′*, spanwise velocity rms *w′* and the shear stress *u′v′* are shown in Figures 3.7, 3.8, and 3.9. It can be seen that the agreement between the current predictions (dashed line) and the LES results of Yang and Voke (2001) is

similar to those of *u′*. Generally speaking the current predicted values for all three variables are smaller at all stations and the discrepancies are slightly larger at the 3rd and the last locations for all three quantities. This is understandable for the last location as the discrepancy between *u′* is also quite large. However this seems strange for the 3rd location initially but careful observation of the *u′* profiles at the same location may explain this. Although the predicted magnitude of *u′* at the 3rd location from the current LES and the LES of Yang and Voke (2001) is similar but the profile shape is quite different, i.e., the current predicted profile has two peaks which means that quite different flow structures are predicted in that region, leading to bigger differences in *v′*, *w′* and *u′v′*. At all other locations the agreement is reasonably good for all three variables.

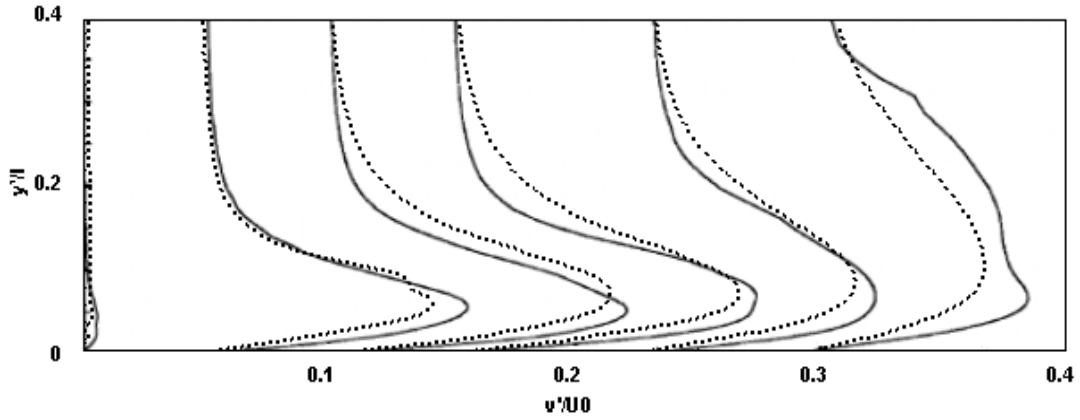

Fig. 3.7. Vertical velocity rms *v′* at six streamwise stations (NFST case), Left to right: *x/l* = 0.22, 0.44, 1.09, 1.27, 1.64, 2.55. Present LES (dashed), LES of Yang & Voke (2001) (solid line).

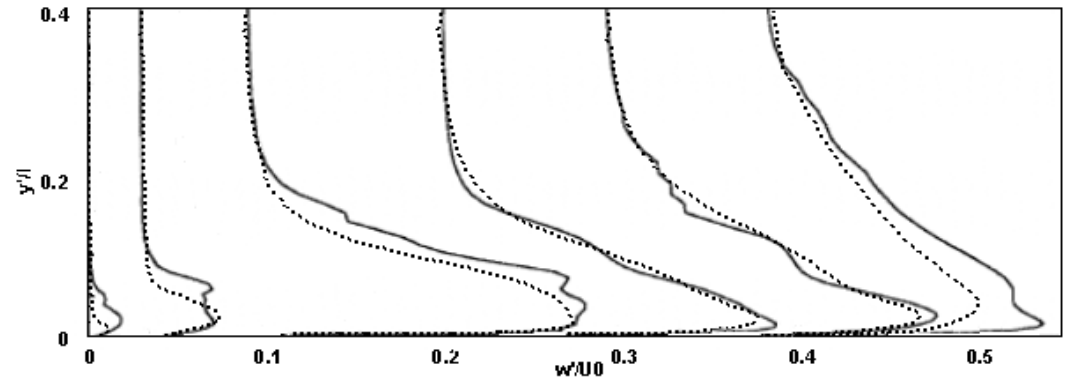

Fig. 3.8. Spanwise velocity rms *w′* at six streamwise stations (NFST case), Left to right: x/l = 0.22, 0.44, 1.09, 1.27, 1.64, 2.55. Present LES (dashed), LES of Yang & Voke (2001) (solid line).

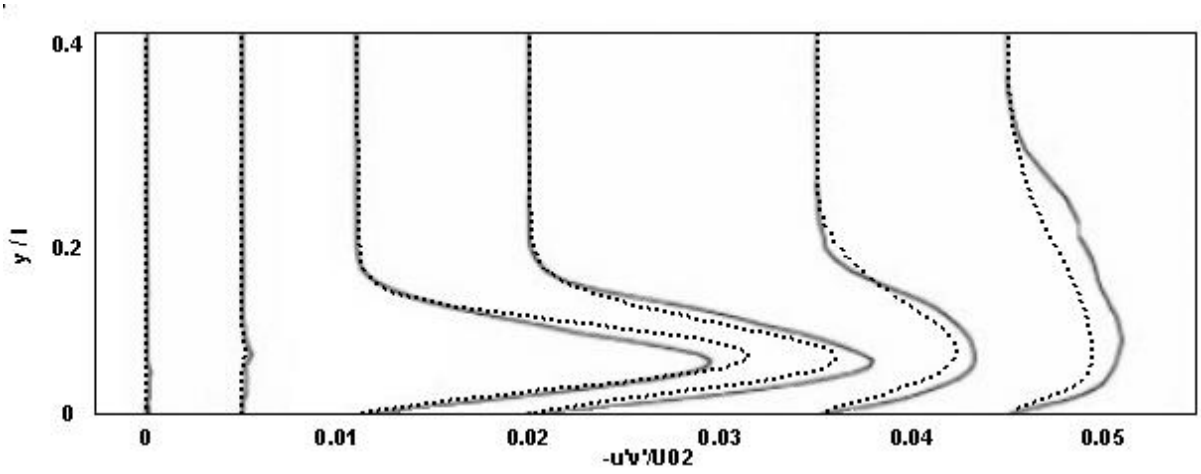

Fig. 3.9. Shear stress $u'v'$ at six streamwise stations (NFST case), Left to right: x/l = 0.22, 0.44, 1.09, 1.27, 1.64, 2.55. Present LES (dashed), LES of Yang & Voke (2001) (solid line).

Figure 3.10 presents isosurfaces of instantaneous spanwise vorticity at three different time, showing the transition process. The laminar boundary layer starts developing from the mean stagnation point, and then separates at the blend point due to the curvature change, leading to unstable free shear layer formed in the separation bubble. It can be seen that the free shear layer becomes unstable at about x/D = 2.1 via an inviscid instability, Kelvin-Helmholtz instability observed also in the study by Yang & Voke (2001). Any small disturbances present grow downstream causing the deformation and distortion of the initial two-dimensional spanwise vortices. Further downstream those two-dimensional vortices become more distorted/deformed, and roll up leading to the formation of streamwise vortices associated with significant three-dimensional motions, eventually breaking down at about the reattachment point and developing rapidly into a turbulent layer downstream. The instability and transition features of the NFST case will be revisited in the next chapter when comparing with the FST case.

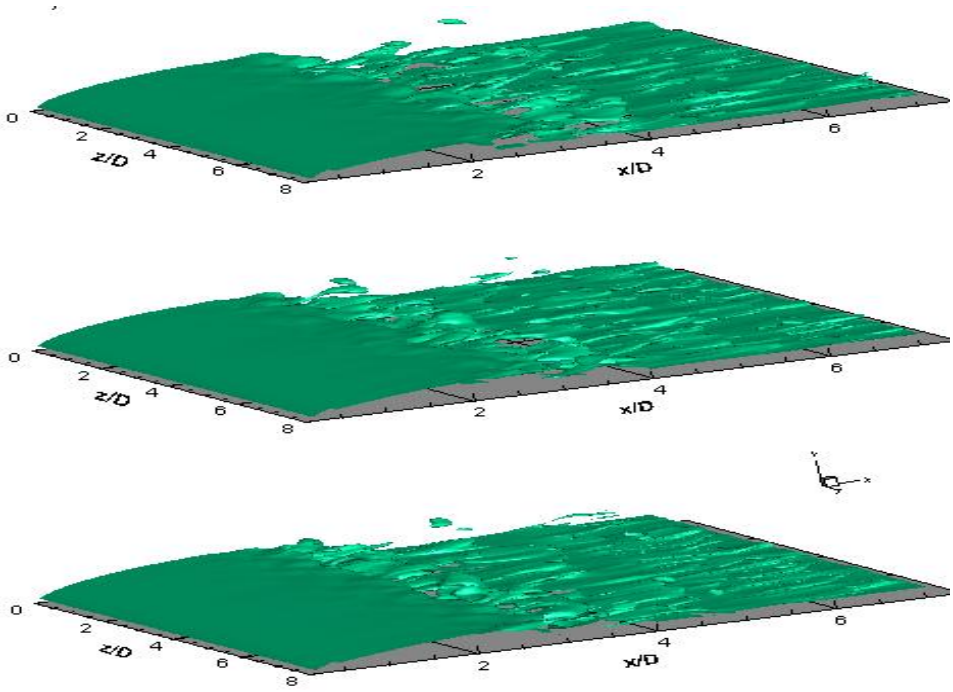

Fig. 3.10. Isosurfaces of instantaneous spanwise vorticity at three different time

3.3 Staggered vs. Co-located Grid

There have been two main kinds of grid systems in the CFD community: staggered grid and co-located grid (also called non-staggered grid). In a co-located grid system all variables are stored at exactly the same location, e.g., at the centre of a cell, whereas in a staggered grid system velocity components and pressure are stored at different locations (pressure and other scalar quantities are usually stored at the cell centre and velocity components are stored at cell faces). Most of the compressible flow solvers have used the co-located grid since it is certainly beneficial to discretise the governing equations using the same control volume for all variables while different control volumes are needed for different variables in the staggered grid, leading to complexity and a large amount of computer memory, especially for complex geometry where non-orthogonal mesh has to be used the co-located grid holds significant advantages over the staggered grid . However, it is rare for incompressible flow solvers to employ the co-located grid mainly due to the fact that the use of such a grid system with a primitive variable formulation of the incompressible equations has been shown to produce nonphysical oscillations in the pressure field when central differencing to both

the continuity equations and the pressure gradient term in the momentum equations is applied. This causes the finite difference form of the momentum equations at even-numbered nodes to depend only on pressures at odd-numbered nodes, while the momentum equations for odd-numbered nodes depend solely on pressures at even-numbered nodes. Similarly, the continuity equation for an even-numbered node depends only on velocities at odd-numbered nodes, etc. If no pressure-density coupling exists, such as in an incompressible flow, no interaction exists between the pressures at adjacent nodes. This situation can permit two different pressure fields to coexist, giving rise to the nonphysical "checkerboard" pressure field.

Rhie and Chow (1983) proposed a pressure-weighted interpolation method (called the Rhie and Chow pressure smoothing, which is equivalent to adding a 3^{rd} order pressure derivative term at the cell face, a kind of artificial dissipation term) to eliminate the checker-board pressure problem, which is widely used in the finite-volume framework with co-located grid scheme. Miller and Schmidt (1988) carried out a detailed comparative study for two incompressible flow test cases, a flow in a shear-driven cavity and a laminar contraction flow, using both staggered and co-located grids with the Rhie and Chow pressure smoothing. Their results show that the co-located grid produces more accurate predictions than the staggered grid**.** Peric, Kessler and Scheuerer (1988) performed incompressible flow calculations with the staggered and the co-located grid. Three test cases were considered: lid driven cavity flow, backward facing step flow and flow through a pipe with sudden contraction. Their results demonstrate that the accuracy are almost identical for both grids. The co-located method converges faster in some cases, and has advantages when extensions such as multigrid techniques and non-orthogonal grids are considereded. Another detailed comparative study was conducted by Melaaen (1992) using both the staggered and co-located grids for three incompressible flow problems: rotating Couette flow, flow through gradual expansion channels and flow through axisymmetric constrictions. The results confirm that equal accuracy are achieved for both grids.

All the comparative studies discussed above were carried out for steady state laminar flow problems and Zang, Street and Koseff (1994) calculated incompressible unsteady flow problems including LES of a rotating stratified upwelling flow in an irregular container using the co-located grid with the Rhie-Chow pressuring smoothing.

Their results compare reasonably well against experimental data but no direct comparison was made against any results obtained from the staggered gird. Breuer and Rodi (1994) applied LES with a co-located grid to predict fully developed incompressible trubulent flow through a 180° bend square duct at Re = 56690 and their results are poor compared against available measurements due to mainly that the complicated secondary flow in the corner regions of the duct could not be captured properly with their grid resolution. Few LES of incompressible flow studies have been carried out using the co-located mesh so far and Morinishi *et. al*. (1998) demonstrated that it is much more difficult to develop fully conservative numerical schemes with the co-located grid whereas in LES it is absolutely crucial that the numerical methods should discretely conserve mass, momentum and kinetic energy. For relatively simple geometries conservative property can be achieved on a staggered grid with second-order central differencing scheme for incompressible flow. Furthermore, instantaneous large-scale turbulent structures need to be captured accurately in LES, which is fundamentally different from the RANS calculations, the numerical methods used in LES must represent the turbulence with sufficient accuracy and avoid the smearing effect brought about by any artificial dissipation. Therefore, staggered grids have been favoured by the LES community and successfully applied to many flow simulations (Nagarajan, Lele and Ferziger 2003; Tang, Yang and McGuirk 2004; Kobayashi, Ham and Wu 2008; Taylor and Sarkar 2008; Shetty et. al. 2010; Yuan, Xu and Khalid 2011). So far most of the transitional flow simulations have employed staggered grid (Yang and Voke 2001; Abdalla and Yang 2004&2005; Padilla and Neto 2008; McMullan, Gao and Coats 2009; Yang and Abdalla 2009) and LES of transitional flows using co-located grids is very rare. Nevertheless as discussed above for complex solution domains with non-orthogonal mesh, a co-located variable arrangement holds significant advantages over the staggered one. In addition the full conservative property of the numerical schemes with the staggered grid cannot be ensured for complex solution domains with non-orthogonal mesh and hence it is very necessary to investigate the accuracy of LES using the co-located grid.

The current LES of transitional separated flow used a co-located variable arrangement on a curvilinear coordinate system with Rhie-Chow pressure smoothing method. From the above comparison and discussion it is evident that the accuracy of the co-located grid arrangement with the Rhie-Chow pressure smoothing when applied

to separated boundary layer transition simulations is as good as using a staggered grid arrangement (judged from the comparisons of mean streamwise velocity and rms against the experimental data) which is consistent with the previous studies for steady flow calculations (Miller and Schmidt 1988; Peric, Kessler and Scheuerer 1988; Melaaen 1992) and unsteady flow calculations by Zang, Street and Koseff (1994). This is very encouraging as the co-located gird has distinct advantages over the staggered grid when computational domains are complex and non-orthogonal meshes have to be used.

Chapter 4

Separated-Reattached Flow under Elevated Free-Stream Turbulence

To investigate effects of considerably high free-stream turbulence level on transition of separated-reattached flow, T3L case presented in the previous chapter (for NFST case) is considered under turbulence intensity of 5.6%, referred to as FST case.

Initially the recycling-rescaling method described in Chapter 2 was used to achieve the experimental FST level at the leading edge. However, unrealistic and somehow repeated bulks of turbulent structures appeared in the free stream (Figure 4.1) which was believed to notably influence the separated shear layer of interest in terms of evolution of coherent structures in the free shear layer and also shedding characteristics. The numerical trip method however appeared to produce more realistic turbulence in the free-stream approaching the plate. The numerical trip was applied at plane $x = -10D$ upstream, where at each computational time step the solution was perturbed in the same manner as white noise described for NFST case, but additionally, half and quarters of generated disturbance magnitude are imposed on neighbouring cells as described in chapter 2. This method leads to an increased coherence of disturbances compared to the simple white noise perturbations. Figure 4.1 shows the instantaneous velocity field for the FST case using both recycling-rescaling and trip methods for free-stream turbulence generation. The tripping disturbance level $A = 0.7$ was adjusted so that the experimental turbulence intensity of $Tu = 5.6\%$ at the leading edge is achieved. A convective boundary condition is used ensuring the convection of the flow through the outlet plane. Periodic boundary condition is used in the spanwise direction. At lateral boundaries free-slip condition is applied and no-slip wall condition is applied at the plate surface. Time step used in the present LES is $\Delta t = 5.0\times10^{-06}$ sec. The simulation ran for 20 flow-through times to allow the flow to become well established and reach a statistically stationary state. Then the averaged results were gathered over further 80 flow-through times with samples taken every 20 steps and averaged over spanwise

direction too. Instantaneous flow fields and time trace of velocity components and pressure at certain points were also stored during the simulations for spectral analysis.

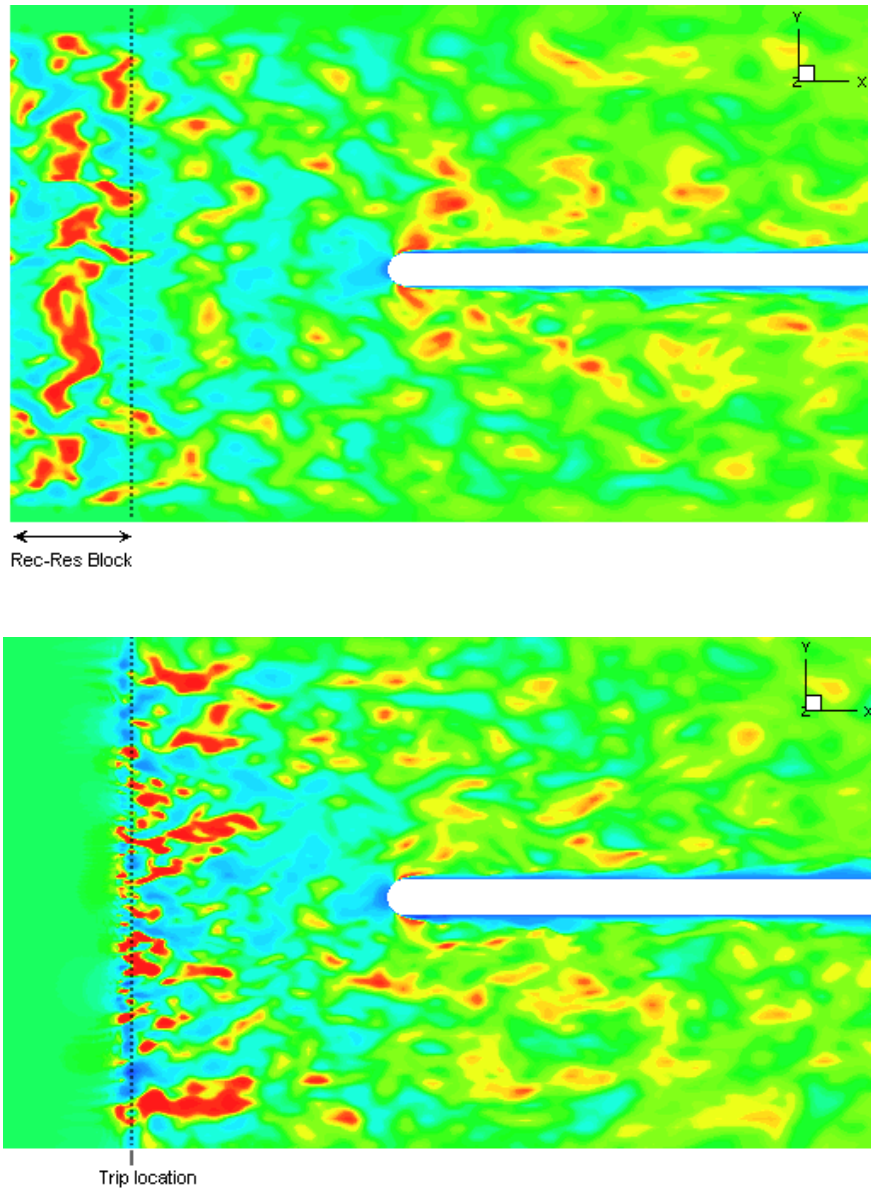

Fig. 4.1. instantaneous velocity field for the FST case using recycling-rescaling (top) and trip (down) methods for free-stream turbulence generation

Figure 4.2 shows decay rate of the free-stream turbulence intensity and it can be seen clearly that a reasonably good agreement has been obtained between the LES prediction and the experimental data at y/D = 4.0 although the LES results show a

continuous decay further downstream while the measured turbulence intensity seems to be constant, not decaying anymore which is unusual. The difference was initially thought to be due to the fact that further downstream experimental data are available only at a lower vertical location of y/D = 1.5, but plotting the LES results at the same vertical location of y/D = 1.5 (dashed line) confirms that this is not the case as the LES results still show a continuous decay which seems to be logical. Nevertheless at the leading edge the LES results match the targeted experimental FST level of 5.6% very well, indicating that the numerical trip applied upstream is a successful technique for generating the required FST at the leading edge.

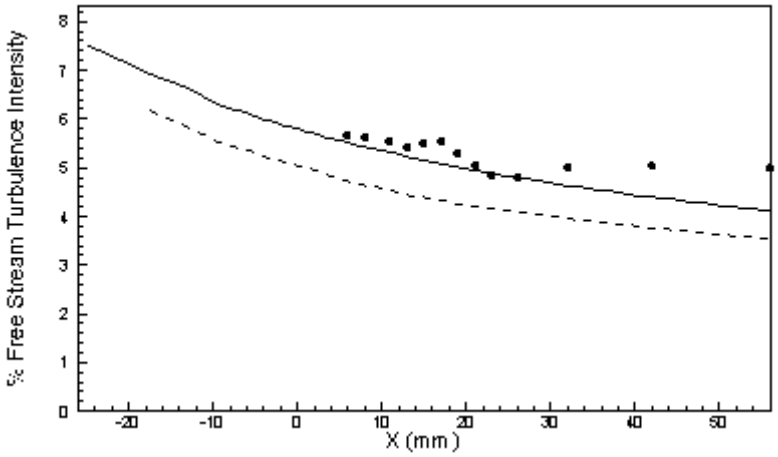

Fig. 4.2. Decay of free-stream turbulence intensity for FST case (5.6% at leading edge), Solid line: y/D = 4.0; Dashed line: y/D =1.5

4.1 Mean Flow Variables

It is well known that increasing free-stream turbulence level will enhance shear-layer entrainment rates, reduces the mean reattachment distance, and causes early transition to turbulence. Hillier and Cherry (1981) showed that increasing FST level would produce considerable contraction of the bubble length and Nakamura and Ozono (1987) reached similar conclusion in their study of effects on a separated and reattaching flow. Kalter and Fernholz (2001) studied the effect of FST on a boundary layer with an adverse pressure gradient and found that by adding FST the mean reverse

flow region was shortened or completely eliminated. Yang and Abdalla (2009) carried out LES of separated boundary layer transition over a flat plate with a blunt leading edge and their predicted mean bubble length reduced 14% when the free-stream turbulence level increased from about 0.2% to 2%. In the current study under 5.6% FST the predicted mean reattachment length (separation bubble length) is 1.2*D*, about 60% reduction compared with the NFST case (2.997*D*); see figures 4.3 and 3.3 showing the mean velocity fields for two cases. This is consistent with previous studies on the effects of FST to reduce the bubble size.

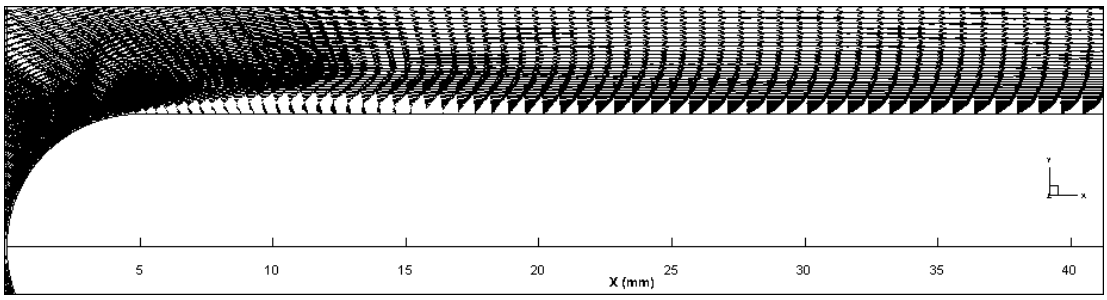

Fig. 4.3. Time-averaged velocity vectors (FST case)

Figures 4.4 and 4.5 present comparison between the current predicted mean streamwise velocity and rms of fluctuations with the experimental data for the FST case (Yang and Voke only carried out study for the NFST case). Excellent agreement has been obtained between the predicted mean profiles and the experimental data at all eight streamwise locations except the last station where the mean profile is slightly over-predicted. The predicted rms of streamwise fluctuations compare very well with the experimental data too in terms of both peak values and the location of peak value. There is a slight under-prediction at three streamwise locations (x = 17mm, 19mm, 21mm) but overall a good agreement has been obtained. Since Δz^+ is 24 which is much bigger than the minimum Δx^+ and Δy^+, a grid refinement has been carried out in the spanwise direction (increased from 64 nodes to 100 nodes) and the peak rms values obtained with the refined mesh closer to the experimental data as shown in Figure 4.6.

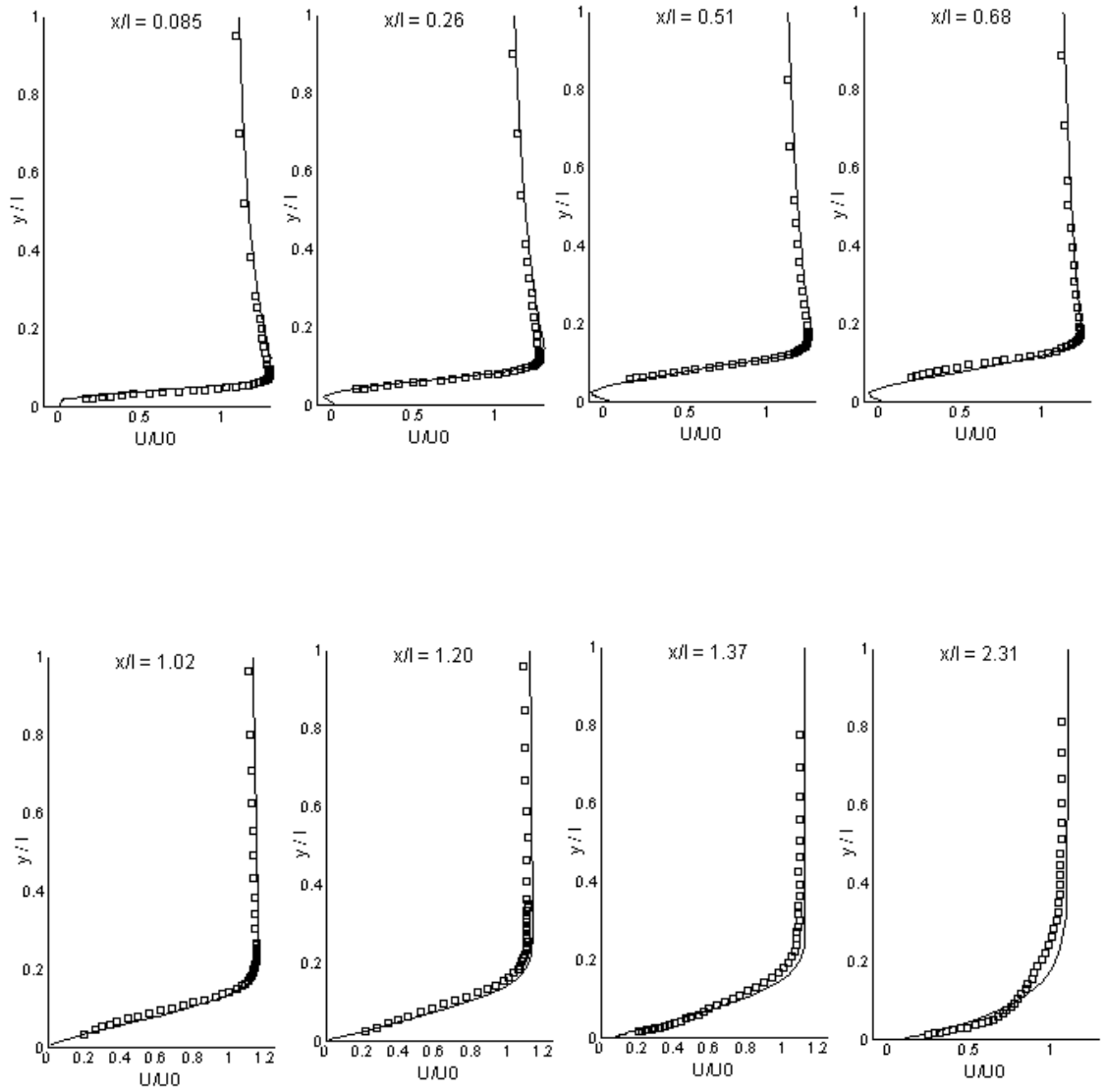

Fig. 4.4. Mean streamwise velocity at different streamwise stations (ETL-case), Present LES (solid lines), Exp. Data (symbols)

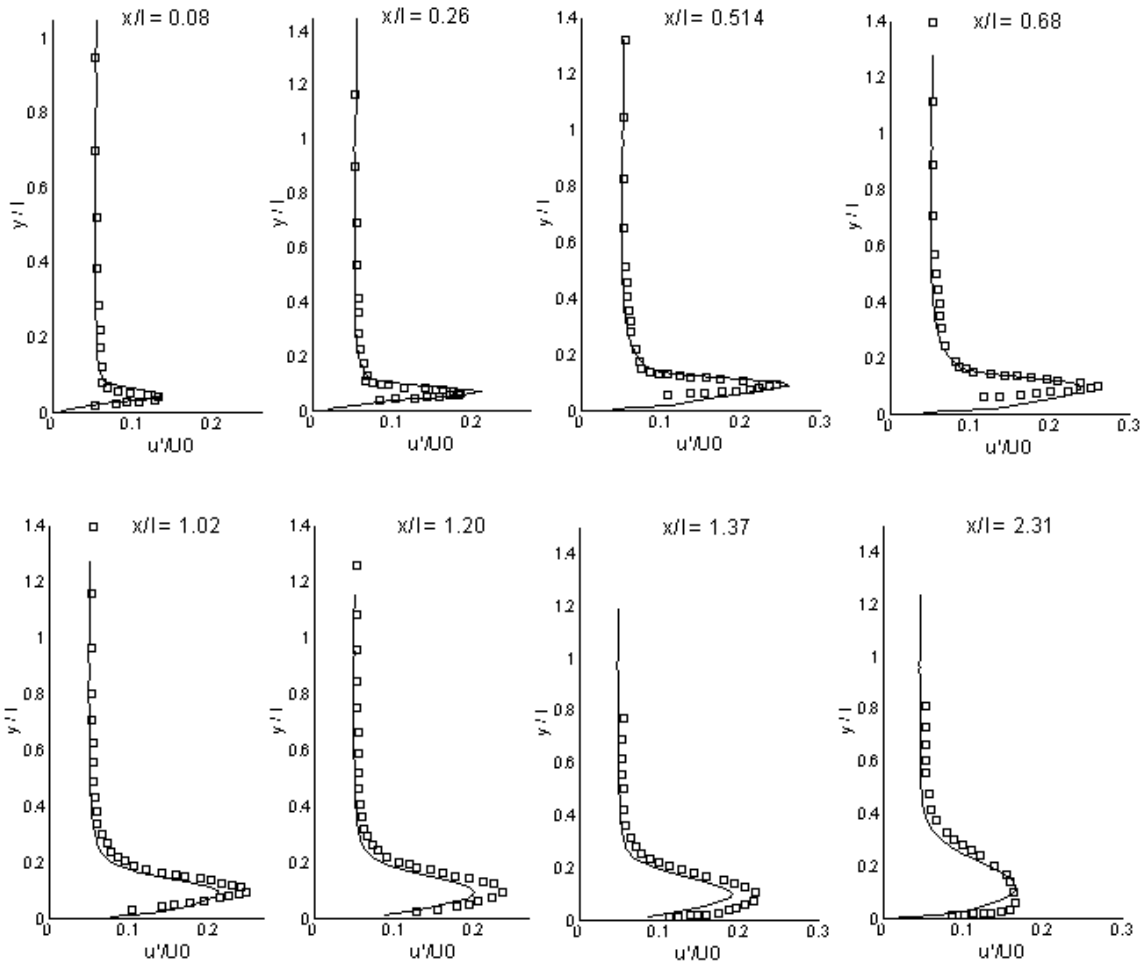

Fig. 4.5 rms streamwise velocity fluctuation *u'* at different streamwise stations (ETL-case), Present LES (solid lines), Exp. Data (symbols)

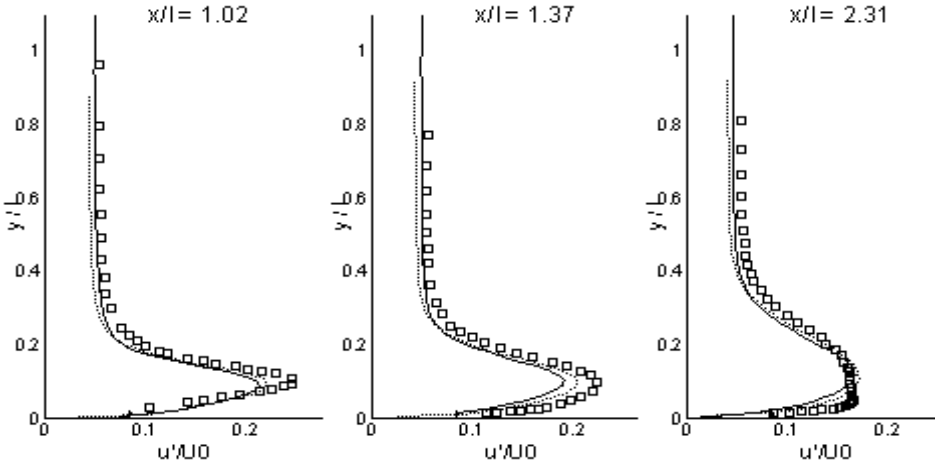

Fig. 4.6. rms streamwise velocity fluctuation *u'* at different streamwise stations (ETL-case), coarser grid (solid lines), refined grid (dotted lines), Exp. Data (symbols)

4.2 Transition Process

Under increased free-stream disturbances transition process and the flow structures involved are known to be remarkably different. As shown in Figure 4.7, disturbances in the free shear layer have larger amplitudes much earlier than NFST case at about x/D = 0.8 due to disturbances from free-stream turbulence. Furthermore it can be seen that the flow in the attached thin boundary layer prior to separation is quite smooth, indicating that it is still laminar boundary layer but is already disturbed to some extent. Careful observation reveals that the spanwise vorticity in the FST case is distorted/deformed very early on and the attached thin laminar boundary layer prior to separation is not quite two-dimensional as some kind of streaky-like structures are visible. There is an increasing amount of evidence (Schlatter *et al.* 2008, Watmuff *et al.* 2010, Brandt & Henningson, 2004) that streaky streamwise-oriented structures confined in the laminar boundary layer are the beginning stage towards the so called "bypass" transition in attached boundary layer flows. Whether the Kelvin-Helmholtz mechanism observed in the NFST case is bypassed in the current study under high turbulence intensity is investigated below.

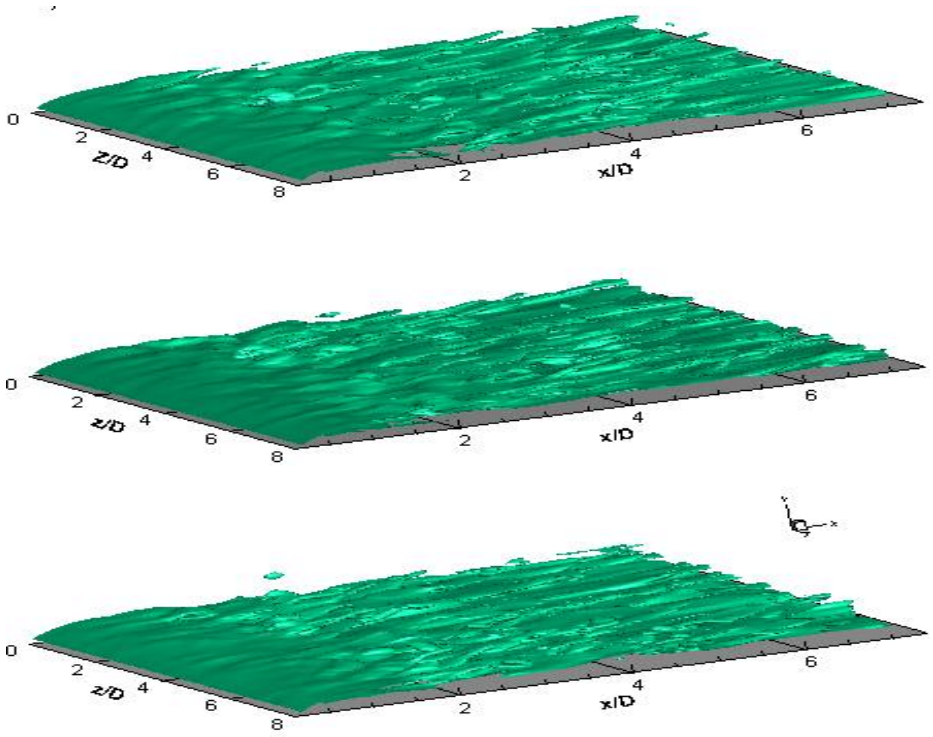

Fig.4.7. Isosurfaces of instantaneous spanwise vorticity at three different time (FST case)

4.2.1 Discussion

Figure 4.8 presents spanwise vorticity for both NFST and FST cases coloured by the magnitude of streanwise velocity fluctuation showing the whole transition process. It can be seen that for the NFST case, initially a steady free shear layer develops associated with formation of two-dimensional spanwise vortices; the free shear layer becomes unstable via an inviscid instability, Kelvin-Helmholtz instability as shown in the study by Yang and Voke (2001), and any small disturbances present grow downstream causing the deformation and distortion of the initial two-dimensional spanwise vortices. Further downstream those two-dimensional vortices become more distorted and deformed, and roll up leading to streamwise vorticity formation associated with significant three-dimensional motions, eventually breaking down at about the reattachment point and developing rapidly into a turbulent layer downstream. The transition process is quite similar for the FST case but the free shear layer becomes unstable much earlier (further upstream) due to disturbances from free-stream turbulence. The initial 2*D* spanwise vortices are so clearly visible in the NSFT case but are not so obvious in the FST case.

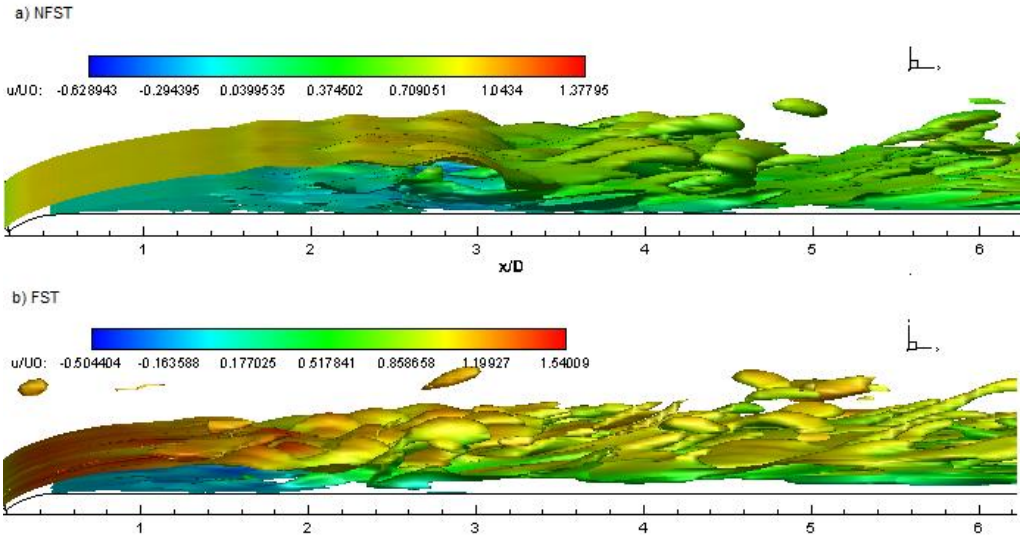

Fig.4.8. spanwise vorticity for both NFST and FST cases coloured by the magnitude of streanwise velocity

Under very low free-stream turbulence, LES of Yang & Voke (2001) for a separated shear layer on a flat plate with a semi-circular leading edge and LES of Abdalla & Yang (2004) on a flat plate with a sharp leading edge proved vigorously for both cases that the free shear layer in the bubble is inviscidly unstable via the Kelvin–Helmholtz mechanism. Similar mechanism was reported by McAuliffe & Yaras (2010) who performed DNS of a separation bubble on a flat plate in adverse pressure gradient with low incoming disturbances. Many experiments have been carried out to study separated boundary layer transition at low free-stream turbulence level. Burgmann et al. (2008) studied a transitional separation bubble on the upper surface of an SD7003 airfoil using time-resolved and volumetric PIV measurements. It was shown from their measurements that the temporal dynamics of the vortex roll-up is initialised by the Kelvin–Helmholtz instability. McAuliffe & Yaras (2009) carried out a through experimental study on the nature of transition in a separation bubble and manipulations of the resultant breakdown to turbulence through passive means of control. Their results confirmed that the Kelvin-Helmholtz instability is the dominant transition mechanism for all conditions. Satta et al. (2010) performed experimental studies of the transition and separation processes occurring along the suction side boundary layer of a high-lift low pressure turbine profile under both steady and unsteady inflow conditions. Under steady inflow condition, their results show that the beginning of boundary layer transition occurs in correspondence of the separated shear layer, along the line of inflection points in the velocity profiles, where the velocity fluctuations are larger due to the shear layer instability taking place through the Kelvin-Helmholtz mechanism. Dahnert et al. (2012) based on their detailed experimental work concluded that the instability involved in the transition process of a separation bubble with low Reynolds number, low free-stream turbulence, and steady main flow conditions is the inviscid Kelvin-Helmholtz instability mode.

It is known that free-stream turbulence results in an earlier transition to turbulence and hence usually a shorter separation bubble (Hillier & Cherry, 1981; Kalter & Fernholz, 2001; Yang & Abdalla, 2005). McAuliffe & Yaras (2010) studied the effect of elevated FST (1.45% at separation) on a laminar separated boundary layer due to an adverse pressure gradient over a flat plate. The Kelvin-Helmholtz instability observed in their low-disturbance case (0.1% FST at separation) was bypassed at the higher FST where streamwise streaks appeared upstream of separation in the laminar boundary

layer leading to production of turbulent spots in the separated shear layer. Bypass mode has also been observed in a few experiments on separation bubbles (Volino & Bohl 2004; Volino, 2002), however in all cases separation took place after relatively long streamwise development of the attached boundary layer which had a big impact on the transition in the following separated free shear layer. In cases where separation is due to the leading edge geometry and the boundary layer separates immediately or very shortly after the leading edge, transition may be different. Yang & Abdalla (2005, 2009) investigated effect of 2% FST at the sharp leading edge of a flat plate and observed that transition process started earlier with a reduction of 14% in the mean bubble length compared against the very low FST case. Nevertheless, 2D Kelvin-Helmholtz rolls were still observable and the primary instability was shown to be the same (the KH mechanism) as in the low FST case. However, as appears from figure 4.7, it is quite possible that under higher level of FST in the current study (5.6%) transition process in a separated boundary layer with the separation point fixed due to the leading edge geometry may take a quite different route, i.e., Kelvin-Helmholtz instability stage may be bypassed, similar to the so called "bypass transition" in attached boundary layer flows. To clarify this point, instability of the free shear layer formed in the separated-reattached flow is examined for the two free-stream turbulence cases addressed in the previous sections.

4.3 Stability Analysis

A. NFST case

As can be seen from figure 4.8, a free shear layer takes form as the apparently-laminar boundary layer separates from the edge of the blunt plate. For the NFST case The flow separates at the curvature change and the free shear layer is two-dimensional up to a distance downstream, where the instabilities and three-dimensionality set in. The free shear layer then undergoes the transition leading to the turbulent reattachment of the shear layer. This can be seen from figures 4.9 and 4.10 which show the instantaneous iso-surfaces of streamwise and spanwise velocity components at three arbitrary times. It can be seen evidently that the velocities at three different times are almost the same up to the streamwise location x/D = 1.9 with the spanwise velocity being zero showing that the the flow is two-dimensional and steady up to this station.

This velocity iso-surfaces drawn at velocity ranges of the shear layer indicate that the unsteadiness begins at streamwise location about *x/D* = 1.9. The instantaneous spanwise velocity first appears at this location until *x/D* = 2.1 where three-dimensionality in the shear layer begin to increase dramatically.

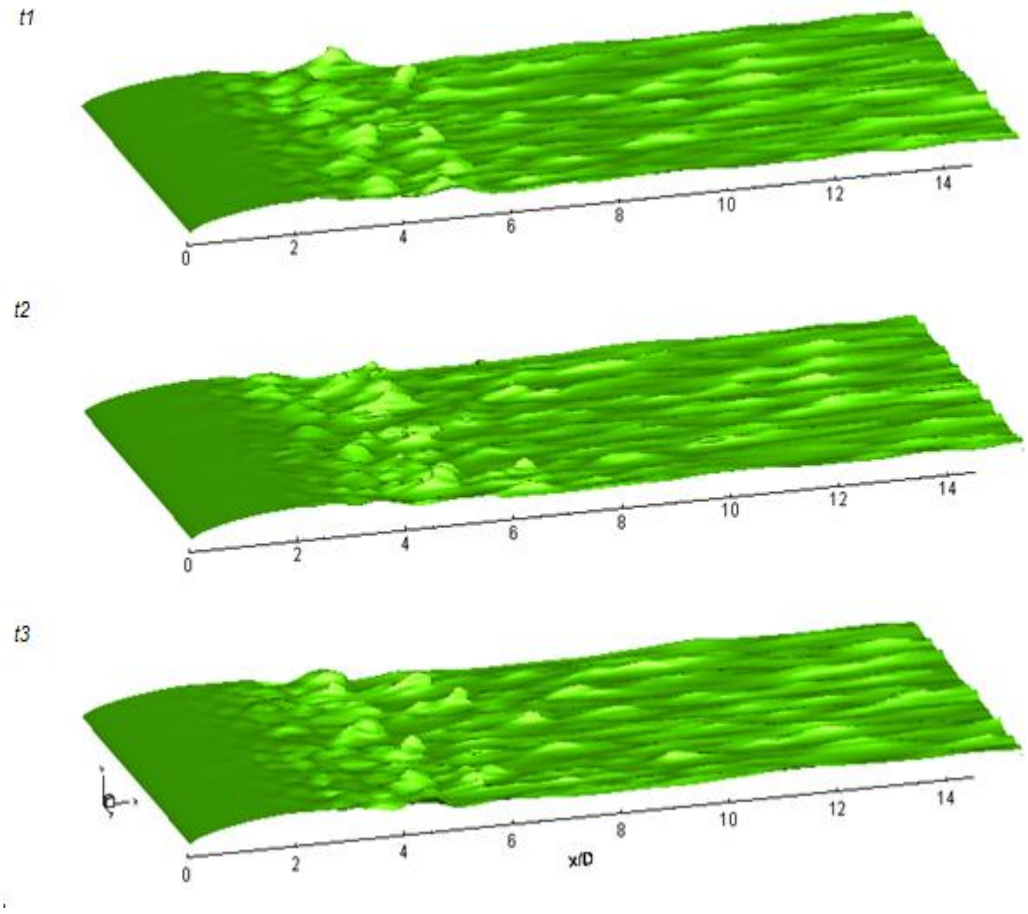

Fig.4.9. instantaneous iso-surfaces of the streamwise velocity at three arbitrary times (NFST case)

The streamwise and wall-normal velocity components show the same sort of behaviour with the initial unsteady motions developing gradually and starting to grow very rapidly at about *x/D* = 2.1 where non-linear rapid growth and breakdown sets in. Examining the instantaneous streamwise velocity along the streamwise direction and at three different times, the initial incidence of the unsteadiness can be located by looking at the discrepancies between velocities at three different times. The difference between

the instantaneous velocities is hardly seen up to the region *x/D* = 2.0. The discrepancy becomes more noticeable downstream and clearly apparent at *x/D* = 2.1. Further downstream at *x/D* = 2.3 the streamwise velocities at different times are very distorted due to the unsteady large-scale motions inducing severe fluctuations. Development of the three-dimensional motions can be examined by following the variation of the instantaneous streamwise velocities along the spanwise direction at different streamwise locations. As can be seen from Figure 4.8, the spanwise variation of the instantaneous streamwise velocity amplifies along the streamwise direction. Up to *x/D* = 1.9 the streamwise velocity is smooth and flat in the span, which indicates that the flow is two-dimensional. Distortions can hardly be observed at *x/D* = 2.0 and increase gradually up to *x/D* = 2.3 where significant three-dimensional motions start to appear and then develop rapidly afterwards.

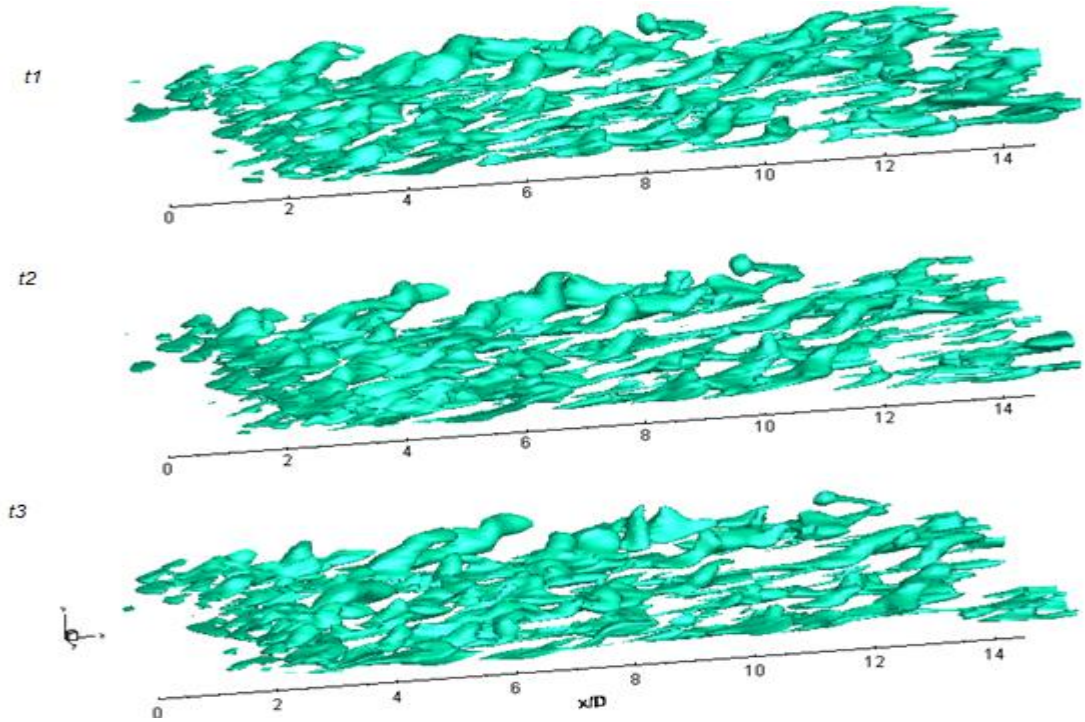

Fig.4.10. instantaneous iso-surfaces of spanwise velocity component at three arbitrary times (NFST case)

The breakdown of the laminar separated shear layer can also be clearly followed in figures 4.8 to 4.10 above. Low amplitude perturbations initially appear in the separated

laminar shear layer, followed by significant increase in the amplitude at about x/D = 2.1. Moving towards the reattachment, the shear layer appears to become irregular at x/D = 2.3 followed by the full breakdown of the spanwise regularity at about x/D = 2.8 within the reattachment region. Overall, snapshots of the vorticity and velocity components presented above provide qualitative information regarding the development of instability towards the three-dimensionality in the separated shear layer under virtually zero free-stream turbulence level (NFST case).

To further clarify the instability of the shear layer developing from the stagnation point to the blend point where separation occurs and then further downstream, the growth of maximum turbulent kinetic energy (k_{max}, the spanwise-averaged peak value of k profile along the wall normal direction in the boundary layer and free shear layer) is presented in Figure 4.11. It can be seen clearly that k_{max} is zero in the attached thin boundary layer and starts to grow at about x/D = 1, well after the separation at a very low rate until at about x/D = 1.8 where k_{max} grows very rapidly at a much higher rate, reaching the peak at about x/D = 3.2.

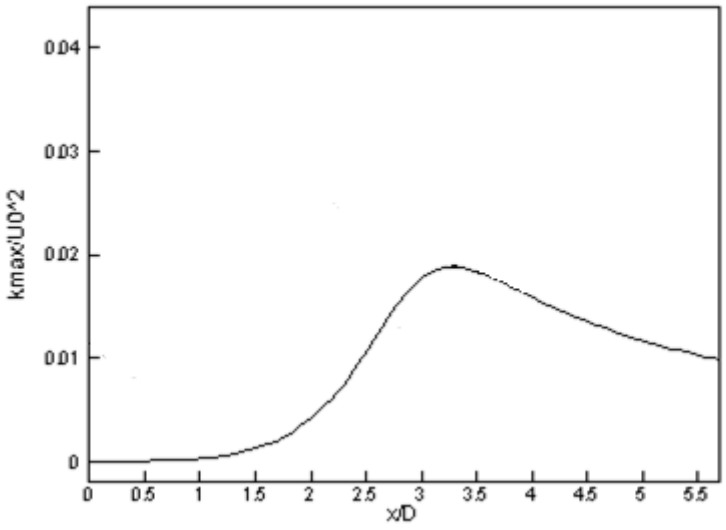

Fig.4.11. Development of the maximum turbulent kinetic energy (NFST case)

Figure 4.12 shows contours of the spanwise vorticity at three instantaneous times in the mid-span plane, clearly indicating presence of the rolled up vortices in the region

x/D = 2-3. From this and velocity snapshots presented above it can be evidently observed that upstream of this region the vortices are initially two-dimensional reminiscent of the well-known Kelvin-Helmholtz instability.

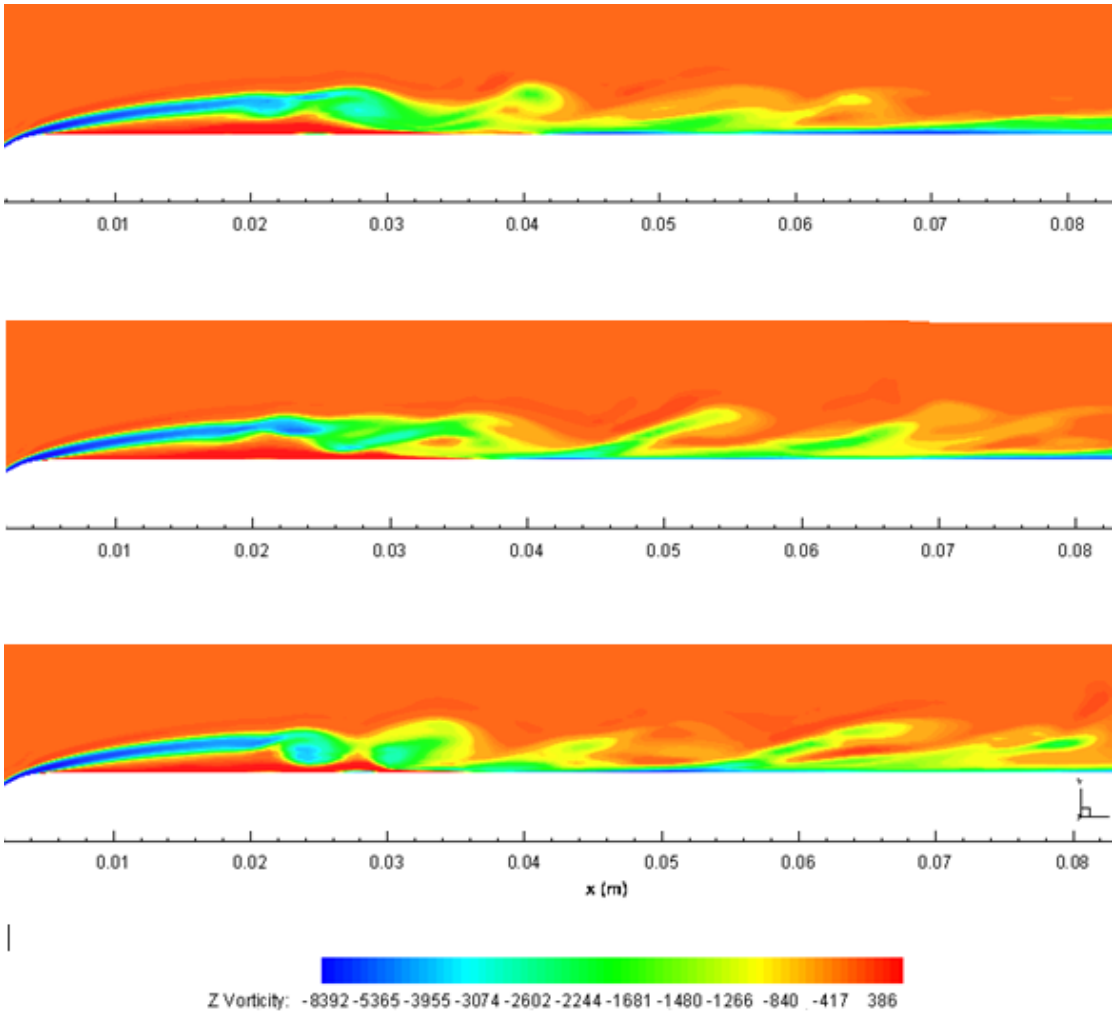

Fig.4.12. spanwise vorticity slices at three instantaneous times in the mid-span plane, (NFST case)

To further support the presence of the Kelvin-Helmholtz instability of the separated shear layer, it is beneficial to analyse the results from linear stability theory. Considering the case of two uniform incompressible, inviscid fluids of densities ρ_1 and ρ_2 separated by a horizontal boundary, let the density ρ_2 of the upper fluid be less than the density ρ_1 of the lower fluid, yielding a stable arrangement in the absence of streaming i.e. when $U_1 = U_2 = 0$. Then for any difference $U_1 - U_2$, no matter how small it is, instability occurs for all wave-numbers greater than a minimum value. When the streaming takes place and disturbances of sufficiently small wavelengths are present,

the stability of the static configuration of layers in the absence of streaming is unable to restrain the instability. This is the Kelvin-Helmholtz instability mechanism as declared by Chandrasekhar (1981). To further explain whether the independence of the Kelvin-Helmholtz instability on | U_1 - U_2 | is due to the sharp discontinuities in the ρ and U which have been assumed in its derivation, Chandrasekhar considered the case of continuous and linear variation of U and certain distribution of ρ (characterised by the Richardson number) and from the inviscid linear stability analysis concluded that for any values of the Richardson number there are always bands of wavelengths for which the Kelvin-Helmholtz instability occurs. When the Richardson number is zero, i.e. for constant density, the condition for the Kelvin-Helmholtz instability is $0 < Kh < 1.2785$ where K is the wave number and h is the shear layer thickness. Compared to the linear variation of the stream velocity discussed above, a more reasonable approximation to a separated shear layer is a hyperbolic tangent profile $U=U_0$ *tanh(y/d)* shown in Figure 4.13.a. Analysis of Chandrasekhar (1981) for instability of shear layer in this case when the Richardson number is zero (i.e. constant density), demonstrates that the shear layer is inviscidly unstable to disturbances in the range $0 < Kd < 1.0$ (Figure 4.13).

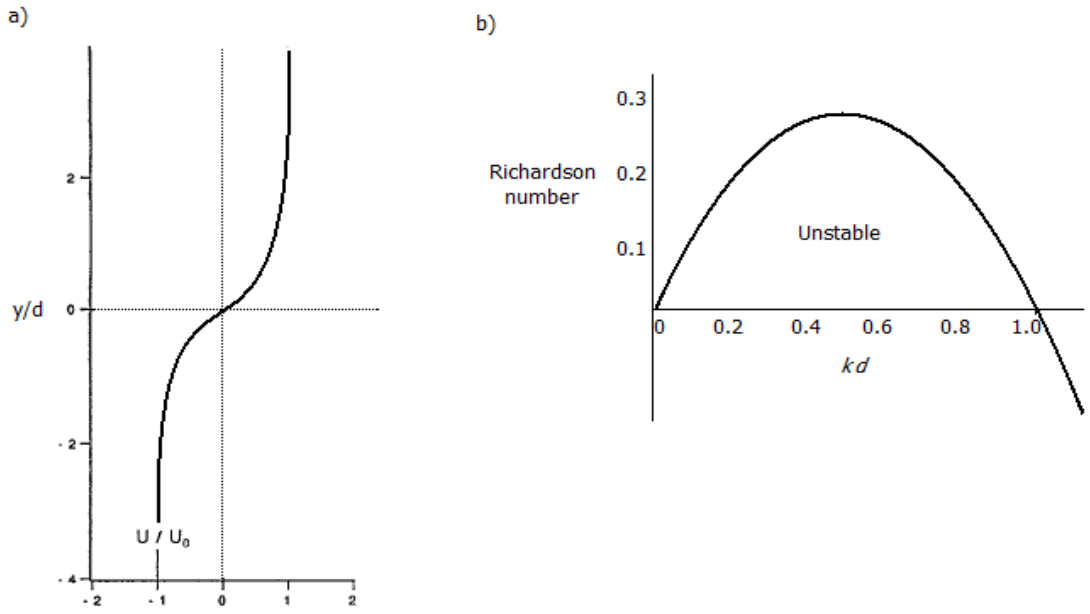

Fig.4.13. *a*) shear layer with the *tanh* velocity distribution and *b)* instability region for this shear layer (Chandrasekhar, 1981). For the Richardson number zero i.e. constant density across the layer, the shear layer is unstable to disturbances in the range $0 < Kd < 1.0$

The instability criteria $0 < Kd < 1.0$ from the linear stability theory discussed above is adopted to investigate the presence of KH instability in the current study. Figure 4.14 shows a typical velocity profile in the separated region (x/l = 0.44) highlighting the shear layer within the free stream and the recirculation flow region.

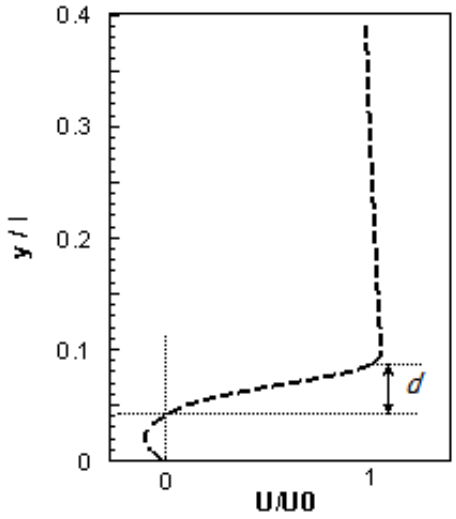

Fig.4.14. a typical velocity profile in the separated region (x/l = 0.44) highlighting the shear layer within the free stream and the recirculation flow region

In the current study, the shear later thickness at the region where the unsteadiness sets in (about x/l = 0.2) is $d = 0.056l$ and hence the unstable region for K is $0 < K < 17.857/l$. Spectral analyses of the separated shear layer at various locations are explored in the next section. It will be seen that for the NFST case a clear frequency content at about f = 146 Hz is dominant (Figure 4.15), in very close agreement with the spectra of Yang & Voke (2001) and equivalent to $f = 0.86U_0/l$ (l is the mean bubble length) which is close to the value previously predicted by Yang and Voke and the measured characteristic frequency discussed before. The wave number K is defined as $K = 2\pi f/c$ where c is the wave speed (propagation speed of the rolled-up vortices). This value is assumed equal to the flow velocity at the inflection point, according to Yang & Voke (2001), Simoni et al. (2012) and confirmed by PIV results using the procedure proposed by Adrian et al. (2000) where different constant transformation velocities were subtracted from the instantaneous flow fields, and the most appropriate value in order to track KH vortices propagation was the velocity at the inflection point. At x/l = 0.2 this equals $c = 0.42U_0$ and hence $K = 2\pi f/c = 12.86/l$ which satisfies the KH

instability criterion ($0 < K < 17.857/l$). It is hence confirmed that the instability mechanism at work in the current study at nearly zero free stream turbulence is through the Kelvin-Helmholtz instability mode.

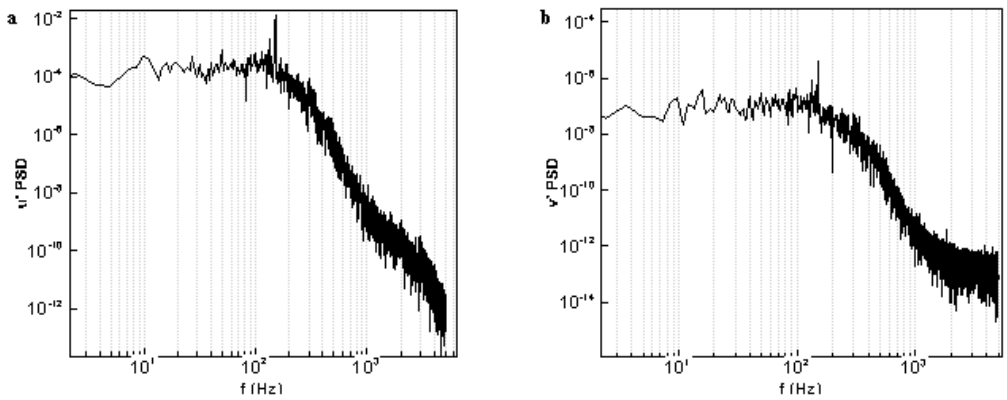

Fig.4.15. velocity spectra at *x/D* = 3.28, *y/D* = 0. 504, NFST case

B. FST case

Figure 4.16 shows the instantaneous iso-surfaces of the streamwise velocity with a spanwise slice at a downstream location. The first sign of perturbations can be observed at about *x/D* = 0.8 and perturbations become considerably larger at about *x/D* = 1.3. This can further be supported by the following figures depicting the spanwise snapshots of the velocity and pressure contours at three different times and at different stations moving along the streamwise direction. Figures 4.17-19 show the instantaneous velocity at different streamwise locations at different times. The discrepancy between velocities at three different times can hardly be seen at *x/D* = 0.6 (figure 4.17). The discrepancy between the instantaneous velocities grows downstream and becomes clearly apparent at *x/D* = 0.8 as shown in figure 4.18. Discrepancy becomes considerably larger at about *x/D* = 1.3 as can be seen in figure 4.19. From the instantaneous velocity contours at *x/D* = 0.6 it may be conjectured that even with the high free stream turbulence level considered, the separation is still laminar as the instantaneous velocity and pressure at *x/D* = 0.6 are more or less the same.

Spanwise variation of the instantaneous streamwise velocities at different streamwise locations can also be seen in figures 4.16-19. At *x/D* = 0.8 the streamwise

velocity contours are not totally free from waviness and some weak distortions can be identified, an indication that at this early location of the separation bubble weak perturbations exist. Compared against figure 4.9, which shows the instantaneous velocities for the NFST simulation, it is apparent that the addition of free-stream turbulence has led to unsteady flow at much earlier stage. Comparing figures 4.16-19 to the results from NFST case, supports the idea that addition of the free-stream turbulence is speeding up the transition compared to the NFST case which is consistent with all the experimental results obtained up to date.

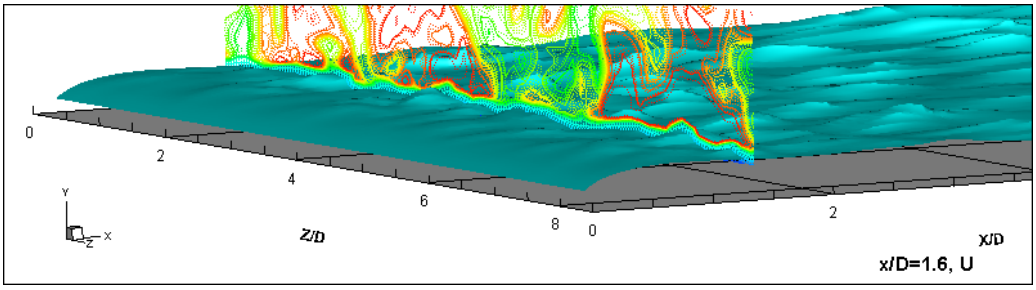

Fig.4.16 instantaneous iso-surfaces of the streamwise velocity with a spanwise slice at *x/D* =1.6 (FST case)

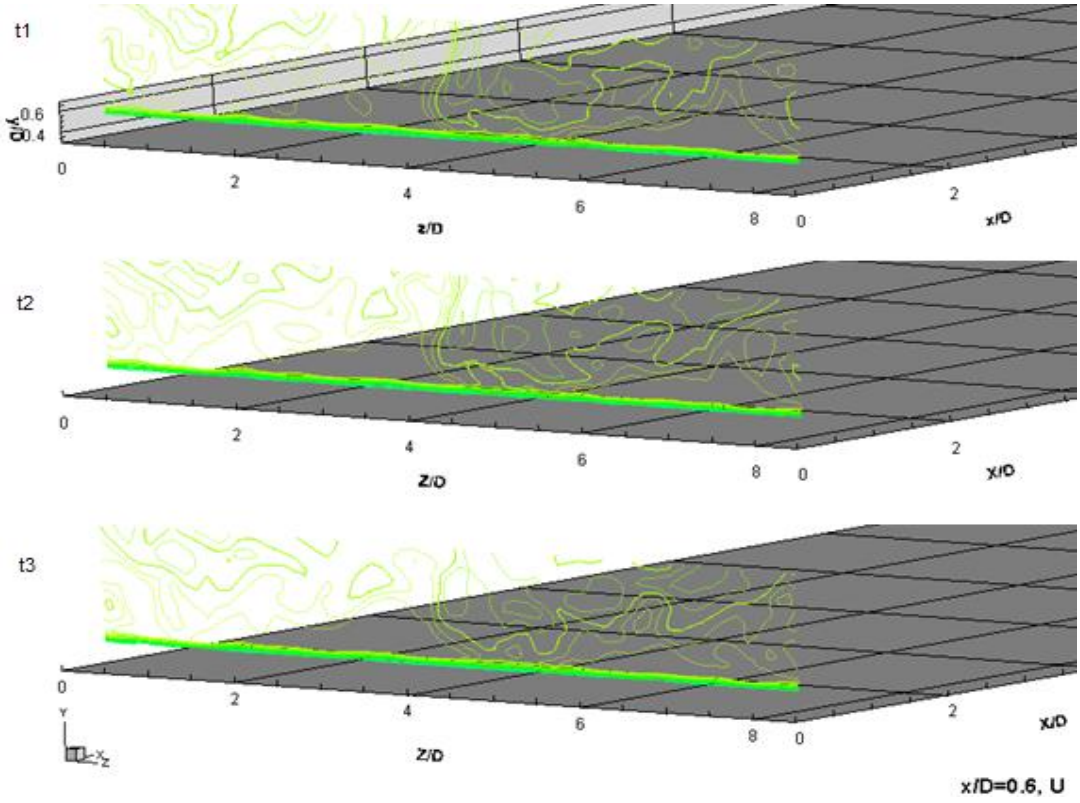

Fig.4.17 instantaneous U velocity at x/D = 0.6 at different times (FST case)

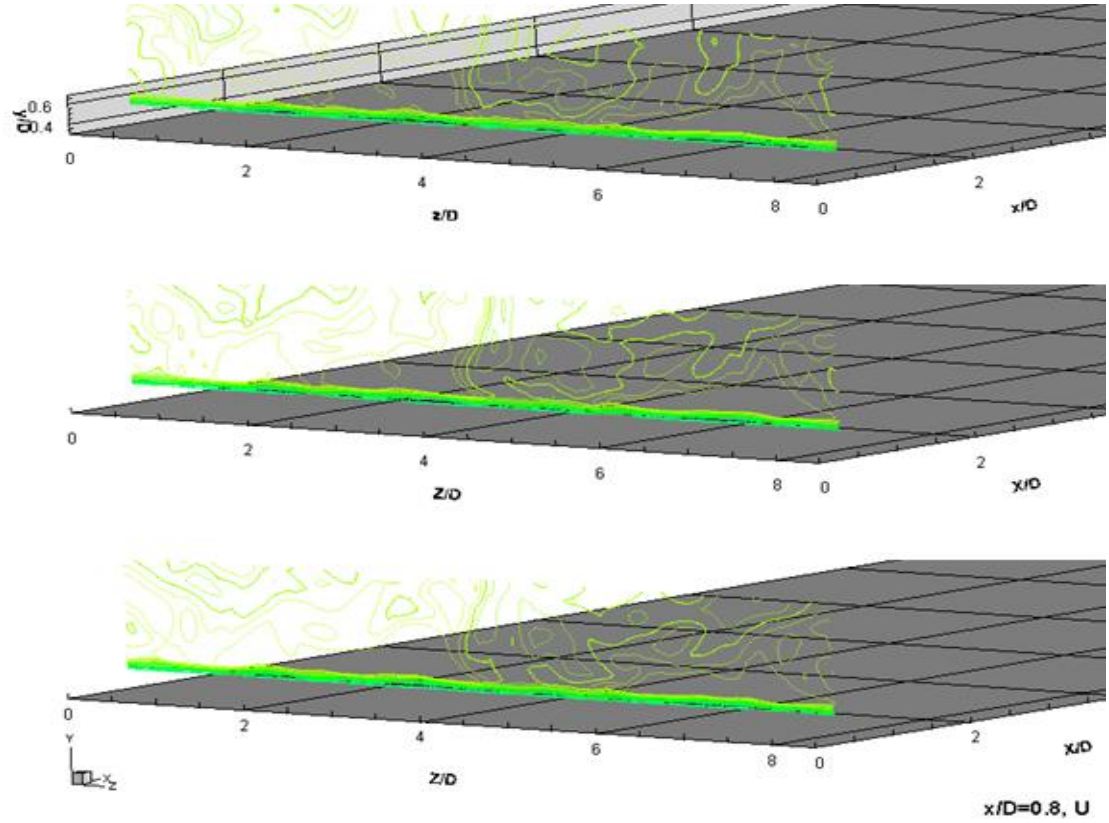

Fig.4.18 instantaneous U velocity at x/D = 0.8 at different times (FST case)

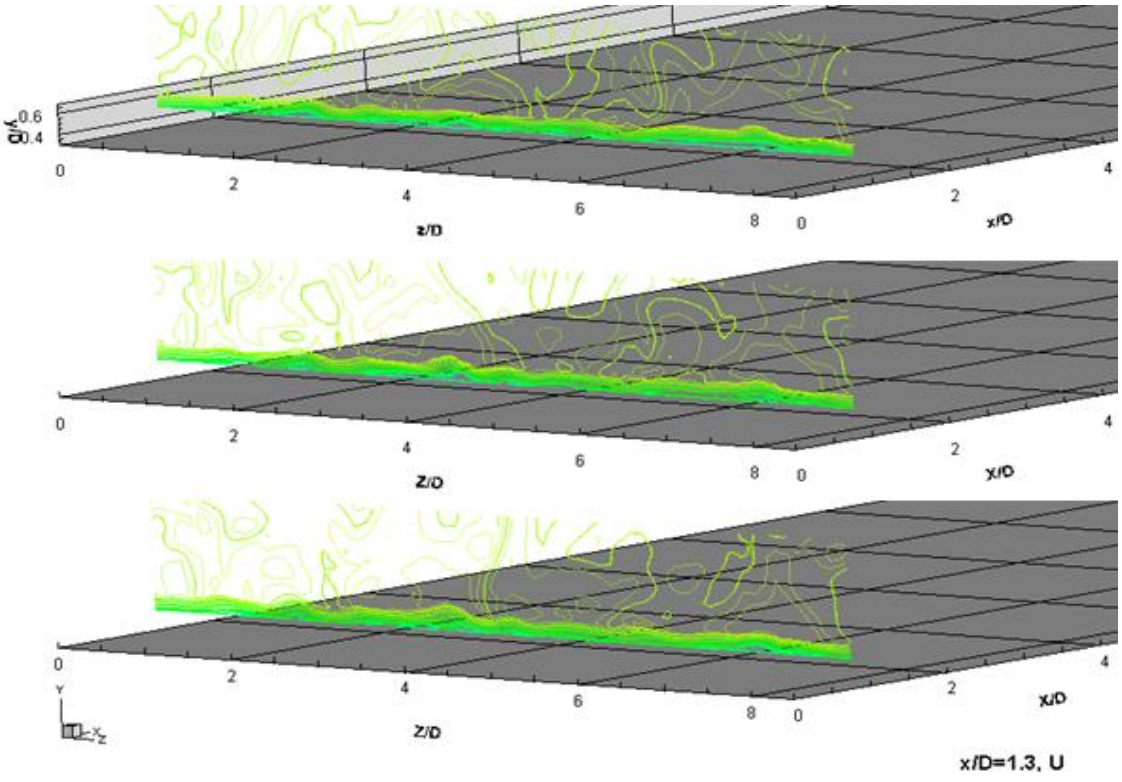

FIG.4.19 instantaneous U velocity at x/D =1.13 at different times (FST case)

To further clarify the instability of the shear layer at high free-stream turbulence the growth of maximum turbulent kinetic energy in the shear layer is compared with the NFST case as presented in figure 4.20. The shear layer develops from the stagnation point to the blend point where separation occurs and then further downstream. It can be seen clearly that k_{max} is non-zero before separation for the FST case, decreasing slightly in the attached thin boundary layer since the flow accelerates along the semi-circular leading edge but starting to grow very rapidly after separation and reaching the peak in the separation bubble at about x/D = 1.1. The maximum turbulence energy profile along the plate for the FST case clearly shows that the attached thin boundary layer is receptive to the free stream turbulence before separation, carrying a small amount of turbulent kinetic energy at separation which grows very rapidly after the separation, leading to much earlier transition and breakdown to turbulent flow compared to the NFST case where k_{max} is zero in the attached thin boundary layer and starts to grow at about x/D = 1, well after the separation at a very low rate until at about x/D = 1.8 where k_{max} grows very rapidly reaching the peak at about x/D = 3.2.

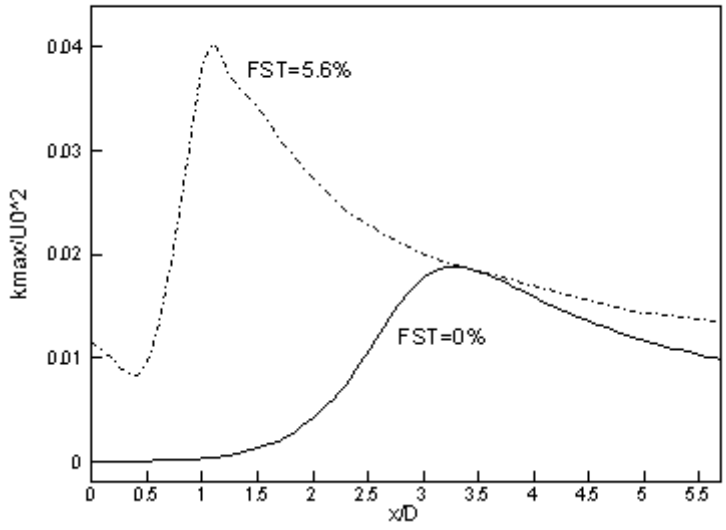

Fig. 4.20. Development of the maximum turbulent kinetic energy; NFST case (solid line), FST case (dashed line)

The above discussion has indicated that for the FST case a kind of “bypass” transition may have taken place, i.e., the Kelvin-Helmholtz instability is bypassed. To

further investigate this the *Kd* criteria applied to the NFST case is also followed here. According to the extensive spectral analysis presented in the next section, and unlike the NFST case, only a mild peak region could be observed in the region $0.8 < x/D < 1.45$ within the bubble shear layer. Figure 4.21 show the spectra at $x/D = 1.03$, $y/D = 0.528$ where a mild characteristic frequency at about $f = 670$ Hz can be observed. This is equivalent to the average characteristic frequency $f = 1.56U_0/l$. The wave speed c is equal to the velocity at the critical layer, i.e. the streamwise velocity at the inflection point ($x/D = 1.03$, $y/D = 0.59$), which is $0.61U_0$ so that the wave number $K = 2\pi f/c = 16.107/l$. The shear layer thickness at this streamwise location ($x/D = 1.03$) is about $d = 0.1l$ and hence $Kd = 1.61$ which does not satisfy the Kelvin-Helmholtz instability criterion ($0 < Kd < 1.0$). The same calculation for the upstream location $x/D = 0.83$ where shedding frequency first appears gives: $f = 600$ Hz ($1.39U_0/l$), $c = 0.59U_0$, $K = 2\pi f/c = 14.91/l$, $d = 0.09l$, and $Kd = 1.34$ which also does not satisfy the Kelvin-Helmholtz instability criterion ($0 < Kd < 1.0$). Therefore from all the evidences above it can be concluded that the primary Kelvin-Helmholtz instability observed under low free-stream turbulence is bypassed at the high free-stream turbulence level of 5.6% examined in the current study.

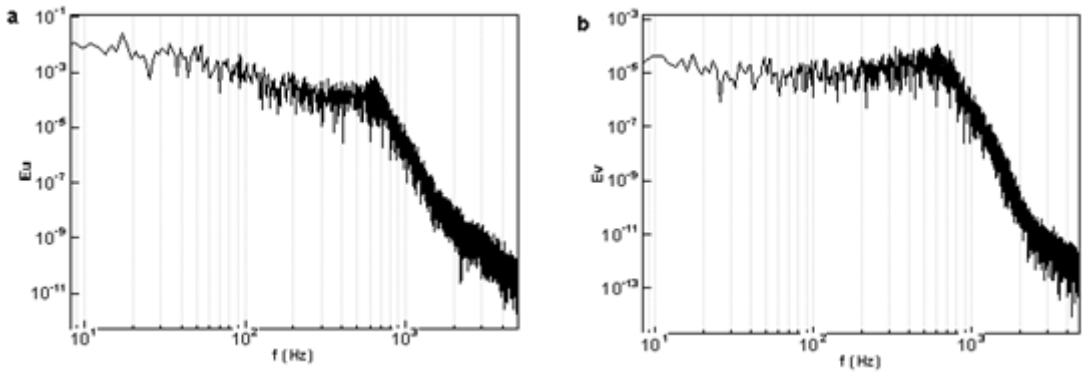

Fig. 4.21. Power spectrum of streamwise velocity fluctuations u', v' at $x/D = 1.03$, $y/D = 0.528$ (FST case)

4.4 Spectral Analysis

Of fundamental feature of separated-reattached flows is the potential presence of two different shedding frequencies (Kiya & Sasaki 1983; Hillier & Cherry 1981a; Cherry et al. 1984; Castro & Haque 1987; Laura et al. 2003): a characteristic frequency

shedding mode which is associated with the usual large scale motions in the free shear layer and a low-frequency mode reflecting overall separation bubble growth/decay dynamics, the so called low-frequency shear layer flapping in the literature. In this section shedding characteristics of the separated-reattached flow and possible effect of FST is examined.

Kiya and Sasaki (1983) measured the cross-spectrum $|E_{u'v'}|$ at the edge and centre of the shear layer over a blunt flat plate geometry at Re number of 26,000 based on the free stream velocity and the plate thickness. The cross spectra showed a peak at the frequency $fl/U_0 \approx 0.51$ (f is the shedding frequency, l is the mean separation bubble length and U_0 is the free stream velocity) which was close to the peak frequency of measured power spectra for streamwise velocity and surface pressure fluctuations in the reattachment region. It was conjectured that these spectra peaks correspond to large-scale vortices shedding from the separation bubble which they estimated to be 0.6 – $0.8fl/U_0$. Near the separation at $x/l = 0.02$, a high frequency periodic wave was detected, with the non-dimensional frequency fl/U_0 being approximately 30. This high-frequency component was interpreted as the frequency at which the rolled-up vortices in the shear layer pass through the position of the fixed hot-wire probe. They also reported a low-frequency flapping motion of the shear layer near the separation line. Their measured surface pressure spectrum at x/l = 0.2 had a clear peak at a much low frequency, $fl/U_0 \approx$ 0.12. They suggested that this low frequency peak may be caused by a large-scale unsteadiness, possibly related to the shrinkage and enlargement of the separation bubble. Hillier and Cherry (1981) observed a peak in the pressure spectra at similar frequency range and stated it could be due to shear layer flapping near the separation line. This low-frequency flapping (fl/U_0= 0.12) was also confirmed in the experiment of Cherry et al. (1984).

Separated flow behind a normal flat plate with a long central splitter plate was studied by Castro & Haque (1987), Hudy et al. (2003) and both the low and the characteristic frequency modes were detected too. However, for the same flow configuration Ruderich & Fernholz (1986) did not observe any dominant frequencies in their power spectra. Flow separation behind a backward-facing step showed both frequency modes in velocity measurements by Eaton & Johnston (1981). They suggested that the low-frequency motion may be associated with an instantaneous

imbalance between the entrainment rate from the recirculation zone and its resupply near the reattachment. Two frequency modes were also detected by Lee & Sung (2001) in their measured spectra of the surface pressure close to separation in a backward-facing step flow.

Cherry *et al.* (1984) studied a separated–reattached flow over a blunt flat plate at a Reynolds number of 32,000 based on the free-stream velocity and the plate thickness. However, the difference was that the flow was laminar before but transition occurred very close to separation while in all cases mentioned above it was turbulent flow at separation. The measured power spectra of surface-pressure fluctuations near separation showed a low-frequency peak band estimated about fl/U_0 = 0.12. They suspected that transition was behind this behaviour but as transition occurred extremely close to separation and hence the transition effect was ruled out. As a result of this Cherry *et al.* (1984) suggested that the low-frequency flapping only occurs when it is turbulent flow at separation, not for transitional flow cases. This was later supported by the study of Abdalla & Yang (2005) for a separated–reattached flow over a blunt flat plate under very low free-stream turbulence where the flow at separation was laminar.

Several DNS studies of transition to turbulence within a laminar separation bubble have been carried out (Alam & Sandham 2000, Spalart & Strelets 2000, Marxen *et al.* 2003, Marxen *et al.* 2004) and recently Jones *et al.* (2008) performed DNS of laminar separation bubbles on a NACA-0012 airfoil. However, the two shedding modes, especially the low-frequency shear layer flapping, were not shown in all those DNS studies.

It is well known that FST has a great impact on a separated-reattached flow, e.g., increasing FST level would produce considerable contraction of the bubble length (Hillier & Cherry 1981), or even eliminate the reverse flow region completely (Kalter & Fernholz 2001). However, most of the previous studies did not address the effect of FST on the low-frequency flapping of the shear layer. Castro & Haque (1988) mentioned in their study of a separated-reattached flow behind a normal flat plate with a long central splitter plate that FST led to an increased ‘flapping motion’ of the shear layer just after separation. Yang and Abdalla (2009) carried out a detailed numerical study of a separated boundary layer transition on a flat plate with a blunt leading edge

with 2% FST and their study did not show the existence of such a low-frequency flapping.

In this section spectral analysis for both NFST and FST cases is presented to investigate frequency characteristics of the transitional separated shear layer under low and high free-stream turbulence. The results presented below correspond to 20,000 samples taken every 20 time-steps at each point which is equivalent to 2.0 seconds, providing enough samples for reliable results over the relevant shedding frequency range (the maximum frequency that can be resolved is 5 kHz and the lowest is about 1 Hz) as the typical low-frequency flapping occurs at about fl/U_0 = 0.12 (Hillier & Cherry, 1981; Kiya & Sasaki, 1983; Cherry et al., 1984). For the current study this is equivalent to f = 20 Hz for the NFST case and f = 51.7 Hz for FST case so the low-frequency flapping would happen every 0.05sec and 0.02sec respectively. This means that the samples collected over the time of 2.0 sec are able to cover 40 and 100 low-frequency flapping cycles and should have been able to capture this low-frequency flapping if it exists in the current study.

4.4.1 NFST case

Extensive point data were stored at 12 streamwise stations covering the whole bubble length, and 7 wall-normal locations at each streamwise station to cover the bubble height from the very near wall region to the free stream above the free shear layer. Figure 4.22 shows the mean streamlines and the locations considered for spectral analysis. The coordinate origin is at stagnation point and separation occurs at blend point x/D = 0.5. The streamwise stations are: x/D = 0.33, 0.61, 0.86, 1.15, 1.46, 1.72, 1.94, 2.19, 2.51, 2.87, 3.28, and 3.62. At each streamwise location, time traces of velocity components were collected at wall-normal locations y/D = 0.504, 0.516, 0.528, 0.542, 0.558, 0.59, 0.85. The above mentioned locations are considered at four spanwise locations z/D = 2.0, 2.5, 3.0, 4.0. The figures below correspond to the mid spanwise location z/D = 4.0.

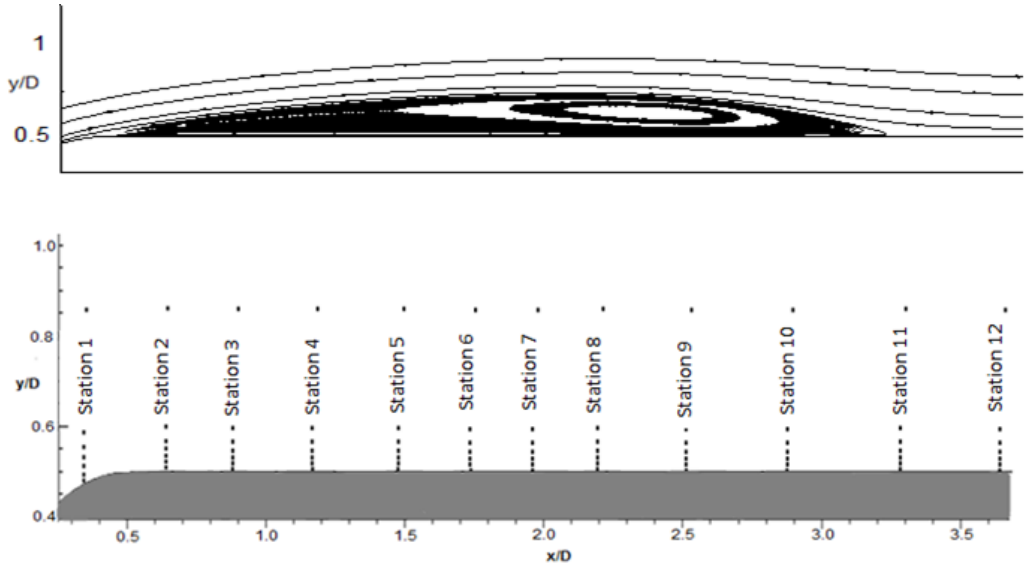

Fig.4.22. mean bubble streamlines and point locations for spectral analysis (12 streamwise stations with 7 wall-normal locations each)

Considering spectral characteristics of the free-stream near the leading edge and far away from the wall (figure 4.22, station 1, y/D = 0.85), the spectra for the velocity components u', v', w' are shown in figure 4.23 *a*, *b*, *c*, respectively which reflect the very low amplitude random (non-periodic) perturbations imposed on the free-stream flow. The spectra are quiet and do not show any high- or low-frequency contents. Since the spectra for u', v' and w' are quite similar at all other locations only u' and v' spectra are presented for the rest of the points. Close to the separation line and very close to the surface (figure 4.22, station 2, y/D = 0.504), the spectra for the velocity components u', v' are shown in figure 4.24*a*, *b* respectively. The *u*-spectrum clearly shows a peak at a frequency approximately 146 Hz. This is equivalent to $0.86U_0/l$, which is in close agreement with the experimental values discussed above. Other studies for separated reattached flows (different geometries) reported similar ranges of this value. Yang & Voke (2001) reported a value of $0.82U_0/l$ in their LES for the same flow configuration. For the backward-facing step, Lee & Sung (2001) identified a value of $f = 0.5U_0/l$. A frequency range of $0.5–0.8U_0/l$ was reported by Mabey (1992) and Driver *et al* (1987) identified a frequency at $f = 0.6U_0/l$. This frequency peak has been attributed to the shedding of large scale vortices from the separation bubble.

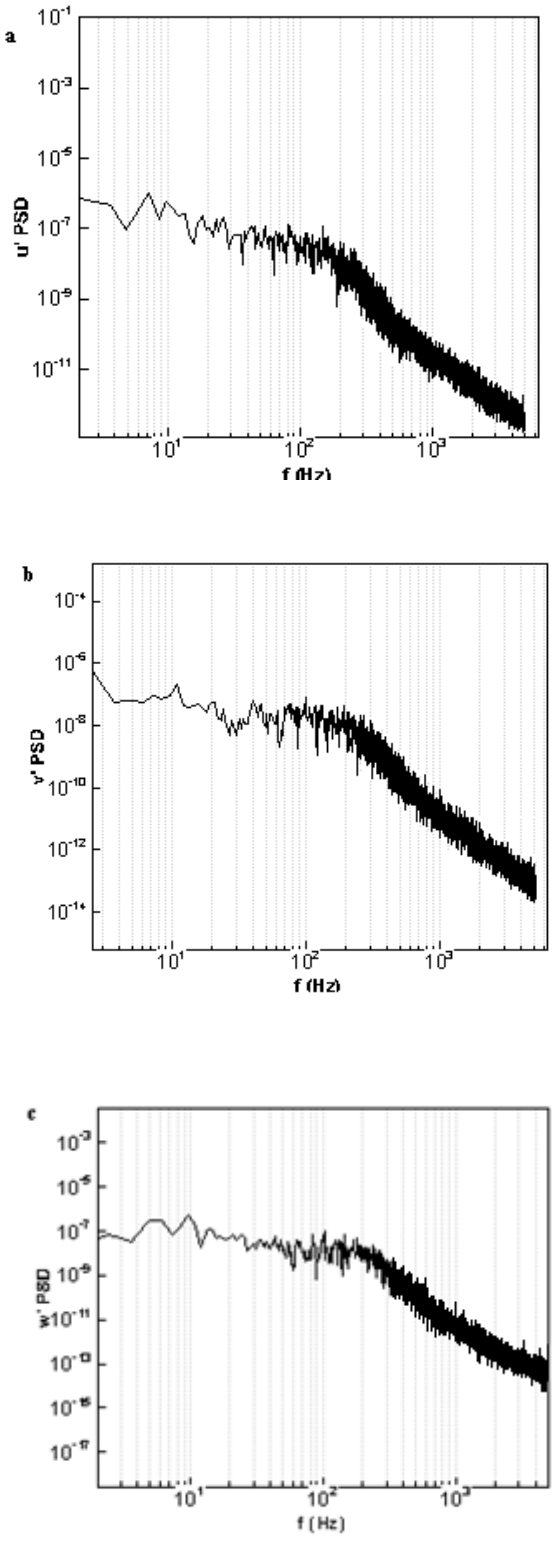

Fig.4.23. *u'*, *v'*, *w'* spectra at *x/D* = 0.33, *y/D* = 0.85, NFST case

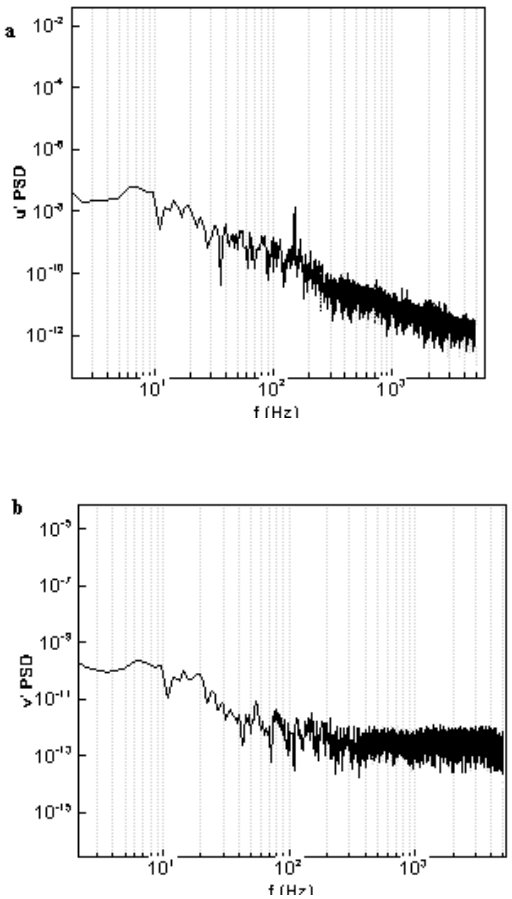

Fig.4.24. *u', v'* spectra at *x/D* = 0.61, *y/D* = 0.504, NFST case

Moving upward at the same *x*-location (figure 4.22, station 2, 2nd – 6th wall-normal locations: *y/D* = 0.516, 0.528, 0.542, 0.558, 0.59) figures 4.24 to 4.28 show the spectra of the streamwise and wall-normal velocity components. These positions extend from slightly below the center of the shear layer to the edge of shear layer. As can be seen from the figures, both the velocity components show the regular high shedding frequency at 146 Hz. The experimental work of Kiya & Sasaki (1983) and Cherry et al (1984) emphasised the fact that close to separation, the spectra is dominated by a low-frequency content which they attributed to the flapping of the shear layer as discussed before. A low frequency activity was also reported in the LES of Yang of Voke (2001) for the same case with the low-frequency flapping fl/U_0 = 0.12. However at this station close to the separation no apparent low-frequency peak can be observed.

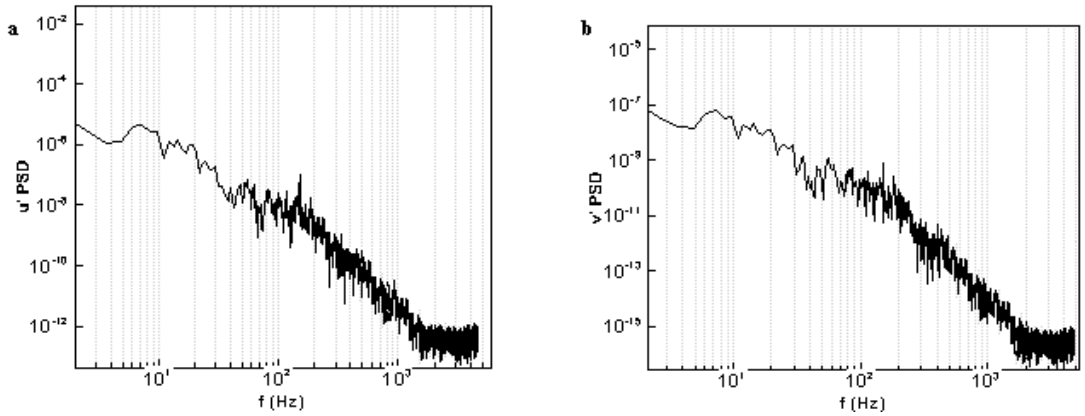

Fig.4.24. u', v' spectra at *x/D* = 0.61, *y/D* = 0.516, NFST case

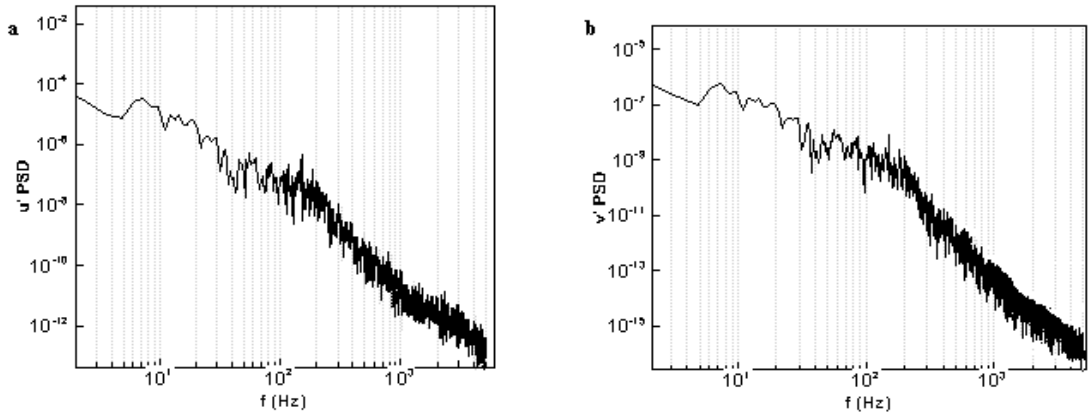

Fig.4.25. u', v' spectra at *x/D* = 0.61, *y/D* = 0.528, NFST case

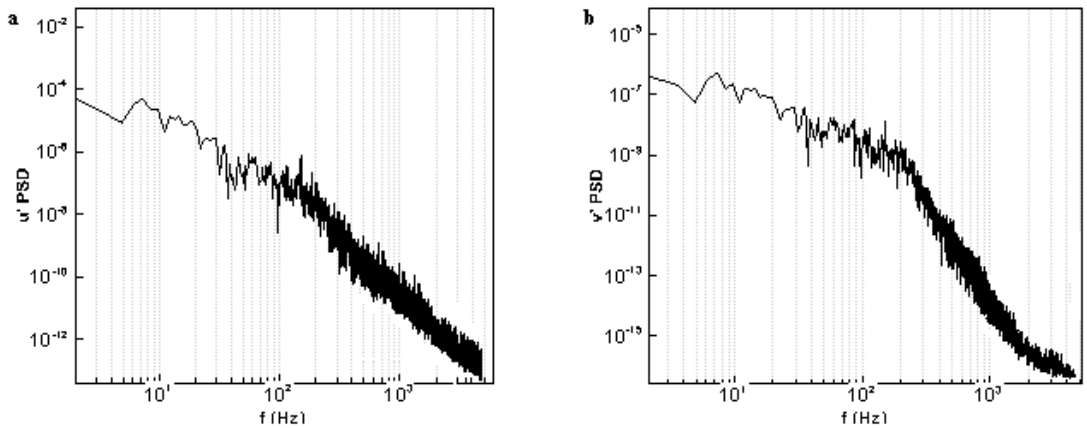

Fig.4.26. u', v' spectra at *x/D* = 0.61, *y/D* = 0.542, NFST case

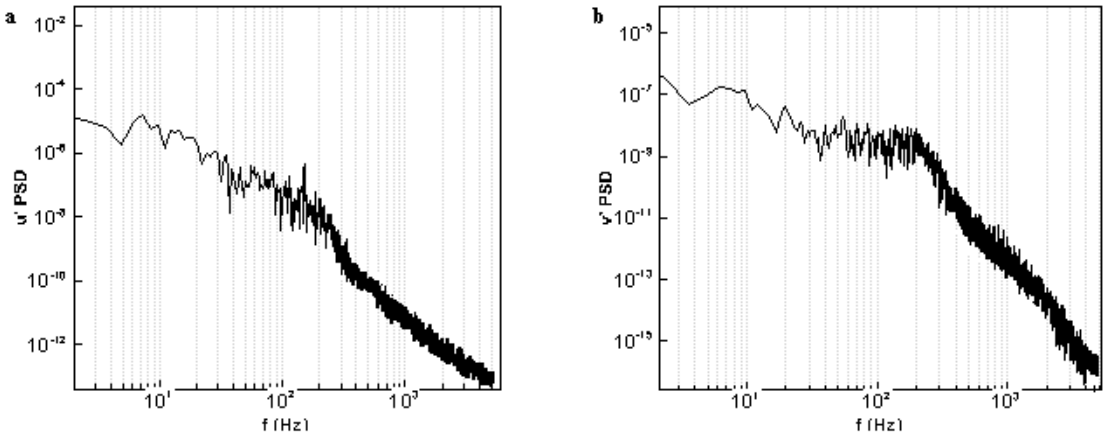

Fig.4.27. u', v' spectra at *x/D* = 0.61, *y/D* = 0.558, NFST case

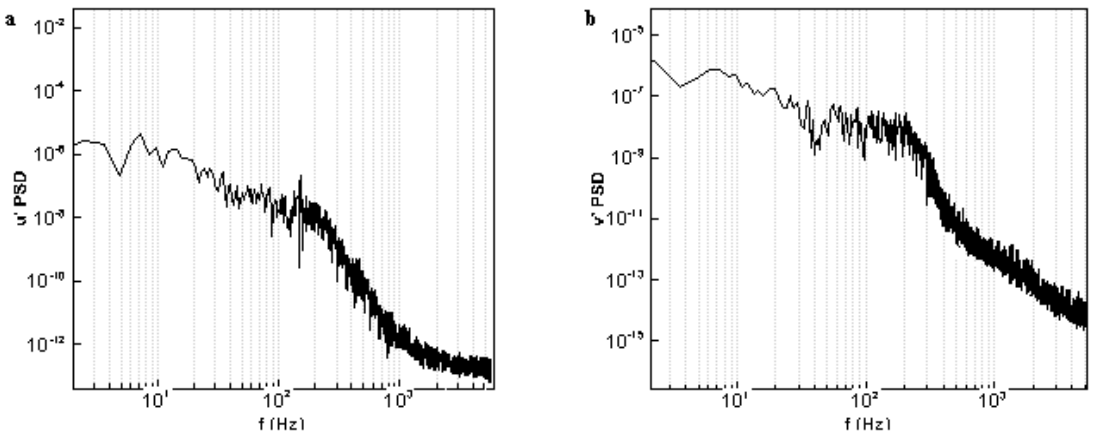

Fig.4.28. u', v' spectra at *x/D* = 0.61, *y/D* = 0.59, NFST case

Moving downstream to the station 3 (*x/D* = 0.86) and then moving upward across the same wall-normal locations as discussed above, exactly the same regular shedding frequency with more pronounced peak is repeated. Figures 4.29 to 4.31 show the spectra of the streamwise and wall-normal velocity components at 1st, 3th, and 5th locations, from very close to the surface to the edge of shear layer. All the plots clearly show the regular shedding frequency identified previously. Figure 4.35 also shows trace of a very mild low-frequency activity *f* = 15-20 Hz (0.104 U_0/l) besides the regular shedding frequency, in close agreement with the study of Yang of Voke (2001) for the same case.

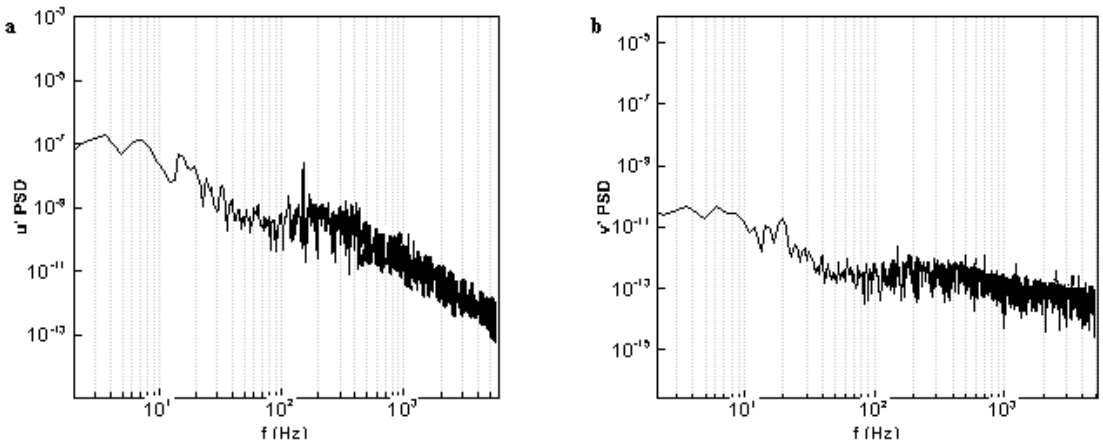

Fig.4.29. u', v' spectra at *x/D* = 0.86, *y/D* = 0.504, NFST case

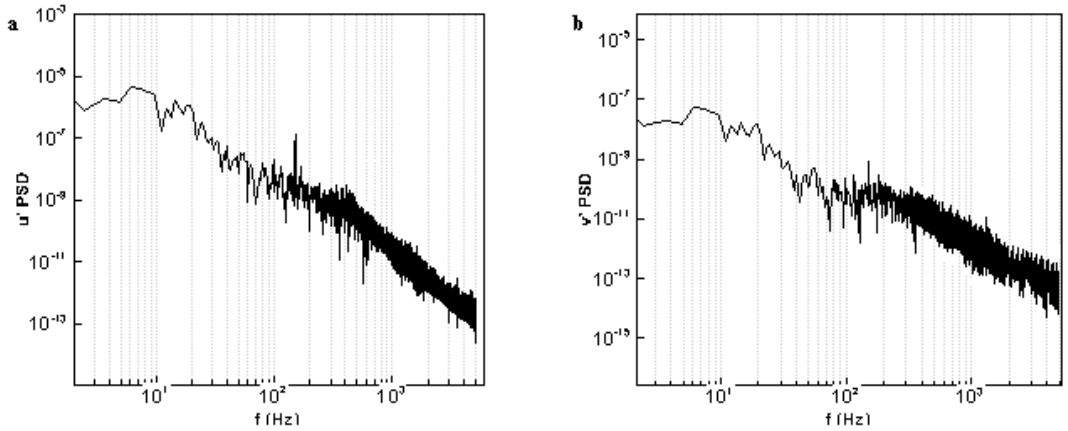

Fig.4.30. u', v' spectra at *x/D* = 0.86, *y/D* = 0.528, NFST case

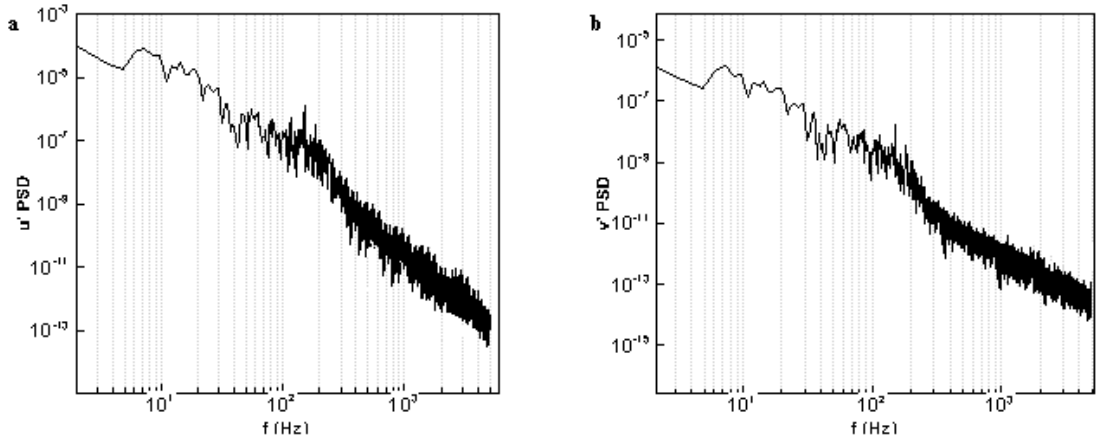

Fig.4.31. u', v' spectra at *x/D* = 0.86, *y/D* = 0.558, NFST case

Moving further downstream to the station 4 (x/D = 1.15) and then moving upward in the wall-normal locations as above, Figures A.1 to A.7 (Appendix) show the spectra of the streamwise and wall-normal velocity components at all the seven wall-normal locations, from very close to the surface to the free-stream. Again, for all locations within the shear layer, the spectra clearly show the regular shedding frequency 146 Hz except for the point located in the free-stream (figure A.7). Again a mild low frequency band appears at wall normal location y/D = 0.558, figure A.5.

Moving further downstream to the station 5 (x/D = 1.46) and then moving upward in the wall-normal locations as above, the same frequency peak recurs. Figures A.8 to A.11 show the spectra of the streamwise and wall-normal velocity components at 1st, 3rd, 5th, and 7th wall-normal locations. For all locations within the shear layer, the spectra clearly show the regular shedding frequency as identified previously. No trace of low-frequency activity is apparent at this station. Moving further downstream to the station 6 (x/D = 1.72) and then moving upward in the wall-normal locations as above, the same frequency peak for the regular shedding dominates. Figures A.12 to A.14 show the spectra of the streamwise and wall-normal velocity components at 1st, 5th, and 7th wall-normal locations. For all locations within the shear layer, the spectra clearly show the regular shedding frequency 146 Hz as identified in upstream locations. No apparent low frequency band can be seen at this station.

Moving further downstream to the station 7 (x/D = 1.94) and then moving upward in the wall-normal locations as above, the same frequency peak dominates. Figures A.15 to A.17 show the spectra of the streamwise and wall-normal velocity components at 1st, 5th, and 7th wall-normal locations. Again, for all locations within the shear layer, the spectra clearly show the regular shedding frequency 146 Hz as identified previously. No apparent low frequency band can be seen at this station. Moving further downstream to the station 8 (x/D = 2.19) and then moving upward from the near wall to the edge of the shear layer in the wall-normal locations as above, the same frequency peak appears. Figures A.18 to A.20 show the spectra of the streamwise and wall-normal velocity components at 1st, 5th, and 7th wall-normal locations. For all locations within the shear layer, the spectra clearly show the regular shedding frequency 146 Hz as identified previously. Very mild low frequency activity of about f = 20 Hz can also be identified at y/D = 0.558 (Figure, A.19 a). Moving further downstream to the station 9

(*x/D* = 2.51) and then moving upward in the wall-normal locations as above, the same frequency peak can be identified. Figures A.21 to A.23 show the spectra of the streamwise and wall-normal velocity components at 1st, 5th, and 7th wall-normal locations. For all locations within the shear layer, the spectra clearly show the regular shedding frequency *f* = 146 Hz. Again, a mild low frequency activity at about *f* = 20 Hz can be identified at *y/D* = 0.558.

Moving further downstream to the station 10 (*x/D* = 2.87) and then moving upward in the wall-normal locations as above, the same regular shedding frequency peak prevails. Figures A.24 to A.26 show the spectra of the streamwise and wall-normal velocity components at 1st, 5th, and 7th wall-normal locations. For all locations within the shear layer, the spectra clearly show the regular shedding frequency *f* = 146 Hz as identified previously. Also a mild low frequency of average *f* = 20 Hz can be identified at *y/D* = 0.558, Figure A.25a. Moving further downstream to the station 11 (*x/D* = 3.28) and then moving upward in the wall-normal locations as above, the same regular frequency peak is dominant. Figures A.27 to A.29 show the spectra of the streamwise and wall-normal velocity components at 1st, 5th, and 7th wall-normal locations. For all locations within the shear layer, the spectra clearly show the regular shedding frequency *f* = 146 Hz as identified previously. No low-frequency activity can be seen.

Finally at the last streamwise location i.e. station 12 (*x/D* = 3.62) and then moving upward in the wall-normal locations as above, Figures 4.32 – 4.38 show the spectra of the streamwise and wall-normal velocity components at 7 wall-normal locations. As can be seen there is no frequency peak and the spectra looks similar to a fully developed canonical boundary layer.

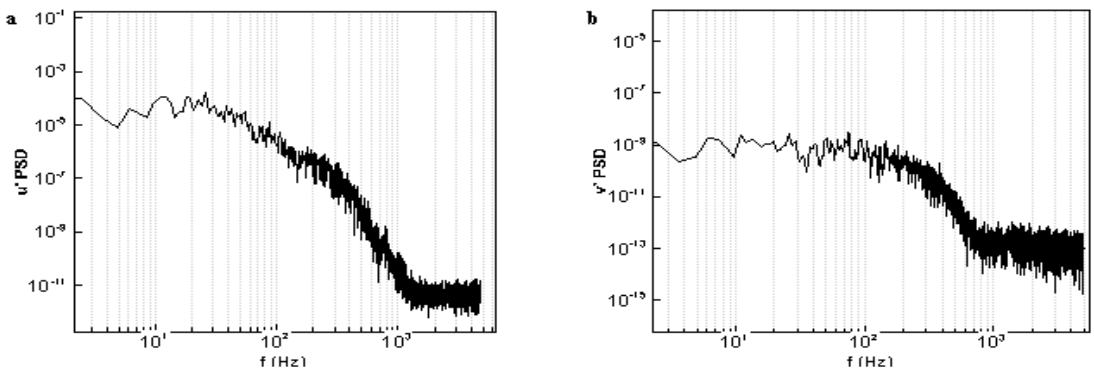

Fig.4.32. u', v' spectra at *x/D* = 3.62, *y/D* = 0. 504, NFST case

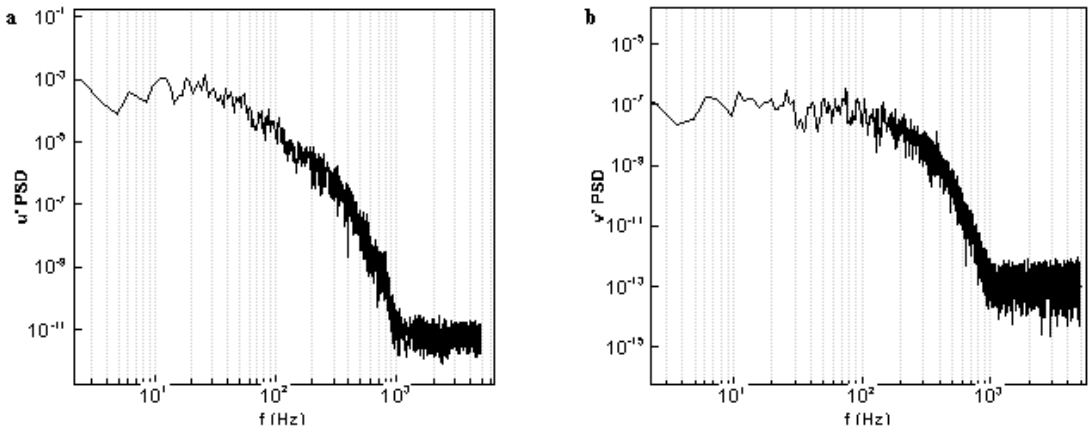

Fig.4.33. u', v' spectra at *x/D* = 3.62, *y/D* = 0. 516, NFST case

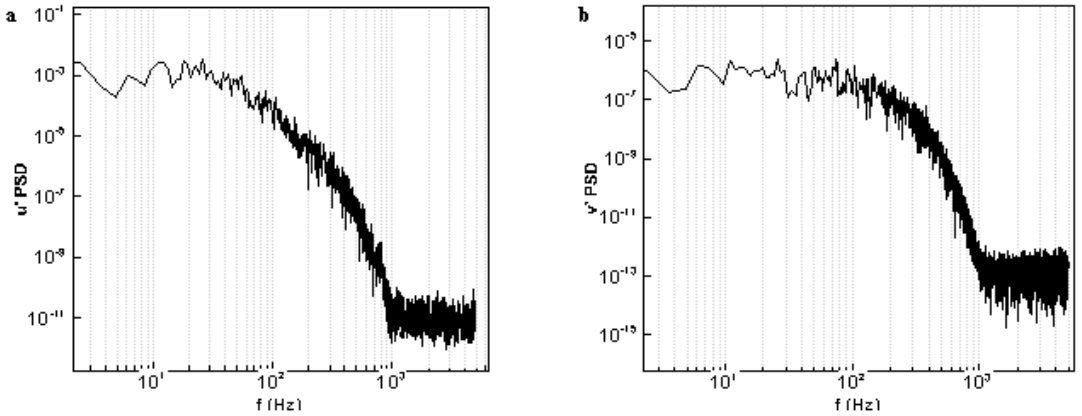

Fig.4.34. u', v' spectra at *x/D* = 3.62, *y/D* = 0. 528, NFST case

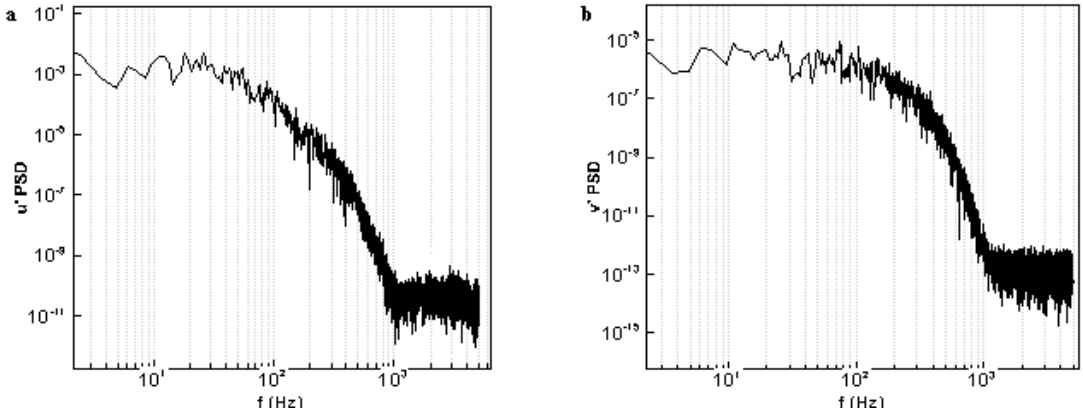

Fig.4.35. u', v' spectra at *x/D* = 3.62, *y/D* = 0. 542, NFST case

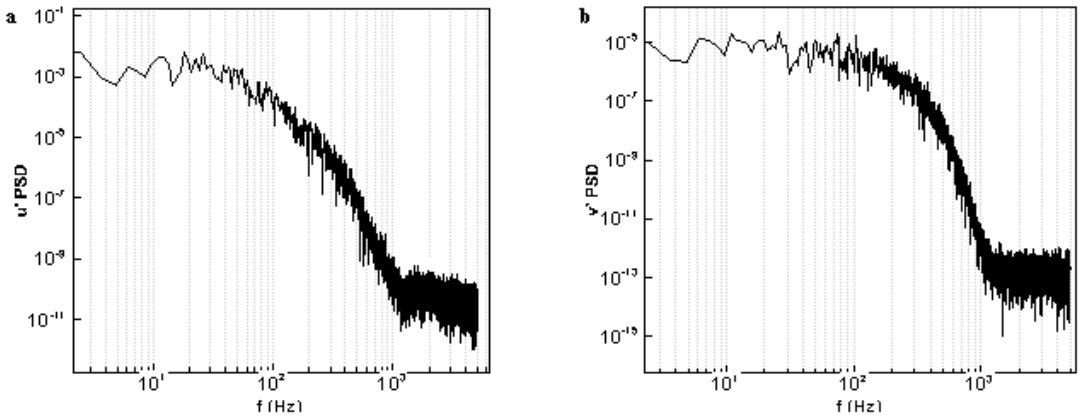

Fig.4.36. u', v' spectra at *x/D* = 3.62, *y/D* = 0. 558, NFST case

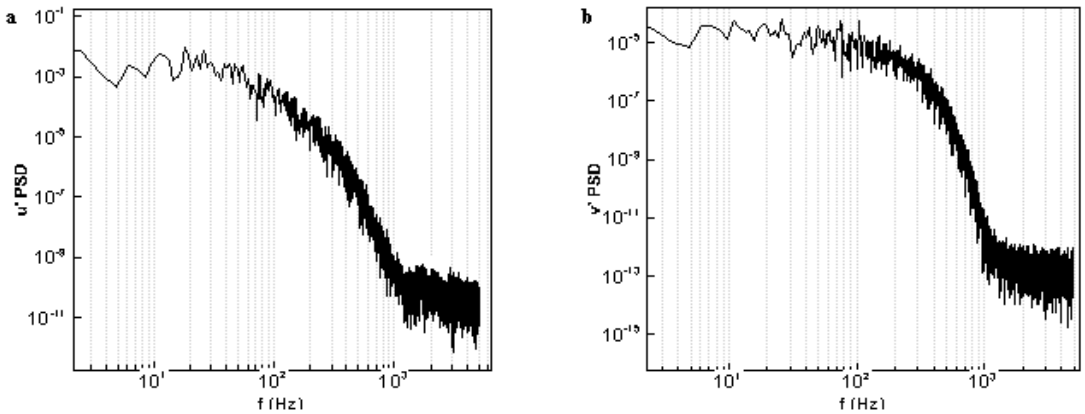

Fig.4.37. u', v' spectra at *x/D* = 3.62, *y/D* = 0. 59, NFST case

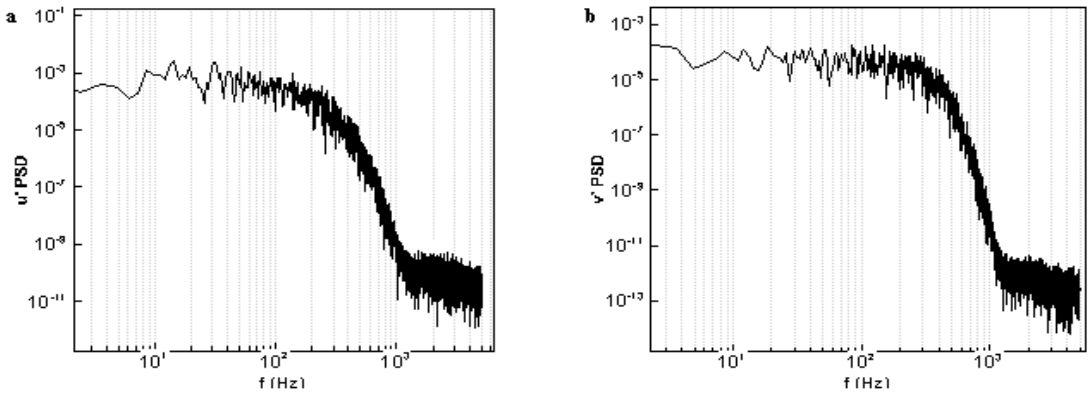

Fig.4.38. u', v' spectra at *x/D* = 3.62, *y/D* = 0. 85, NFST case

The spectra of the velocity components were also investigated at spanwise planes z/D = 2.0, 2.5, 3.0. Data for these variables were stored in exact locations as for the midspan plane discussed above. Only spectra at z/D = 2.0 are shown here as the results at other plans are quite the same. Figures A.30 – A.32 show the spectra of the streamwise and wall-normal velocity components at z/D = 2.0 for station 3 at 2^{st}, 4^{th}, and 6^{th} wall-normal locations respectively. Both regular shedding frequency f = 146 Hz and low frequency band can be identified. Moving downstream at the same spanwise plane z/D = 2.0, Figures A.33 to A.38 show the spectra of the streamwise and wall-normal velocity components for stations 7 and 11 (x/D = 1.94 and 3.28) at 2^{st}, 4^{th}, and 6^{th} wall-normal locations. The regular shedding frequency f = 146 Hz observed in the midspan plane is also observable at z/D = 2.0. The same low frequency band of average f = 20 Hz observed in the midspan plane can also be identified in this spanwise plane at station 7 (figures A.33, 34, and 35).

4.3.2 FST case

It is of great interest to explore the effect of free-stream turbulence on the characteristic shedding frequency and hence the primary instability mechanism. Effect of higher FST (5.6% at leading edge) on spectral characteristics of transitional separated-reattached flow over a flat plate with semi-circular leading edge was also examined through extensive spectral analysis. Data were stored within 9 streamwise stations (covering the whole bubble and further the reattachment region), and 7 wall-normal locations at each streamwise station (to cover the bubble height from the very near wall region to the free stream region above the free shear layer), to investigate the regular shedding and existence of low-frequency flapping at 5.6% FST. Figure 4.39 shows the mean streamlines and the locations considered for spectral analysis. The coordinate origin is at stagnation point and separation occurs at blend point x/D = 0.5. The streamwise stations are: x/D = 0.33, 0.52, 0.65, 0.83, 1.03, 1.23, 1.45, 1.68, 1.93. At each streamwise location, time traces of velocities and pressure were collected at wall-normal locations y/D = 0.504, 0.516, 0.528, 0.542, 0.558, 0.59, 0.85. The above mentioned locations are considered at four spanwise locations z/D = 2.0, 2.5, 3.0, 4.0. The figures below correspond to midspan plane z/D = 4.0.

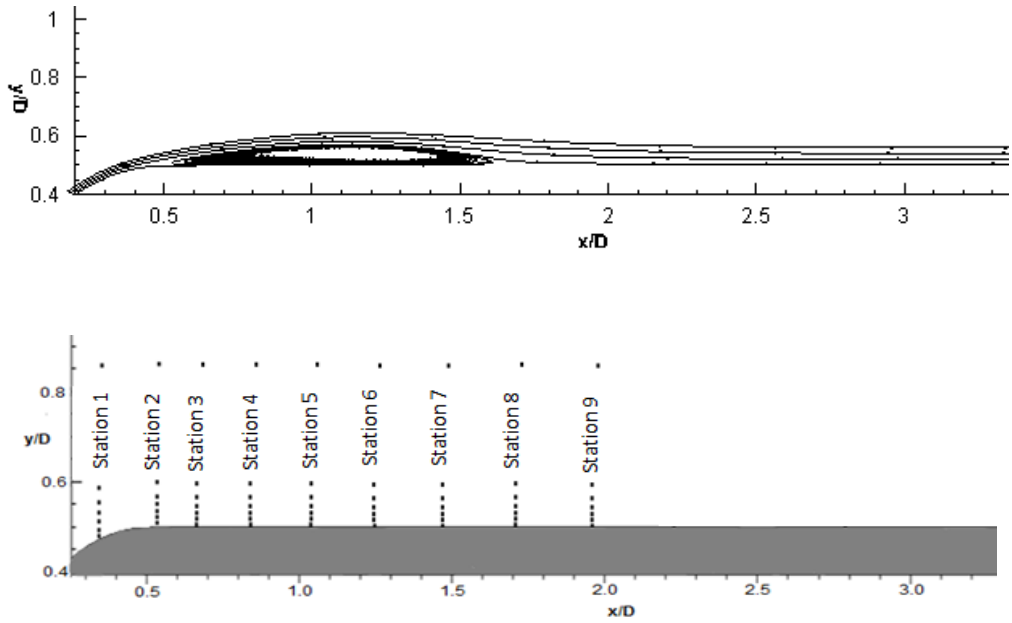

Fig.4.39. mean streamlines and point locations for spectral analysis (FST case)

At station 1 (*x/D* = 0.33) close to the separation line and very close to the wall (*y/D* = 0.504) the spectra for the velocity components are shown in figures 4.40 *a*, *b*, *c*, compared to the free stream spectra (grey lines). At this station very close to the separation line the spectra is quiet and does not show any spectacular high- or low-frequency contents.

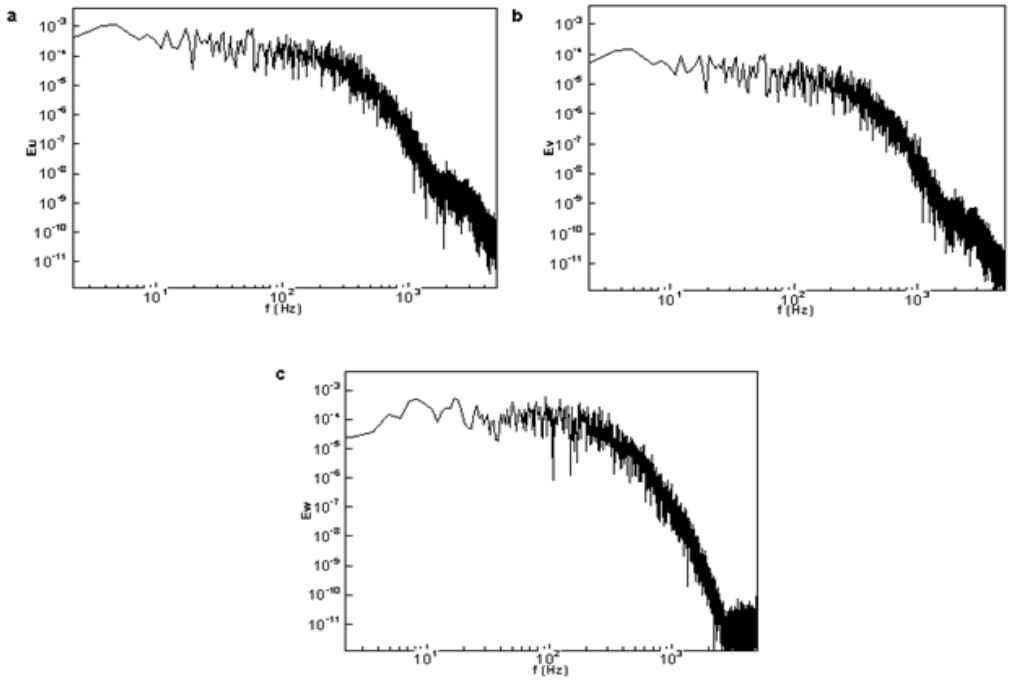

Fig.4.40. spectra at *x/D* = 0.33, *y/D* = 0. 504 (a) u', (b) v', (c) w' (FST case)

Moving upward at the same *x*-location (station 1) and 2nd to 7th wall-normal locations (*y/D* = 0.516, 0.528, 0.542, 0.558, 0.59, 0.85) figures B.1 to B.6 (Appendix B) show the spectra of the streamwise and wall-normal velocity components compared to the free stream spectra. These positions extend from the attached boundary layer to the free-stream before the separation line. The spectra are quiet and do not show any spectacular high- or low-frequency contents. Spectra are similar for the velocity component so only *u'* spectra will be presented for the rest of the locations. Moving downstream to the station 3 (*x/D* = 0.65) and then moving upward across the same wall-normal locations as above, figures B.7 – B.13 show the spectra of the streamwise velocity components from the first to 7th wall-normal locations (*y/D* = 0.504, 0.516, 0.528, 0.542, 0.558, 0.59, 0.85). These positions extend from the very close wall region to the bubble shear layer and further to the free-stream. No traces of regular shedding or low frequency activity can be identified at this station.

Moving downstream to the station 4 (*x/D* = 0.83) and then moving upward across the same wall-normal locations as discussed above, Figures 4.41 – 4.47 show the spectra of the streamwise velocity components from the first to 7th wall-normal locations (*y/D* = 0.504, 0.516, 0.528, 0.542, 0.558, 0.59, 0.85). A very mild frequency peak region can be identified at *y/D* = 0.516 to *y/D* = 0.542 with average frequency about *f* = 600 Hz (1.39U_0/l). No low frequency activity is apparent.

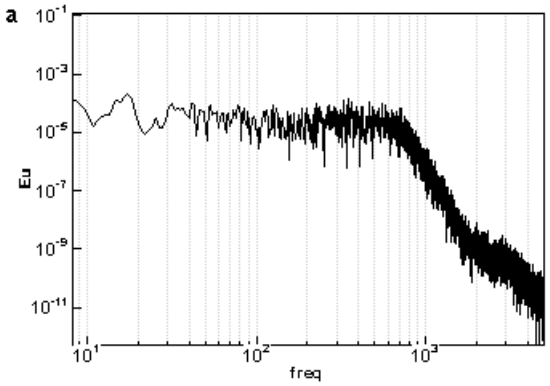

Fig.4.41. spectra at *x/D* = 0.83, *y/D* = 0.504. (FST case)

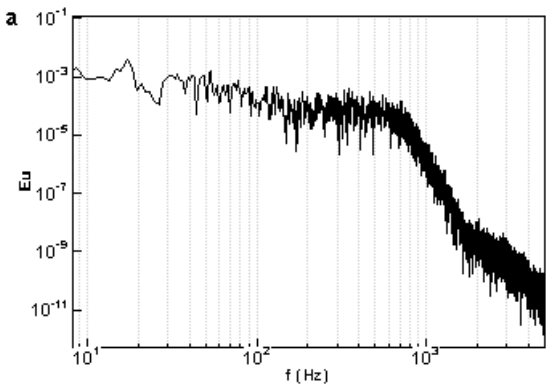

Fig.4.42. spectra at *x/D* = 0.83, *y/D* = 0.516. (FST case)

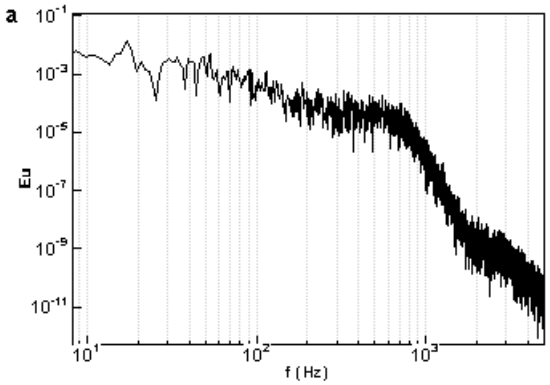

Fig.4.43. spectra at *x/D* = 0.83, *y/D* = 0.528. (FST case)

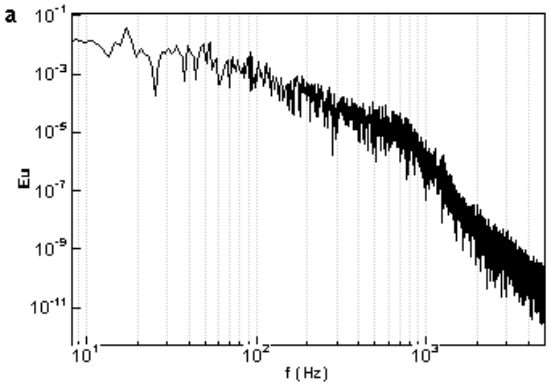

Fig.4.44. spectra at *x/D* = 0.83, *y/D* = 0.542. (FST case)

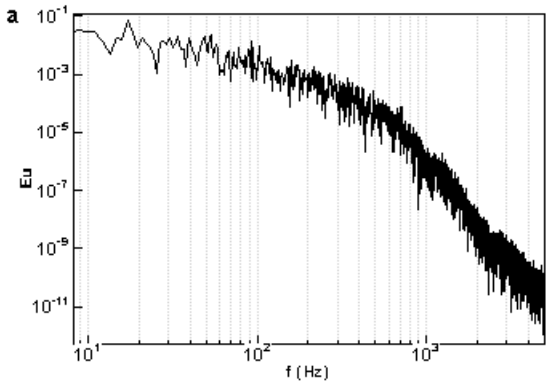

Fig.4.45. spectra at *x/D* = 0.83, *y/D* = 0.558. (FST case)

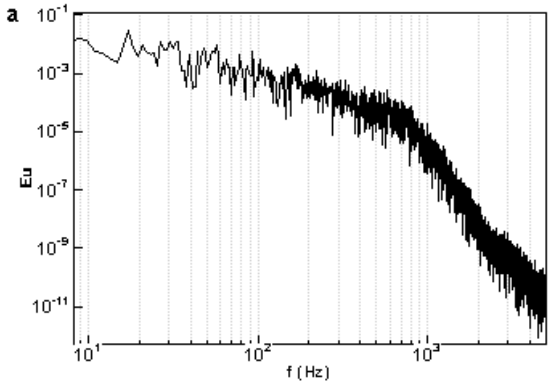

Fig.4.46. spectra at *x/D* = 0.83, *y/D* = 0.59. (FST case)

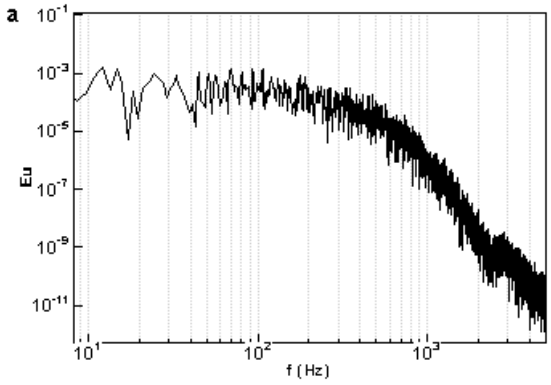

Fig.4.47. spectra at *x/D* = 0.83, *y/D* = 0.85. (FST case)

Moving downstream to the station 5 (x/D = 1.03) and then moving upward across the same wall-normal locations as discussed above, Figures B.14 – B.20 show the spectra of the streamwise velocity components from the first to 7th wall-normal locations (y/D = 0.504, 0.516, 0.528, 0.542, 0.558, 0.59, 0.85). Again, a mild frequency peak region can be identified at y/D = 0.516 to y/D = 0.542 with average frequency about f = 670 Hz ($1.55U_0/l$). No low frequency activity can be observed. Moving downstream to the station 6 (x/D = 1.23) and then moving upward across the same wall-normal locations as discussed above, Figures B.21 – B.27 show the spectra of the streamwise velocity components from the first to 7th wall-normal locations (y/D = 0.504, 0.516, 0.528, 0.542, 0.558, 0.59, 0.85). The mild frequency peak region with average about f = 600 Hz ($1.39U_0/l$) up to y/D = 0.542 can be seen. No low frequency activity is apparent. Moving downstream to the station 7 (x/D = 1.45) and then moving upward across the same wall-normal locations as discussed above, Figures B.28 – B.34 show the spectra of the streamwise velocity components from the first to 7th wall-normal locations (y/D = 0.504, 0.516, 0.528, 0.542, 0.558, 0.59, 0.85). Again the mild frequency peak region can be seen up to y/D = 0.542 exists. No trace of low frequency activity can be identified.

Moving downstream to the station 8 (x/D = 1.68) and then moving upward across the same wall-normal locations as discussed above, Figures B.35 – B.41 show the spectra of the streamwise and wall-normal velocity components from the first to 7th wall-normal locations (y/D = 0.504, 0.516, 0.528, 0.542, 0.558, 0.59, 0.85). This station is in the reattachment region, and all the spectra at this station do not show any apparent frequency peak. Moving further downstream to the last station which is downstream of reattachment (station 9, x/D = 1.93) and then moving upward across the same wall-normal locations as discussed above, Figures B.42 – B.48 show the spectra of the streamwise and wall-normal velocity components from the first to 7th wall-normal locations (y/D = 0.504, 0.516, 0.528, 0.542, 0.558, 0.59, 0.85). It can be seen that in this station far in the reattached boundary layer, the spectra do not show any obvious frequency peak.

The spectra of the velocity components were also investigated at z/D = 2.0, 2.5, 3.0. Data for these variables were stored in exact locations as for the spanwise location z/D = 4.0 (midspan plane) as discussed above. Figures B.49 – B.51 show the spectra of the

streamwise and wall-normal velocity components at z/D = 2.0, station 3 (x/D = 0.65) for 2st, 4th, and 6th wall-normal locations. No regular shedding frequency or low-frequency activity exist in this region. Since the spectra at other spanwise locations are quite similar so only spectra at plane z/D = 2.0 are presented to compare with those at the mid-span plane discussed above. Figures B.52 – B.54 show the spectra of the streamwise and wall-normal velocity components at z/D = 2.0, station 5 (x/D = 1.03), and 2st, 4th, and 6th wall-normal locations. It can be seen that similar to the spectra at mid-span plane, a frequency peak region can also be identified with average frequency about f = 600 Hz ($1.39U_0/l$). No low frequency activity is apparent in the shear layer.

Figures B.55 – B.57 show the spectra of the streamwise and wall-normal velocity components at z/D = 2.0, station 7 (x/D = 1.45), and 2st, 4th, and 6th wall-normal locations. Spectra are calm in both the regular shedding and low-frequency range and do not show any frequency peak. Moving downstream to station 9 (x/D = 1.93), figures B.58 – B.60 show the spectra of the streamwise and wall-normal velocity components at z/D = 2.0, and 2st, 4th, and 6th wall-normal locations. Again similar to the mid-span plane, spectra are calm in both the regular shedding and low-frequency range and do not show any frequency peak.

It can be concluded from the spectra analysis shown above that under high free stream turbulence level of 5.6% in the current study, much more chaotic motions in the free shear layer exist and the characteristic frequency peak clearly observed in the NFST case can be barely observed. Instead, a mild high-frequency shedding with average $f = 1.45U_0/l$ is present. These results along with previous studies at free stream turbulence levels up to 2% strongly indicate that the higher the level of free stream turbulence, the weaker is the frequency peak in the spectra and hence the shedding phenomena. As shown in the previous section, the weak shedding frequency values observed under the current 5.6% turbulence level suggest that the Kelvin-Helmholtz instability mechanism of the NFST case is no longer working at such high free stream turbulence.

4.3.3 Discussion

The current LES study of a low Reynolds number transitional separated boundary layer at two different free-stream turbulence conditions shows a distinct regular vortex shedding and traces of very mild low-frequency flapping phenomena at very low free-stream turbulence condition (NFST case). These low frequency excitation may be attributed to the flapping motion of the bubble often mentioned in the literature as reviewed in the previous sections. Under the higher free-stream turbulence (FST case) a high-frequency band is detected (higher than the characteristic frequency range of the regular shedding) and the low frequency oscillations no longer exist.

The low-frequency flapping has been identified in a few experiments and numerical studies and believed to be due to the flapping of the shear layer. It has been associated with large-scale unsteadiness related to the shrinkage and enlargement of the separation bubble (Yang & Voke, 2001; Kiya & Sasaki, 1983) or low frequency up – down oscillations of the shear layer (Hain et al., 2009). Some numerical and experimental works have also suggested that the low-frequency flapping only occurs for turbulent separation and not for transitional flow cases (Abdalla & Yang, 2005; Cherry *et al*., 1984) but the current study on a laminar separation flow under low free-stream turbulence level, still suggests the existence of low-frequency activity in the bubble. Nevertheless the physical explanation for the low frequency shedding is not yet fully understood.

Chapter 5

Flow Visualisation

To shed more light on the nature of the flow and the instabilities involved in the separated-reattached flow, coherent structures and their temporal/spatial evolution are investigated in this chapter.

Many experimental studies have revealed that large-scale vortical coherent structures dominate the entrainment and mixing phenomena in free shear flows (Hussain, 1986). These large scale structures are such easily identifiable features within the flow commonly referred to as coherent structures. Understanding the physics of coherent structures is important for having a better insight into turbulence phenomena (such as entrainment and mixing, heat and mass transfer, drag and aerodynamic noise generation, etc.) and also for appropriate modelling of turbulence. Their topology and dynamics along with their evolution, interaction, and breakdown, would be beneficial in the study of shear flow development. It is known that the large scale motions in the flow provide the straining required for small-scale vorticity production. These small scale motions are characterised by large gradients (shear) and viscous diffusion of vorticity which cause the vorticity to spread into the non-shear region. Therefore, large scale structures would dominate the entrainment rate and thus shear flow transition (Tennekes & Lumley, 1972).

It is well known that the turbulent shear flows are dominated by spatially coherent, temporally evolving vortical motions generally known as coherent structures (Cantwell, 1981; Hussain, 1986). The primary structures in these flows seem to be dependent on the mean flow configuration e.g. geometry and the location of the solid-surface constraints. For example, large-scale spanwise vortices appear to dominate the dynamics in plane mixing layer (Brown & Roshko, 1974; Browand & Trout, 1974). For the plane boundary layer on the other hand, dominant structures may be a vortex with a

hairpin or horseshoe shape (Perry & Chang, 1982) and low-speed streaks (Schlatter et al. 2008; Watmuff et al. 2010; Brandt & Henningson, 2004). Analysing the coherent structures involved in the separated-reattached transitional flow may provide further insight into the transition process.

Development and interactions of the coherent structures with background turbulence is governed by vortex dynamics which is a useful tool for understanding the turbulence phenomena such as; entrainment and mixing, mass and heat transfer, drag and aerodynamic noise, chemical reaction and combustion, and also for realistic modelling of turbulence (Hussain & Melander, 1991). Therefore a wide range of approaches have been developed to try to have a better understanding of the coherent structures and their dynamical roles in the turbulence. Different methods can be identified in the literature for investigating the coherent structures: wavelet analysis (Hui Li, 1998), conditional sampling (Jeong et al., 1997), pattern recognition (Scarano et al. 1999; Giralt & Ferre, 1993), proper orthogonal decomposition (Gordeyev & Thomas, 2000), and flow visualisation which is the traditional method for capturing the large coherent fluid motions.

Despite considerable usage in the literature it seems that an approved universal definition for coherent structures does not yet exist. There is, however, no doubt about their important role in the dynamics of turbulent flows. Cantwell (1981) described coherent structures as spatially coherent and temporally evolving vortical structures. Glickman (1999) defined coherent structures as three-dimensional regions in a turbulent flow with characteristic structures and lifetimes in terms of velocity, temperature, etc., that are significantly larger or longer-lived than the smallest local scales. Sherif (1989) reported various definitions given to the coherent structures as:

1. Large-scale organised motions,
2. A pattern recurring in the flow which there is not necessarily an order to it showing random scale and velocities but fixed orientation,
3. Predominant modes of instability,
4. Flow entities that cause transport of momentum across a finite distance in a non-diffusive way.

Ferziger (2005) stated that lack of regularity -either in time or in space- in the appearance of coherent structures in a particular flow, makes them difficult to define and describe. Hussain (1986) defined coherent structures as connected, large-scale turbulent fluid mass with a phase-correlated vorticity over its spatial extent. He introduced a triple decomposition where any instantaneous variable consisted of three components: mean component, the coherent component, and the incoherent turbulence. However, implicit in this decomposition is that the coherent structure is a perturbation of the time-mean flow while arguably coherent structure is the flow and not a mere perturbation. He then introduced a double decomposition so that the turbulent shear flow consisted of coherent and incoherent motions only, and governing equations with triple and double decomposition were derived. Robinson (1991) defined coherent structure as a three dimensional region of the flow over which at least one fundamental flow variable (velocity component, density, etc) exhibited significant correlation with itself or with another variable over a range of space and/or time that was significantly larger than the smallest local scales of the flow. Berkooz et al. (1993) defined coherent structure as organised spatial features of flow which repeatedly emerged (often in flows dominated by local shear) with a characteristic temporal life cycle. Lesieur (1997) described the coherent vortices as regions of the flow which satisfied following conditions:

1. The vorticity concentration ω is high enough so that a local roll up of the surrounding fluid is possible,
2. The vortices should keep their shape during a time far enough in front of the local turnover time ω^{-1},
3. They should be unpredictable.

Therefore high vorticity modulus ω can be a considered for coherent-vortex identification especially in the free shear flows e.g. Comte et al (1998) which extensively analysed streamwise vorticity dynamics of a mixing layer on the bases of ω – isosurfaces. However in the presence of a wall, the mean shear created by the no-slip condition is usually considerably higher than the typical vortical intensity of the near-wall vortices and therefore more refined criterion is required to distinguish vortices from internal shear layers in these types of flows.

Dubief & Delcayre (2000) based on the definitions of Lesieur (1997) proposed a local minimum pressure criteria for vortex identification as a fluid parcel twisting around a vortex needed to be (in a frame moving with parcel) in approximate balance between centrifugal force and pressure-gradient effects and the pressure should decrease inside a vortex tube in order to counter balance the centrifugal force. Comte et al. (1998) and Robinson's (1991) used iso-surfaces of pressure to explore coherent structures in a turbulent boundary layer and suggested that as a vortex visualisation criterion the pressure criteria may be superior compared with the vorticity modulus. Nevertheless, the threshold to be used for proper iso-pressure surfaces strongly depends on the pressure surrounding the vortical structure and Abdalla (2004) speculated that in regions of high concentration of vortices, this criterion may fail to capture the details of the vortical structure.

Hunt et al (1998) proposed a criterion incorporating some properties of both the vorticity and the pressure criterion known as the Q-criterion which is the second invariant of velocity gradient tensor Δu:

$$Q = \frac{1}{2}\left(\Omega_{ij}\Omega_{ij} - \mathrm{S}_{ij}\mathrm{S}_{ij}\right)$$

Where $\Omega_{ij} = (u_{i,j} - u_{j,i})/2$ and $S_{ij} = (u_{i,j} + u_{j,i})/2$ are the antisymmetric and the symmetric components of Δu respectively. In other words, Q is the balance between the rotation rate $\Omega^2 = \Omega_{ij}\Omega_{ij}$ and the strain rate $S^2 = S_{ij}S_{ij}$. Hence it can be implied that the positive Q iso-surfaces are indicative of the flow regions where the strength of the rotation take over the strain rate and so making the structures eligible to be identified as vortex envelops.

Kelvin-Helmholtz rolls, Streaks, Hairpin vortices, Ribs and Lambda-shaped vortices are some of the common structures which are referred to as coherent structures in the literature. Streaky structures are characterised with narrow regions of low velocity fluid stretched in the streamwise direction (Kim et al., 1971; Smith & Metzler, 1983). Streamwise vortices are referred to as vortical structures which are predominantly oriented in the streamwise direction, although they may be bent and make an angle with the streamwise direction (Robinson, 1991). Kim et al. (1971) reported the streamwise vortices to be the dominant mode of oscillatory motions during the bursting. Spanwise

vortices are referred to as those primarily oriented in the spanwise direction and generally are produced as fluid of different velocities are twisted around as a result of Kelvin-Helmholtz instability. Hairpin vortices are those with two legs (quasi-streamwise vortex pairs with opposite signs) and a tip (spanwise vorticity) (Head & Bandyopadhyay, 1981).

Large scale vortical coherent structures in separated-reattached flows have been subject of much research. In the separation bubble the identification of vortices is more difficult compared with the zero-pressure gradient flows such as turbulent boundary layer and turbulent mixing layer. This is due to the fact that the vortices are comparatively weak in the laminar region leading to the transition and may considerably vary in strength near the reattachment and in the developing boundary layer. Generally, vortical structures in separated shear layers grow, merge and shed periodically from the reattachment region. The separated shear layer on a flat plate can be considered as a mixing layer modified by a recirculation zone below and an unsteady reattachment region. Some aspects of similarity of the flow structures visualised in the present study were found to be correlated with those present in the case of plain mixing layers and the backward-facing step. Winnant & Browand (1974) in their mixing layer experiment observed the mixing layer to be dominated by occurrence of quasi- two-dimensional spanwise vertical structures. It was observed that that adjacent pairs of vortices rolled around each other at some distance downstream. They believed that the viscous diffusion spread out the identities of the individual vortices, forming a single large vortex from the two originally distinct vortices. They believed this vortex pairing process to be the mechanism leading to the transition in the mixing layers. Since then the vortex pairing phenomenon is known as a 2D interaction whereby neighbouring vortices join together to form a large vortex.

Kiya & Sasaki (1985) experimentally studied large scale structures within a bubble over a sharp leading edge. Existence of a counter-rotating vortex pair as hairpin vortices was identified. These hairpin-like vortices were reported to shed from the reattaching zone. Yang & Voke (2001) also reported hairpin vortices at around the mean reattachment point. In the study of Yang (2002) streaky structures, which are known to be associated with counter-rotating streamwise vortices, and hairpin vortices were observed around and after the reattachment. Detailed studies have been performed

by Abdalla and Yang (2004) to understand and visualise the large scale structures involved in the transition of separated boundary layers, where Kelvin-Helmhotlz rolls, Lambda-shaped and streamwise ribs were captured. Regarding the effect of geometry, very recently Abdalla et.al (2009) in a study of transitional separated-reattached flow over a surface mounted obstacle and a forward-facing step, demonstrated that the coherent structures such as the Lambda-shaped and rib-like vortices which are often associated with a flat plate boundary layer and also found in the separated-reattached flow over leading edge of a plate (Abdalla & Yang, 2004), are not common in the separated-reattached flow over obstacles and forward-facing steps.

Yang & Abdalla (2005) considered the effects of 2% FST on the large-scale structures present in separated boundary layer transition. They reported a 14% reduction of the mean bubble length and an earlier breakdown of the separated boundary layer. It was demonstrated that with increased FST the position of first unsteadiness moved closer to the separation line. Increased rates of randomness of the flow and degraded coherency of the early stage structures along both the span and streamwise directions were also reported as consequences of the added FST. At 2% FST, 2D Kelvin-Helmhotlz rolls were not as apparent as in the case with no FST, but still observable in the early part of the bubble. Lambda-shaped (hairpin) vortices could hardly be identified and streamwise structures were enlarged in the spanwise direction and shortened in the streamwise direction compared with the case of no FST. It was concluded that in the presence of 2% FST the primary instability of the free shear layer was still the same as in the no FST case (Kelvin-Helmhotlz instability mechanism) but secondary instability was different and needed to be further investigated.

In the present chapter three vortex visualisation methods including the low-pressure, high vorticity ω, and the positive Q iso-surfaces will be employed to visualise the flow structures. The flow filed of the separated-reattached flow under two free-stream turbulence levels is visualised to elucidate large-scale vortical structures evolving in the separated shear layer and their development downstream of reattachment. The objective is that by processing the extensive LES data, the large-scale structures associated with the separated boundary layer transition under the low and high free-stream turbulence could be revealed.

A .NFST case

Two dimensional velocity and pressure contours (at the same instantaneous times) on the midspan *x-y* plane are presented in Figures 5.1 and 5.2 indicating vortex formation and shedding of vortical structures from the separated boundary layer. It can be seen from the velocity and pressure fields that the vortices begin to form from *x/D* = 1.1 and become large and stronger as they move towards the reattachment region at about *x/D* = 3.0. The vortices then shed from the bubble while new structures taking form upstream in the shear layer. The vorticity roll up and shedding process can be more clearly seen by following sequential snapshots of the two dimensional spanwise vorticity as shown in figures 5.3 and 5.4. An incidence of two spanwise vortices merging together at about *x/D* = 2.8 could be detected as shown in figure 5.4.

Visualisation through the three-dimensional low-pressure isosurfaces can be seen in figures 5.5 and 5.6 and 5.7. revealing several important features of the flow. At the beginning of Kelvin-Helmholtz instability, Kelvin-Helmholtz billows are shed downstream of the separation and grow in size as they travel downstream downstream. This is clearly displayed in figures showing the spanwise vortex tubes or rolls dominating the flow topology.

The Kelvin-Helmholtz rolls grow up in size and are subjected to some waviness along the spanwise direction. It is clearly observed that the axis of the spanwise billows retain their perpendicular direction with the flow direction keeping their coherency and two-dimensional nature. The structures shown in these figures do support the idea that at least in some occasions, the process of pairing occurs in the current study for NFST case. By close inspection of figures 5.5 and 5.6 and 5.7 it can be seen that the above described two-dimensional spanwise coherent vortical structures become more distorted (specially the initially shed roll) while convecting downstream.

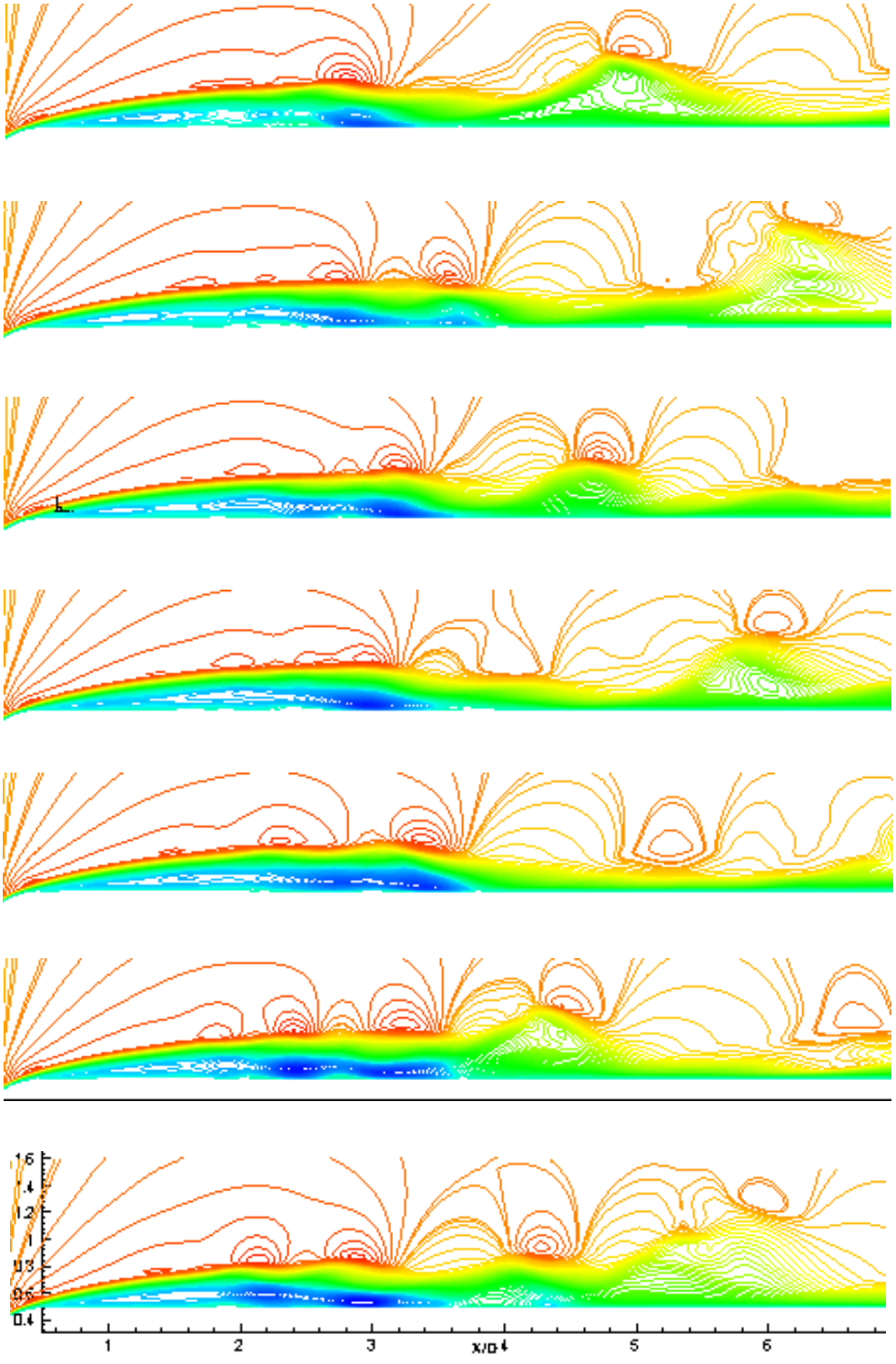

Fig. 5.1. Velocity Contours displaying vortex formation and shedding

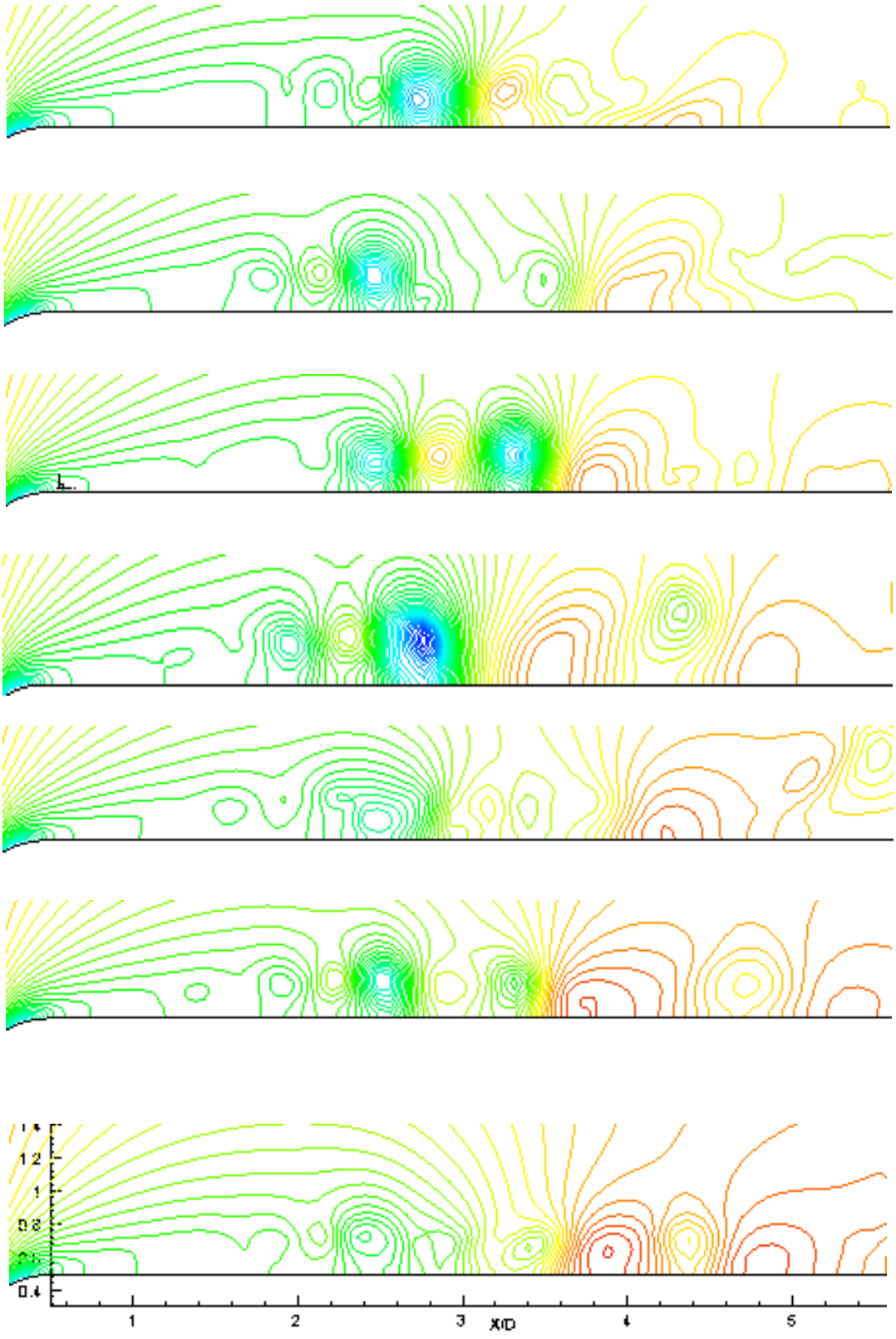

Fig. 5.2. 2D pressure contours displaying vortex formation and shedding

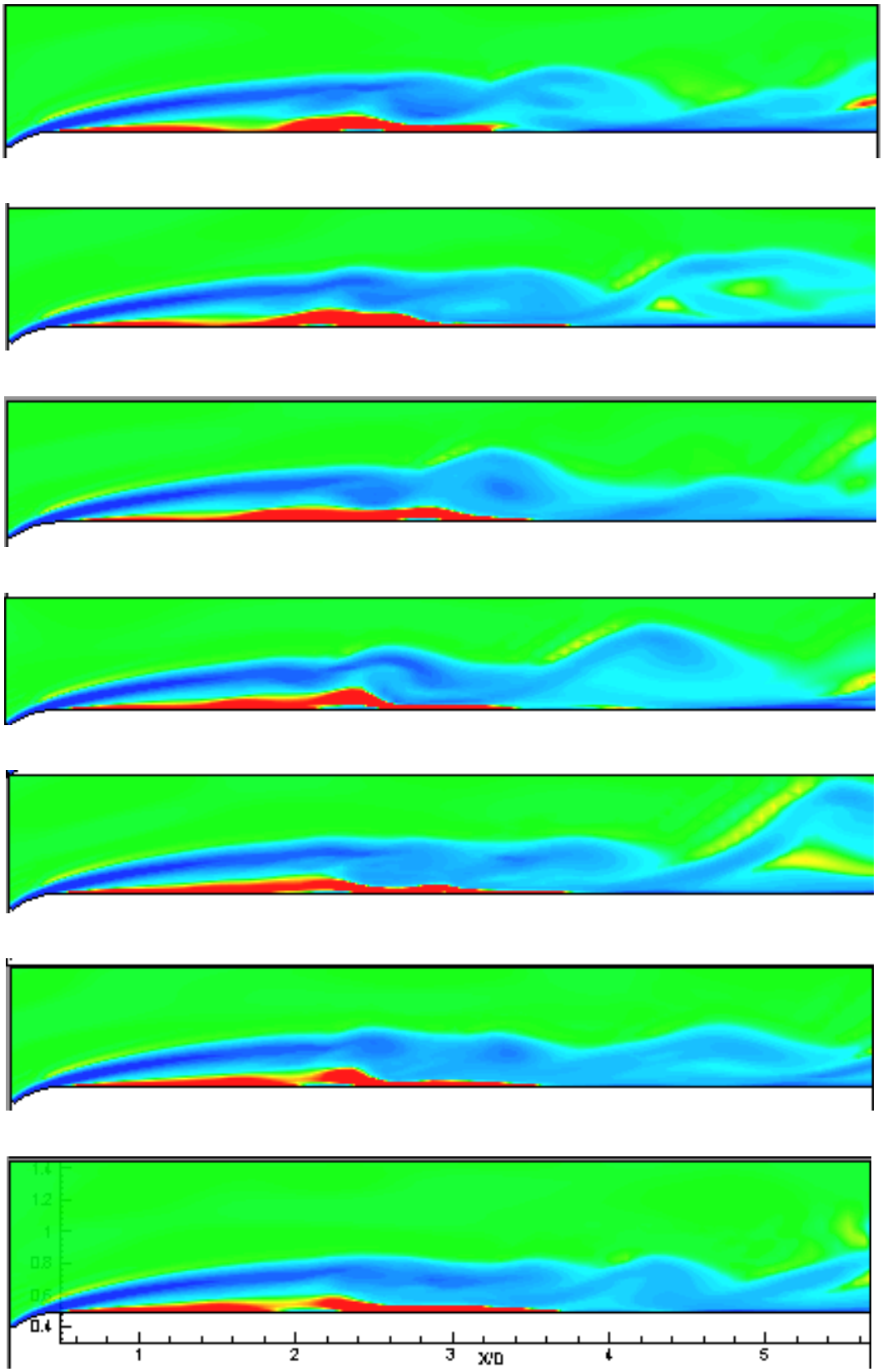

Fig. 5.3. Snapshots of spanwise vorticity showing vorticity roll up and shedding

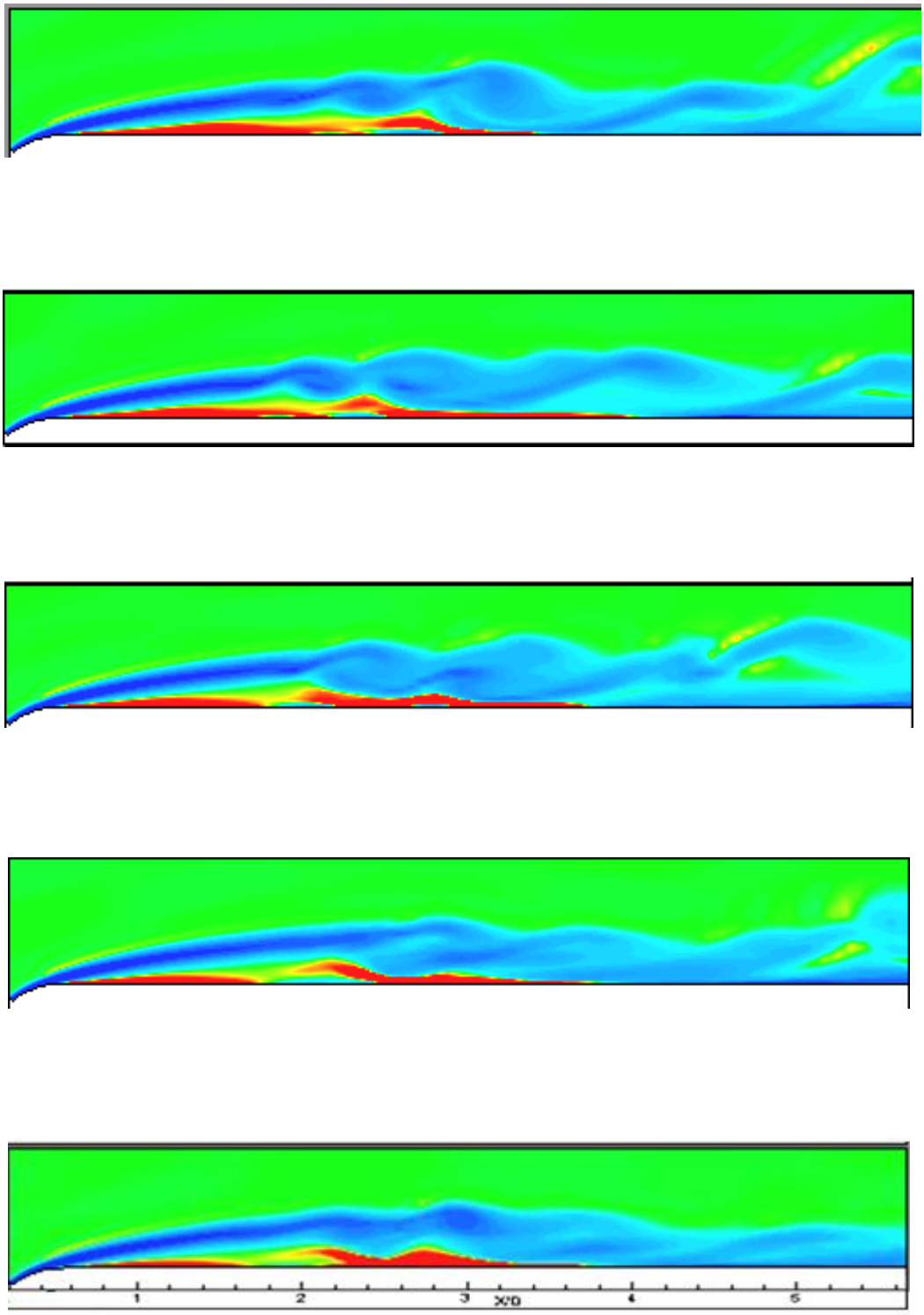

Fig. 5.4. Sequential snapshots of spanwise vorticity showing vorticity roll up and pairing

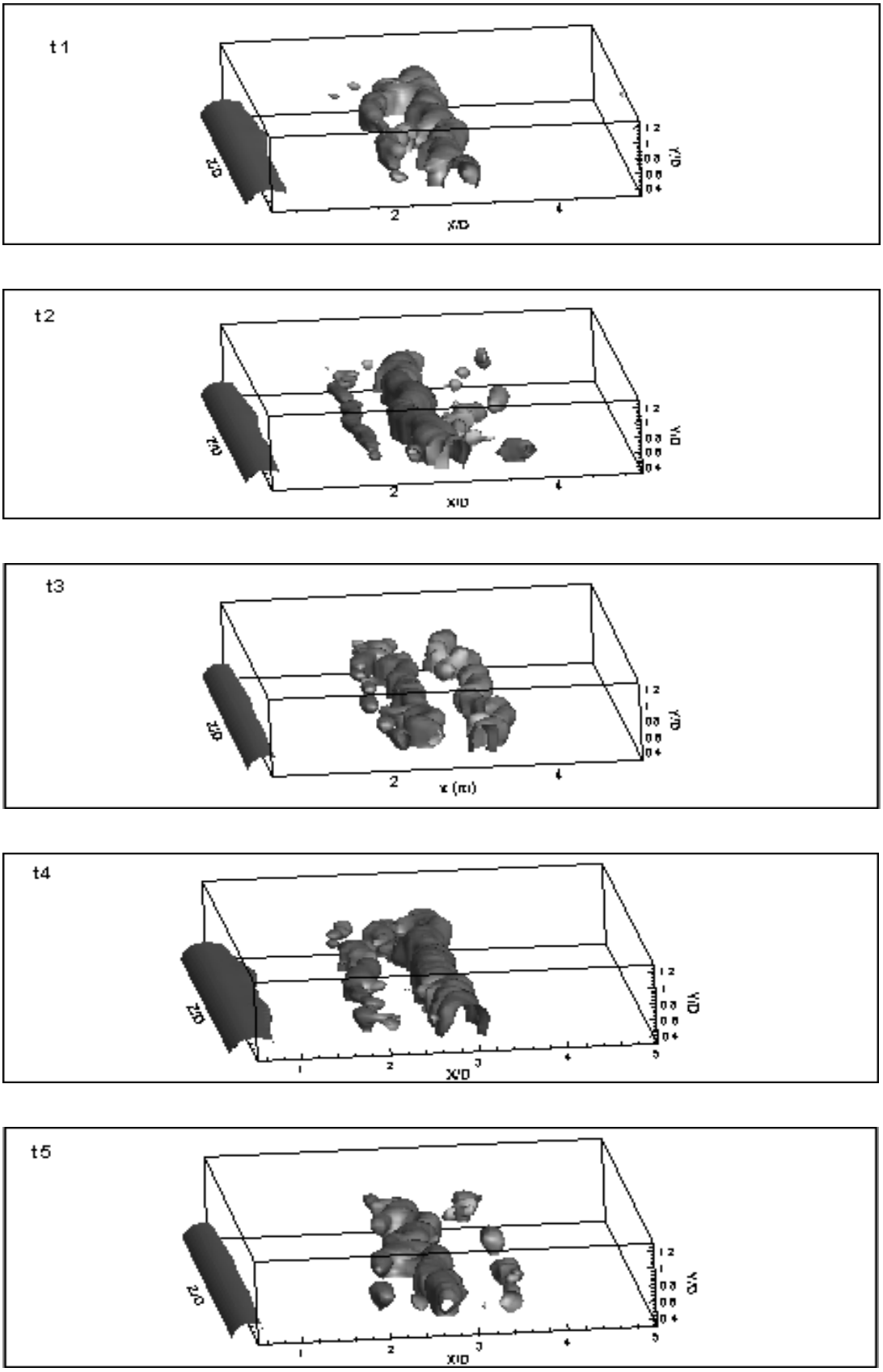

Fig.5.5. Sequential three-dimensional isosurfaces of low-pressure (NFST case)

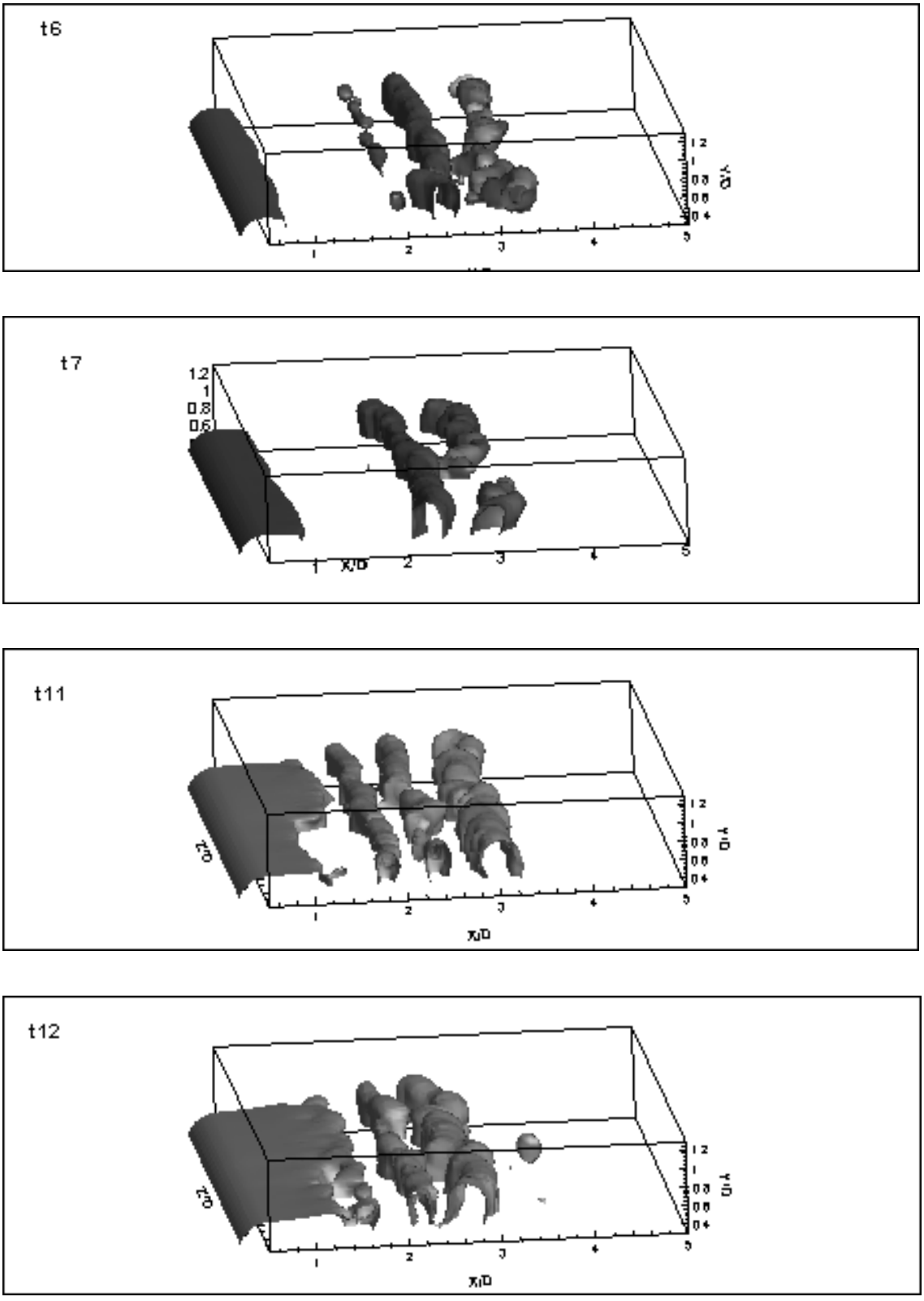

Fig.5.6. Sequential three-dimensional isosurfaces of low-pressure (NFST case)

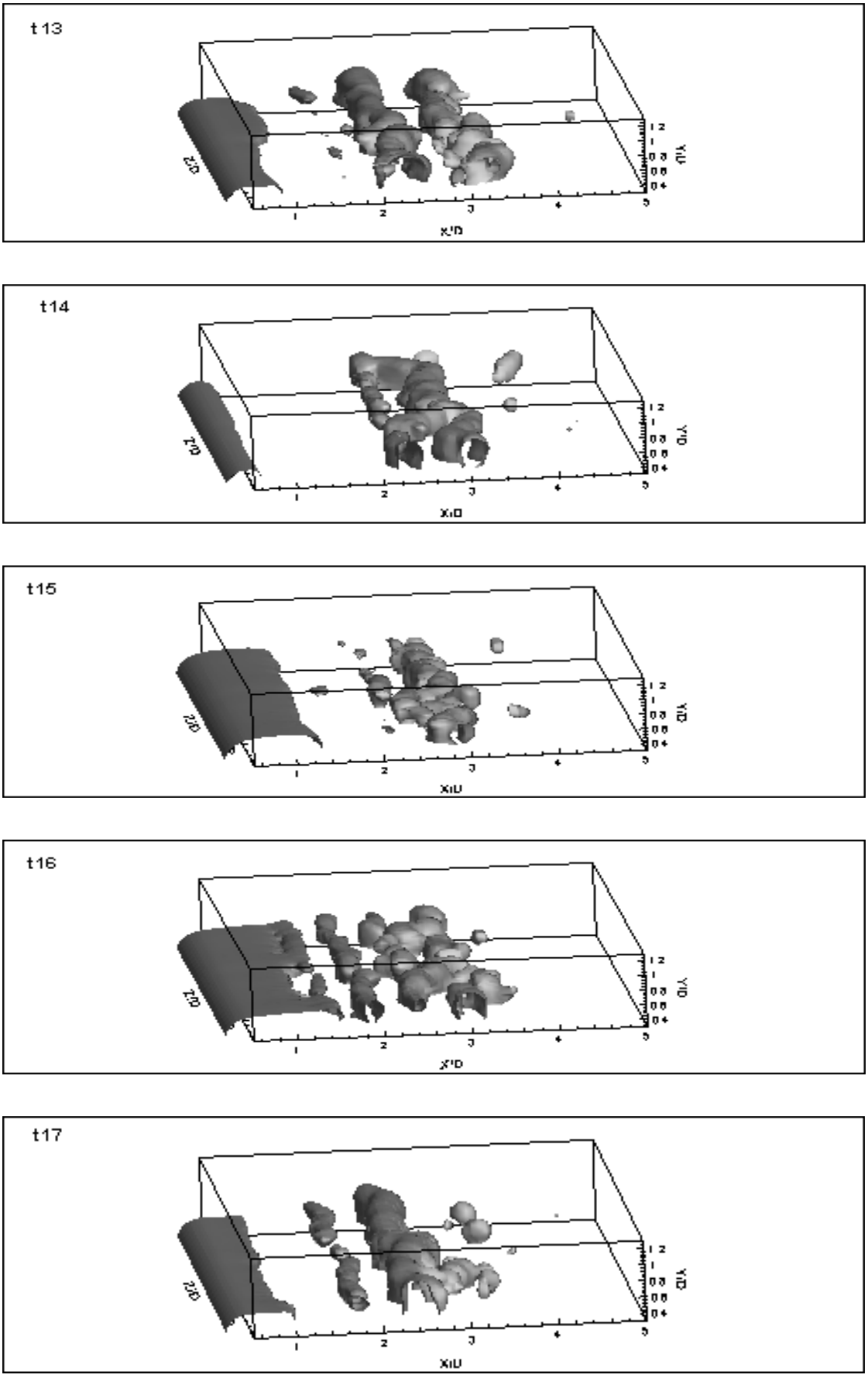

Fig.5.7. Sequential three-dimensional isosurfaces of low-pressure (NFST case)

Evolution and breakdown of the two-dimensional Kelvin-Helmholtz rolls into organised Λ-shaped vortical structures after the reattachment region can be seen through the Q-criterion isosurfaces shown in figures 5.8, 5.9, and 5.10. Compared to the low-pressure criteria, it seems that the Q-criterion can be used to reveal better the structures of smaller scales than those visualised by the low-pressure field.

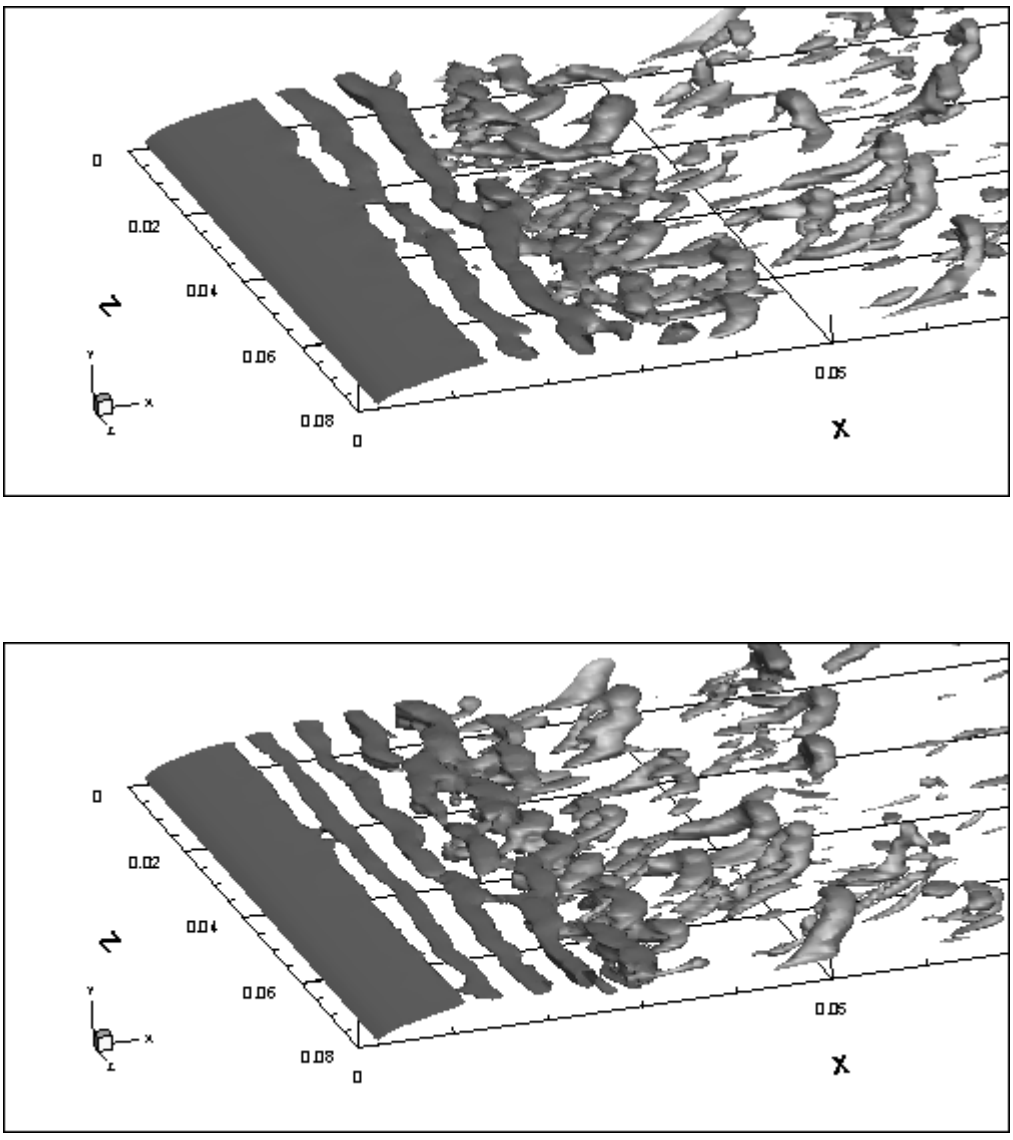

Fig.5.8. Sequences of Q-isosurfaces showing two-dimensional Kelvin-Helmholtz rolls breakdown into horse-shoe vortices (NFST case)

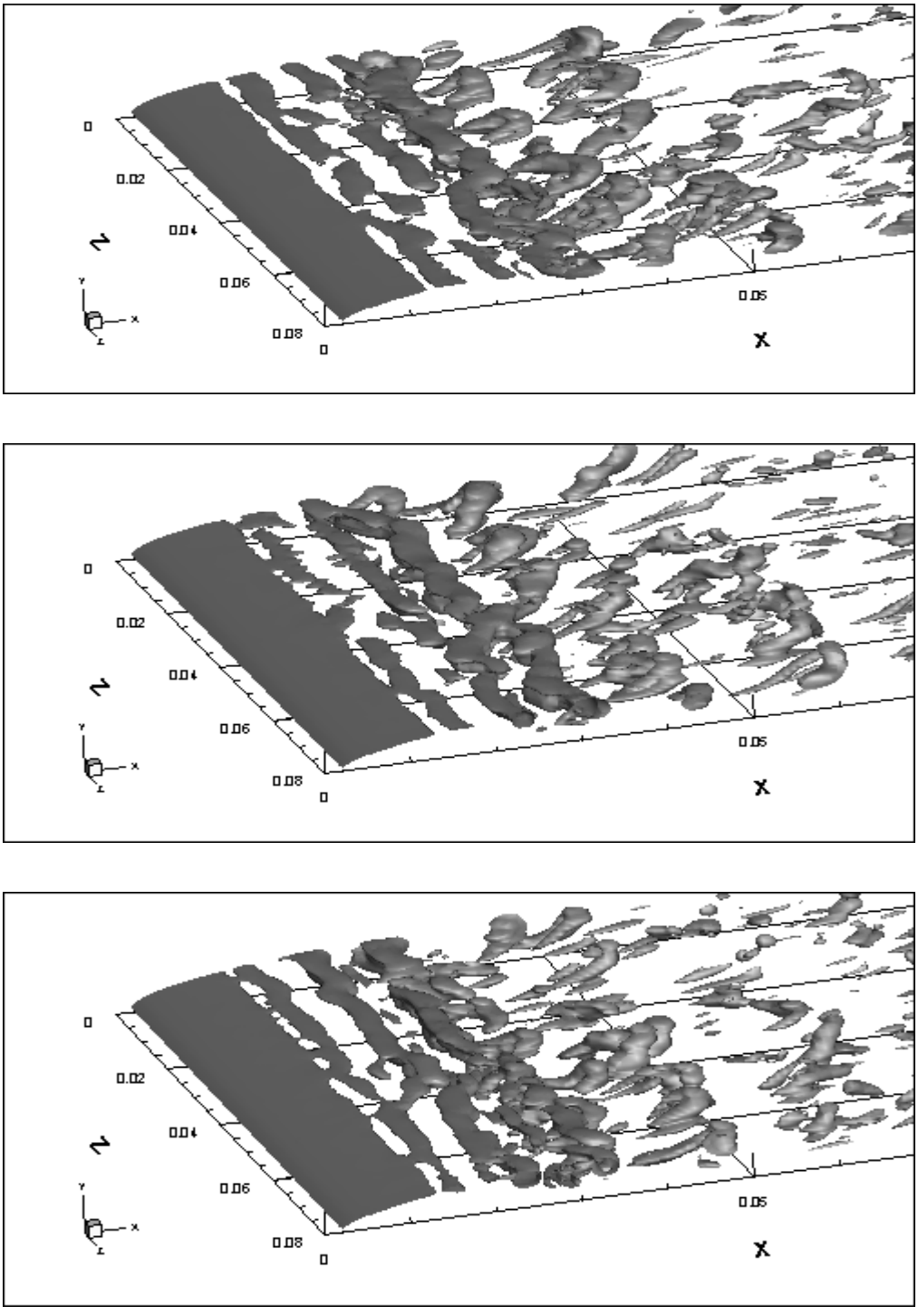

Fig.5.9. Sequences of Q-isosurfaces showing two-dimensional Kelvin-Helmholtz rolls breakdown into horse-shoe vortices (NFST case)

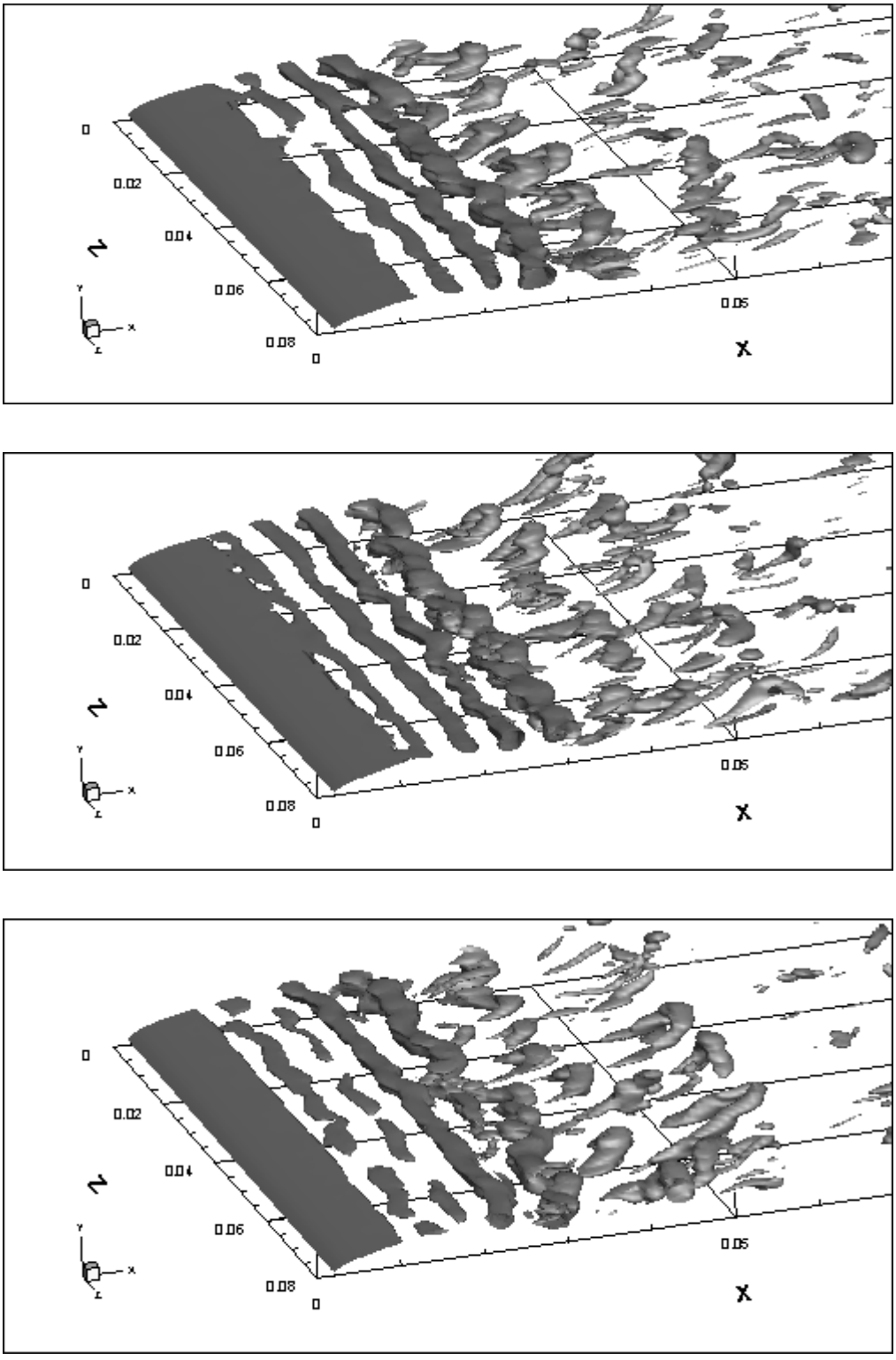

Fig.5.10. Sequences of Q-isosurfaces showing two-dimensional Kelvin-Helmholtz rolls breakdown into horse-shoe vortices (NFST case)

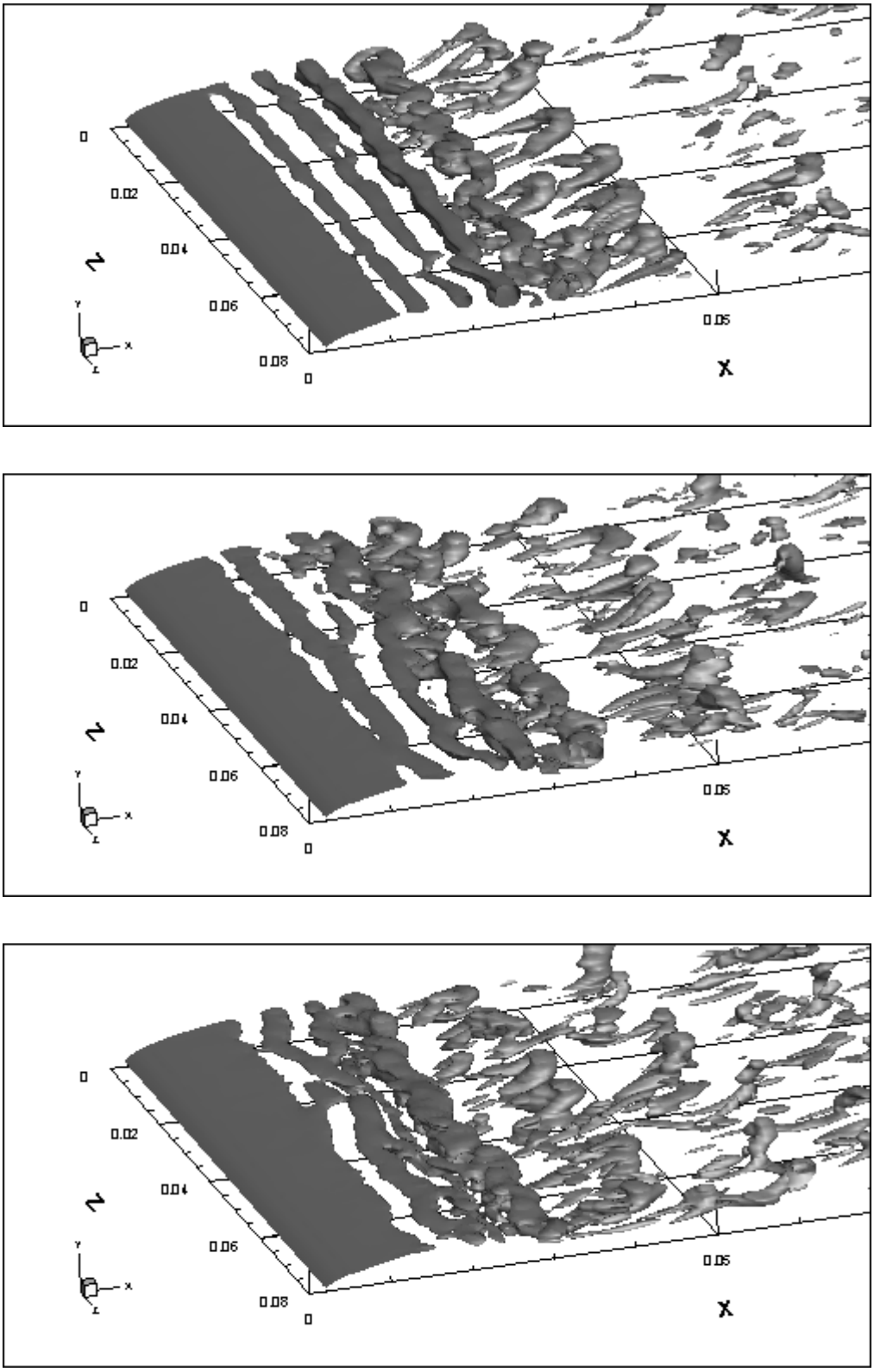

Fig.5.11. Sequences of Q-isosurfaces showing two-dimensional Kelvin-Helmholtz rolls breakdown into horse-shoe vortices (NFST case)

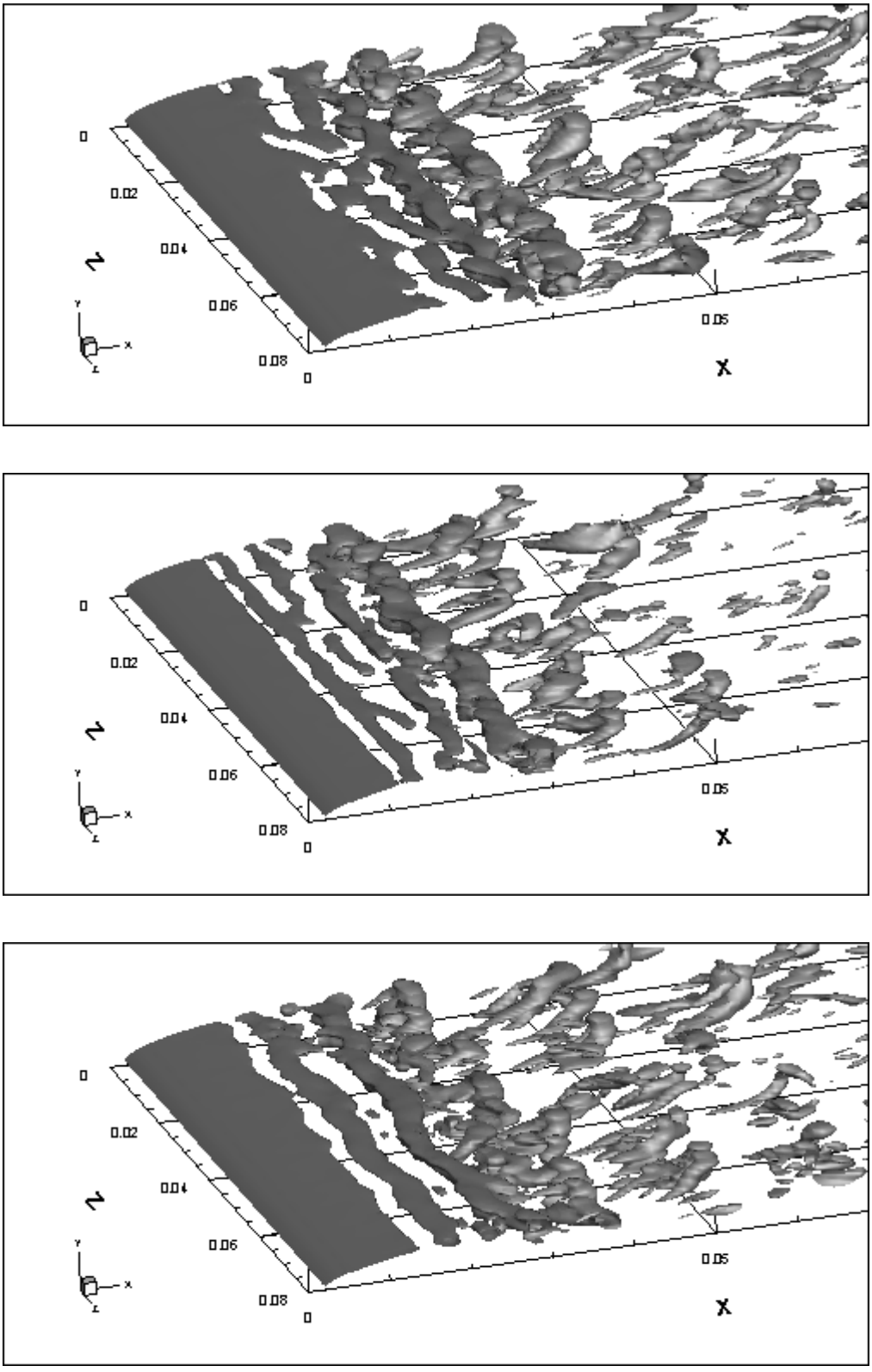

Fig.5.12. Sequences of Q-isosurfaces showing two-dimensional Kelvin-Helmholtz rolls breakdown into horse-shoe vortices (NFST case)

Three-dimensional streamwise vorticity iso-surfaces at sequential times are shown in figures 5.13 to 5.16. It can be seen that traces of streamwise vorticity appear in the early stages of transition at about x/D = 2.0. It can be seen that the main region of concentration of the streamwise vorticity is within the reattachment region x/D = 2.0-4.0. This is where most of the transition events and reattachment take place. It appears that the emerging vortical structures are gradually lifted up and move away from the wall while becoming stretched along the axial direction. Overall, the streamwise vorticity shown in the figures 5.13 to 5.16 present rather organised and distinguishable longitudinal structures.

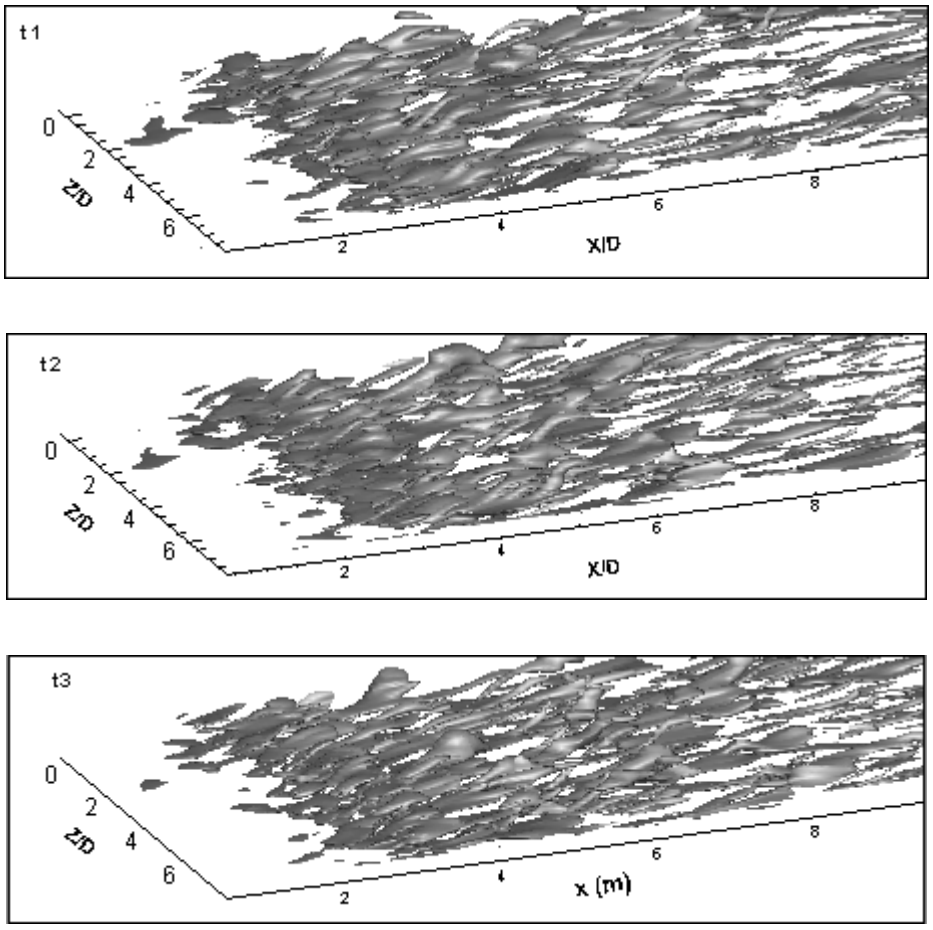

Fig.5.13. Sequences of streamwise vorticity isodurfaces (NFST case)

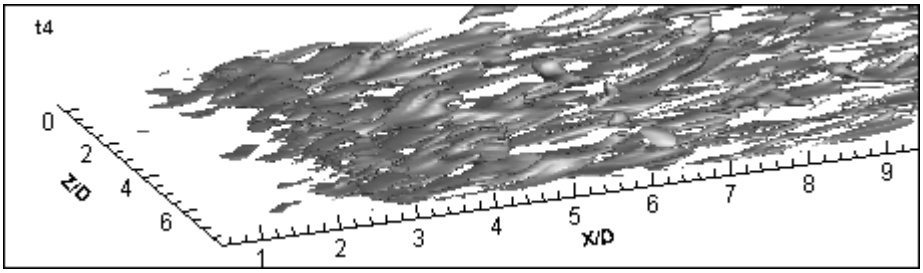

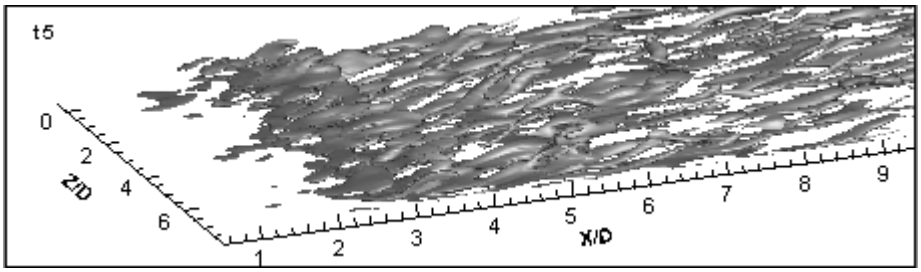

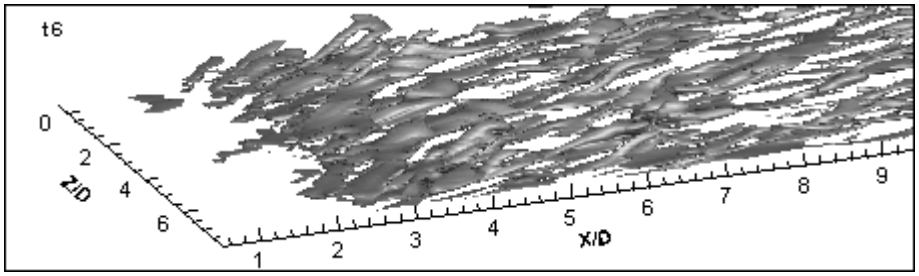

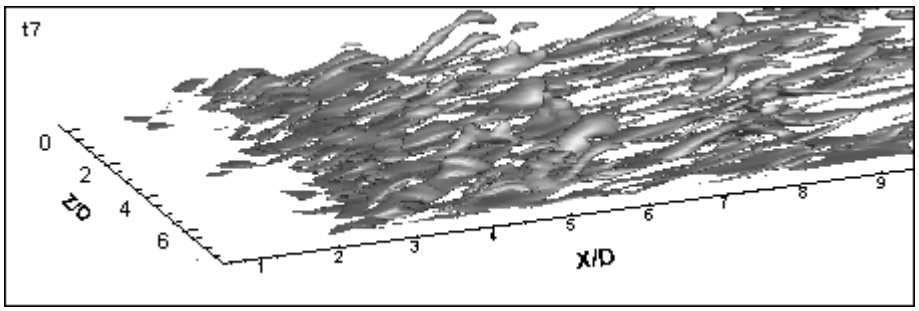

Fig.5.14. Sequences of streamwise vorticity isodurfaces (NFST case)

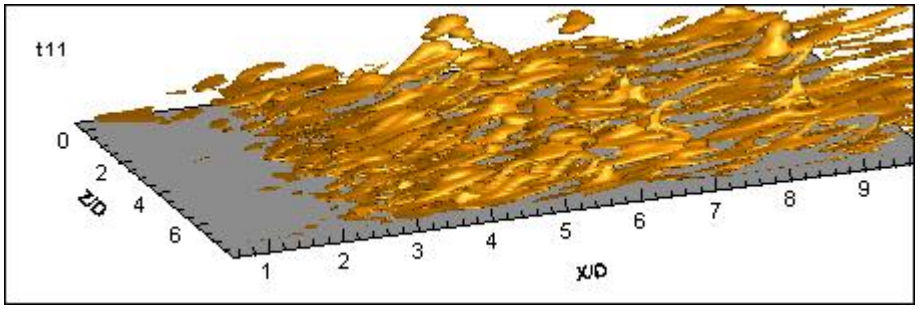

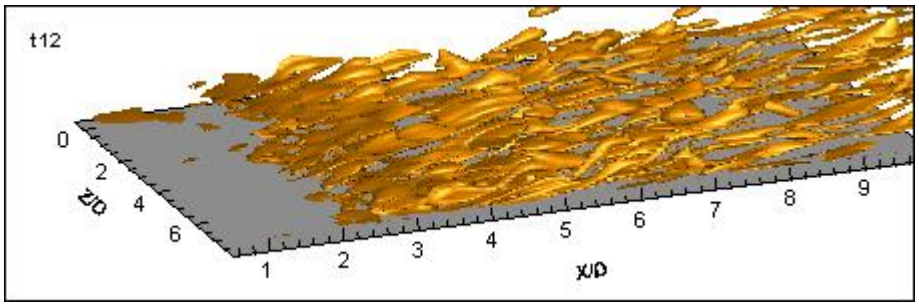

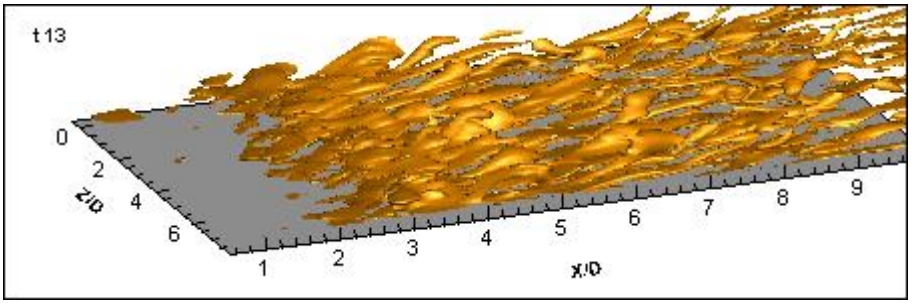

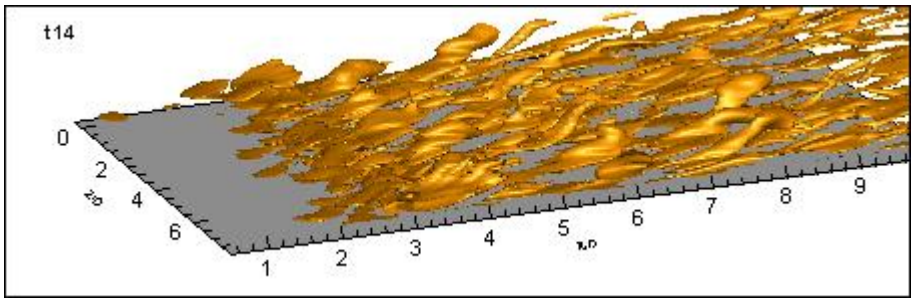

Fig.5.15. Sequences of streamwise vorticity isodurfaces (NFST case)

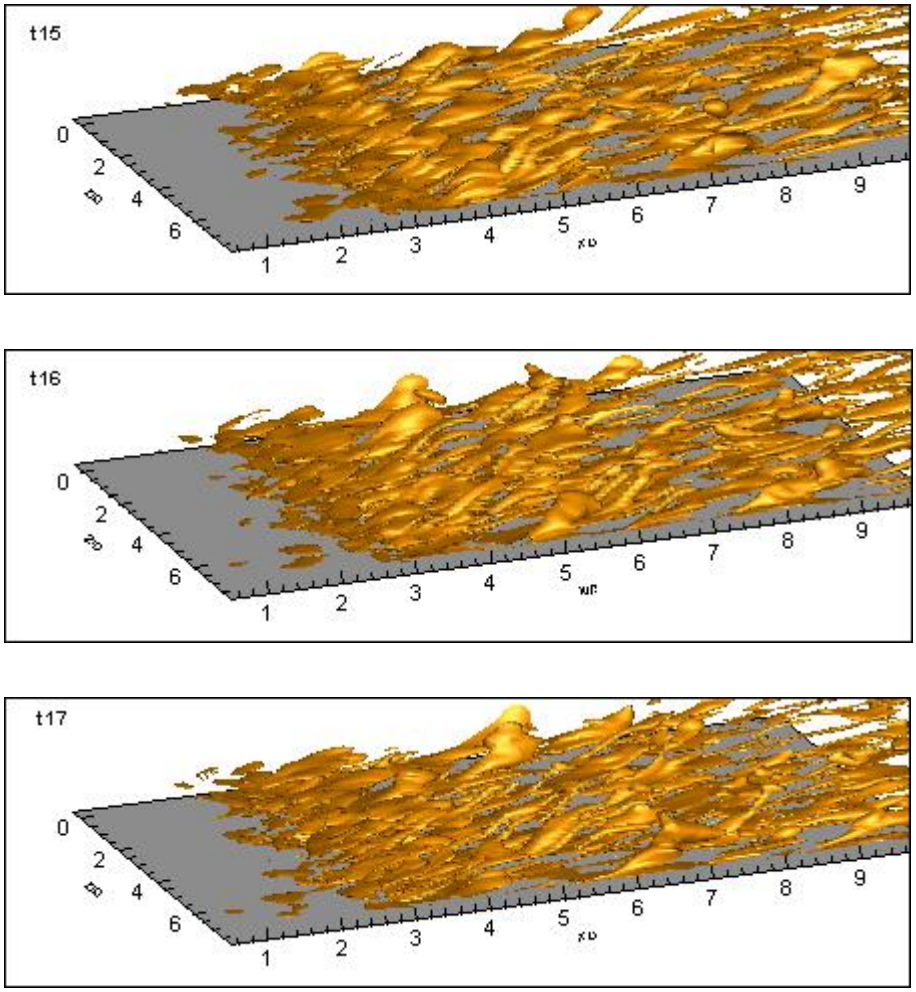

Fig.5.16. Sequences of streamwise vorticity isodurfaces (NFST case)

Figures 5.17, 5.18, and 5.19 show the three-dimensional spanwise vorticity iso-surfaces where a plane vorticity sheet develop from the leading edge and starts to become unsteady at around *x/D* = 2.0 where three-dimensional motions develop rapidly as discussed in the previous chapter. The vorticity sheet eventually breaks down into severe longitudinal vortical structures in the reattachment region around *x/D* = 3.0 – 4.0.

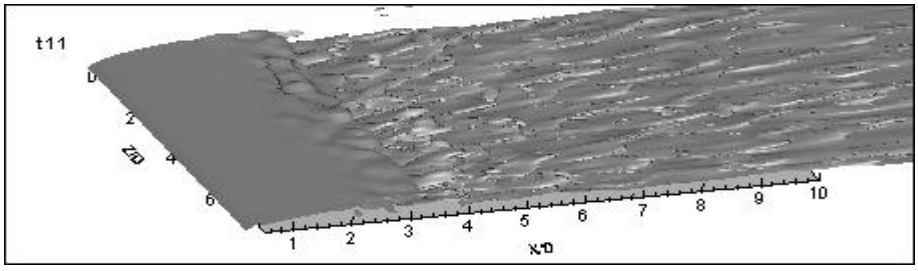

Fig.5.17. spanwise vorticity isodurfaces (NFST case)

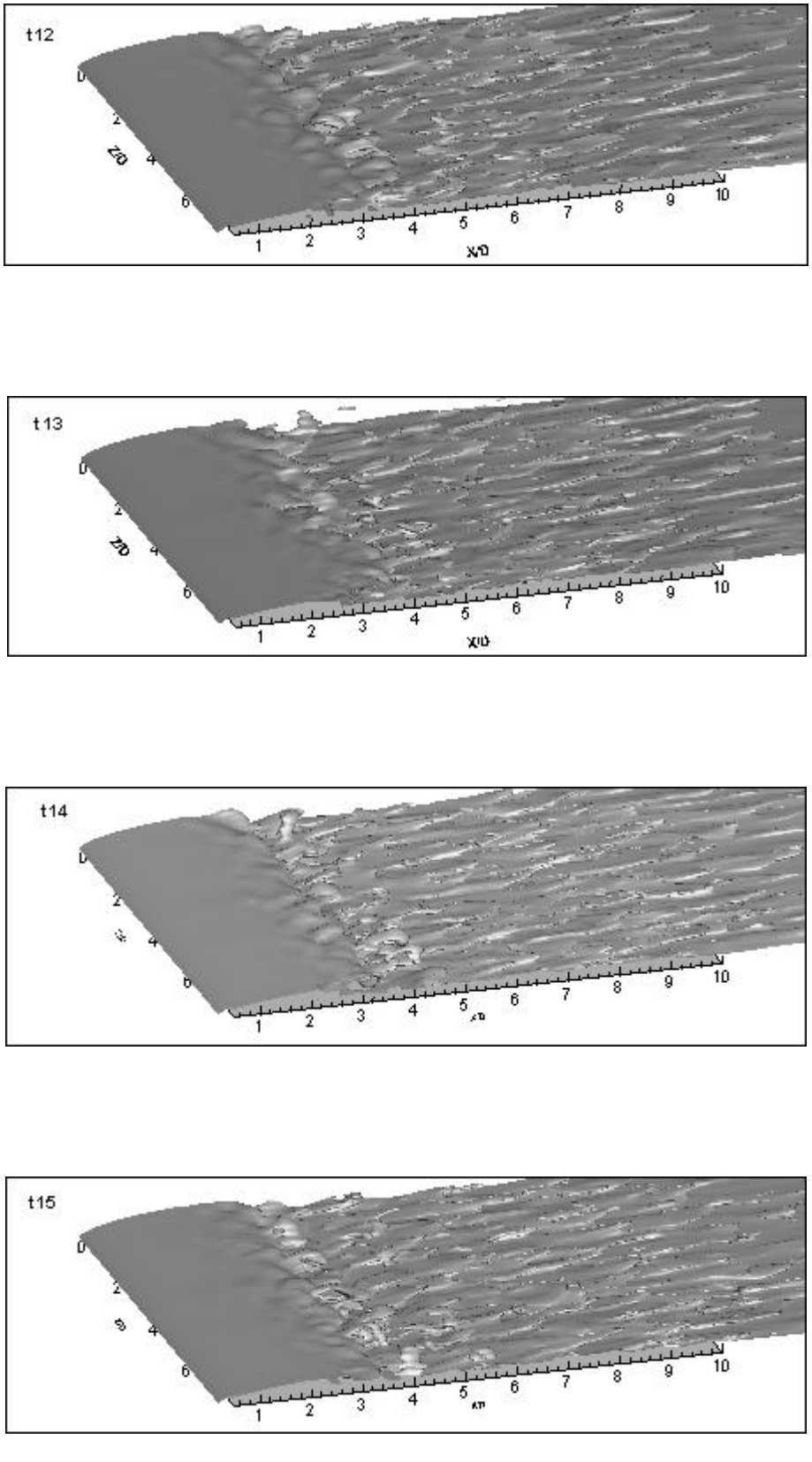

Fig.5.18. Sequences of spanwise vorticity isodurfaces (NFST case)

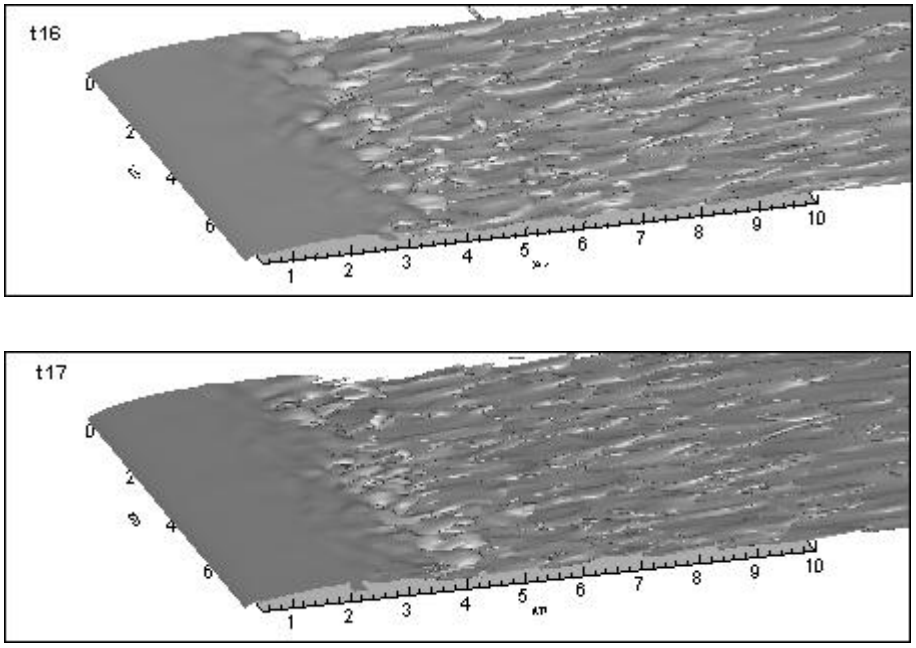

Fig.5.19. Sequences of spanwise vorticity isodurfaces (NFST case)

B. FST case

In the same manner as above for the NFST case, the pressure iso-surfaces, the Q-criterion, and the vorticity field are also employed to visualise the flow structures for the FST case and to compare qualitatively with the NFST case.

Figures 5.20, 5.21, and 5.22 show sequential pressure iso-surfaces for the FST case. The chaotic behaviour of the flow compared with the NFST case is apparent. No traces of the two-dimensional Kelvin-Helmholtz rolls could be identified through the low pressures field visualisations. The addition of free-stream turbulence with the intensity of 5.6% has smeared the coherent two-dimensional structures observed in the NFST case and resulted in earlier transition.

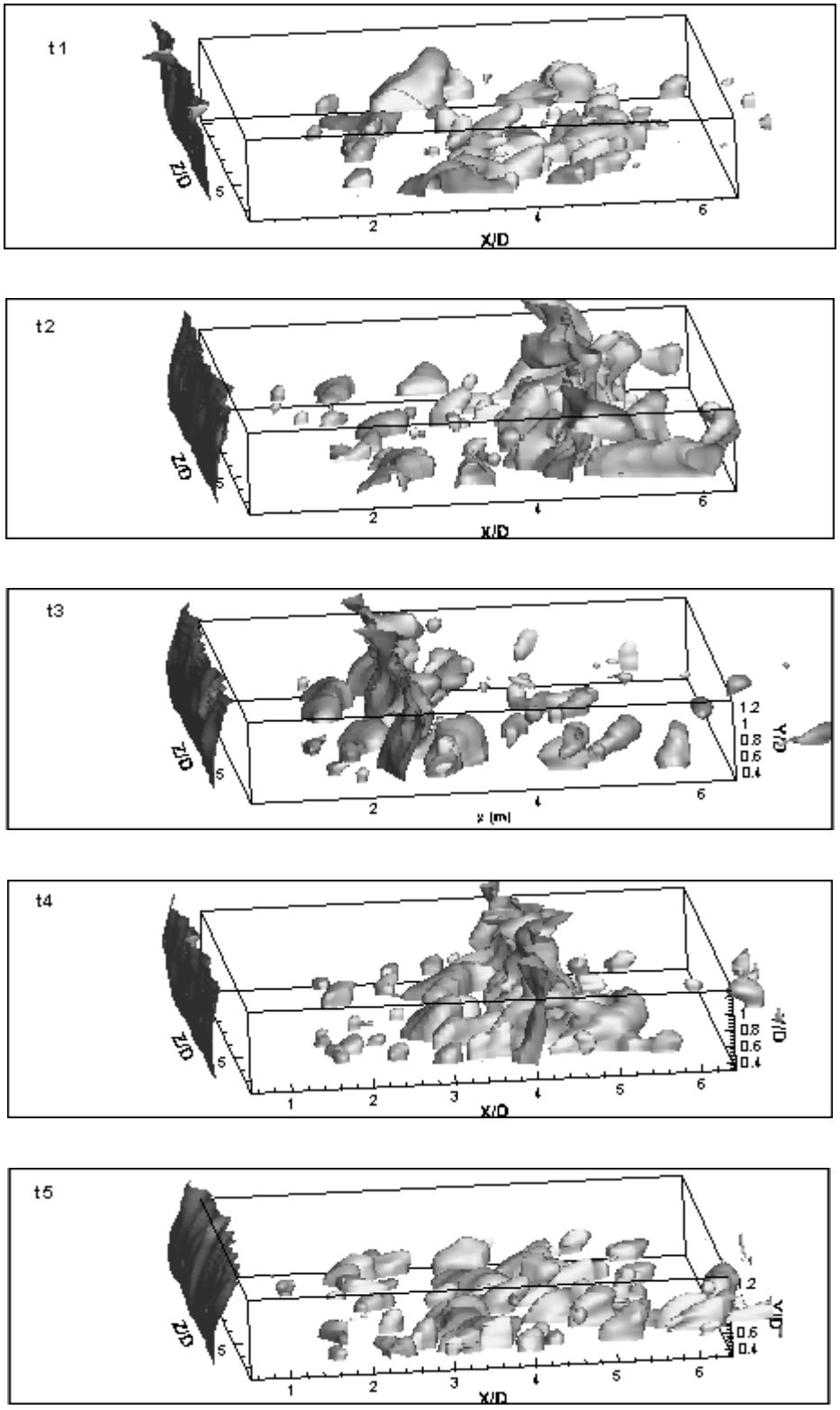

Fig.5.20. Sequences of low-pressure isosurfaces (FST case)

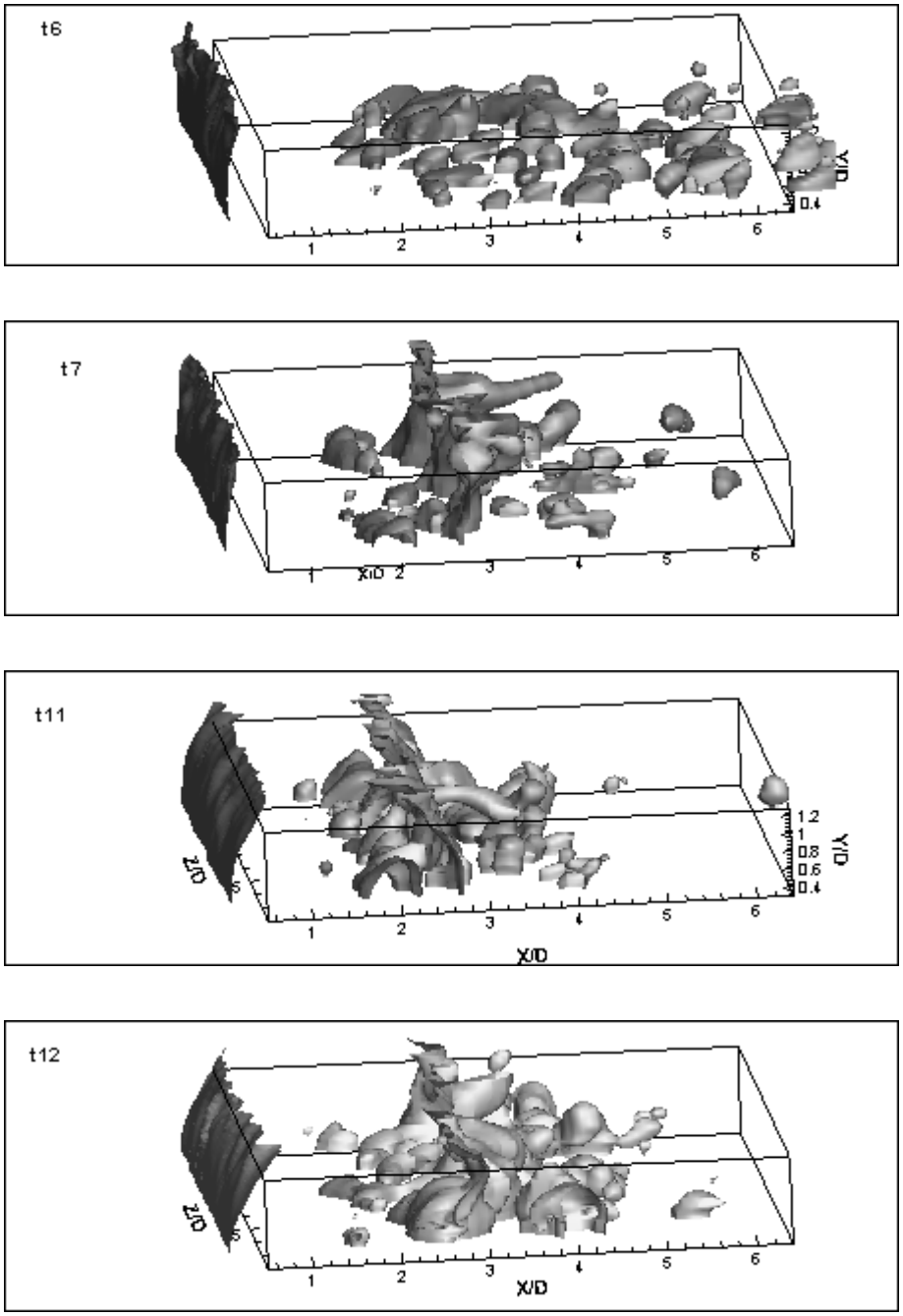

Fig.5.21. Sequences of low-pressure isosurfaces (FST case)

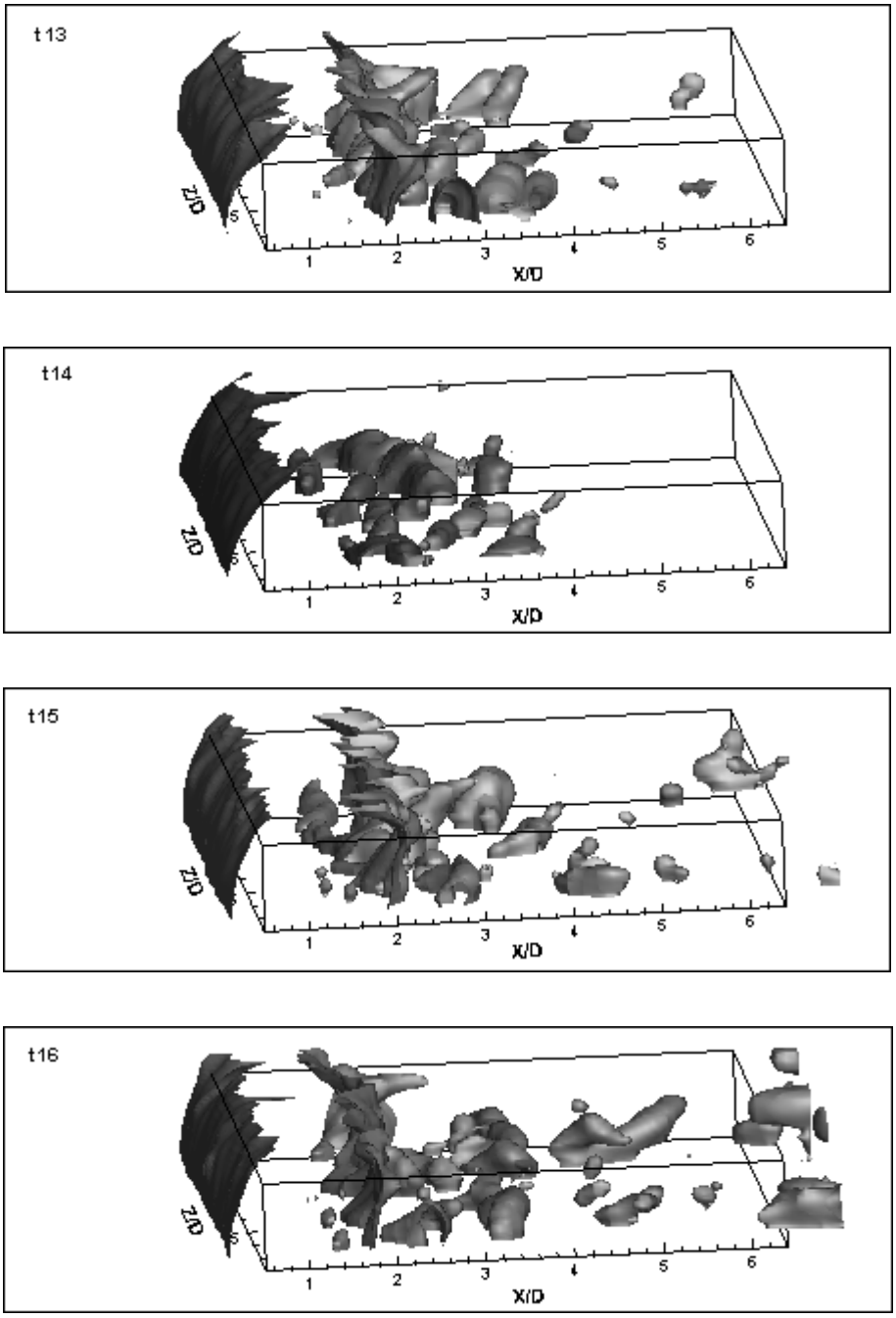

Fig.5.22. Sequences of low-pressure isosurfaces (FST case)

Figures 5.23, 5.24, 5.25, 5.26, 5.27, and 5.28 show sequential snapshots of the Q-criterion isosurfaces depicting the flow structures developing in the FST case. Two-dimensional structures associated with the Kelvin-Helmholtz instability as seen for NFST, are no longer visible at high free-stream turbulence level. Fot the NFST case, the spanwise oriented quasi-two dimensional rolls was clearly visible at the early stage of the bubble and then became distorted/deformed due to three-dimensional motion setting in as a result of a possible secondary instability. It was seen for the NFST case that some sorts of three-dimensional structures similar to the so called hairpin vortices appeared and eventually brokdown to turbulence at about or just after the reattachment. However, for the FST case it can be seen that spanwise oriented quasi-two dimensional Kelving-Helmholtz rolls are not visible anymore and spanwise irregularity appears at the early stage of the bubble in the separated shear layer leading to the formation of three-dimensional hairpin like structures, bypassing the stage where the Kelvin-Helmholtz rolls would appear and leading to much earlier breakdown to turbulenece compared with the NFST case.

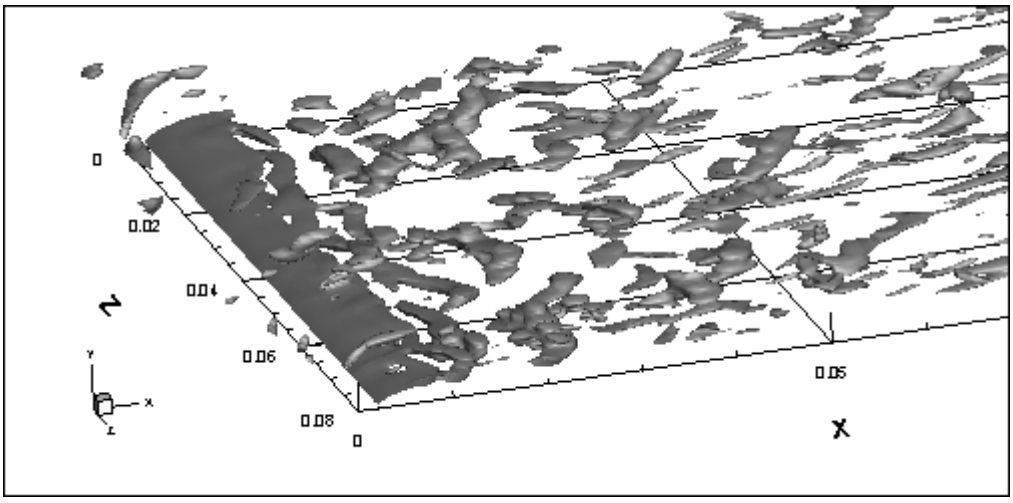

Fig.5.23. Q- isosurfaces (FST case)

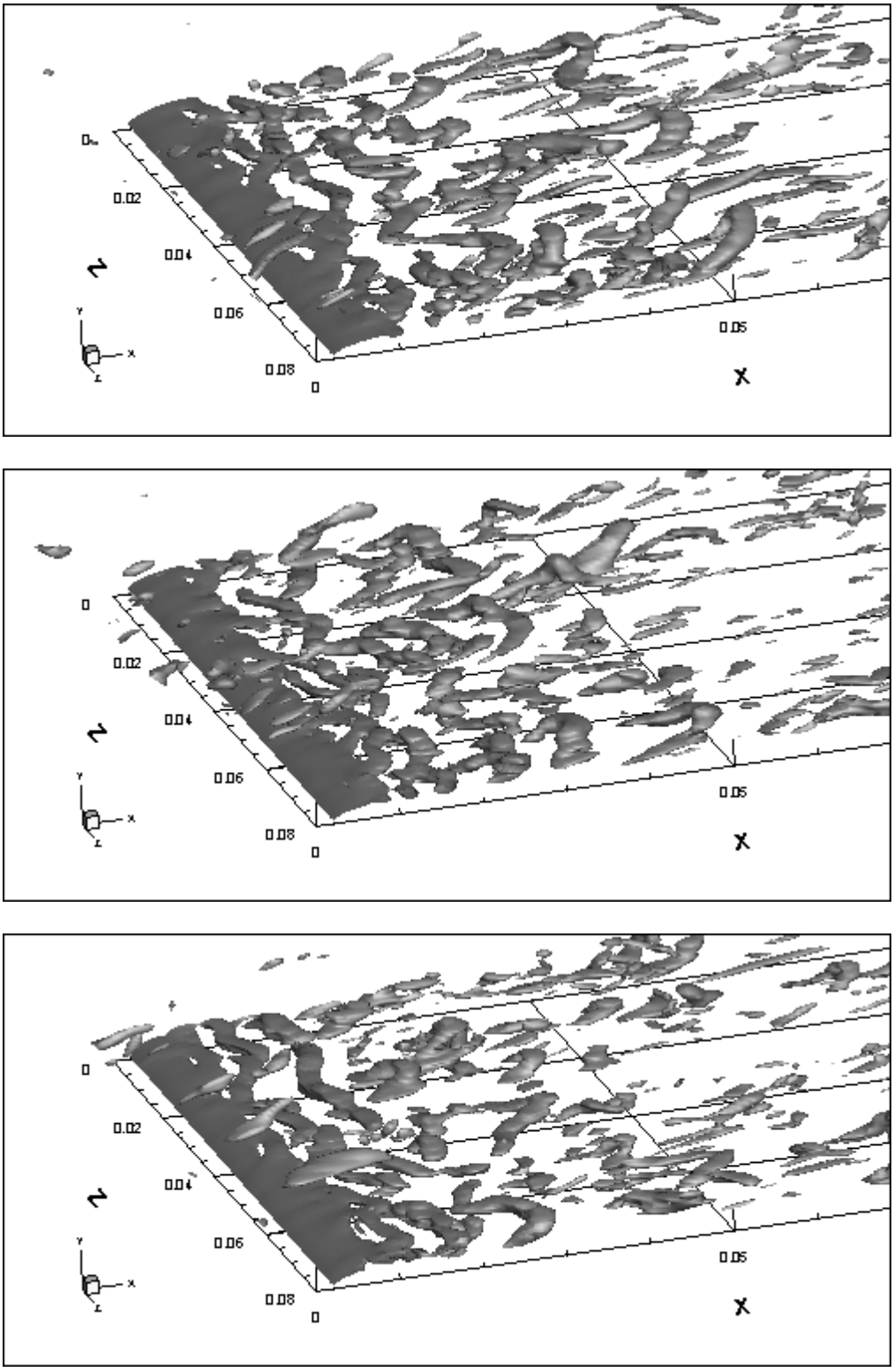

Fig.5.24. Sequences of Q- isosurfaces (FST case)

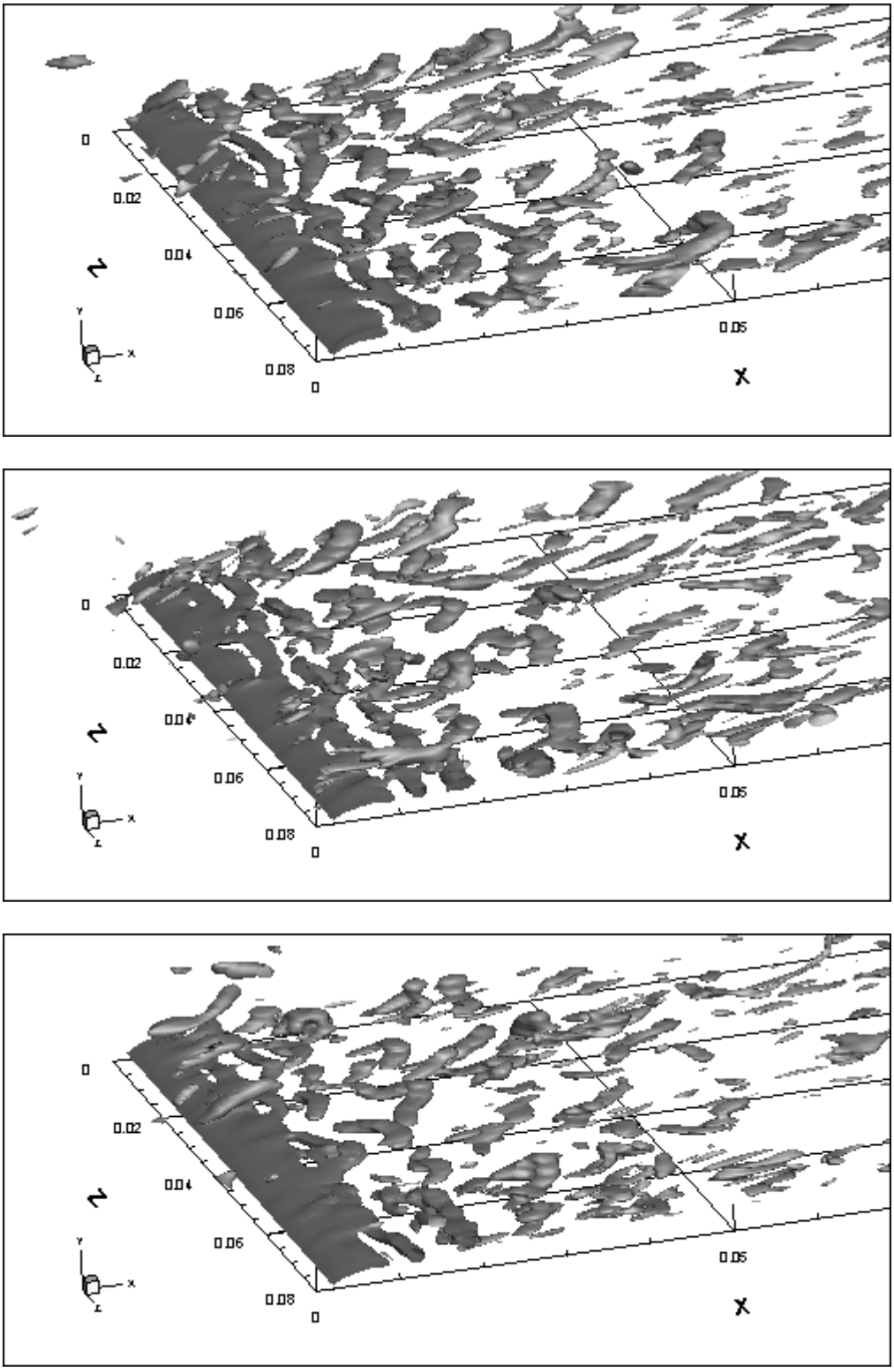

Fig.5.25. Sequences of Q- isosurfaces (FST case)

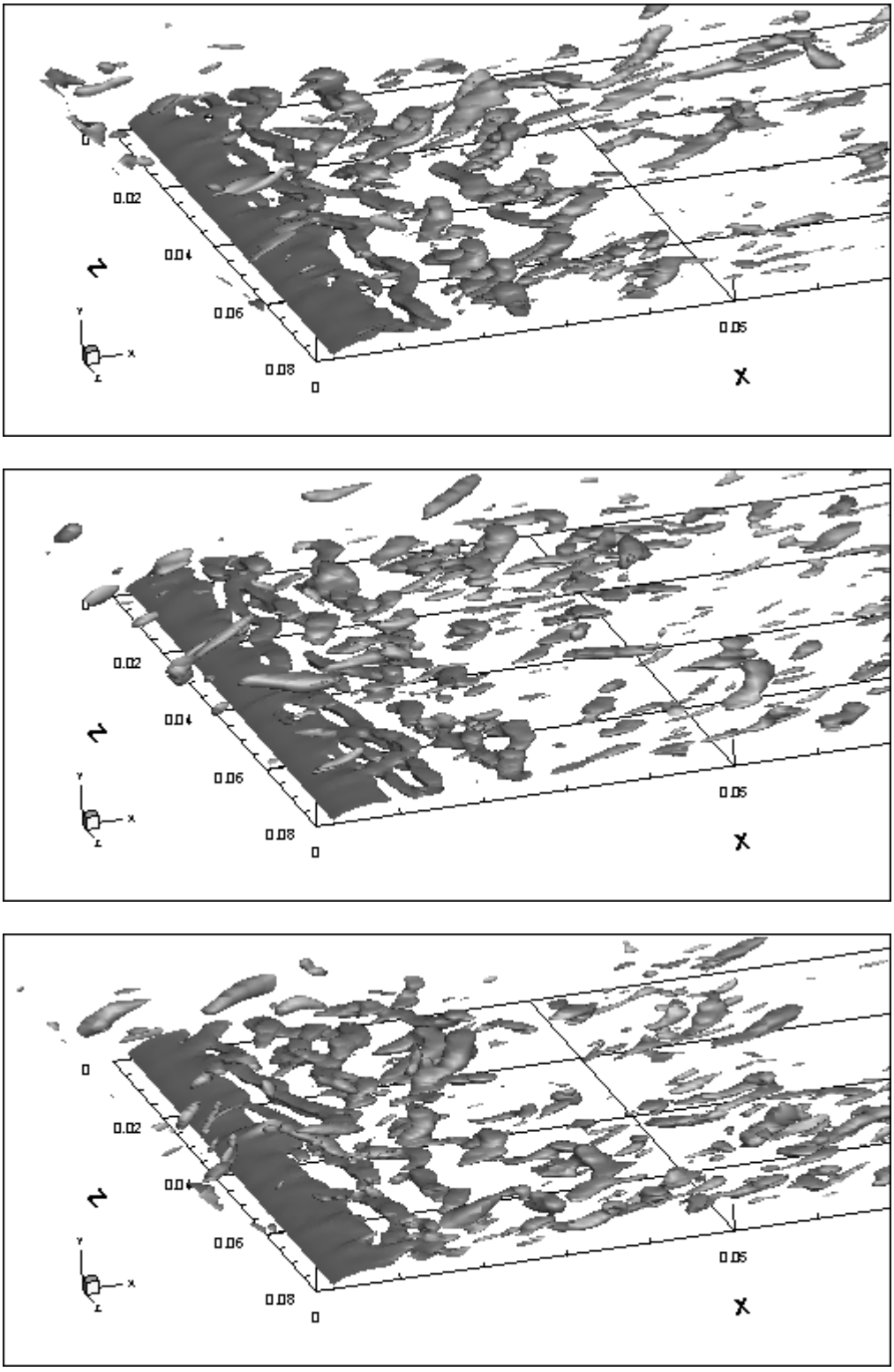

Fig.5.26. Sequences of Q- isosurfaces (FST case)

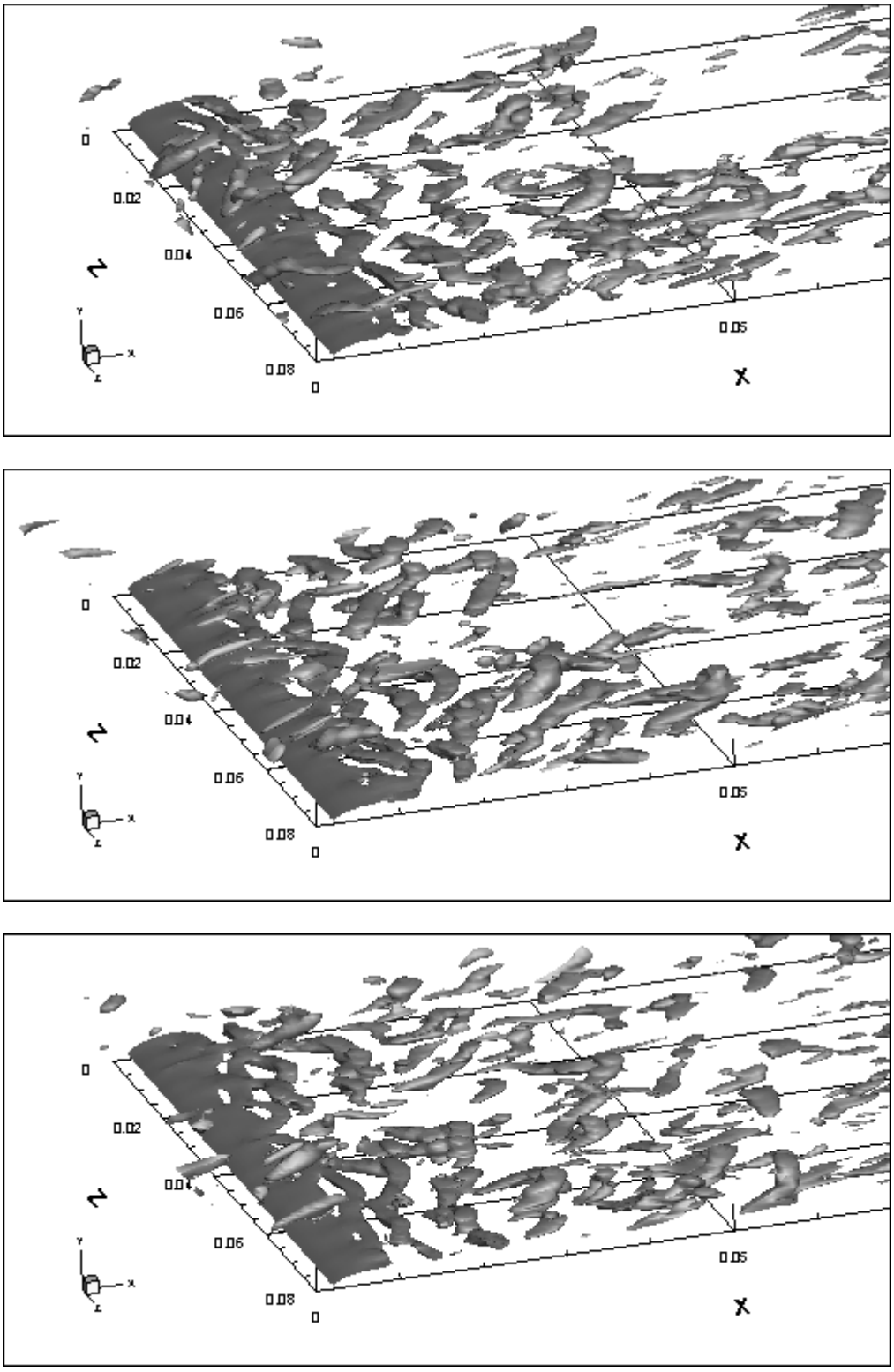

Fig.5.27. Sequences of Q- isosurfaces (FST case)

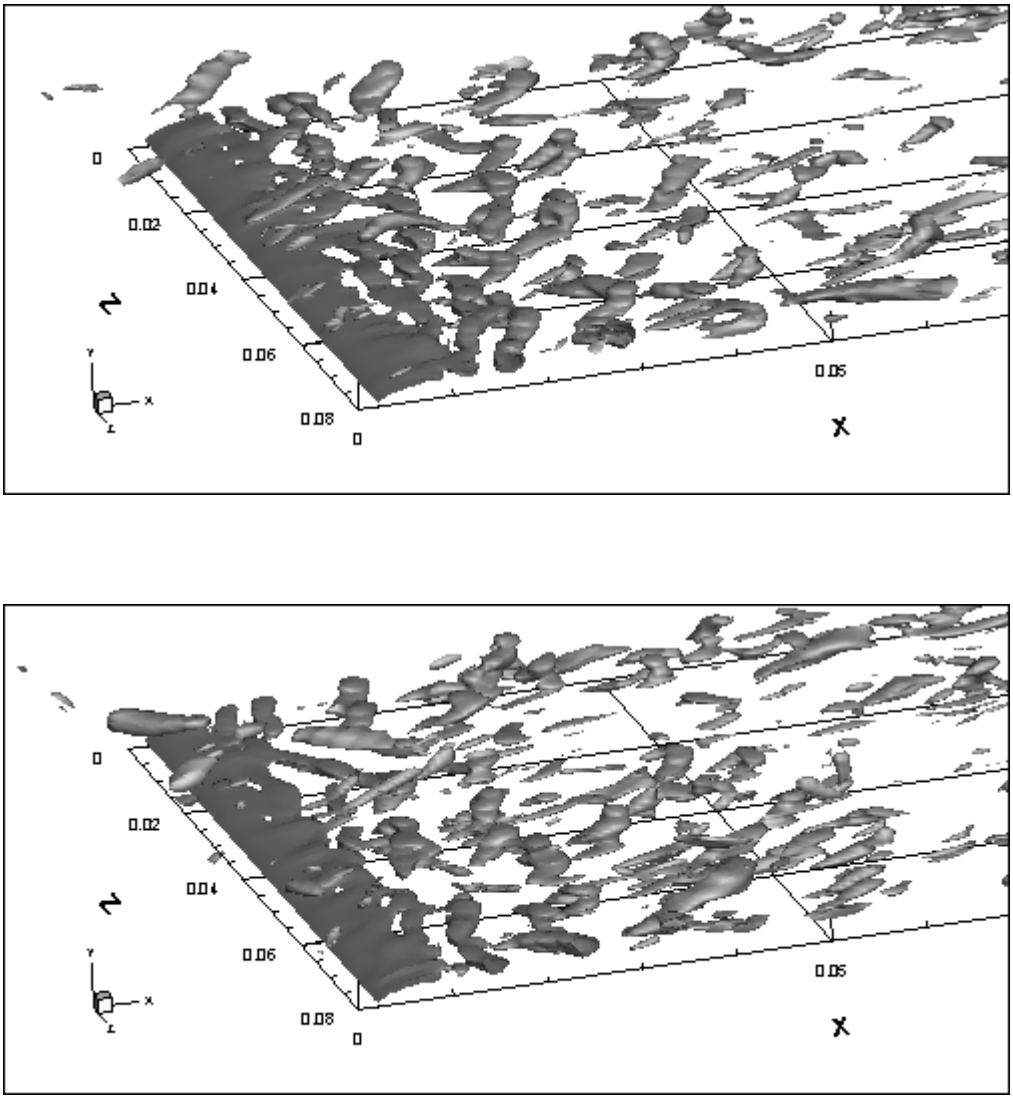

Fig.5.28. Sequences of Q- isosurfaces (FST case)

Figures 5.29 show streamwise vorticity isosurfaces for the FST case. It can be seen that unlike the NFST case, streamwise vorticity appear from the early stage of separation and show much more unorganised features as compared with the NFST case.

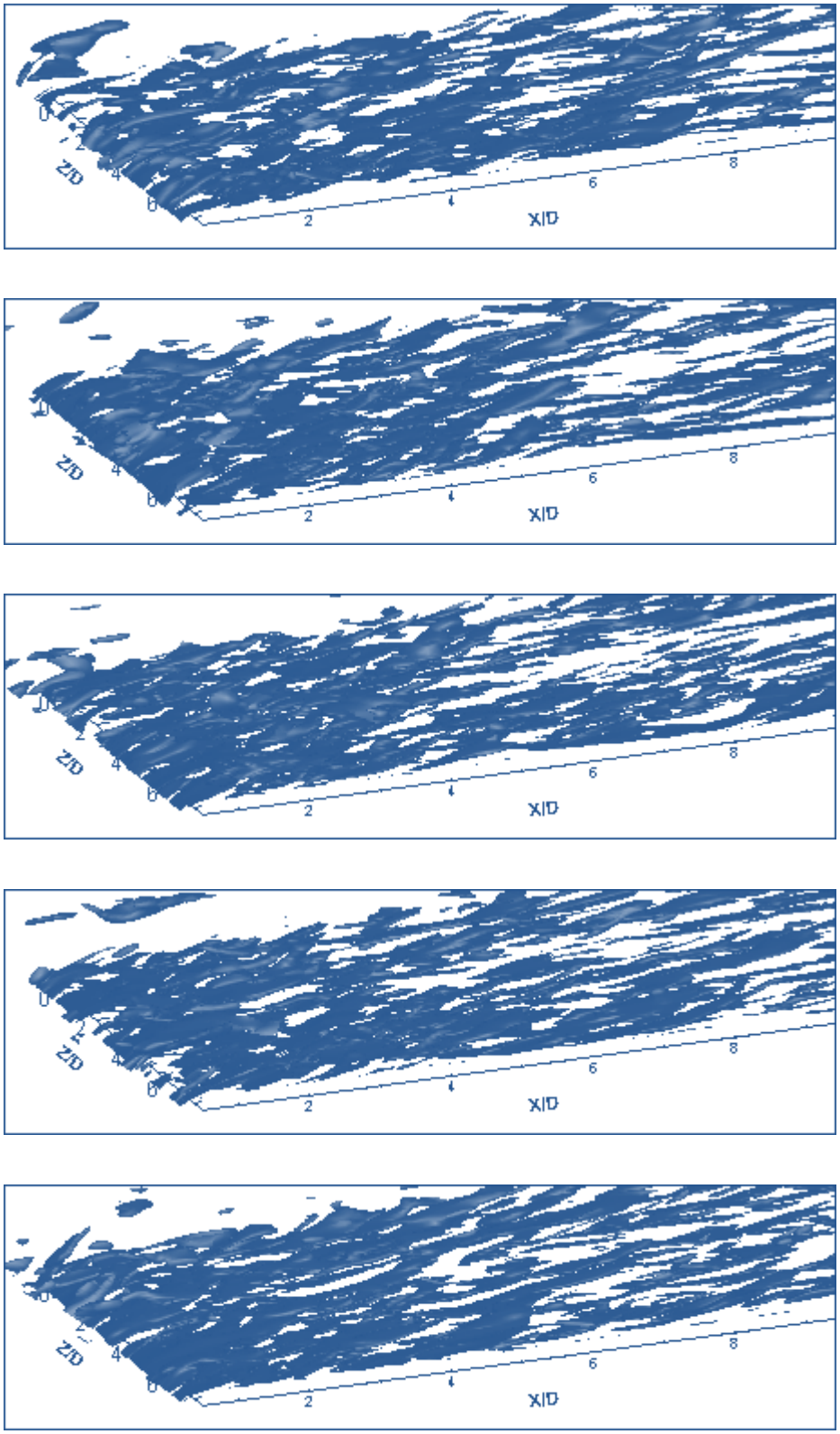

Fig.5.29. Sequences of streamwise vorticity isosurfaces (FST case)

Spanwise vorticity field for the FST case are shown in figures 5.30. Similar to the NSFT case a plane vorticity sheet can be seen developing from the leading edge but with some irregularities associated with streaky structures. It can be seen that compared with the NFST case disturbances in the free shear layer have larger amplitudes much earlier at about *x/D* = 0.8 due to disturbances from free-stream turbulence. Furthermore, it can be seen that the flow in the attached thin boundary layer prior to separation is still rather smooth, indicating that it is still laminar boundary layer but is already disturbed to some extent. Close inspection of spanwise vorticity isosurfaces reveals that the spanwise vorticity in the FST case is distorted much earlier than the NFST case and the attached thin laminar boundary layer prior to separation is not quite two-dimensional and contain some kind of streaky-like structures encouraging the bypass transition of the separated shear layer as investigated in the previous chapter.

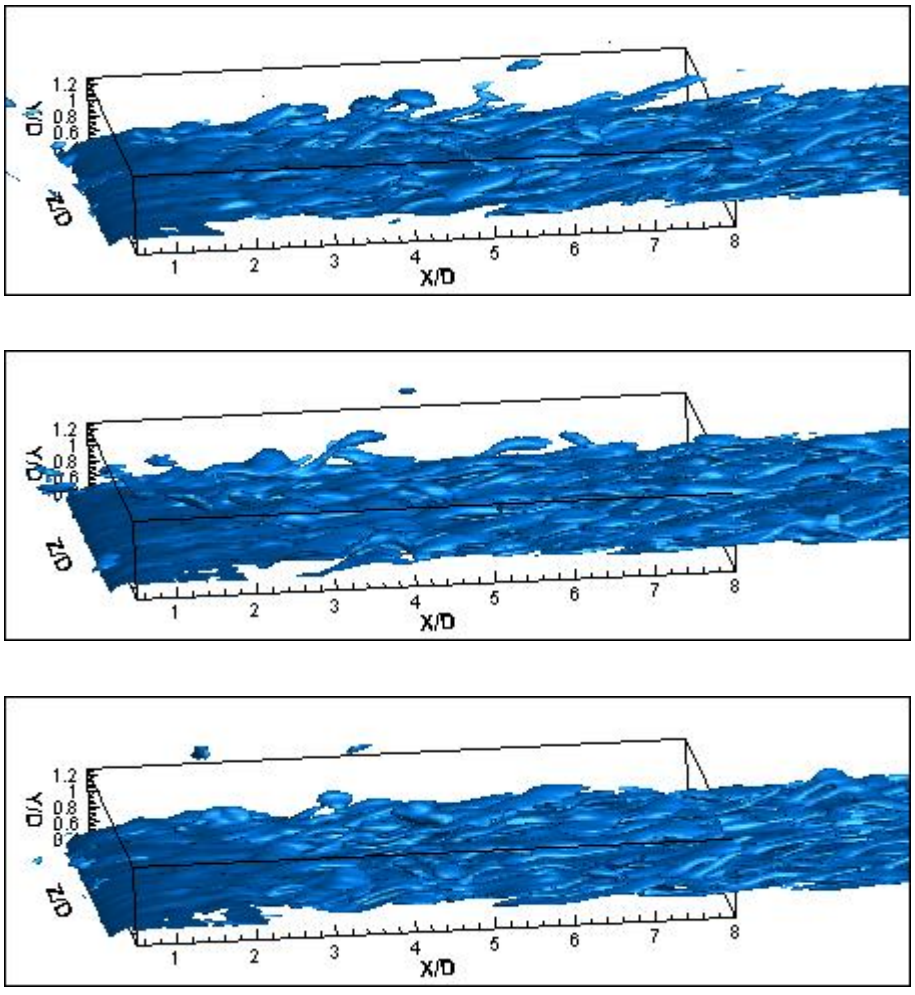

Fig.5.30. Sequences of spanwise vorticity isosurfaces (FST case)

From the above visualisation of the flow structures for both NFST and FST cases the following conclusions regarding the effect of free-stream turbulence can be drawn:

1. Free-stream turbulence results in an earlier breakdown of the separated shear layer.
2. The spanwise coherence of structures are distorted and the vortical structures are no longer organised as seen at low free-stream turbulence condition.
3. The two-dimensional Kelvin-Helmholtz instability seen at low free-stream turbulence condition is bypassed and the breakdown of shear layer occurs much earlier than the NFST case.

Chapter 6

Concluding Remarks and Recommendations

Two transitional separated-reattached flows developed over a flat plate with a semi-circular leading edge (T3L test cases) at two free-stream turbulence levels have been investigated using Large Eddy Simulation (LES). A dynamic sub-grid scale model was employed where the sub-grid eddy-viscosity was calculated dynamically at each time step. A numerical trip method has been successfully used to generate a realistic turbulence field of high turbulence intensity. The numerical approach employed yields a very well agreement with experimental data regarding both the free-stream turbulence decay rate and the mean velocity profiles as well as the Reynolds stresses.

The whole transition process leading to the breakdown of the separated shear layer has been shown through flow visualisation. Large scale coherent structures have been identified within the shear layer depicting the transition of process. For the NFST case, the two-dimensional Kelvin-Helmholtz rolls are the dominant large-scale structures prior to the reattachment. They grow in size as being convected downstream and are prone to unsteadiness as any small disturbances present grow downstream causing the distortion of the initial two-dimensional spanwise vortices. Further downstream these two-dimensional vortices become more distorted and roll up leading to the formation of streamwise vortices associated with significant three-dimensional motions. The Kelvin-Helmholtz vortices eventually breakdown at about the mean reattachment point and develop rapidly into a turbulent layer downstream. The well-known hairpin vortices have been clearly shown at about the mean reattachment point.

From the detailed analysis of the LES data it has been concluded that at low levels of free-stream turbulence, transition of the separated shear layer is initiated with the two-dimensional inviscid instability via the Kelvin-Helmholtz instability mechanism consistent with numerous studies on transition of the separated shear layer at low disturbance environment.

Detailed analysis of LES data for the case under 5.6% free-stream turbulence level reveal that transition occurs earlier compared with the NFST case with no presence of the Kelvin-Helmholtz rolls in the separated shear layer. In fact, for the FST case the instability analysis shows that the criterion for the Kelvin-Helmholtz instability to happen is not satisfied anymore. There are already disturbances in the attached thin boundary layer before separation and the disturbances grow very rapidly immediately after separation, leading to very rapid transition. This is further confirmed by visualising the transition process using isosurfaces of the vorticity and Q-criterion which prove that the transition process is quite different at such high level of free stream turbulence. The early stage where the Kelvin-Helmholtz instability dominates under low free-stream turbulence is bypassed under such elevated free-stream turbulence conditions similar to the bypass transition process in attached boundary layers. Under such free-stream turbulence level the mean reattachment length reduced by 60%, consistent with the findings of many numerical and experimental studies concerning the effect of free-stream turbulence in separated-reattached flow. From the extensive flow visualisation data it can also be concluded that the free-stream turbulence increased the randomness and reduced the coherency of the large-scale structures comparing with the NFST case.

A detailed spectral analysis was performed for both the NFST and FST cases over the whole separation region. For the NFST case, it is revealed that fluctuations are amplified in the separated region within two frequency ranges; a regular shedding frequency and a low-frequency band. The dimensionless regular shedding frequency is in good agreement with many numerical and experimental studies and through the wave number analysis (the *kh* criteria) it proves that the Kelvin-Helmholtz instability is at work. Existence of the low-frequency band is believed in some literature to be due to the flapping of the shear layer associated with enlargement and shrinkage of the bubble.

Detailed spectral analysis was also performed for the case at 5.6% free-stream turbulence. Only a mild peak region could be observed within the shear layer with a high-frequency range which does not satisfy the Kelvin-Helmholtz instability criterion. No trace of low-frequency activity as seen for the NFST case could be observed. This low frequency activity is not well understood and further investigation is needed.

The present study has shown that the accuracy of the co-located grid arrangement with the Rhie-Chow pressure smoothing when applied to separated boundary layer transition simulations is as good as using a staggered grid arrangement, which is consistent with the previous studies of mainly steady flow calculations. This is very encouraging as the co-located gird has distinct advantages over the staggered grid when computational domains are complex and non-orthogonal meshes have to be used but there is a general misconception in the incompressible LES community that the staggered gird is superior to the co-located gird.

Scope for Further Research

The current study employed LES to explore effects of reasonably high free-stream turbulence level on instability characteristics of separated boundary layer on a plate with a semi-circular leading edge. The focus has been on how the primary instability and shedding frequencies are affected by such high free-stream turbulence level. The later stages of the transition i.e. secondary instabilities leading to breakdown of the primary vortices into the smaller scales is still not well understood. Instances of vorticity pairing could be observed for the low free-stream turbulence case, however more research is required in this field to clarify the later stage instabilities leading to the breakdown.

The low-frequency flapping hardly observed at very low free-stream condition but more research is required to clarify this so that a much better understanding can be achieved.

Influence of free-stream turbulence on characteristics of the developing boundary layer downstream of the reattachment is an interesting aspect of the separated-reattached flow and needs to be investigated further.

Appendices

A. Spectra for NFST case

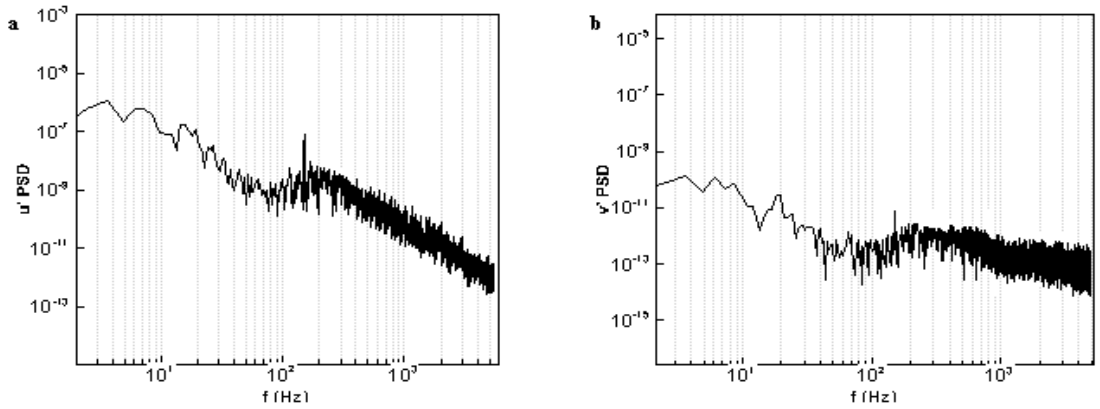

Fig.A.1. u', v' spectra at *x/D* = 1.15, *y/D* = 0.504, NFST case

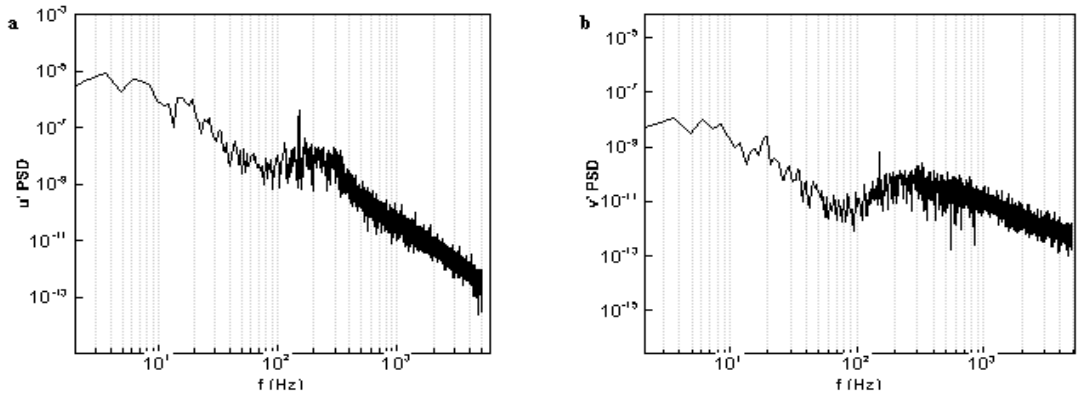

Fig.A.2. u', v' spectra at *x/D* = 1.15, *y/D* = 0.516, NFST case

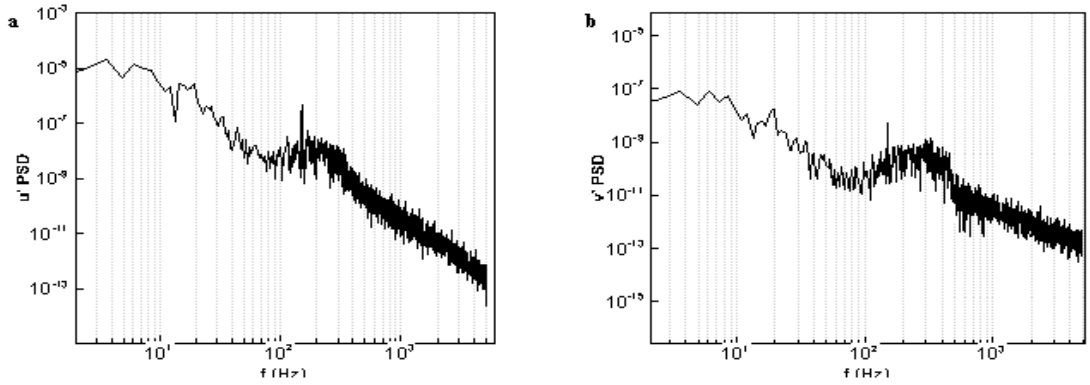

Fig.A.3. u', v' spectra at *x/D* = 1.15, *y/D* = 0.528, NFST case

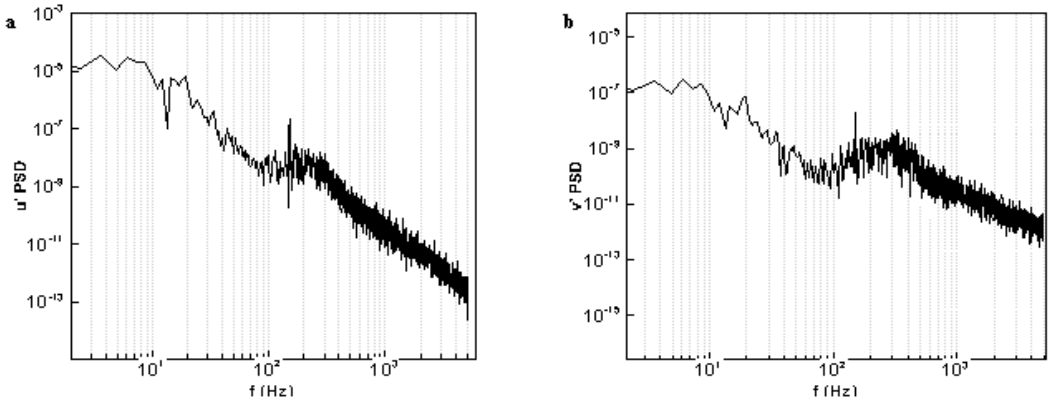

Fig.A.4. u', v' spectra at *x/D* = 1.15, *y/D* = 0.542, NFST case

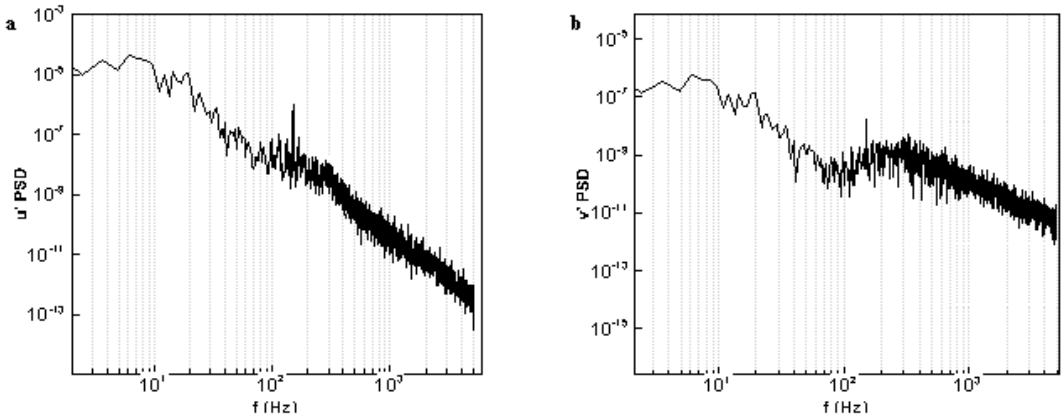

Fig.A.5. u', v' spectra at *x/D* = 1.15, *y/D* = 0.558, NFST case

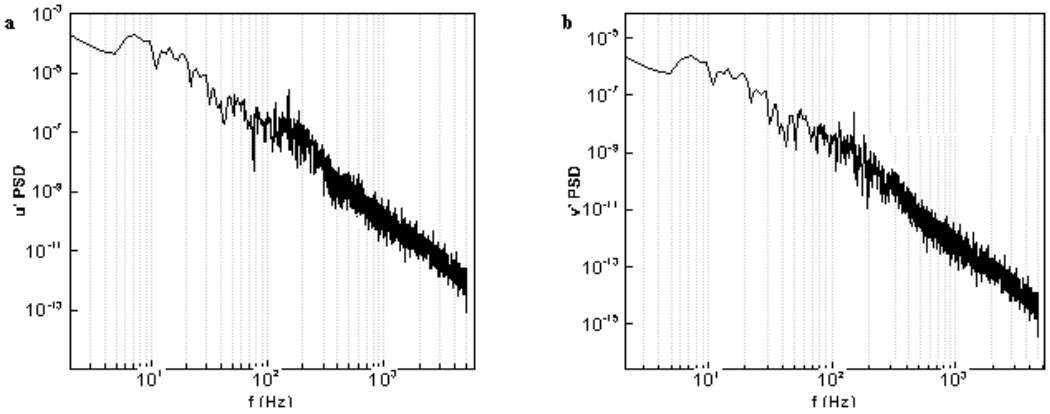

Fig.A.6. u', v' spectra at *x/D* = 1.15, *y/D* = 0.59, NFST case

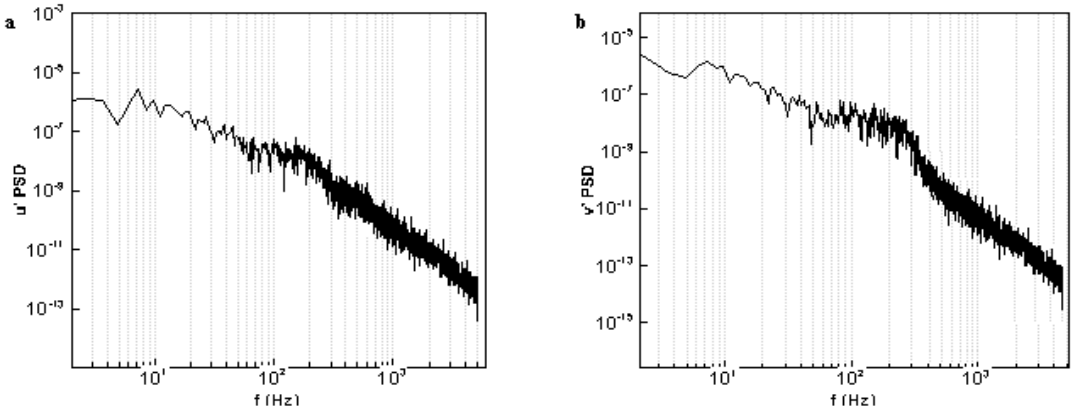

Fig.A.7. u', v' spectra at *x/D* = 1.15, *y/D* = 0.85, NFST case

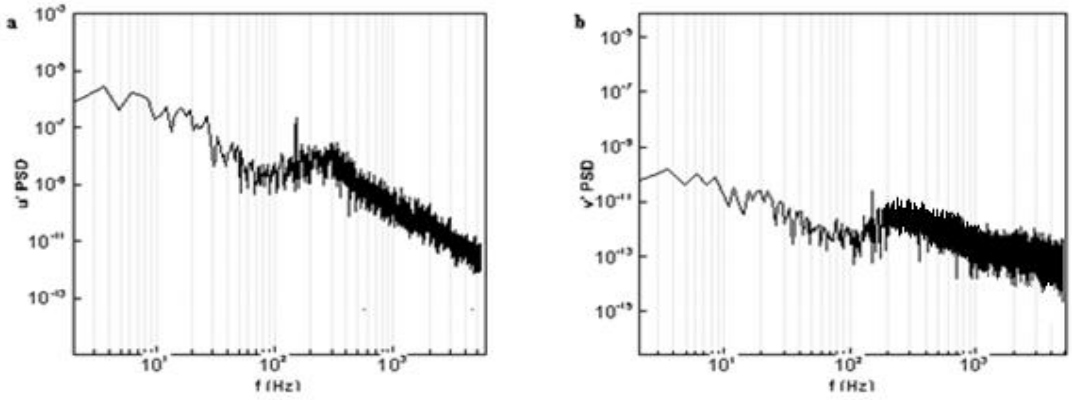

Fig.A.8. u', v' spectra at *x/D* = 1.46, *y/D* = 0.504, NFST case

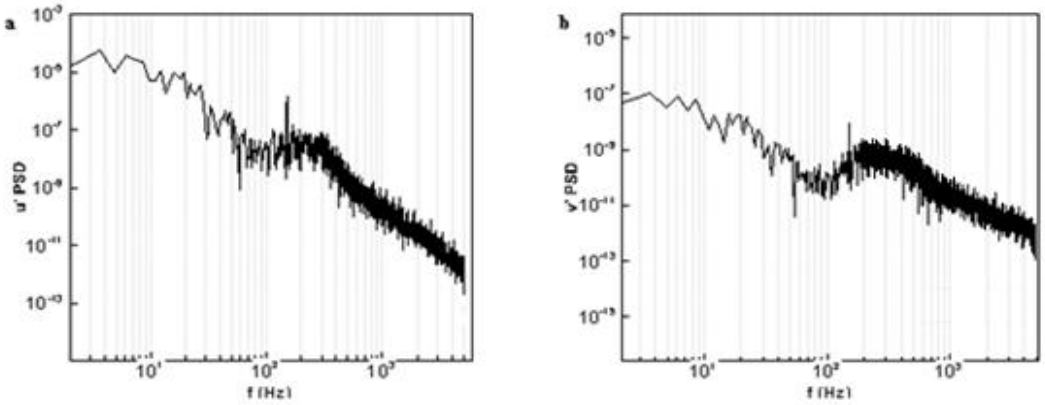

Fig.A.9. u', v' spectra at *x/D* = 1.46, *y/D* = 0.528, NFST case

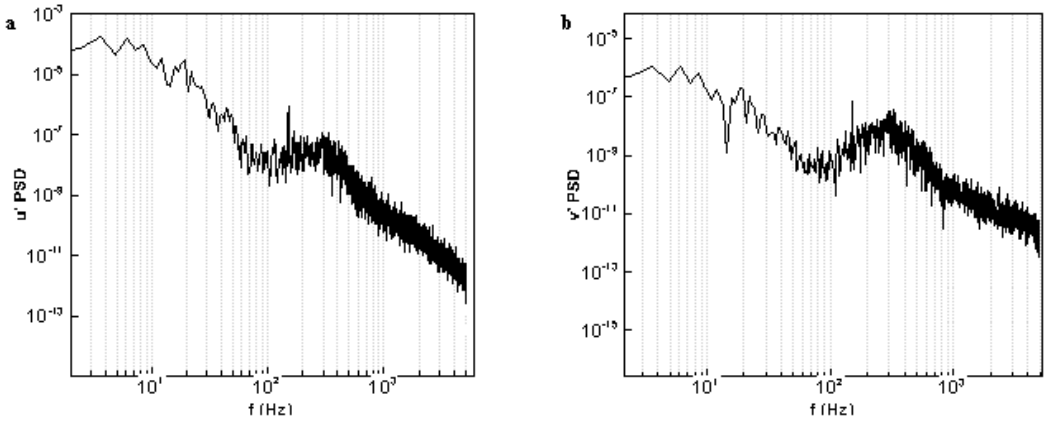

Fig.A.10. u', v' spectra at *x/D* = 1.46, *y/D* = 0.558, NFST case

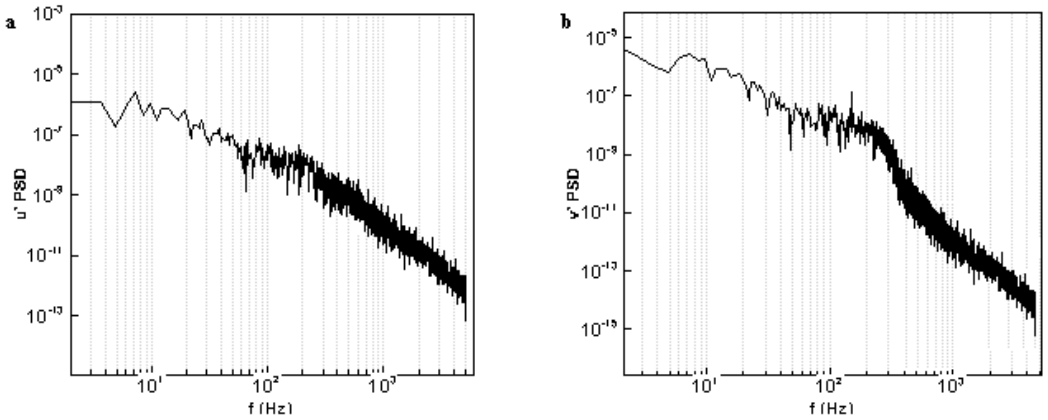

Fig.A.11. u', v' spectra at *x/D* = 1.46, *y/D* = 0.85, NFST case

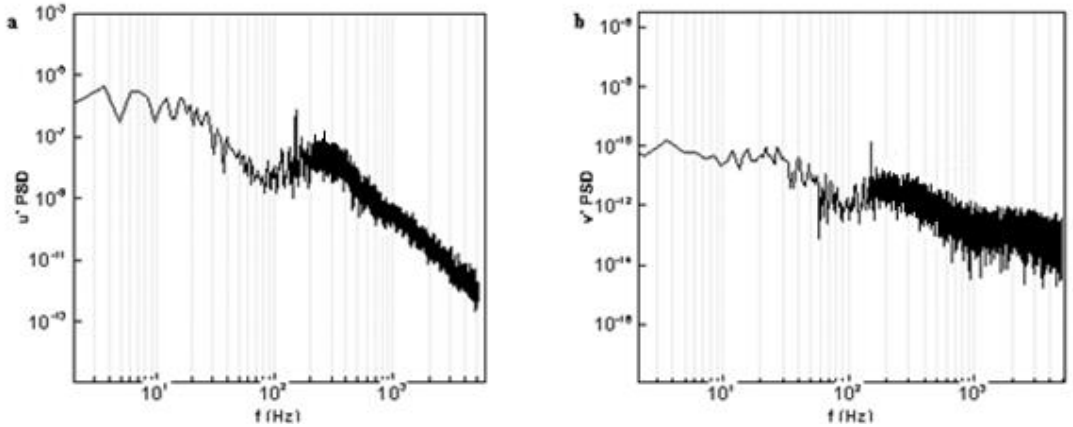

Fig.A.12. u', v' spectra at *x/D* = 1.72, *y/D* = 0.504, NFST case

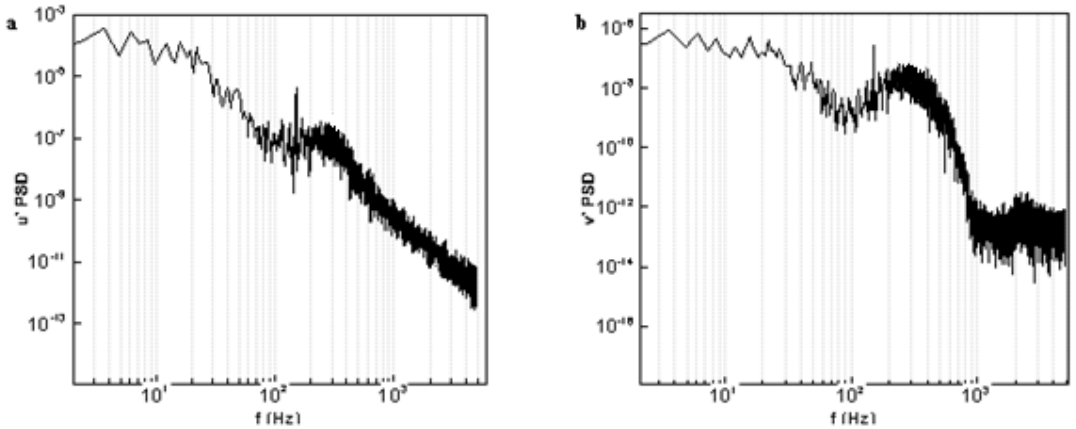

Fig.A.13. u', v' spectra at *x/D* = 1.72, *y/D* = 0.558, NFST case

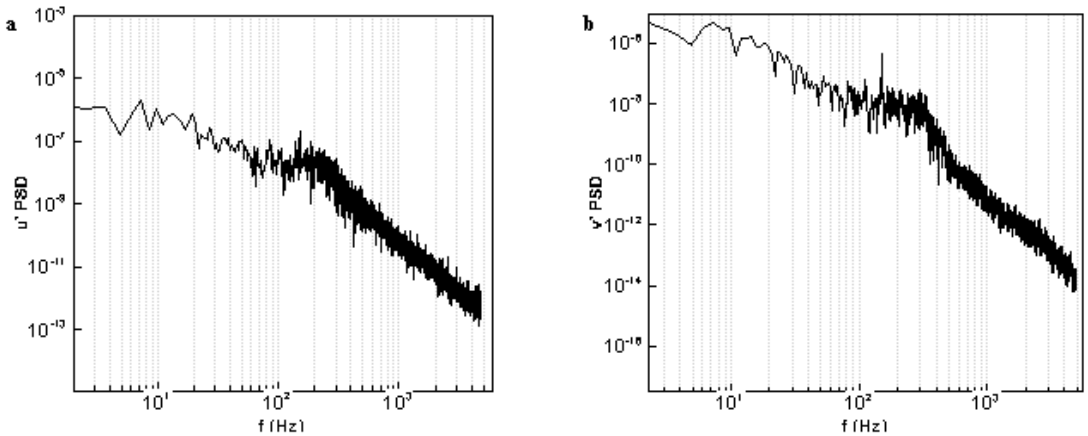

Fig.A.14. u', v' spectra at *x/D* = 1.72, *y/D* = 0.85, NFST case

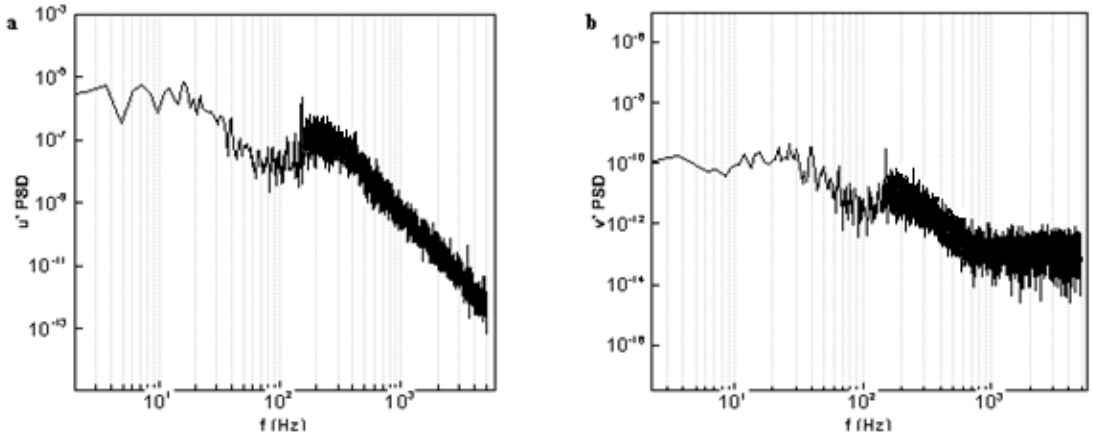

Fig.A.15. u', v' spectra at *x/D* = 1.94, *y/D* = 0.504, NFST case

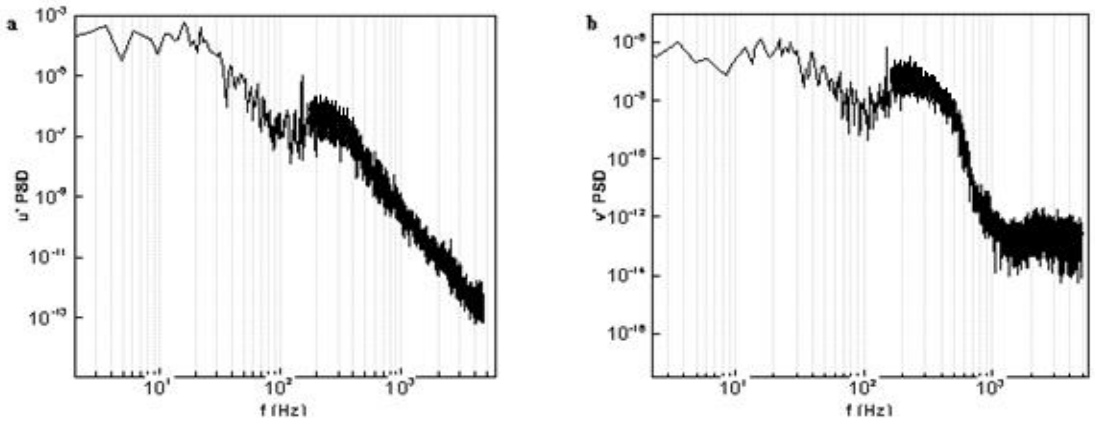

Fig.A.16. u', v' spectra at *x/D* = 1.94, *y/D* = 0.558, NFST case

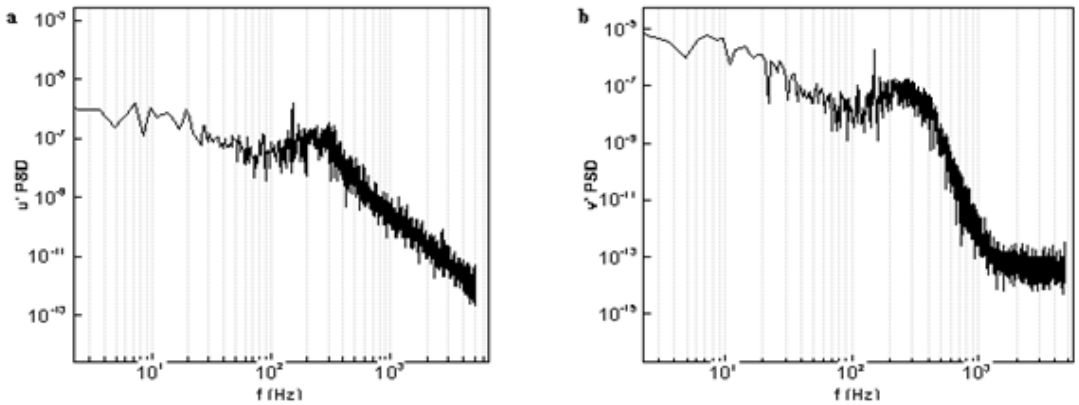

Fig.A.17. u', v' spectra at *x/D* = 1.94, *y/D* = 0.85, NFST case

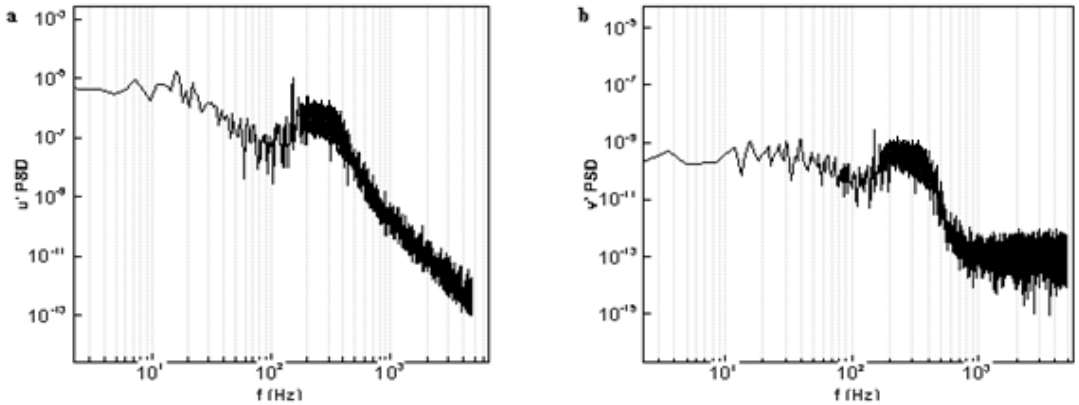

Fig.A.18. u', v' spectra at *x/D* = 2.19, *y/D* = 0.504, NFST case

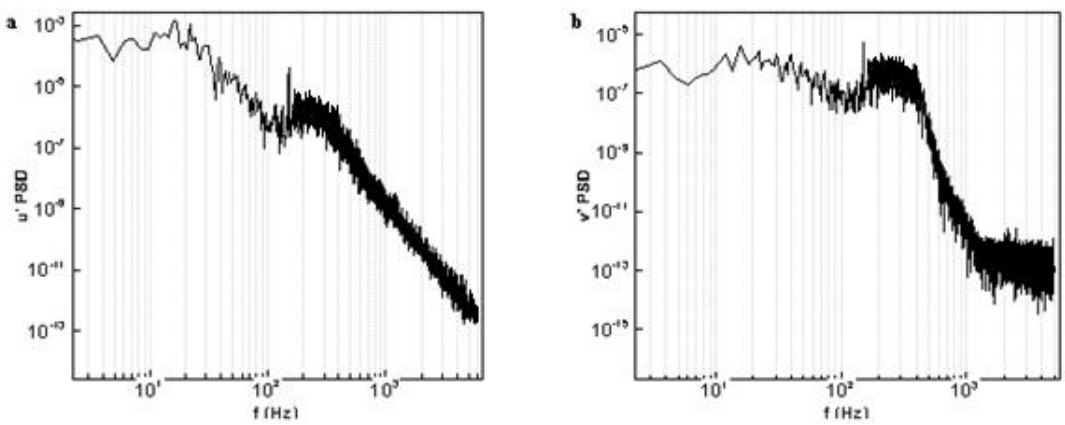

Fig.A.19. u', v' spectra at *x/D* = 2.19, *y/D* = 0.558, NFST case

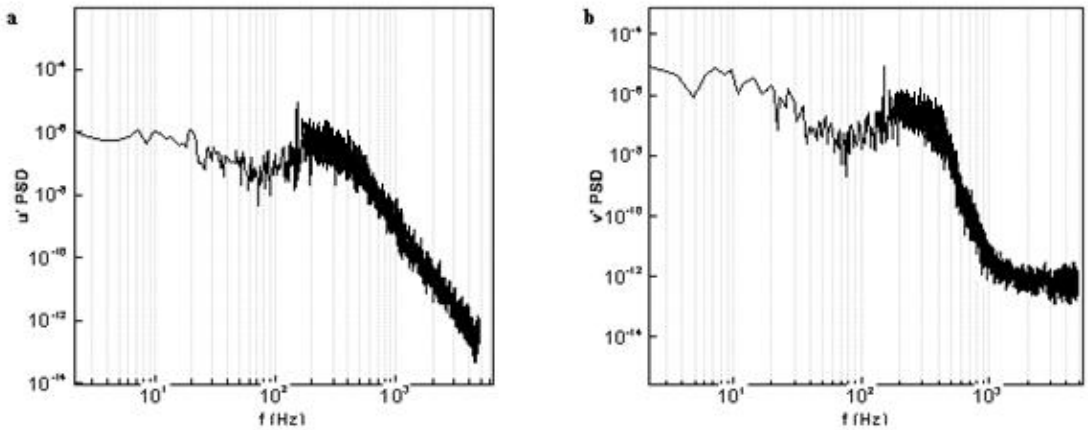

Fig.A.20. u', v' spectra at *x/D* = 2.19, *y/D* = 0.85, NFST case

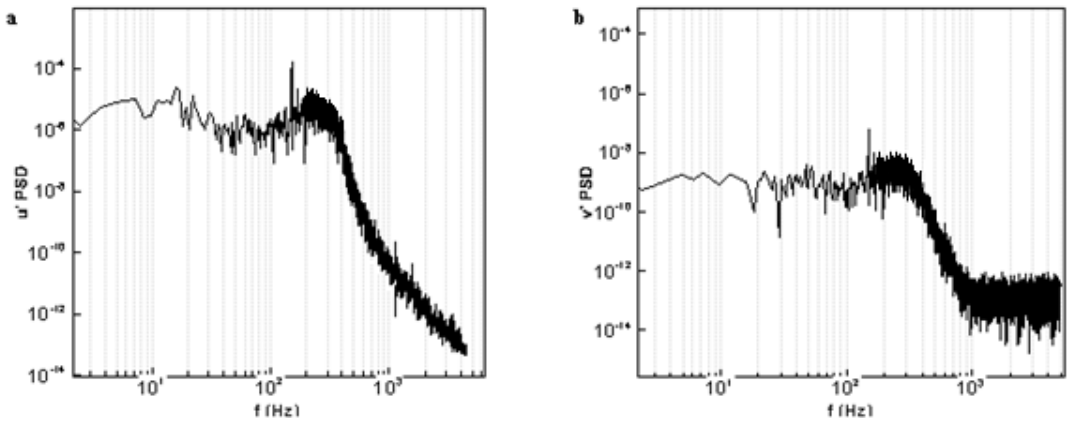

Fig.A.21. u', v' spectra at *x/D* = 2.51, *y/D* = 0.504, NFST case

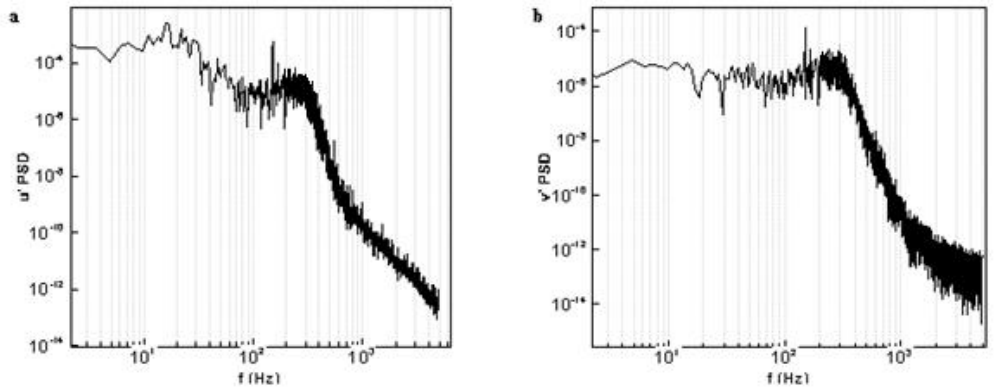

Fig.A.22. u', v' spectra at *x/D* = 2.51, *y/D* = 0.558, NFST case

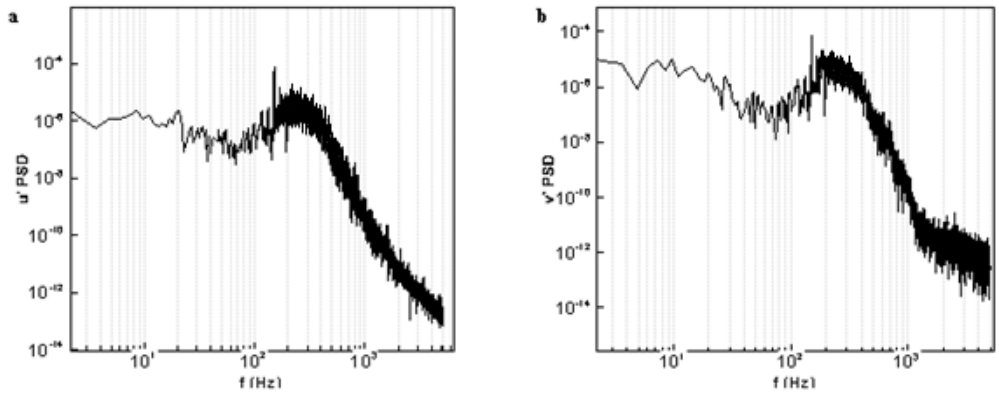

Fig.A.23. u', v' spectra at *x/D* = 2.51, *y/D* = 0.85, NFST case

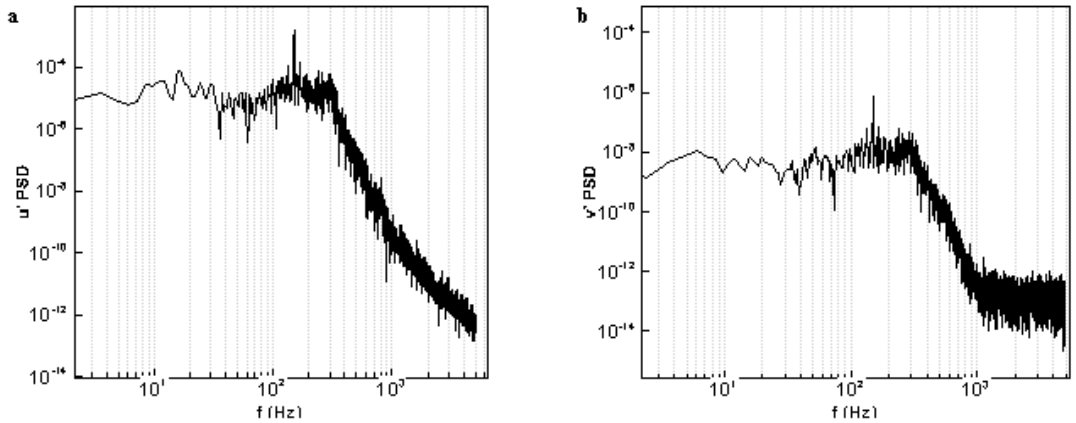

Fig.A.24. u', v' spectra at *x/D* = 2.87, *y/D* = 0.504, NFST case

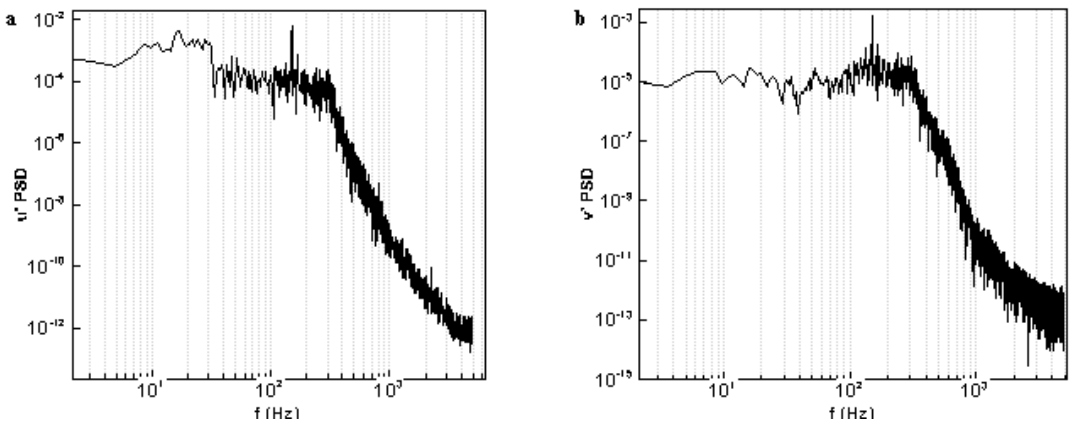

Fig.A.25. u', v' spectra at *x/D* = 2.87, *y/D* = 0.558, NFST case

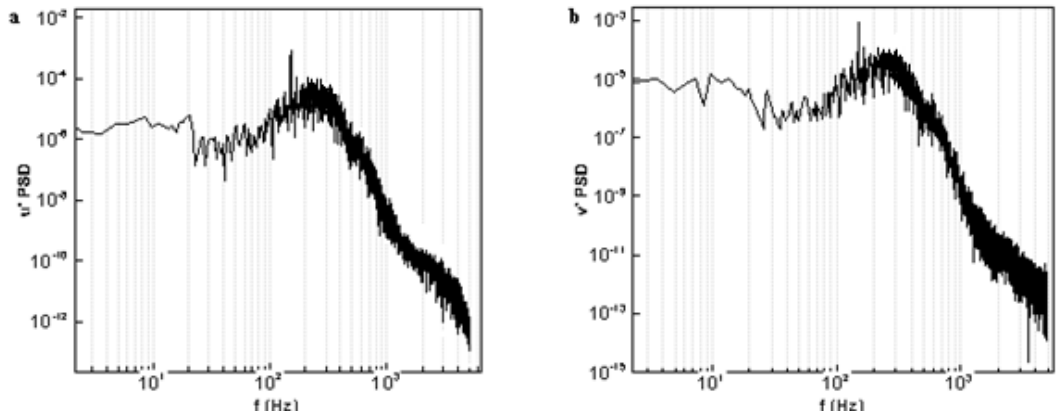

Fig.A.26. u', v' spectra at *x/D* = 2.87, *y/D* = 0.85, NFST case

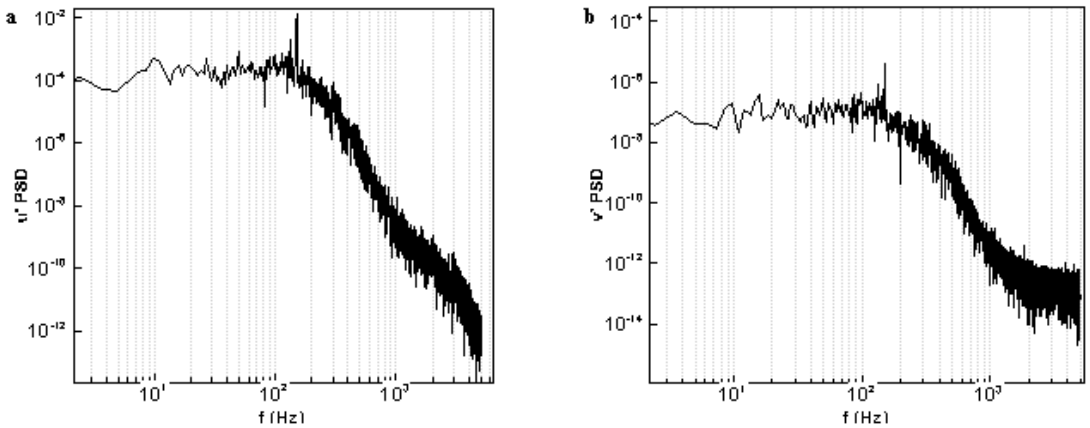

Fig.A.27. u', v' spectra at *x/D* = 3.28, *y/D* = 0. 504, NFST case

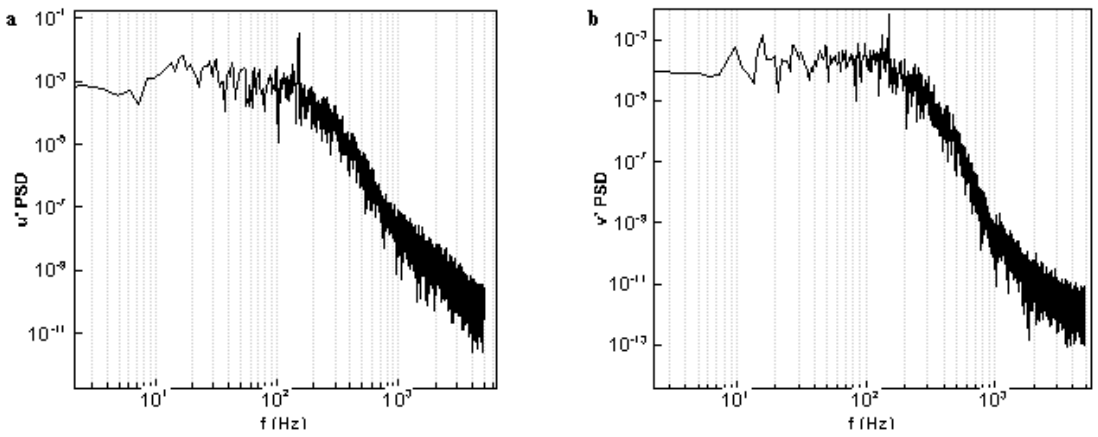

Fig.A.28. u', v' spectra at *x/D* = 3.28, *y/D* = 0. 558, NFST case

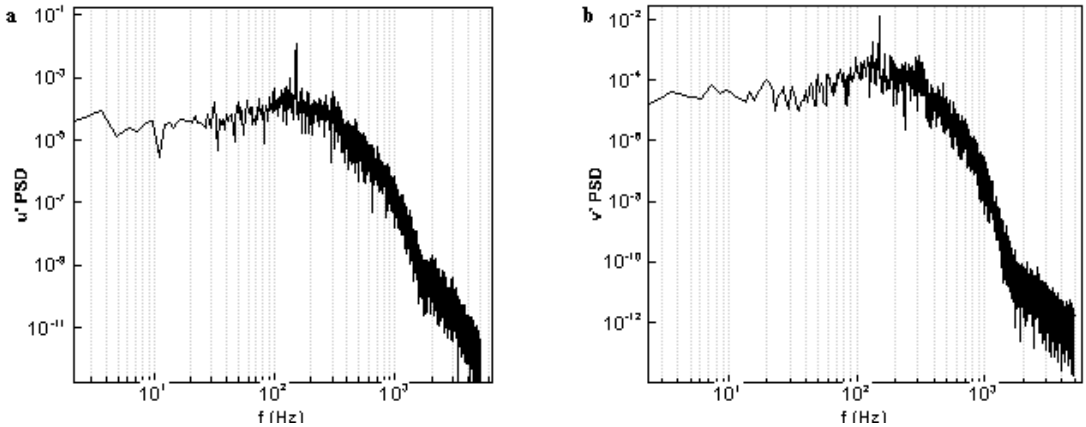

Fig.A.29. u', v' spectra at *x/D* = 3.28, *y/D* = 0. 85, NFST case

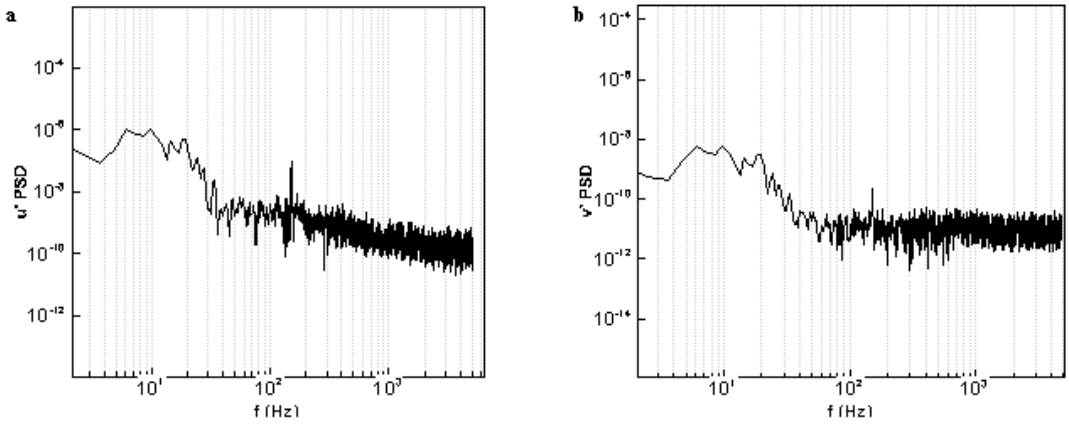

Fig.A.30. u', v' spectra at *x/D* = 0.86, *y/D* = 0. 516 and spanwise plane *z*/D = 2.0 , NFST case

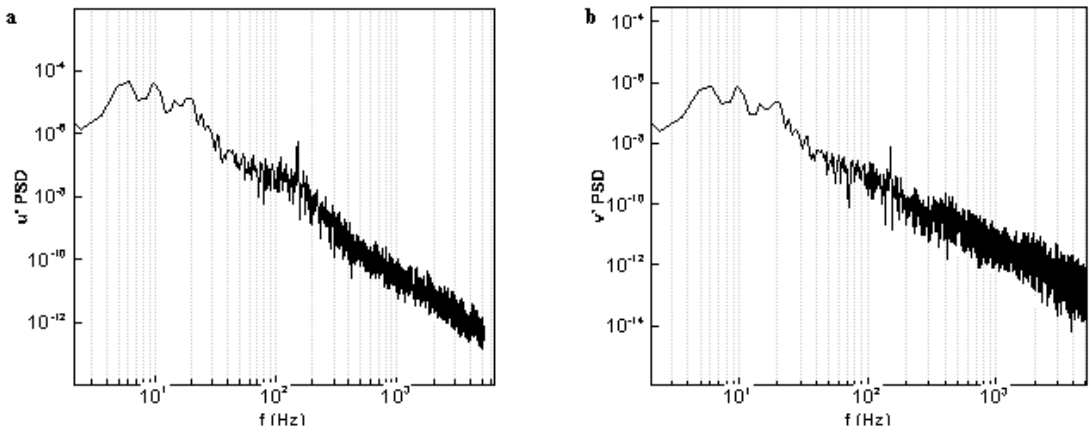

Fig.A.31. u', v' spectra at *x/D* = 0.86, *y/D* = 0. 542 and spanwise plane *z*/D = 2.0 , NFST case

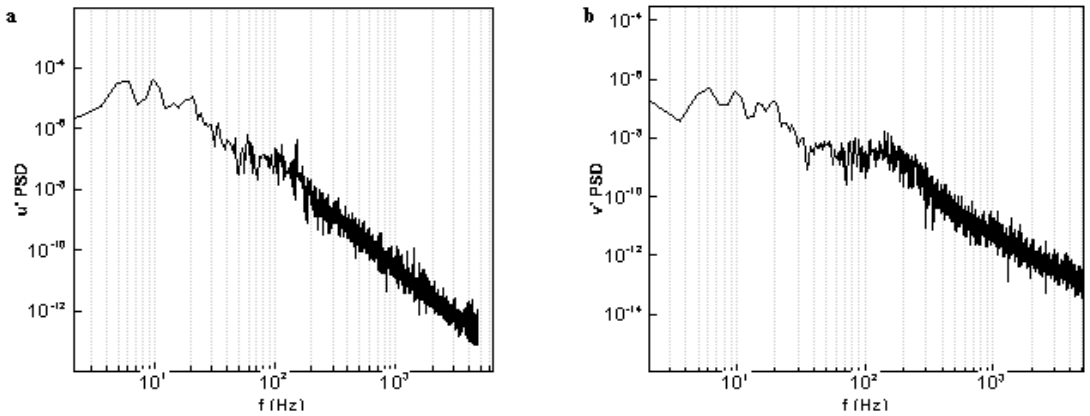

Fig.A.32. u', v' spectra at *x/D* = 0.86, *y/D* = 0. 59 and spanwise plane *z*/D = 2.0 , NFST case

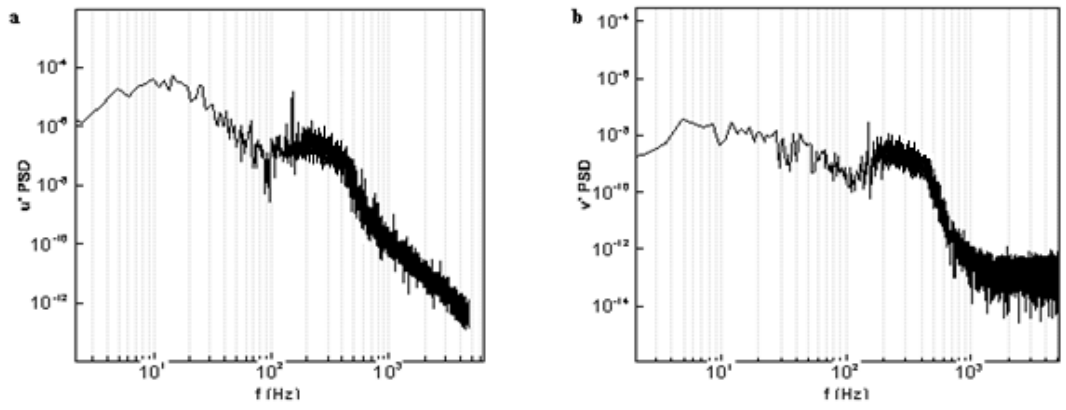

Fig.A.33. u', v' spectra at *x/D* = 1.94, *y/D* = 0. 516 and spanwise plane *z*/D = 2.0, NFST case

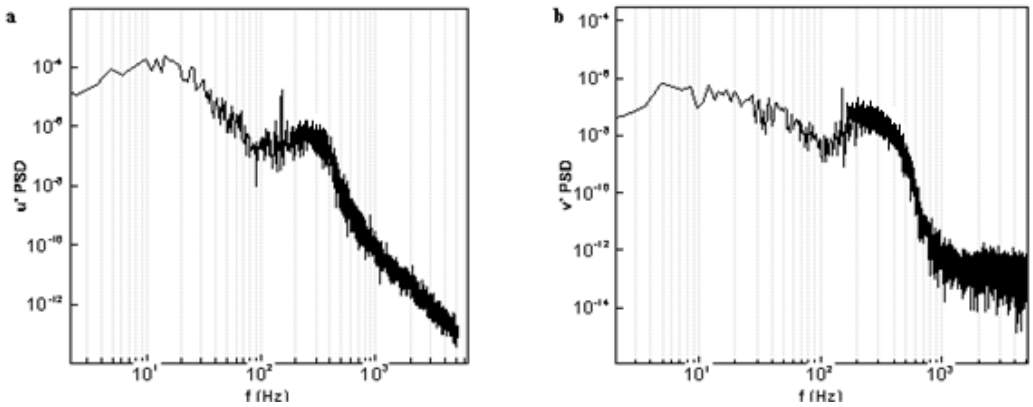

Fig.A.34. u', v' spectra at *x/D* = 1.94, *y/D* = 0. 542 and spanwise plane *z*/D = 2.0, NFST case

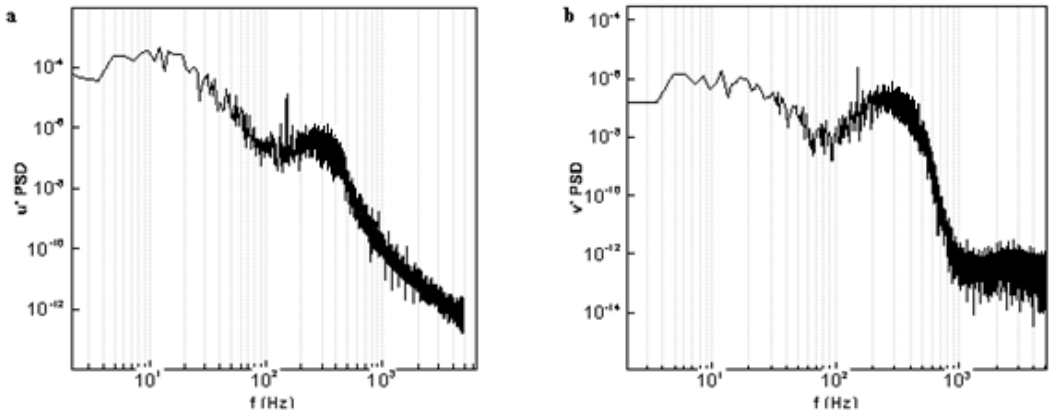

Fig.A.35. u', v' spectra at *x/D* = 1.94, *y/D* = 0. 59 and spanwise plane *z*/D = 2.0, NFST case

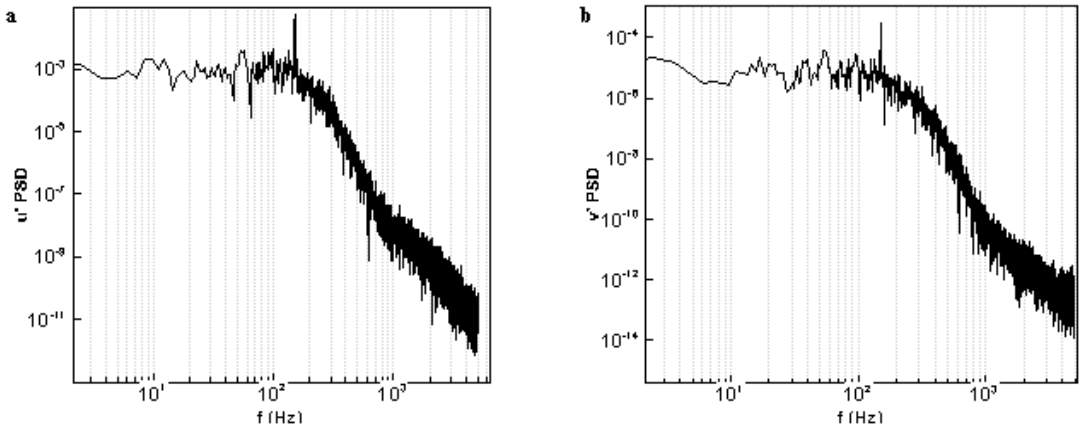

Fig.A.36. u', v' spectra at *x/D* = 3.28, *y/D* = 0. 516 and spanwise plane *z*/D = 2.0, NFST case

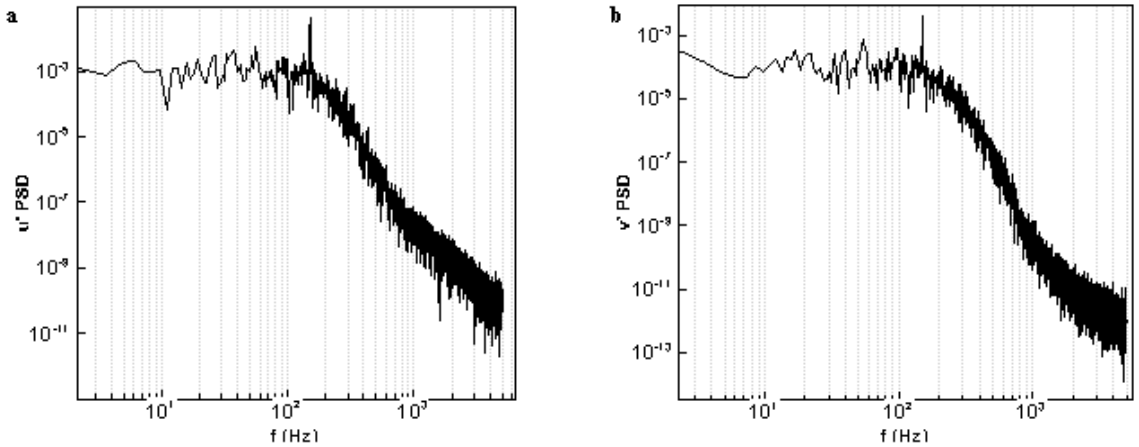

Fig.A.37. u', v' spectra at *x/D* = 3.28, *y/D* = 0. 542 and spanwise plane z/D = 2.0 , NFST case

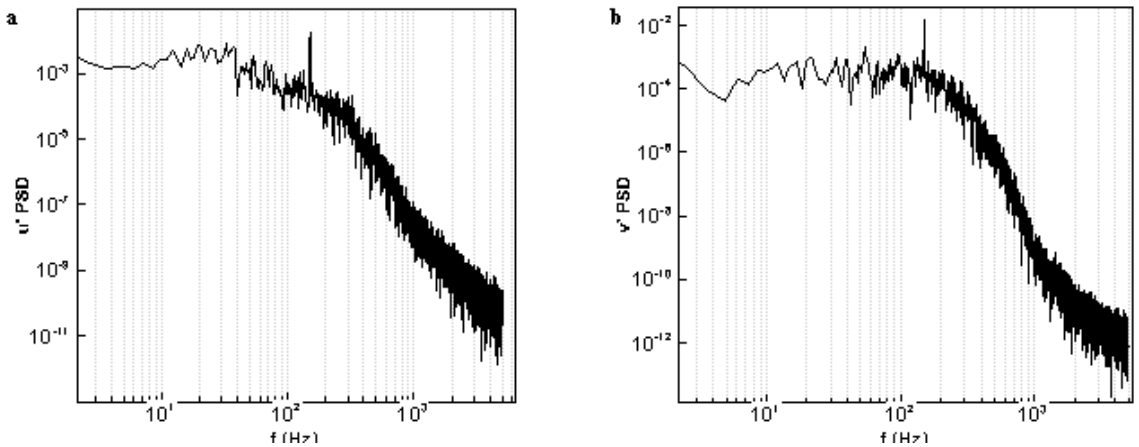

Fig.A.38. u', v' spectra at *x/D* = 3.28, *y/D* = 0. 59 and spanwise plane z/D = 2.0 , NFST case

B. Spectra for FST case

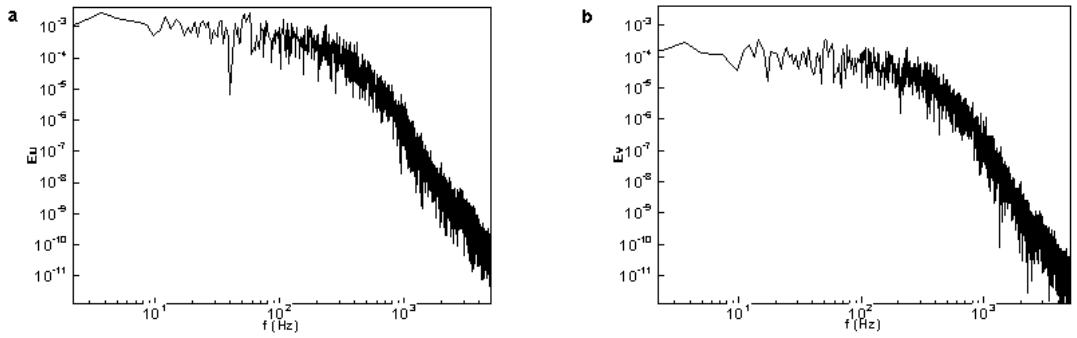

Fig.B.1. spectra at *x/D* = 0.33, *y/D* = 0.516. (a) u', (b) v'. (FST case)

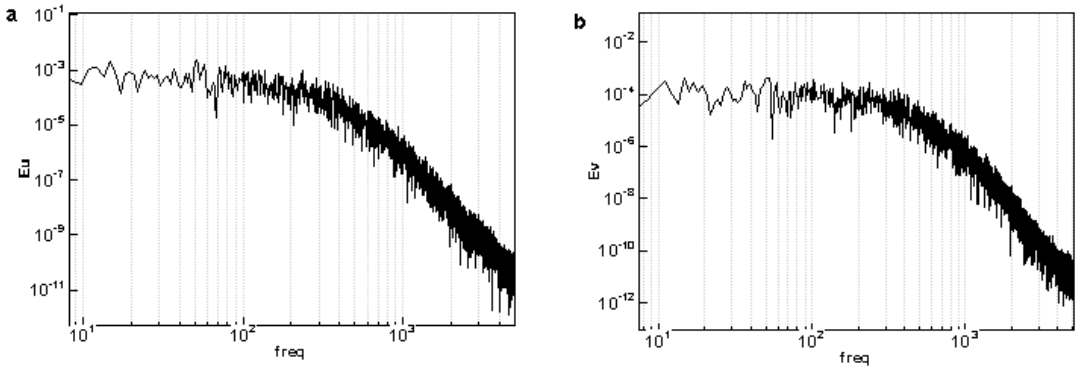

Fig.B.2. spectra at *x/D* = 0.33, *y/D* = 0.528. (a) u', (b) v'. (FST case)

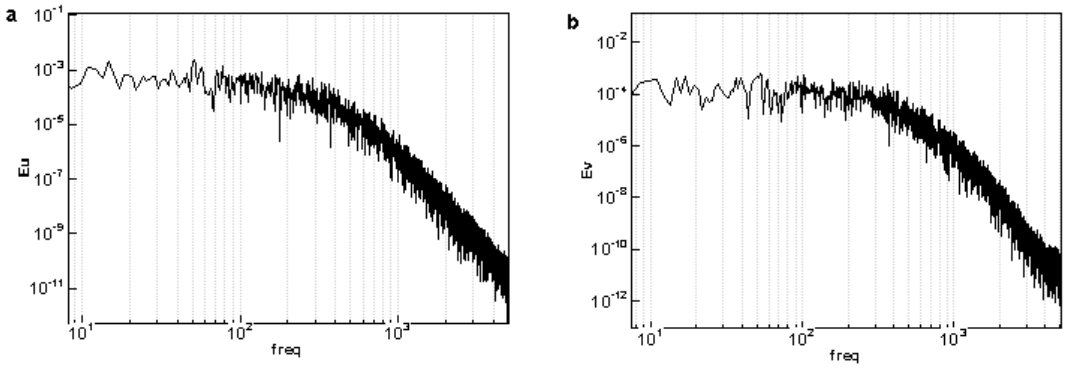

Fig.B.3. spectra at *x/D* = 0.33, *y/D* = 0.542. (a) u', (b) v'. (FST case)

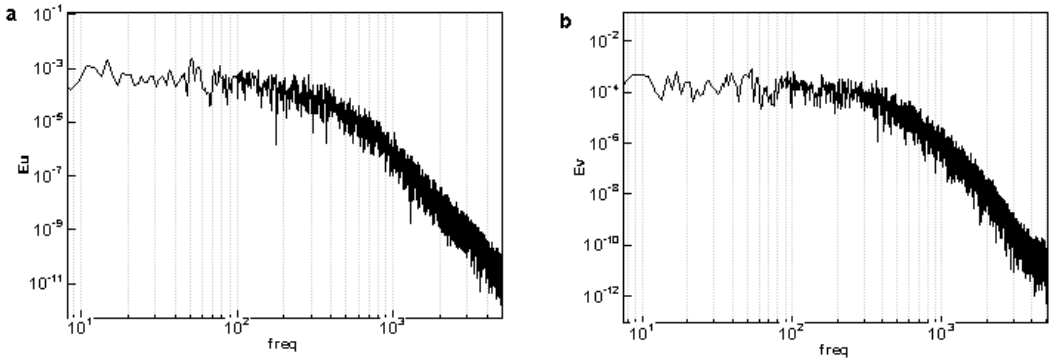

Fig.B.4. spectra at *x/D* = 0.33, *y/D* = 0.558. (a) u', (b) v'. (FST case)

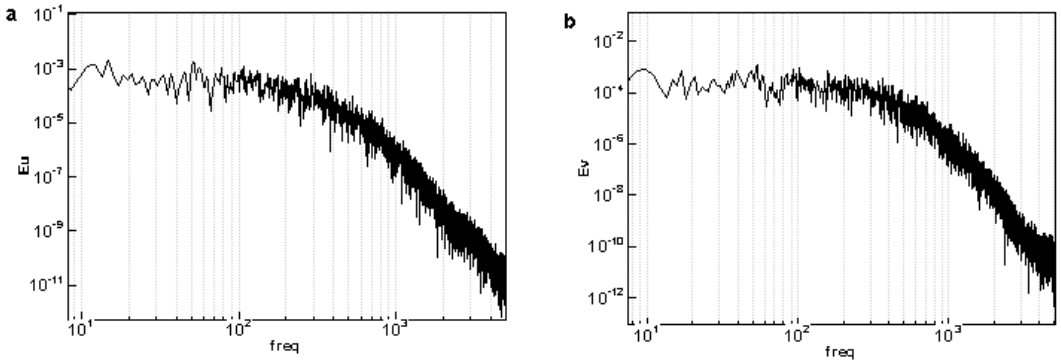

Fig.B.5. spectra at *x/D* = 0.33, *y/D* = 0.59. (a) u', (b) v'. (FST case)

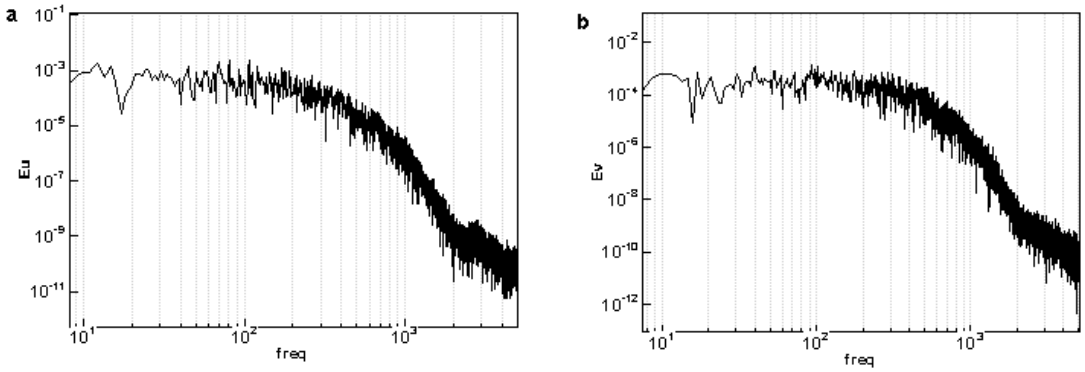

Fig.B.6. spectra at *x/D* = 0.33, *y/D* = 0.85 (Free stream) (a) u', (b) v' (FST case)

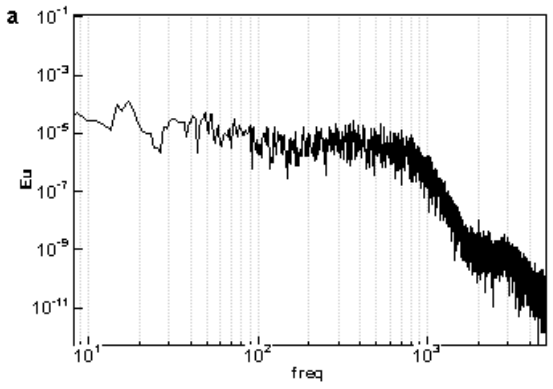

Fig.B.7. u' spectra at *x/D* = 0.65, *y/D* = 0.504. (FST case)

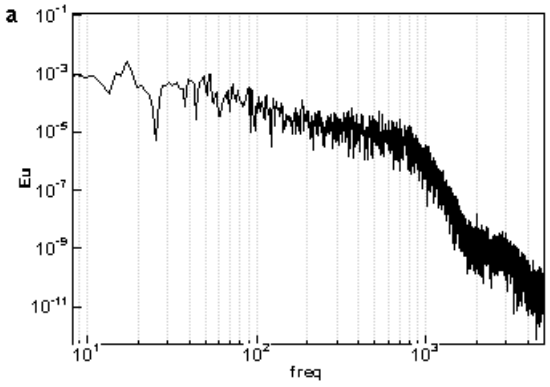

Fig.B.8. spectra at *x/D* = 0.65, *y/D* = 0.516. (FST case)

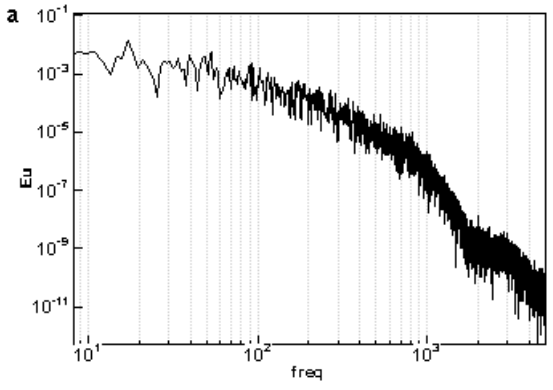

Fig.B.9. spectra at *x/D* = 0.65, *y/D* = 0.528. (FST case)

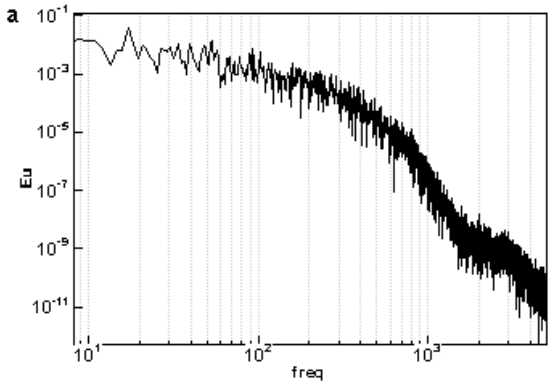

Fig.B.10. spectra at *x/D* = 0.65, *y/D* = 0.542. (FST case)

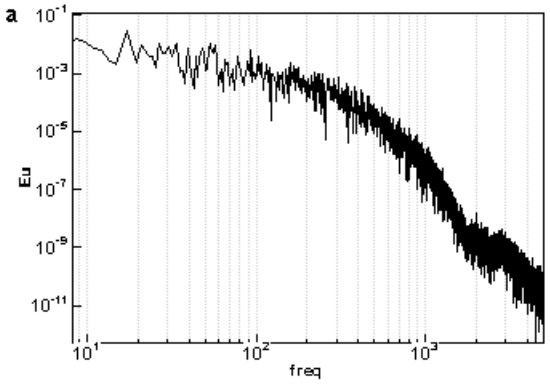

Fig.B.11. spectra at *x/D* = 0.65, *y/D* = 0.558. (FST case)

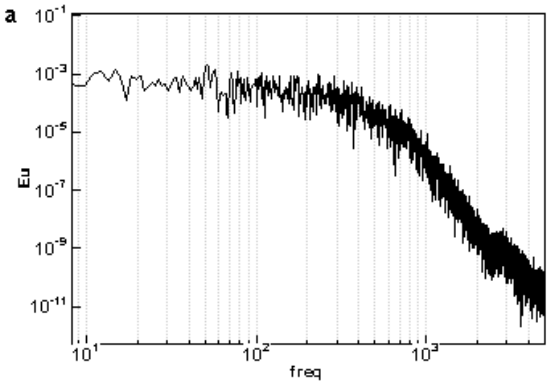

Fig.B.12. spectra at *x/D* = 0.65, *y/D* = 0.59. (FST case)

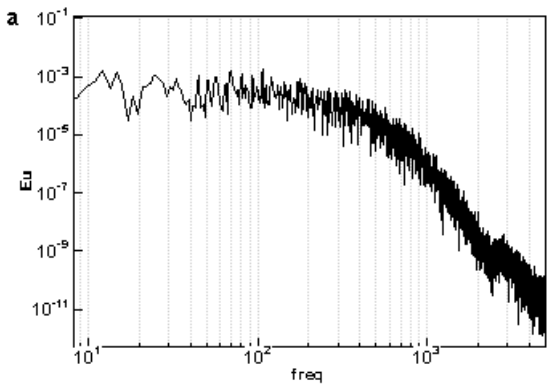

Fig.B.13. spectra at *x/D* = 0.65, *y/D* = 0.85. (FST case)

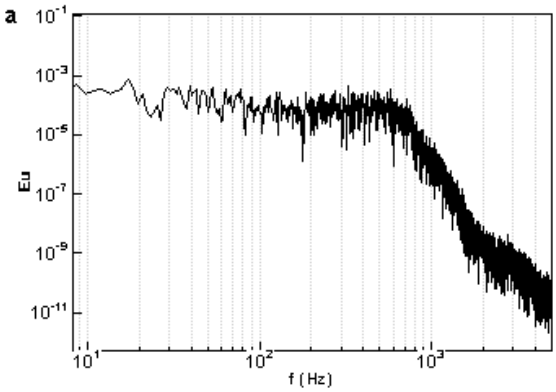

Fig.B.14. spectra at *x/D* = 1.03, *y/D* = 0.504. (FST case)

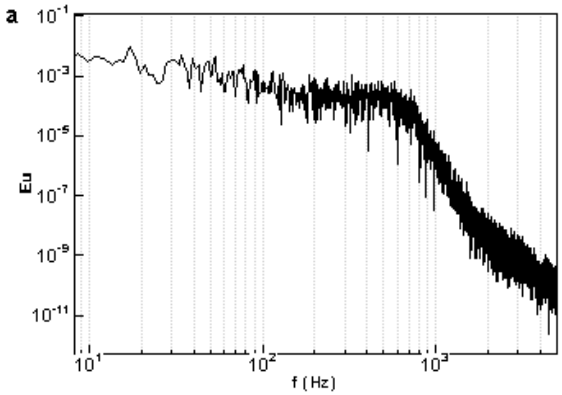

Fig.B.15. spectra at *x/D* = 1.03, *y/D* = 0.516. (FST case)

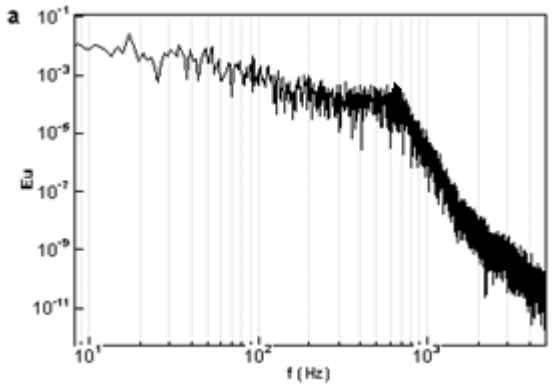

Fig.B.16. spectra at *x/D* = 1.03, *y/D* = 0.528. (FST case)

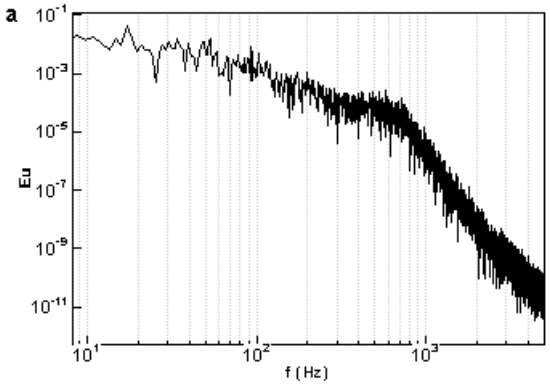

Fig.B.17. spectra at *x/D* = 1.03, *y/D* = 0.542. (FST case)

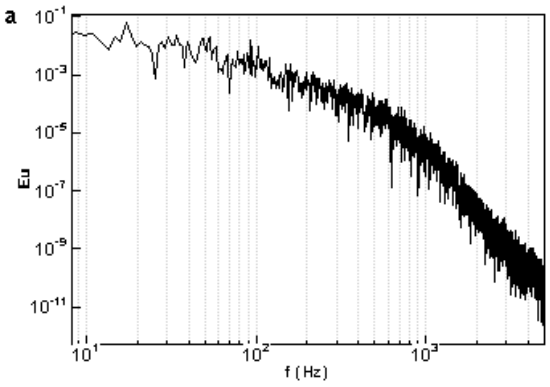

Fig.B.18. spectra at *x/D* = 1.03, *y/D* = 0.558. (FST case)

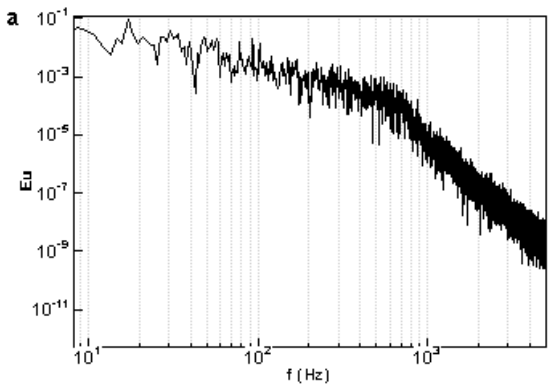

Fig.B.19. spectra at *x/D* = 1.03, *y/D* = 0.59. (FST case)

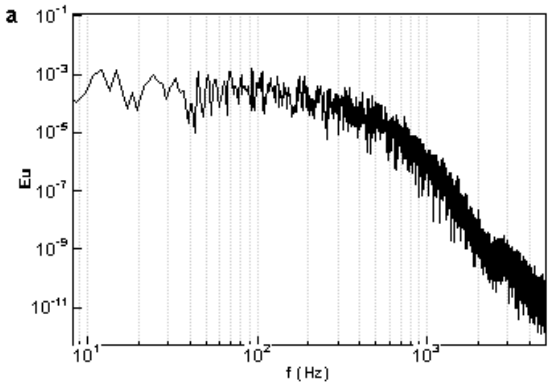

Fig.B.20. spectra at *x/D* = 1.03, *y/D* = 0.85. (FST case)

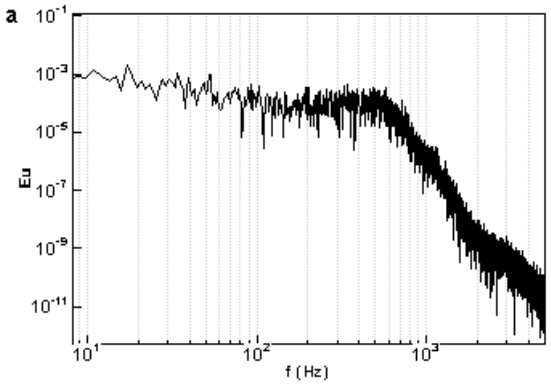

Fig.B.21. spectra at *x/D* = 1.23, *y/D* = 0.504. (FST case)

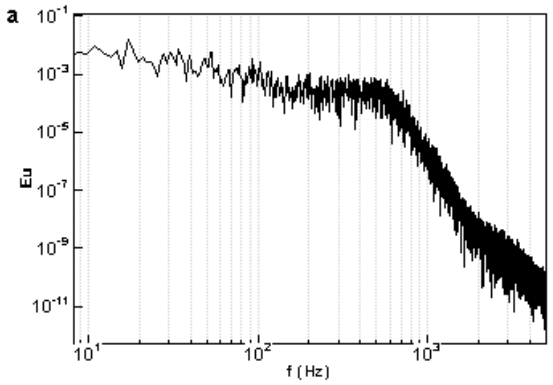

Fig.B.22. spectra at *x/D* = 1.23, *y/D* = 0.516. (FST case)

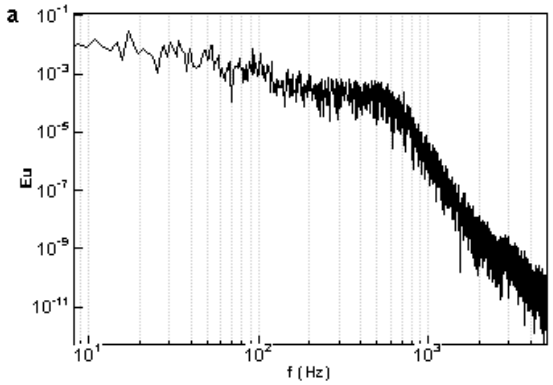

Fig.B.23. spectra at *x/D* = 1.23, *y/D* = 0.528. (FST case)

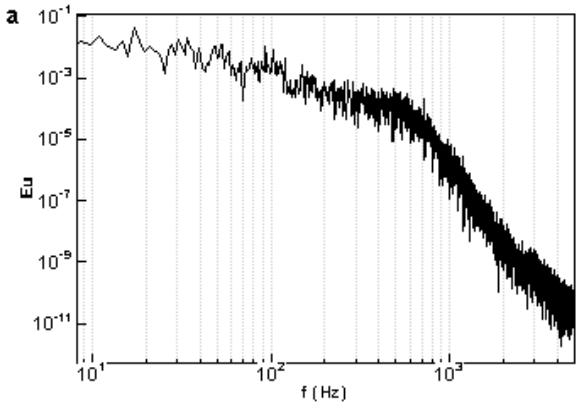

Fig.B.24. spectra at *x/D* = 1.23, *y/D* = 0.542. (FST case)

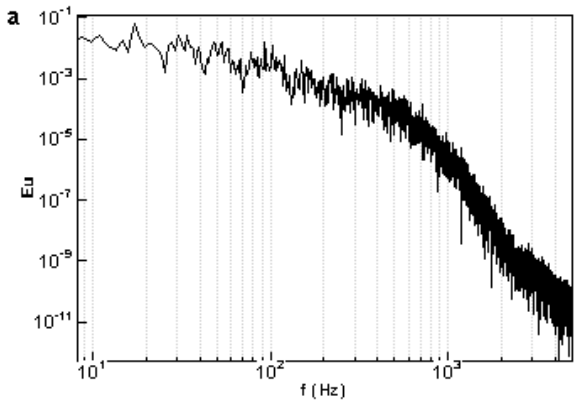

Fig.B.25. spectra at *x/D* = 1.23, *y/D* = 0.558. (FST case)

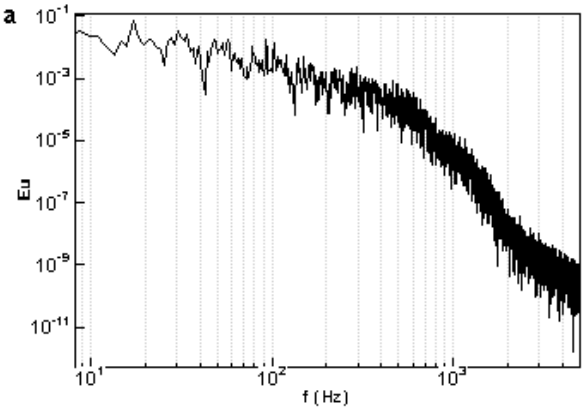

Fig.B.26. spectra at *x/D* = 1.23, *y/D* = 0.59. (FST case)

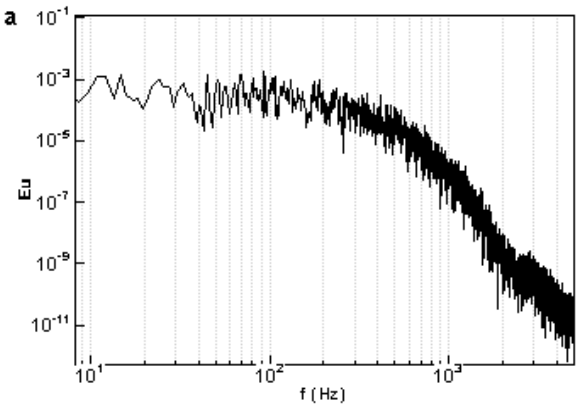

Fig.B.27. spectra at *x/D* = 1.23, *y/D* = 0.85. (FST case)

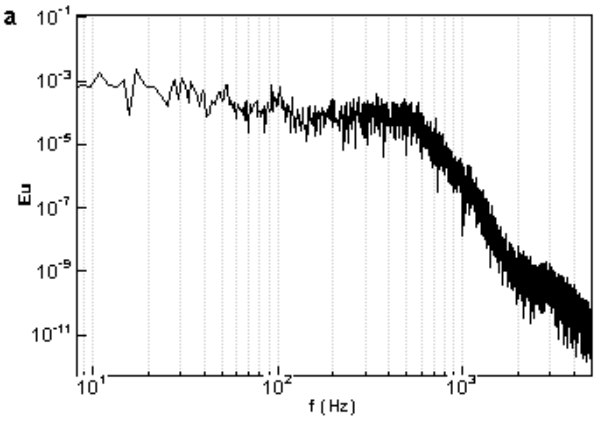

Fig.B.28. spectra at *x/D* = 1.45, *y/D* = 0.504. (FST case)

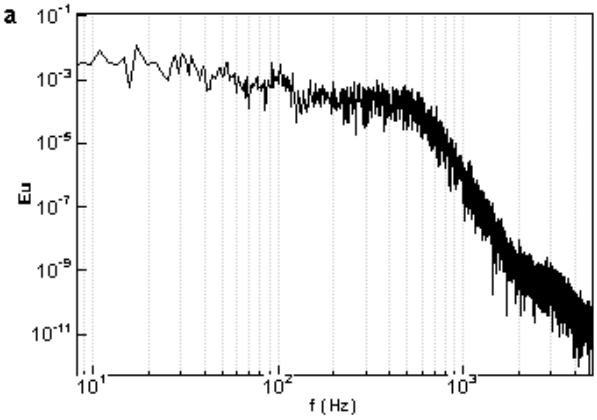

Fig.B.29. spectra at *x/D* = 1.45, *y/D* = 0.516. (FST case)

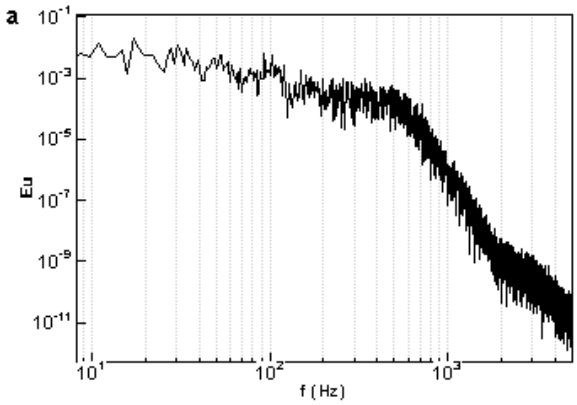

Fig.B.30. spectra at *x/D* = 1.45, *y/D* = 0.528. (FST case)

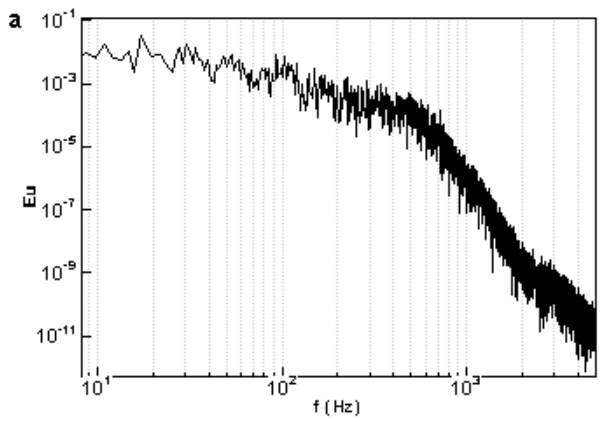

Fig.B.31. spectra at *x/D* = 1.45, *y/D* = 0.542. (FST case)

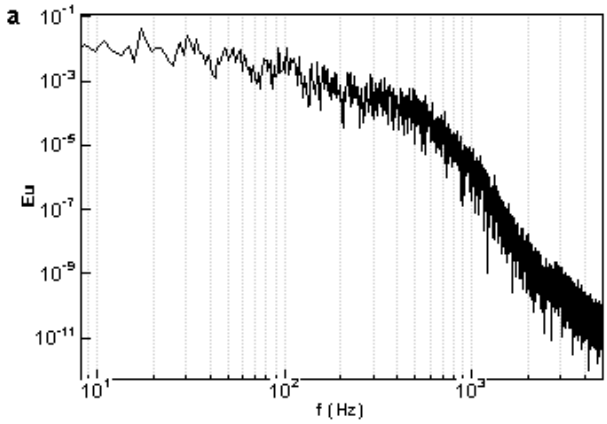

Fig.B.32. spectra at *x/D* = 1.45, *y/D* = 0.558. (FST case)

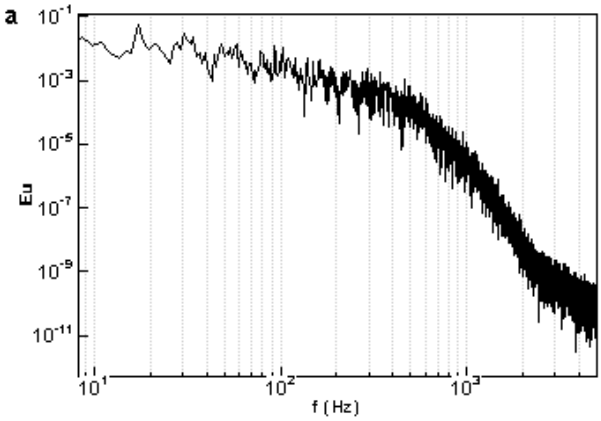

Fig.B.33. spectra at *x/D* = 1.45, *y/D* = 0.59. (FST case)

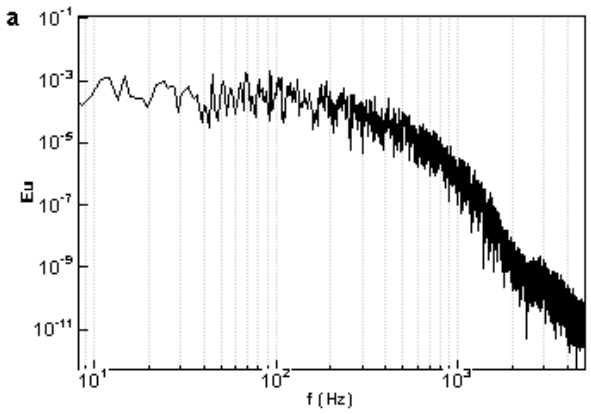

Fig.B.34. spectra at *x/D* = 1.45, *y/D* = 0.85. (FST case)

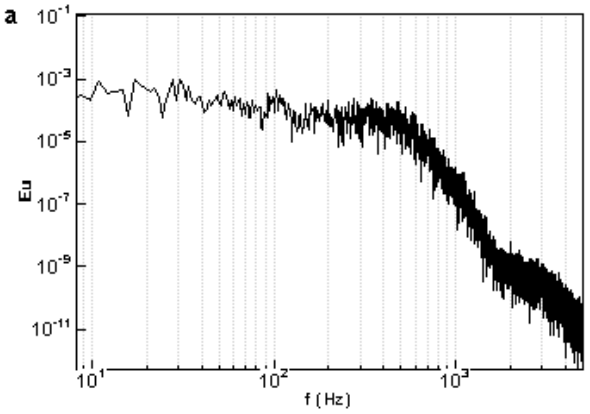

Fig.B.35. spectra at *x/D* = 1.68, *y/D* = 0.504. (FST case)

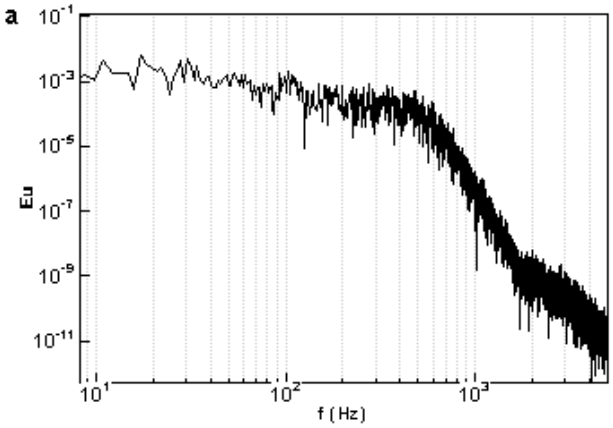

Fig.B.36. spectra at *x/D* = 1.68, *y/D* = 0.516. (FST case)

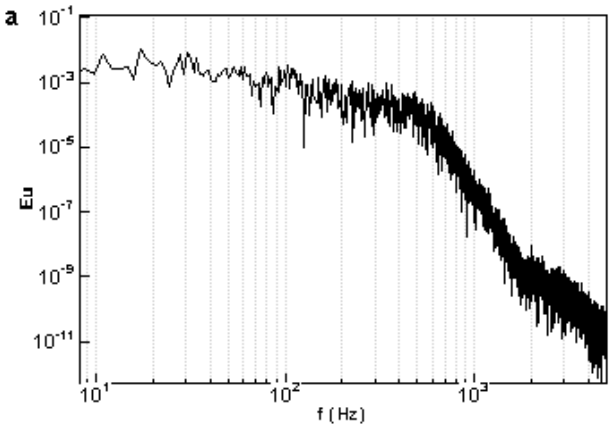

Fig.B.37. spectra at *x/D* = 1.68, *y/D* = 0.528. (FST case)

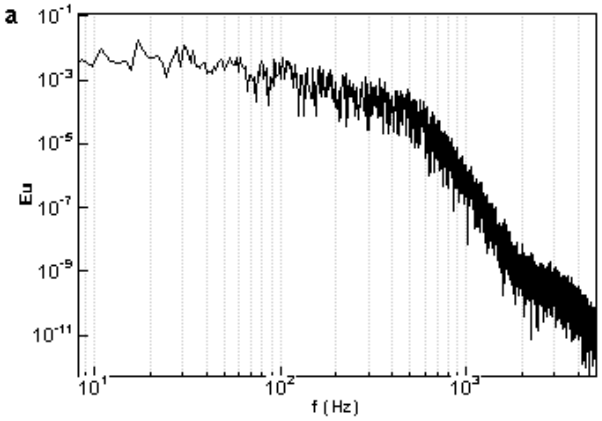

Fig.B.38. spectra at *x/D* = 1.68, *y/D* = 0.542. (FST case)

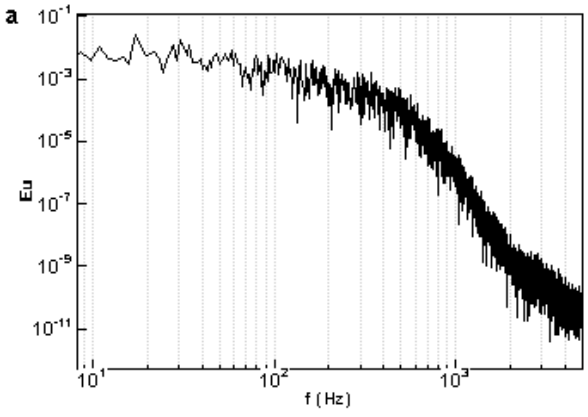

Fig.B.39. spectra at *x/D* = 1.68, *y/D* = 0.558. (FST case)

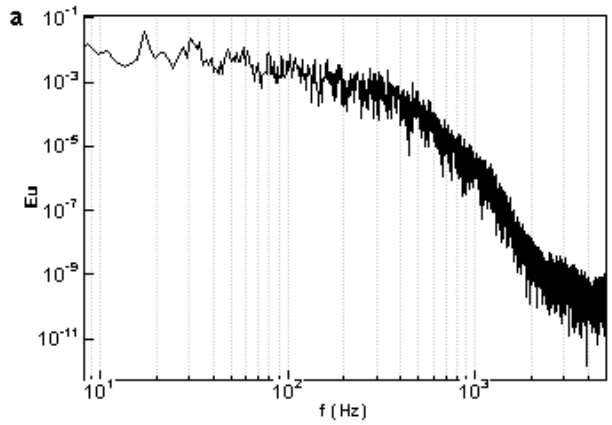

Fig.B.40. spectra at *x/D* = 1.68, *y/D* = 0.59. (FST case)

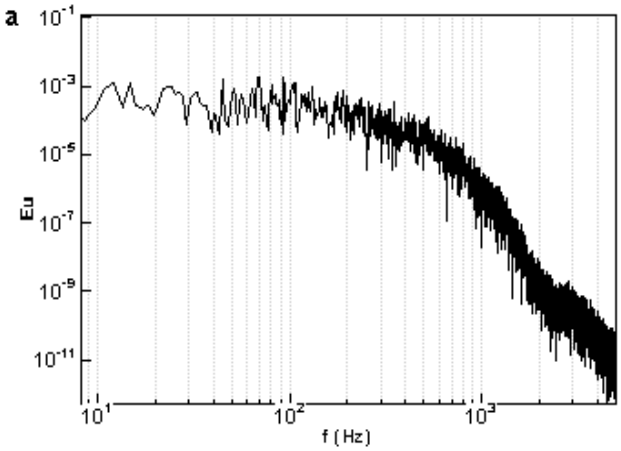

Fig.B.41. spectra at *x/D* = 1.68, *y/D* = 0.85. (FST case)

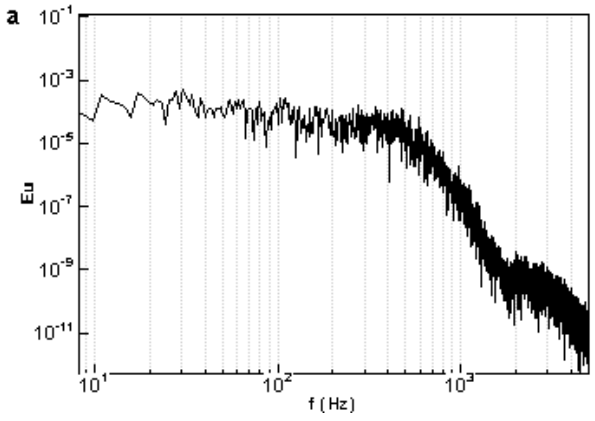

Fig.B.42. spectra at *x/D* = 1.93, *y/D* = 0.504. (FST case)

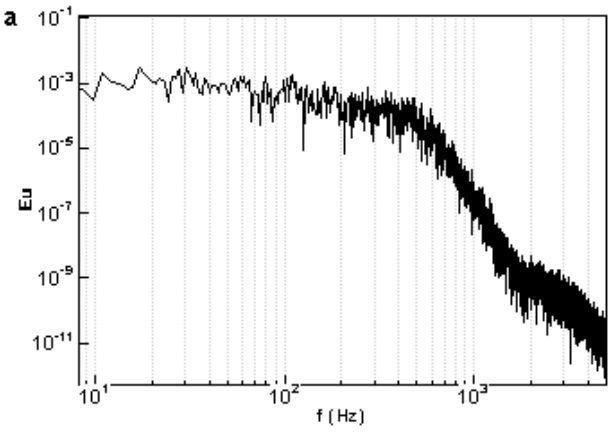

Fig.B.43. spectra at *x/D* = 1.93, *y/D* = 0.516. (FST case)

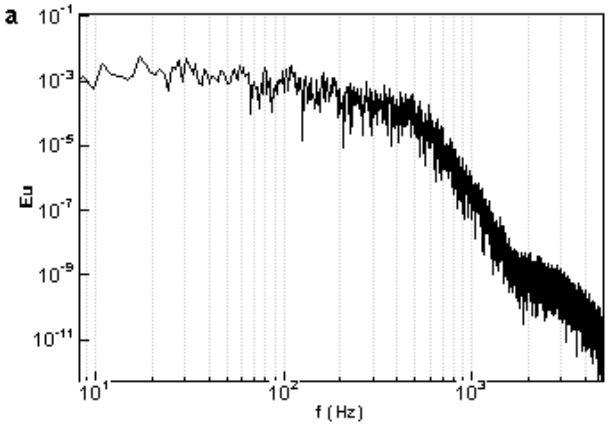

Fig.B.44. spectra at *x/D* = 1.93, *y/D* = 0.528. (FST case)

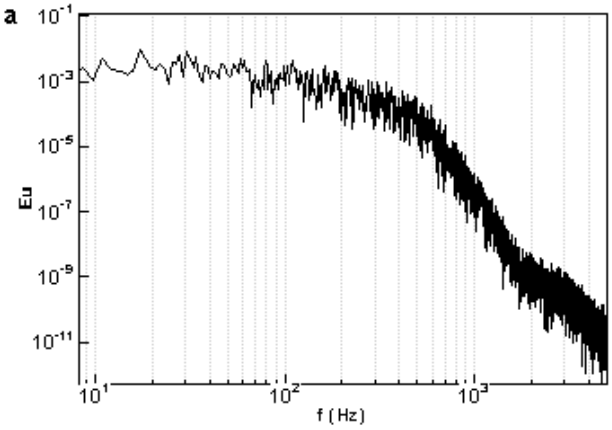

Fig.B.45. spectra at *x/D* = 1.93, *y/D* = 0.542. (FST case)

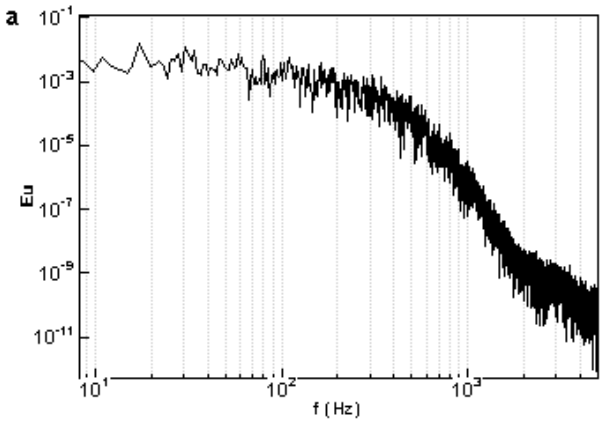

Fig.B.46. spectra at *x/D* = 1.93, *y/D* = 0.558. (FST case)

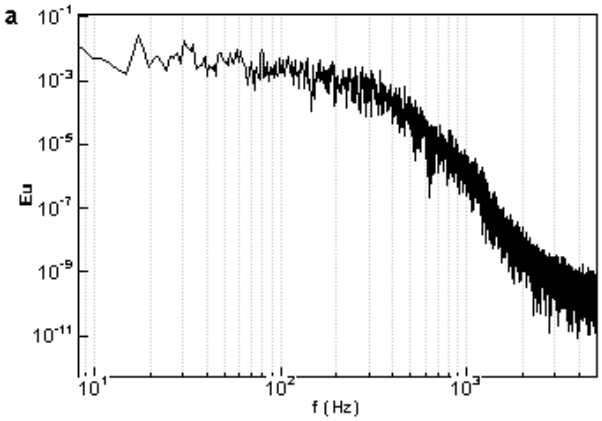

Fig.B.47. spectra at *x/D* = 1.93, *y/D* = 0.59. (FST case)

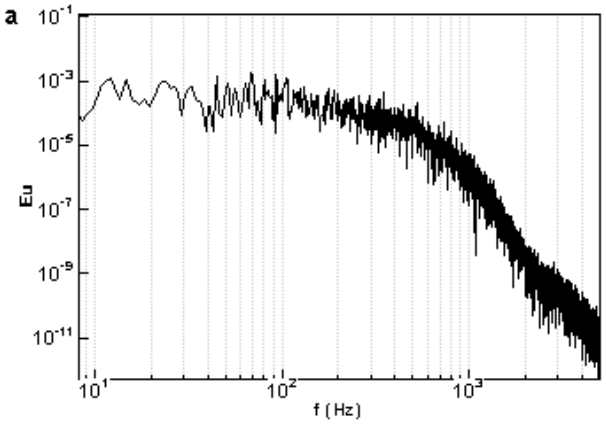

Fig.B.48. spectra at *x/D* = 1.93, *y/D* = 0.85. (FST case)

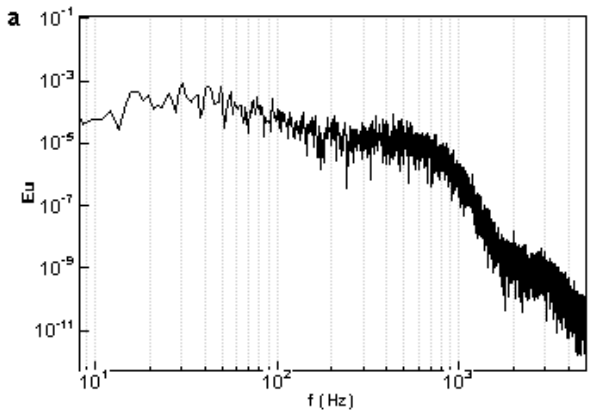

Fig.B.49. spectra at *x/D* = 0.65, *y/D* = 0.516 and spanwise plane z/D = 2.0. (FST case)

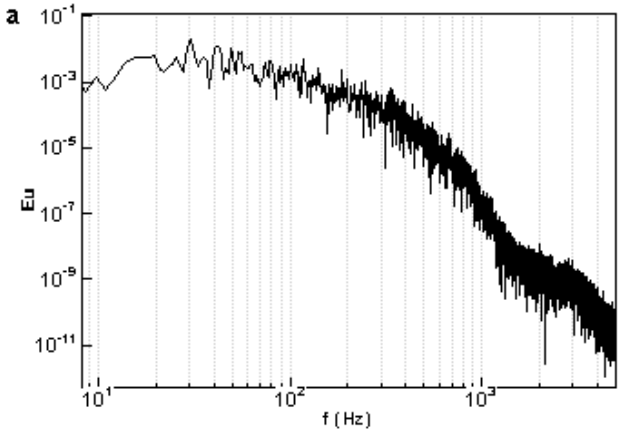

Fig.B.50. spectra at *x/D* = 0.65, *y/D* = 0.542 and spanwise plane z/D = 2.0. (FST case)

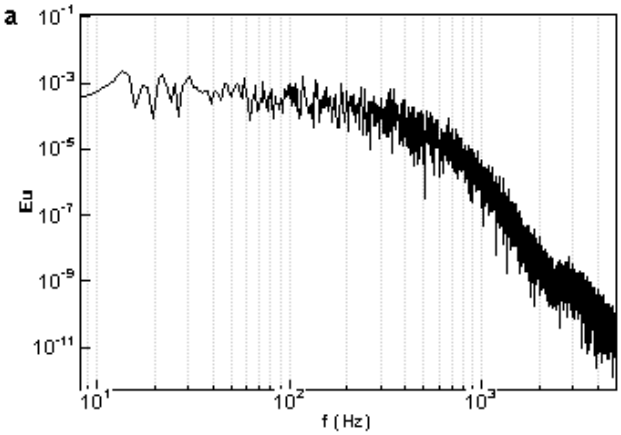

Fig.B.51. spectra at *x/D* = 0.65, *y/D* = 0.59 and spanwise plane z/D = 2.0. (FST case)

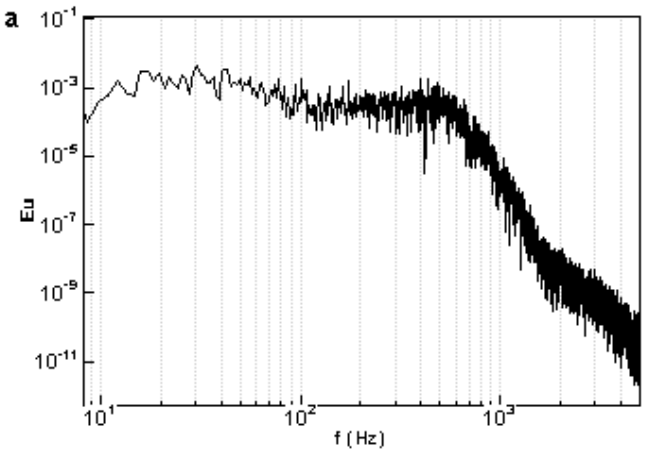

Fig.B.52. spectra at *x/D* = 1.03, *y/D* = 0.516 and spanwise plane z/D = 2.0. (FST case)

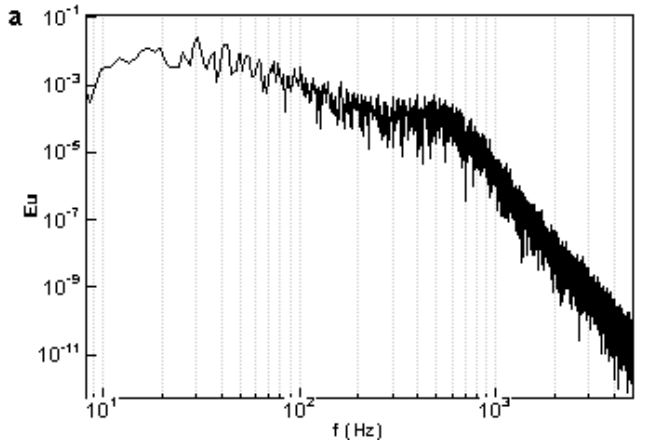

Fig.B.53. spectra at *x/D* = 1.03, *y/D* = 0.542 and spanwise plane z/D = 2.0. (FST case)

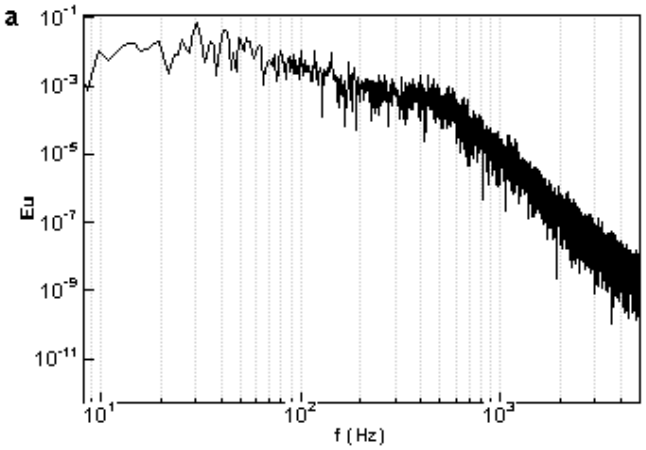

Fig.B.54. spectra at *x/D* = 1.03, *y/D* = 0.59 and spanwise plane *z*/D = 2.0. (FST case)

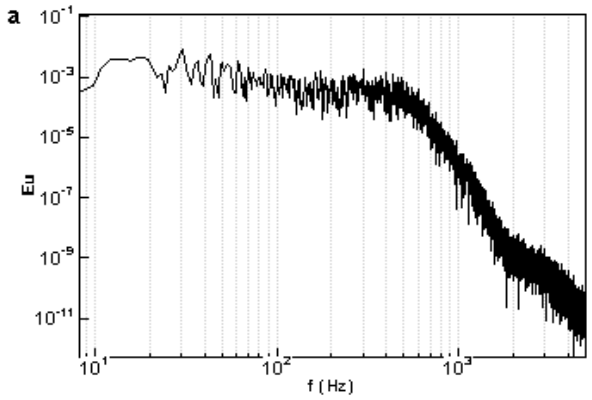

Fig.B.55. spectra at *x/D* = 1.45, *y/D* = 0.516 and spanwise plane *z*/D = 2.0. (FST case)

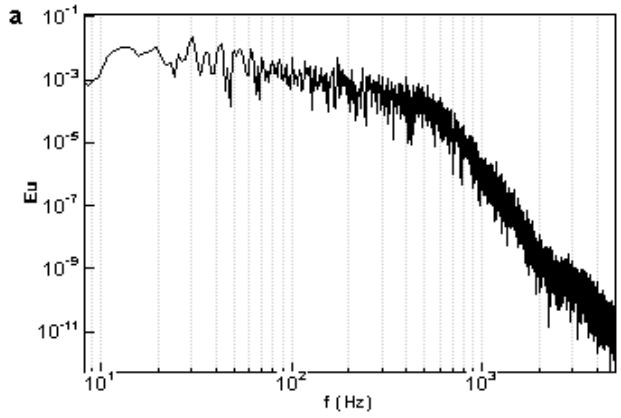

Fig.B.56. spectra at *x/D* = 1.45, *y/D* = 0.542 and spanwise plane *z*/D = 2.0. (FST case)

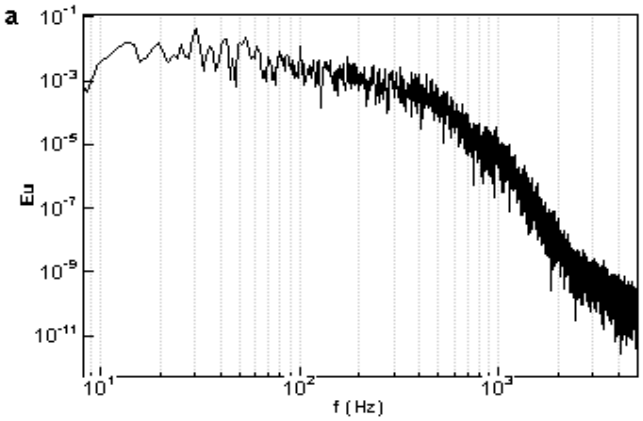

Fig.B.57. spectra at *x/D* = 1.45, *y/D* = 0.59 and spanwise plane *z*/D = 2.0. (FST case)

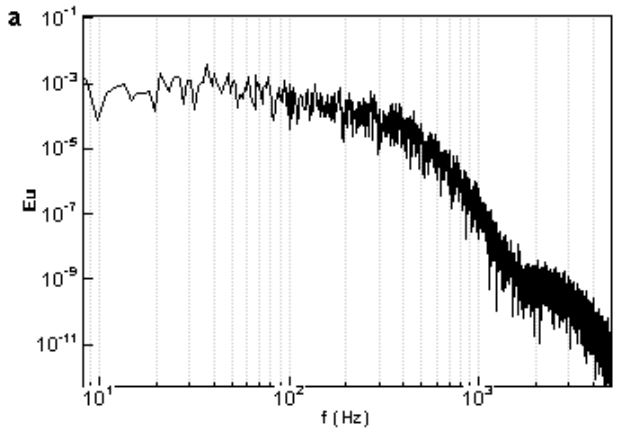

Fig.B.58. spectra at *x/D* = 1.93, *y/D* = 0.516 and spanwise plane *z*/D = 2.0. (FST case)

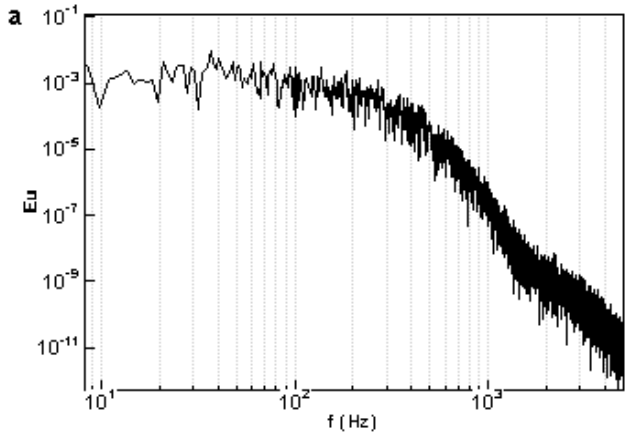

Fig.B.59. spectra at *x/D* = 1.93, *y/D* = 0.542 and spanwise plane *z*/D = 2.0. (FST case)

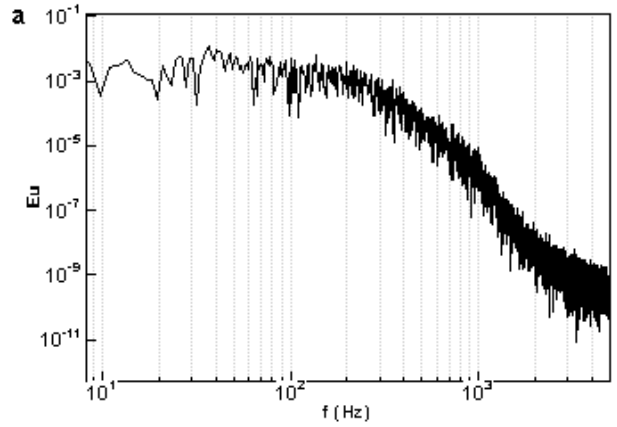

Fig.B.60. spectra at *x/D* = 1.93, *y/D* = 0.59 and spanwise plane *z*/D = 2.0. (FST case)

BIBLIOGRAPHY

Abdalla, I.E., 2004. Numerical studies of separated boundary layer transition on a flat plate with a blunt leading edge. PhD Dissertation, Loughborough University.

Abdalla, I.E., Cook, M., Yang, Z., 2007. Numerical study of transitional separated–reattached flow over surface-mounted obstacles using large-eddy simulation. Int. J. Numer. Meth. Fluid. 54, 175-206.

Abdalla, I.E., Yang, Z., 2005. Numerical study of a separated–reattached flow on a blunt plate. AIAA J. 43, 2465–2474.

Abdalla, I.E., Yang, Z., 2004a. Numerical study of the instability mechanism in transitional separating-reattaching flow. International Journal of Heat and Fluid Flow, 25, 593-605.

Abdalla, I.E., Yang Z., 2004b. Computational visualisation of separated–reattached transitional flow on a blunt plate. Journal of Flow Visualization and Image Processing, 11, 1-28.

Abdalla, I.E., Yang, Z., Cook, M., 2009. Computational analysis and flow structure of a transitional separated-reattached flow over a surface mounted obstacle and a forward-facing step. International Journal of Computational Fluid Dynamics, 23:1, 25-57.

Adrian, R., Christensen, K., Liu, Z., 2000. Analysis and interpretation of instantaneous turbulent velocity fields. Exp. Fluids 29, 275-290.

Alam, M., Sandham, N. D., 2000. Direct numerical simulation of short laminar separation bubbles with turbulent reattachment. J. Fluid Mech. 410, 1–28.

Alving Amy E., Fernholz H. H., 1996. Turbulence measurements around a mild separation bubble and downstream of reattachment. Journal of Fluid Mechanics, 322 , pp 297-328.

Brandt, L., Henningson, Dan S., 2004. Direct numerical simulations of streak breakdown in boundary layers. In Direct and Large-Eddy Simulation V, ERCOFTAC Series Vol. 9, p. 175.

Breuer, M., Rodi. W., 1994. Large-eddy simulation of turbulent flow through a straight square duct and a 1800 bend. Direct and Large-Eddy Simulation I, P.R. Voke et al. (Eds), Kluwer, 273-285.

Brevdo L., 1988. A study of absolute and convective instabilities with an application to the Eady model, Geophys. Astrophys. Fluid Dyn. 40, 1–92.

Browand, F., Trout, T. R., 1974.The turbulent mixing layer: geometry of large vortices. J. Fluid Mech. 158, 489-509.

Brown GL, Roshko A., 1974. On density effects and large structure in turbulent mixing layers. Journal of Fluid Mechanics, 64, 775–816.

Burgmann, S., Dannemann, J., and Schroder, W., 2008. Time-resolved and volumetric PIV measurements of a transitional separation bubble on an SD7003 airfoil. Exp. Fluids 44, 609.

Cantwell BJ., 1981. Organised motion in turbulent flow. Annual Review of Fluid Mechanics, 13, 457–515.

Corral, R. & Jimenez, J. 1994. Direct numerical determination of the minimum bypass Reynolds number in boundary layers. 74th Fluid Dynamics Symp., Chania, Crete, Greece, pp. 19-1-19-9.

Castro IP., Epik E., 1998. Boundary layer development after a separated region. Journal of Fluid Mechanics, 374, 91–116.

Castro, I.P., Haque, A., 1988. The structure of a shear layer bounding a separation region. Part 2. Effects of free-stream turbulence. J. Fluid Mech. 192, 577–595.

Chanderasekhar, S., 1961. Hydrodynamic and Hydromagnetic Stability. Clarendon.

Cherry, N.J., Hillier, R., Latour, M.E.M.P., 1984. Unsteady measurements in a separating and reattaching flow. J. Fluid Mech. 144, 13–46.

Comte, P., Silvestrini, J., Begou, P., 1998. Streamwise vortices in large eddy simulation of mixing layers. Eur. J. Mech., 17, 615-637.

Delcayre, F., 1997. Topology of coherent vortices in the reattachment region of a backward-facing step. In: Proceedings of the 11th Symposium on Turbulent Shear Flows, Grenoble, France, 3, 6–24.

Djilali, N., Gartshore, I.S., 1991. Turbulent flow around a bluff rectangular plate. Part I: experimental investigation. ASME Journal of Fluids Engineering, 113, 51-59.

Dahnert, J., Lyko, C., Peitsch, D., 2012. Transition mechanisms in laminar separated flow under Simulated low pressureturbine aerofoil conditions. J. Turbomach. 135, 011007.

Driver, D.M., Seegmiller, H.L., Marvin J.G., 1987. Time-dependent behaviour of reattaching shear layer. AIAA J., 25, 914-919.

Dubief, Y., Decayre, F., 2000. On coherent-vortex identification in turbulence. J. Turbulence, 1, 011.

Eaton, J.K., Johnston, J.P., 1981. A review on subsonic turbulent flow reattachment, AIAA J., 19, 1093-1100.

ERCOFTAC (European Research Community on Flow, Turbulence and Combustion), 1999. Accessec online, http://ercoftac.mech.surrey.ac.uk/transition/cases.

Ferziger, J., 2005. Marine turbulence: theories, observations, and models; Part 2: Turbulence: its origins and Structure, edited by Baumert, H.Z., Simpson, J., Sundermann, J., Cambridge, United Kingdom; Cambridge University Press, ISBN: 0521837898.

Ferziger, J., Peric, M., 2001. Computational methods for fluid dynamics. Springer, 3rd edition.

Gaster, M., 1962. A note on the relation between temporally-increasing and spatially-increasing disturbances in hydrodynamic stability. J. Fluid Mech., Vol 14, 222-224.

Gaster, M., 1965. The role of spatially growing waves in the theory of hydrodynamic stability. Prog. Aeronautical sciences, Vol. 6, 251-270.

Germano, M., Piomelli, M., Moin, P., Cabot, W. H., 1991. A dynamic subgrid-scale eddy viscosity model. Phys. Fluids A 3, 1760-765.

Giralt, F., Ferre, J., 1993. Structures and flow pattern in turbulent wakes. Phys. Fluids, A5, 1783.

Gordeyev, S.V., Thomas, F.O., 2000. Coherent Structures in the turbulent plannar Jet. Part1. Extraction of proper orthogonal decomposition eigenmodes and their self similarity. Journal of Fluid Mechanics, 414, 145-194.

Glickman TS., 1999. Glossary of Meteorology, 2nd Edition, American Meteorological Society, ISBN: 978-1878220349, accessed online at http://amsglossary.allenpress.com/glossary.

Hain, R., Kahler, C., Radespiel, R., 2009. Dynamics of laminar separation bubbles at low Reynolds number aerofoils. J. Fluid Mech. 630, 129-153.

Hammond, D. A., Redekopp, L. G., 1998. Local and global instability properties of separation bubbles. Eur. J. Mech. B/Fluids 17, 145–164.

Hadzic, I., Hanjalicm, K., 1999. Separation-Induced Transition to Turbulence: Second-Moment Closure Modelling. Flow, Turbulence and Combustion, 63: 153–173.

Hatman, A., and Wang, T., 1999. A Prediction Model for Separated Flow Transition, ASME J. Turbomach., 121, pp. 594–602.

Head, M. R., Bandyopadhyay, P., 1981. New aspects of turbulent boundary-layer structure ,Journal Fluid Mech. v 107, p. 297-338).

Hillier, R., Cherry, N.J., 1981. The effect of stream turbulence on separation bubble. Journal of Wind Engineering and Industrial Aerodynamics, Vol. 8, Issues 1-2, 49–58.

Ho, C. M., Huerre, P., 1984. Perturbed free shear layers. Annu. Rev. Fluid Mech. 16 (1984), pp. 365-424.

Huang, L. S., and Ho, C. M., 1990. Small-Scale Transition in a Plane Mixing Layer. J. Fluid Mech., 210, pp. 475–500.

Hudy, L.M., Naguib, A.M., Humphreys, W.M., 2003. Wall-pressure-array measurements beneath a separating/reattaching flow region. Phys. Fluid. 15, 706–717.

Huerre, P., Monkewitz, P. A., 1985. Absolute and convective instabilities in free shear layers. Journal of Fluid Mechanics, 159 , pp 151-168.

Huerre, P., Monkewitz, P. A., 1990. Local and global instabilities in spatially developing flows. A. Rev. Fluid Mech. 22, 473–537.

Hughes, J. D., and Walker, G. J., 2001. Natural Transition Phenomena on an Axial Compressor Blade. ASME J. Turbomach., 123, pp. 392-401.

Hui, Li.,1998. Identification of coherent structure in turbulent shear flow with wavelet correlation analysis. Journal of Fluid Engineering, 120, 778-785.

Hunt, J., Wray, A., Moin, P., 1998. Eddies, stream, and convergence zones in turbulent flows, report CTR, S88.

Hussain, AKMF., 1986. Coherent structures and turbulence. Journal of Fluid Mechanics, 173, 303-356.

Hussain, AKMF., Hayakawa M., 1987. Eduction of large-scale organised structures in a turbulent plane wake. Journal of Fluid Mechanics, 180, 193–229.

Hussain, AKMF., Melander, M. V., 1991. Understanding turbulence via vortex dynamics. In the Lumely symposium: studies in turbulence, Springer, 158-178.

Jacobs, R. G. & Durbin, P. A. 1998 Shear sheltering and the continuous spectrum of the Orr-Sommerfeld equation. Phys. Fluids 10, 2006-2011.

Jeong J., Hussain F., Schoppa W., Kim J., 1997. Coherent structure near the wall in a turbulent channel flow. Journal of Fluid Mechanics, 332, 185–214.

Jones, L.E., Sandberg, R.D. and Sandham, N.D., 2008. Direct numerical simulations of forced and unforced separation bubbles on an airfoil at incidence. Journal of Fluid Mechanics, 602, 175-207.

Keating, A., Piomelli, U., and Balaras, E., 2004. A Priori and Posteriori Tests of Inflow Conditions for Large-Eddy Simulation. Physics of Fluids, Vol. 16, No. 12, 4696–4712.

Kalter, M., Fernholz, H.H., 2001. The reduction and elimination of a closed separation region by free-stream turbulence. J. Fluid Mech. 446, 271–308.

Kim, H. T., Kline, S. J., Reynolds, W. C., 1971. The production of turbulence near a smooth wall in a turbulent boundary layer. J. Fluid Mech. 50, 133–160.

Kiya, M., Sasaki, K., 1985. Structure of large-scale vortices and unsteady reverse flow in the reattaching zone of a turbulent separation bubble. J. Fluid Mech. 154, pp. 463–491.

Kiya, M., Sasaki, K., 1983. Structure of a turbulent separation bubble. J. Fluid Mechanics, 137, 83-113.

Kobayashi, Ham, and Wu 2008. Application of a local SGS model based on coherent structures to complex geometries. International Journal of Heat and Fluid Flow. 29, 640–653.

Kundu, P.K., Cohen, I.M., 2004. Fluid Mechanics, 3rd ed., Elsevier Academic Press, ISBN: 0121782530.

Lane, J. C., Loehrke, R. I., 1980. Leading Edge Separation from a Blunt Plate at Low Reynolds Number. ASME J. Fluids Eng., 102, 494–496.

Langari, M. and Yang, Z., 2010. On transition process in separated-reattached flows. Advances and Applications in fluid Mechanics, 8, pp. 157-181.

Langtry, R.B., Menter, F.R., 2005. Transition modelling for general CFD applications in aeronautics. AIAA 2005-522.

Lang, M., Rist, U., Wagner, S., 2004. Investigations on Controlled Transition Development in a Laminar Separation Bubble by Means of LDA and PIV. Exp. Fluids, 36, pp. 43–52.

Laura, M. Hudy, Ahmad, M. Naguib, 2002, Wall-pressure-array measurement beneath a separating/reattaching flow region, 40th Aerospace science meeting and exhibit, Reno, NV, 14-17.

Le, H., Moin, P., Kim, J., 1997. Direct numerical simulation of turbulent ow over a backward-facing step. Journal of Fluid Mechanics, 330, 349-374.

Lee, I., Sung, H.J., 2001. Characteristics of wall pressure fluctuations in separated and reattaching flow over a backward-facing step. Exp. Fluid. 30, 262–272.

Leib, S. J., Wundrow, D. W. & Goldstein, M. E., 1999. Effect of free-stream turbulence and other vortical disturbances on a laminar boundary layer. J. Fluid Mech. 380, 169-203.

Lesieur, M., 1997. Turbulence in Fluids. Third ed., Kluwer academic publishers, Dordrecht.

Lilly, D.K., 1992. A proposed modification of the Germano subgrid-scale closure method. Phys. Fluids A4, 633-635.

Lund, T. S., Wu, X., and Squires, K. D., 1998. Generation of Turbulent Inflow Data for Spatially-Developing Boundary Layer Simulations. Journal of Computational Physics, Vol. 140, No. 2, pp. 233–258.

Mabey, D.G., 1972, Analysis and correlation of data on pressure fluctuations in separated flow. J. Aircraft, 9, 642-645.

Malkiel, E., and Mayle, R. E., 1996. Transition in a Separation Bubble. ASME J. Turbomach., 118, pp. 752–759.

Marxen, O., Lang, M., Rist, U., Wagner, S., 2003. A combined experimental/numerical study of unsteady phenomena in a laminar separation bubble. Flow, Turbulence and Combustion 71, 133–146.

Marxen, O., Rist, U., Wagner, S., 2004. Effect of spanwise-modulated disturbances on transition in a separated boundary layer. AIAA J. 42, 937–944.

Maucher, U., Rist, U., Wagner, S., 1997. Secondary instabilities in a laminar separation bubble. Notes on Numerical Fluid Mechanics, Vol. 60 PT, pp. 229–236.

Maucher, U., Rist, U., Wagner, S., 1998. Transitional structures in a laminar separation bubble. New Results in Numerical and Experimental Fluid Mechanics II, Proc. 11th STAB/DGLR Symposium, Berlin, vol. 72, 307–314.

Maucher, U., Rist, U., Wagner, S., 2000. DNS of Laminar-Turbulent transition in separation bubbles. Results and review workshop on high performance computing in science and engineering, pp. 279-294.

Mayle, R.E., 1991. The role of laminar-turbulent transition in gas turbine engine. ASME J. Turbomach. 113, 509-537.

McAuliffe, B. R., Yaras, M. I., 2005. Separation-Bubble-Transition Measurements on a Low-Re Airfoil Using Particle Image Velocimetry. ASME Paper No. GT2005-68663.

McAuliffe, B.R., Yaras, M.I., 2008. Numerical study of instability mechanisms leading to transition in separation bubbles. ASME J. Turbomach. 130, 1-8.

McAuliffe, B. R., Yaras, M. I., 2009. Passive manipulation of separation-bubble transition using surface modifications, J. Fluids Eng. 131(2), 021201.

McAuliffe, B.R., Yaras, M.I., 2010. Transition Mechanisms in Separation Bubbles Under Low- and Elevated-Freestream Turbulence. ASME J. Turbomach. 132, Issue 1, 011004.

McMullan, Gao, and Coats 2009. The effect of inflow conditions on the transition to turbulence in large eddy simulations of spatially developing mixing layers. International Journal of Heat and Fluid Flow, Vol. 30, 2009, pp. 1054-1066.

Melaaen, M.C., 1992. Calaulation of fluid flows with staggered and non-staggered curvilinear non-orthogonal grids – a comparison. Numerical Heat Transfer, 21, 21-39.

Miller, T.F. and Schmidt, F.W., 1988. Use of a pressure-weighted interpolation method for the solution of the incompressible Navier-Stokes equations on a non-staggered grid system. Numerical Heat Transfer, 14, 213-233.

Morinishi, Y., et al., 1998. Fully conservative higher order finite difference schemes for incompressible flow. Joumial of Computational Physics, 143, 90-124.

Nagarajan, Lele and Ferziger 2003. A robust high-order compact method for large eddy simulation. Journal of Computational Physics 191, 392–419.

Nakamura, Y. and Ozono, S., 1987. The effects of turbulence on a separated and reattaching flow. J. Fluid Mech. 178, 477–490.

Ota, T., Narita, M., 1978. Turbulent measurements in a separated and reattached flow over a blunt flat plate. ASME Trans. J. Fluid Eng. 100, pp. 224–228.

Padilla, E.L.M. and Neto, A.S., 2008. Large-eddy simulation of transition to turbulence in natural convection in a horizontal annular cavity. International Journal of Heat and Mass Transfer, 51, 3656-3668.

Papanicolau, E.L., Rodi, W., 1999. Computation of separated-flow transition using a two-layer model of turbulence. J. Turbomachinery, 121: 78–87.

Page, G. J., 2005. Influence of nozzle modelling in LES of turbulent free jets. In Proceedings of Ilth AIAAICEAS Aeroacoustics Conference, number AIAA 2005-2883.

Page, G. J., McGuirk, J. J., Hughes N. J., Hossain, M., Trumper, M. T., 2002. A computational and experimental investigation of serrated coaxial nozzles. In Proceedings of 8th AIAAICEAS Aeroacoustics Conference, number AIAA Paper No. 2002-2554, pp. 1-11.

Palikaras, A., Yakinthos, K., Goulas, A., 2002. Transition on a flat plate with a semi-circular leading edge under uniform and positive shear free-stream flow. Int. J. of Heat and Fluid Flow, 23, 455-470.

Pauley, L. L., 1994. Response of two-dimensional separation to three-dimensional disturbances. Trans. ASME J. Fluids Eng. 116, 433–438.

Pauley, L. L., Moin, P., Reynolds, W. C., 1990. The structure of two-dimensional separation. J. Fluid Mech. 220, 397–411.

Peric, M., Kessler, R. and Scheuerer, G., 1988. Comparison of finite-volume numerical methods with staggered and collocated grids. Computer & Fluids, 16, 389-403.

Perry, A. E., Chang, M., 1982. Vortex pairing: the mechanism of turbulent mixing layer growth at moderate Reynolds number. J. Fluid Mech. 63, 327-361.

Pierce, C. D., 2001. Progress-variable approach for large-eddy simulation of turbulent combustion. Dissertation for PhD. Stanford University.

Piomelli, U., 1999. Large eddy simulation: achievements and challenges. Progress in Aerospace Sciences, 35: 335-362.

Piomelli, Scotti, A., E. Balaras, 2001. Large-eddy simulations of turbulent flows, from desktop to supercomputer. VECPAR 2000.

Pokora, C., McMullan, W., Page, G., and McGuirk, J., 2011. Influence of a numerical boundary layer trips on spatio-temporal correlations within LES of a subsonic jet. AIAA Paper No. 2011-2920.

Pope. S. B., Turbulent Flows. Cambridge University Press, 2000.

Rhie, C. M., Chow, W. L., 1983. Numerical study of the turbulent flow p. Lst in aerofoil with trailing edge separation. AIAA Journal, 21: 1525-1535.

Ripley, M. D., Pauley, L. L., 1993. The unsteady structure of two-dimensional separation. phys. Fluid A 5, 3099-3106.

Rist, U., 1994. Nonlinear effects of 2D and 3D disturbances on laminar separation bubbles. Proc. IUTAM Symp. on Nonlinear Instability of Nonparallel Flows, pp. 324–333. Springer.

Rist, U., Maucher, U., 2002. Investigations of Time-Growing Instabilities in Laminar Separation Bubbles. Eur. J. Mech. B/Fluids, 21, pp. 495–509.

Roberts, S. K., Yaras, M. I., 2003. Effects of Periodic Unsteadiness, Free-Stream Turbulence and Flow Reynolds Number on Separation-Bubble Transition," ASME Paper No. GT2003-38626.

Roberts, S. K., Yaras, M. I., 2005. Modeling Transition in Separated and Attached Boundary Layers. ASME J. Turbomach., 127, pp. 402–411.

Roberts, S.K., and Yaras, M.I., 2006. Large-eddy simulation of transition in a separation- bubble. ASME J. Fluids Eng. 128, 232-238.

Robinson, S. K., 1991. Coherent motions in the turbulent boundary layer. Annual Review of Fluid Mechanics v:23, 601-639.

Ruderich, R., Fernholz, H.H., 1986. An experimental investigation of a turbulent shear flow with separation, reverse flow and reattachment. J. Fluid Mech. 163, 283–322.

Sagaut, P., 2001. Large Eddy Simulation for Incompressible Flows, Springer, Heidelberg.

Savill, A.M., 2002. New strategies in modeling by-pass transition. In: Launder, B.E., Sandham, N. (eds.) Closure strategies for turbulent and transitional flows. Cambridge University Press, Cambridge.

Scarano, F., Banocci, C., Reithmuller, 1999. Pattern recognition analysis of the turbulent flow past a backward facing step. Physics of Fluid, 11, 3808-3818.

Schlatter, P., Brandt, L., de Lange, H. C., Henningson, D. S., 2008. On streak breakdown in bypass transition," Phys. Fluids 20, 101505.

Schlichting, H., Gersten, K., 2000. Boundary layer theory, 8th ed., Springer-Verlag, Berlin.

Schmid, P.J., Henningson, D.S., 2001. Stability and transition in shear flows. Springer-Verlag. ISBN: 0387989854.

Satta, F., Simoni, D., Ubaldi, M., Zunino, P., Bertini, F., 2010. Experimental investigation of separation and transition processes on a high- lift low-pressure turbine profile under steady and unsteady inflow at low Reynolds number, Int. J. Therm. Sci. 19, 26.

Sherif ET (Reporter). 1989. Discussion of 'the role of coherent structures'. In: Whither Turbulence? Turbulence at the Crossroads, Lumley JL (ed.). Springer-Verlag: Berlin, 1989, 170-191.

Shetty, D.A., et. al., 2010. High-order incompressible large-eddy simulation of fully inhomogeneous turbulent flows. Journal of Computational Physics, 229, 8802-8822.

Simoni, D. et al., 2012. An Experimental Investigation of the Separated-Flow Transition Under High-Lift Turbine Blade Pressure Gradients. Flow, Turbulence and Combustion , 88 (1-2), 45-62.

Smith, C.R., Metzler, S.P., 1983. The characteristics of low-speed streaks in the near-wall region of a turbulent boundary layer. J Fluid Mech. 129: 27—54.

Spalart, P. R., 1988. Direct Numerical Simualtion of a Turbulent Boundary Layer Up to Reθ= 1410. Journal of Fluid Mechanics, Vol. 187, pp. 61–98.

Spalart, P. R., Strelets, M. K. H., 2000. Mechanisms of transition and heat transfer in a separation bubble. J. Fluid Mech. 403, 329–349.

Suksangpanomrung, A., Djilali, N., Moinat, P., 2000. Large-eddy simulation of separated flow over a bluff rectangular plate. Int. J. of Heat and Fluid Flow, 21, 655-663.

Tabor, G.R., Baba-Ahmadi, M.H., 2009. Inlet Conditions for Large Eddy Simulation : A Review, Computers & Fluids, doi: 10.1016/j.compfluid.2009.10.007.

Tafti, D.K., Vanka, S.P., 1991a. Numerical study of flow separation and reattachment on a blunt plate. Phys. Fluids A 3 (7), 1749–1759.

Tafti, D.K., Vanka, S.P., 1991b. A three-dimensional numerical study of flow separation and reattachment on a blunt plate. Physics of Fluids A , vol. 3, p. 2887-2909.

Tang, G., Yang , Z., McGuirk, J. J., 2004. Numerical methods for large-eddy simulation in general co-ordinates, Int. J. Numer. Meth. Fluids 2004; 46:1–18

Taylor, J.R., and Sarkar, S., 2008. Direct and large eddy simulations of a bottom Ekman layer under an external stratification. International Journal of Heat and Fluid Flow, 29, 721-–732.

Tennekes H., Lumley JL., 1972. A first course in turbulence. Cambridge, MA: MIT Press.

Versteeg, H.k., Malalasekera, W., 1995. An Introduction to Computational Fluid Dynamics: The Finite Volume Method. ISBN No.: 0-582-21884-5.

Volino, R. J., 2002a. Separated Flow Transition Under Simulated Low-Pressure Turbine Air-Foil Conditions: Part 1-Mean Flow and Turbulence Statistics. ASME J. Turbomach., 124, pp. 645.

Volino, R. J., 2002b. Separated Flow Transition Under Simulated Low- Pressure Turbine Airfoil Conditions: Part 2-Turbulence Spectra," ASME J. Turbomach., 124, pp. 656–664.

Volino, R. J., Bohl, D. G., 2004. Separated Flow Transition Mechanism and Prediction with High and Low Free stream Turbulence Under Low Pressure Turbine Conditions," ASME Paper No. GT2004-53360.

Volino, R. J., Hultgren, L. S., 2001. Measurements in Separated and Transitional Boundary Layers Under Low-Pressure Turbine Airfoil Conditions. ASME J. Turbomach., 123, pp. 189–197.

Watmuff, J. H., Pook, D. A., Sayadi, T., and Wu, X., 2010. Fundamental physical processes associated with bypass transition. in Center for Turbulence Research, Proceedings of the Summer Program (Center for Turbulence Research, 2010), p. 97.

Winant, C. D., Browand, F. K., 1974. Vortex Pairing: The Mechanism of Turbulent Mixing-Layer Growth at Moderate Reynolds Number. J. Fluid Mech., 63, pp. 237–255.

Wissink, W.G., Rodi, W., 2003. DNS of laminar separation bubble in the presence of oscillating external flow. Flow Turbul. Combust. 71, 311-331.

Xiao, F., Dianat, M., McGuirk, J. J., 2010. A rescaling/recycling method for LES inlet condition generation. 8th International ERCOFTAC Symposium on Engineering Turbulence Modelling and Measurements, Marseille, France.

Yanaoka, H., Yoshikawa, H., Ota, T., 1991. Numerical simulation of laminar flow and heat transfer over a blunt flat plate in square channel. ASME J. of Heat Transfer, 124, 8-16.

Yang, Z., 2002. Large-scale structures at various stages of separated boundary layer transition. Int. J. Numer. Meth. Fluid. 40, 723–733.

Yang, Z., Abdalla, I.E., 2009. Effects of free-stream turbulence on a transitional separated-reattached flow over a flat plate with a sharp leading edge. Int. J. Heat Fluid Flow, in press, doi:10.1016/ j.ijheatfluidflow. 2009.04.010.

Yang, Z., Abdalla, I.E., 2005. Effects of free-stream turbulence on large-scale coherent structures of separated boundary layer transition. Int. J. Numer. Meth. Fluid. 49, 331–348.

Yang, Z., Voke, P.R., 2001. Large-eddy simulation of boundary layer separation and transition at a change of surface curvature. J. Fluid Mech. 439, 305–333.

Yarusevych, S., Sullivan, P.E., Kawall, J.G., 2009. Smoke-Wire Flow Visualization in Separated Flows at Relatively High Velocities. AIAA J. 47:6, 1592–1595.

Yeo, K.S., Zhao, H.Z., Khoo, B.C., 2001. Turbulent boundary layer over a compliant surface: absolute and convective instabilities, J. Fluid Mech. 449, 141–168.

Yin, X.Y., Sun, D.-J., Wei, M.J., Wu, J.Z., 2000. Absolute and convective instability character of slender viscous vortices, Phys. Fluids 12, 1062–1072.

Yuan, Xu and Khalid 2011. Large-eddy simulation of curved-geometry flows using contravariant components of velocity. International Journal of Computational Fluid Dynamics, 25(1), 1-16.

Zang, Y, Street, R.L., Koseff, J.R., 1994. A non-staggered grid, fraction step method for time-dependent incompressible Navier-Stokes equations in curvilinear coordinates. Journal of Computational Physics, 114, 18-33.